



Efficacy Analysis of *Candida antarctica* and *Rhizomucor miehei* Regrading Biodiesel Production from Bioresources

S.Nandi^{1*}, R. Bhattacharyya¹ and G. Misra²

¹Department of Chemistry, Narula Institute of Technology, Kolkata, West Bengal, India

²Department of Chemical Technology, University of Calcutta, Kolkata West Bengal, India

Received: 10 Nov 2018

Revised: 12 Dec 2018

Accepted: 14 Jan 2019

*Address for Correspondence

S.Nandi

Department of Chemistry,
Narula Institute of Technology,
Kolkata, West Bengal, India
E-mail: sumitnandi5@gmail.com



This is an Open Access Journal / article distributed under the terms of the **Creative Commons Attribution License** (CC BY-NC-ND 3.0) which permits unrestricted use, distribution, and reproduction in any medium, provided the original work is properly cited. All rights reserved.

ABSTRACT

Biocatalyst plays a significant role for the production of alternative fuel from cheap raw materials. Efficiency of biocatalyst or enzyme determines the successful conversion of raw materials to biodiesel or alternative fuel. So the efficiency of enzyme is an important parameter and in the present study, it has been analysed through the production of biodiesel by utilising bioresources like rice bran oil fatty acid distillates (RBOFADs), a refinery by products from vegetable oil refinery industry with methanol. Two enzymes, namely Novozyme 40013 (lipase from *Candida antarctica*) and Lipozyme RM-IM (lipase from *Rhizomucor miehei*) have been utilised separately for this purpose. The comparison has been done with regard to reaction parameters like molar ratio of FAD to methanol, reaction temperature, catalyst concentration and stirrer speed or mixing effect of the reaction system. Experimental results showed that enzyme Novozyme 40013 is more effective than Lipozyme RM-IM for the production of biodiesel from cheap raw materials like RBOFAD as well as other FADs. The physical properties of biodiesel such as density, flashpoint, kinematic viscosity, cloud point, pour point etc. have been compared with diesel fuel and showed good results.

Keywords: Biodiesel, Fatty acid distillates, *Candida Antarctica*, *Rhizomucor miehei*.

INTRODUCTION

Enzyme contributes a major role as catalyst for biodiesel production from cheap raw materials. Significant advantages of using enzymes are its productivity, ecofriendliness, selective nature, minimum purification stage, consumption of less energy and reuse^{1,2}. So efficiency of enzyme with respect to different parameters is an important area of investigation of current research. Enzyme efficacy with regard to biodiesel production has been reviewed in



**Nandi et al.**

the present study by maintaining selective parameters of reaction like mol ratios of reactants, reaction temperature, concentration of catalyst and mixing intensity. Enzymatic production of biodiesel from cheap raw materials, its performance characteristics and application in diesel engines has been studied by several researchers. Arumugam and Ponnusami³ used waste sardine oil for biodiesel production using *Aspergillus niger* lipase and also analysed the engine performance. Narwal et al⁴ studied the production of biodiesel from non edible castor oil using immobilize lipase from *Bacillus aerius* and characterized it. Yan et al⁵ analysed tandem lipases for production of biodiesel from waste grease through esterification and transesterification process. Lopresto et al⁶ used waste vegetable oil for the production of biodiesel using Lipase from *Pseudomonas cepacia* and recovered the used lipase for further use. Abedin et al⁷ investigated the production of Alexandrian laurel (*Calophyllum inophyllum*) biodiesel (ALB) and studied the effects of its fatty acid methyl ester (FAME) compositions and physicochemical properties on the engine performance, combustion, and emissions. Kumar and Prasanna⁸ investigation the performance and emission characteristics of a diesel engine using Mahua biodiesel and reported satisfactory results. Taher et al⁹ produced biodiesel from waste oil in ionic liquid medium using immobilise lipase and regression models were developed to predict the optimal production which is found to be adequate and statistically acceptable. Katiyar and Ali¹⁰ entrapped enzyme in silica particles and studied the transesterification reaction. They also successfully reused the entrapped enzyme. Verma and Sharma¹¹ reviewed different process parameters for biodiesel production and focused on the various technical aspects of biodiesel production methodology. Prabakaran et al¹² studied the efficacy of enzymatic transesterification of *Chlorococcum* sp. algal oils for biodiesel production. Aarthy et al¹³ successfully used yeast lipase for the enzymatic transesterification to produce biodiesel. Properties and uses of biodiesel in diesel engines were also analysed critically by several researchers. Mahmudul et al¹⁴ studied a critical review on characterization and performance of biodiesel as an alternative fuel in diesel engines. Datta and Mandal¹⁵ made a comprehensive review of biodiesel as an alternative fuel for compression ignition engine. Venkatesan et al¹⁶ analysed the diesel blended with pongamia oil methyl ester for performance and emission characteristics and obtained satisfactory results. Ghazali et al¹⁷, Nursal et al¹⁸ and Silva et al¹⁹ made a critical observations on engine performance, exhaust gas emissions and NOx emissions using biodiesel as fuel or biodiesel blends as fuel produced from different feedstocks.

But the analysis of enzyme efficacy for the production of biodiesel from by products of refinery industries has been little studied. Based on these observations, a parametric analysis has been made in the present study for identifying the efficiency of enzymes between Novozyme 40013 and Lipozyme RM-IM for the production of biodiesel from RBOFAD. Experimental study showed that enzyme Novozyme 40013 is more suitable than Lipozyme RM-IM for biodiesel production from RBOFAD at temperature 60 C with its 3% concentration having a mixing intensity of 500 rpm for 4 hrs maintaining a molar ratio of 2:1 of methanol and RBOFAD.

MATERIALS AND METHODS

Materials

The RBOFAD used in this study was provided by M/s. A.S. Oil Mills, Burdwan, West Bengal, India. The enzyme used in the following studies was Novozyme 40013 (*Candida antarctica*) immobilized lipase and Lipozyme RM-IM (lipase from *Rhizomucor miehei*) which was a kind gift of Novozyme South Asia Pvt. Ltd. Bangalore, India. The chemicals used in this work were methanol and hexane purchased from S.D. Fine Chemicals (Mumbai, India). Except otherwise specified all other chemicals used were A.R. Grade.

Esterification reaction

Initially, RBOFAD was taken in an Erlenmeyer flask and heated up to 80°C to drive off moisture by continuous stirring for about 1 h. After that, this raw material has been divided into two parts. One part was used with enzyme



**Nandi et al.**

Novozyme 40013 and other part with Lipozyme RM-IM in the presence of alcohol maintaining identical reaction conditions. Alcohol was added in stepwise manner in an appropriate proportion using solvent hexane fitted with a water condenser and stirred by a magnetic stirrer at a specified temperature for 3 hours. Stepwise addition of methanol was allowed to minimize the deactivation of enzyme.

Quantification of reaction progress

During the reaction, continuous sampling and analysis were done by withdrawing the sample in to a capped vial and removing enzyme through centrifugation. The progress of reaction or production of biodiesel was monitored by thin layer chromatographic (TLC) method and the typical yield of each reaction product was determined separately by column chromatography. TLC was done by spotting the lipid mixture on a silica-gel G plate (0.2 mm thick) using hexane-diethyl ether-acetic acid (90:10:1) as a developing solvent²⁰. The composition of methyl esters was determined by column chromatography using silicic acid as an adsorbent and 160 mL of hexane-diethyl ether: 99:1 as eluting solvent²¹. After completion of reaction, the enzyme was washed with hexane, dried and reused for the next experiment. Biodiesel characterization was done according to the American Standard Testing Method (ASTM). Values are reported as mean \pm s.d., where n=3 (n=no of observations).

RESULTS AND DISCUSSIONS

The physicochemical properties and fatty acid profiles of RBOFAD are shown in Table 1. It is shown that FFAs are the major component of RBOFAD. They represent approximately 92.35% of the RBOFAD on weight basis. As reported in the literature, the fatty acid composition of the by product from vegetable oil refinery industry is a reflection of fatty acid composition of the parent oil. High Iodine value indicates higher amount of unsaturated FFAs in the RBOFAD which is also reflected in the fatty acid composition. Apart from FFAs, RBOFAD contains minor amount of neutral glycerides and unsaponifiable matters.

Enzyme efficacy w.r.t moles of alcohol

Efficiency of enzyme NS 40013 and Lipozyme RM-IM has been compared through the conversion of biodiesel production by changing the moles of alcohol with fixed amount of RBOFAD at temperature 60°C using 3% (wt/wt) biocatalyst for 4 hours with a mixing intensity 500 rpm. Different molar ratios of methanol to RBOFAD used here are 1:1 to 2.5:1 and the effect is shown in figure 1. It has been observed from the figure that in all mole ratios of methanol to RBOFAD, NS 40013 always contributes higher percentage of biodiesel conversion than Lipozyme RM-IM and maximum biodiesel was obtained with 2:1 molar ratio of methanol to RBOFAD. Increasing concentration of methanol further did not enhance the reaction as evidenced from the figure. Stepwise addition of methanol has been the most important strategy to avoid lipase denaturation in both the cases. Deactivation of enzyme has been prevented by keeping the alcohol concentration low. Two consecutive addition of methanol has been arranged i.e. half alcohol at time 0 and half after 1 hr in both the cases. Stepwise addition also improves the conversion of biodiesel from RBOFAD.

Enzyme efficacy w.r.t enzyme concentration

Concentration of enzyme plays a vital role for the conversion of biodiesel production and so enzyme efficacy of NS 40013 and Lipozyme RM-IM has been analysed w.r.t. its concentration. The concentration of both the enzymes has been increased from 1-4% maintaining the same reaction parameters i.e. temperature 60°C, molar ratio of methanol to RBOFAD 2:1 for 4 hours with a mixing intensity 500 rpm which is indicated in figure 2. It has been observed from the figure that in all the concentrations of enzymes, NS 40013 always contributes higher percentage of biodiesel conversion than Lipozyme RM-IM and maximum biodiesel was obtained with 3% (w/w) concentration of NS 40013.



**Nandi et al.**

Enhancing concentration of enzyme did not show any significant increase in production as, in higher percentage of enzyme, agglomeration may occur. Due to agglomeration of enzyme, some of the active sites of the enzyme may be blocked and conversion rate decreases.

Enzyme efficacy w.r.t. temperature of reaction

Activation energy of a reaction determines the rate and progress of reaction. This is due to the fact that as the temperature rises, activation energy of molecules increases and so kinetic energy of reacting molecules enhance. So temperature is one of the important parameters which determine the rate of conversion of RBOFAD and methanol to biodiesel through the formation of activated complex. In our study, the enzyme efficacy has been compared by varying temperature from 40 - 70 C using molar ratio of alcohol to RBOFAD 2:1, enzyme concentration 3%, mixing intensity 500 rpm for 4 hrs as indicated in figure 3. Experiments showed that NS 40013 is more effective regarding conversion of biodiesel than Lipozyme RM-IM and maximum biodiesel was obtained at temperature 60 C. Increasing temperature did not enhance the percentage conversion may be due to deactivation of enzyme at higher temperature.

Enzyme efficacy w.r.t. mixing intensity

Proper mixing of the reactant molecules with stirrer helps to reach them near active sites of enzyme molecules. After that, rate of conversion enhances due to the right shape and binding power of active sites with the reactant molecules. Here, enzyme efficacy has been compared using enzymes NS 40013 and Lipozyme RM-IM by varying mixing intensity from 300 to 600 rpm using molar ratio of alcohol to RBOFAD 2:1, enzyme concentration 3%, temperature 60 C for 4 hrs which is indicated in figure 4. Experiments showed that in all the mixing intensity, NS 40013 is more efficient in converting biodiesel from RBOFAD and methanol and 500 rpm is the optimum mixing intensity which contributes maximum conversion.

Biodiesel characterization

The characteristics of biodiesel are compared with diesel fuel and it has been shown in Table 2. It is significant that the properties are quite comparable with the standard diesel fuel.

CONCLUSION

Reaction parameters have a key role for biodiesel production from cheap raw materials and the suitable reaction parameters can be identified only when the catalyst enzyme works efficiently. Present comparative study deals with two enzymes, Novozyme 40013 (lipase from *Candida antarctica*) and Lipozyme RM-IM (lipase from *Rhizomucor miehei*) and the operating conditions identified the efficacy of former enzyme than the latter. So biodiesel production rate, its percentage conversion and downstream purification stage would be easier for higher enzyme efficiency and in that the enzyme Novozyme 40013 is found to be more suitable. The biodiesel prepared using this enzyme also meets the characteristics of diesel fuel and found to be suitable for application in diesel engines.

ACKNOWLEDGEMENTS

Our sincere thanks to University Grants Commission (UGC) for financial support for carrying out this research work. (Sanction No. F. PSW-254/15-16 (ERO))



**Nandi et al.****REFERENCES**

1. Noraini MY et al. A review on potential enzymatic reaction for biofuel production from algae. *Renewable and Sustainable Energy Reviews* 2014; 39: 24-34.
2. Nandi S and Bhattacharyya R. Biodiesel from *Jatropha Curcas* oil: A comparative study between chemical and biocatalytic transesterification. *Research Journal of Recent Sciences* 2014 4: 44-50.
3. Arumugam A and Ponnusami V. Production of biodiesel by enzymatic transesterification of waste sardine oil and evaluation of its engine performance. *Heliyon* 3 2017; doi: 10.1016/j.heliyon.2017.e00486.
4. Narwal SK et al. Production and characterization of biodiesel using non edible castor oil by immobilize lipase from *Bacillus aerius*. *Biomed. Res. Int.* 2015; doi: 10.1155/2015/281934.
5. Yan J et al. Efficient production of biodiesel from waste grease: One-pot esterification and transesterification with tandem lipases. *Bioresour. Technol* 2012; 123: 332–337.
6. Lopresto CG et al. Enzymatic transesterification of waste vegetable oil to produce biodiesel. *Ecotoxicology and Environmental Safety* 2015; 121: 229-235.
7. Abedin MJ et al. Production of biodiesel from a non edible source and study of its combustion and emission characteristics: A comparative study with B5. *Renewable Energy* 2016; 88: 20-29.
8. Kumar S and Prasanna B. Experimental Investigation on Performance and Emission Characteristics of a Diesel Engine Fuelled with Mahua Biodiesel Using Additive. *Energy Procedia* 2014; 54: 569-579.
9. Taher H et al. Enzymatic production of biodiesel from waste oil in ionic liquid medium. *Biofuels* 2017; doi: 10.1080/17597269.2017.1316145.
10. Katiyar M and Ali A. One - Pot Lipase Entrapment Within Silica Particles to Prepare a Stable and Reusable Biocatalyst for Transesterification. *J. Am. Oil Chem. Soc.* 2015; 92: 623–632.
11. Verma P and Sharma MP. Review of process parameters for biodiesel production from different feedstocks. *Renew. Sust. Energy Rev.* 2016; 62: 1063–1071.
12. Prabakaran P et al. Waste and Biomass Valorization. 2018; <https://doi.org/10.1007/s12649-018-0211-3>, 1-9.
13. Aarthy M et al. Enzymatic transesterification for production of biodiesel using yeast lipases: An overview. *Chem. Eng. Res. Des.* 2014; 92: 1591–1601.
14. Mahmudul HM et al. Production, characterization and performance of biodiesel as an alternative fuel in diesel engines-A review. *Renew. Sustain. Energy Rev.* 2017; 72: 497–509.
15. Datta A and Mandal BK. A comprehensive review of biodiesel as an alternative fuel for compression ignition engine. *Renew. Sustain. Energy Rev.* 2016; 57: 799–821.
16. Venkatesan M et al. Performance and emission analysis of pongamia oil methyl ester with diesel blend. *Middle-East J. Sci. Res.* 2012; 12: 1758–1765.
17. Wan Ghazali WNM et al. Effects of biodiesel from different feedstocks on engine performance and emissions: A review. *Renew. Sustain. Energy Rev.* 2015; 51: 585–602.
18. Nursal RS et al. Comparative study of the performance and exhaust gas emissions of biodiesels derived from three different feedstocks with diesel on marine auxiliary diesel engine. *ARPN J. Eng. Appl. Sci.* 2017; 12: 2017–2028.
19. Vieira da Silva MA et al. Comparative study of NOx emissions of biodiesel-diesel blends from soybean, palm and waste frying oils using methyl and ethyl transesterification routes. *Fuel* 2017; 194: 144–156.
20. Kates M. *Techniques of lipidology, Separation of Lipid Mixtures*, North-Holland Publishing Company, Amsterdam, London; 1972a. p 428-435.
21. Kates M. *Techniques of lipidology, Separation of Lipid Mixtures*, North-Holland Publishing Company, Amsterdam, London; p 397-405.





Nandi et al.

Table 1: Physicochemical properties of RBOFAD

Characteristics	Amount	Characteristics	Amount
Total acidity (wt%)	92.35±0.273	Iodine value (I ₂ /100g)	77.29±0.207
C 16:0	28.3±0.136	Neutral glycerides (wt%)	4.37±0.053
C 18:0	1.2±0.019	Unsaponifiable matters (wt%)	3.28±0.027
C 18:1	37.1±0.173		
C 18:2	33.2±0.191		

Table 2: Characteristics of Biodiesel with diesel fuel standard

Characteristics	Biodiesel	Diesel fuel	Test method
Density (gm/cc)	0.858±0.025	0.840	ASTMD- 4052-96
Flash point (°C)	215±0.081	56	ASTMD-93
Fire point (°C)	222±0.078	62	-----
Kinematic viscosity @ 40°C (Cst)	4.82±0.047	3.02	ASTMD-445
Specific gravity	0.879±0.001	0.85	-----
Calorific value (Kcal/Kg)	3650±2.567	4285	ASTM-6751
Acid value (mg/KOH)	0.42±0.001	0.36	ASTMD-64-01
Refractive index at 40 C	1.41±0.002	1.45	-----
Cetane number	41±0.234	49	ASTMD- 6751

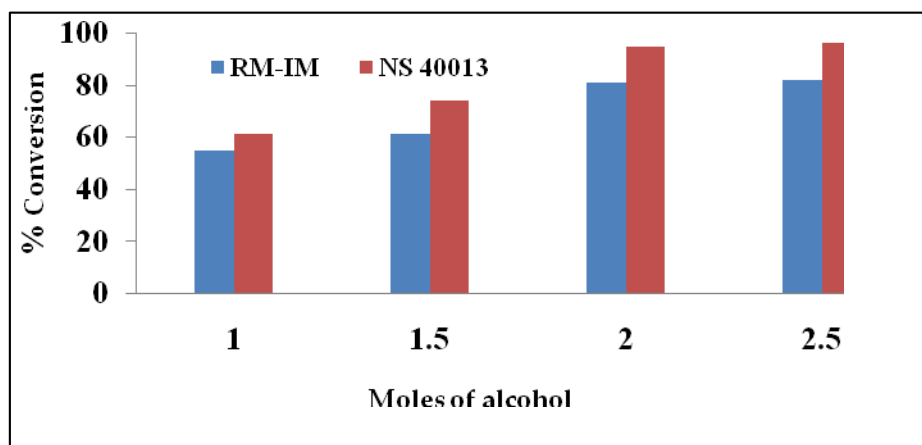


Figure 1: Enzyme efficacy w.r.t. moles of alcohol
(Temperature-60 C, Enzyme- 3%, Mixing intensity- 500 rpm, Time-4hrs)





Nandi et al.

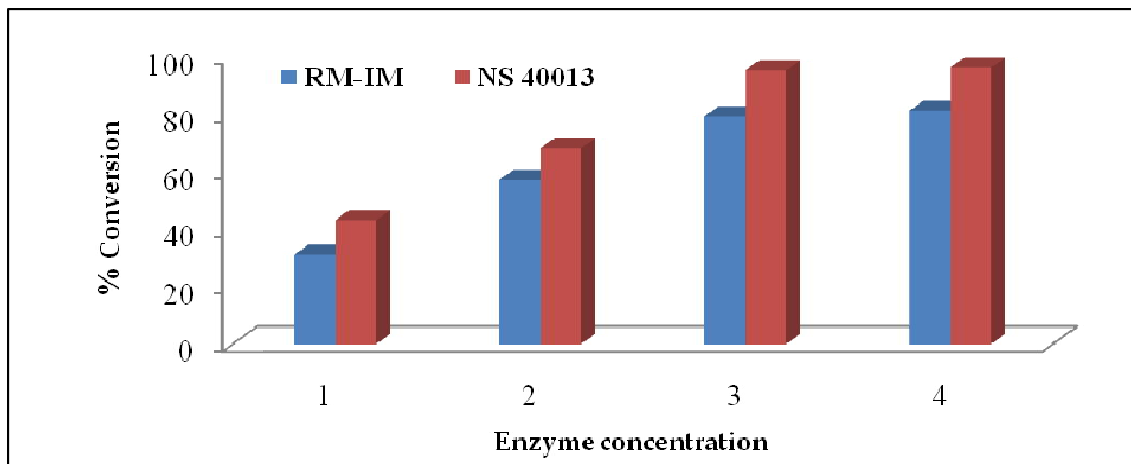


Figure 2: Enzyme efficacy w.r.t. Concentration of enzyme
(Temperature-60 C, Methanol: RBOFAD - 2:1, Mixing intensity- 500 rpm, Time-4hrs)

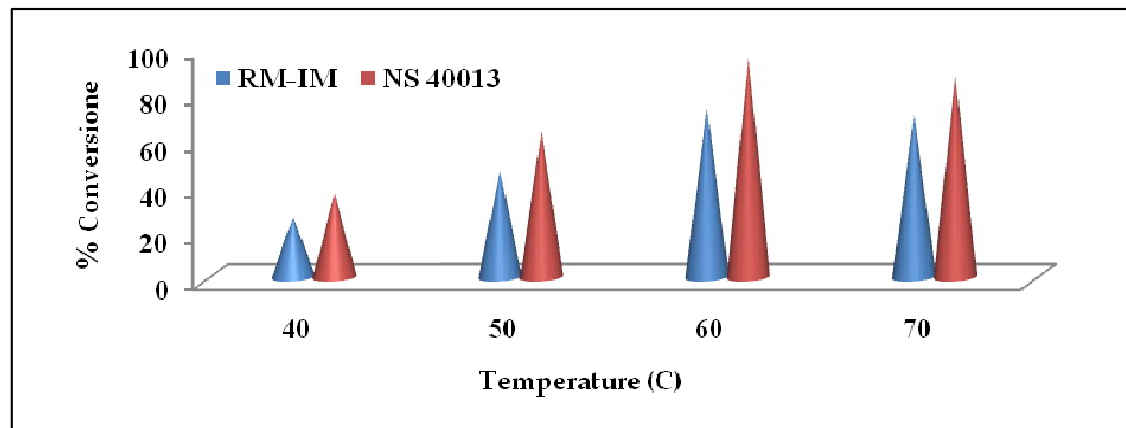


Figure 3: Enzyme efficacy w.r.t. Temperature of reaction
(Enzyme- 3%, Methanol: RBOFAD - 2:1, Mixing intensity- 500 rpm, Time - 4hrs)

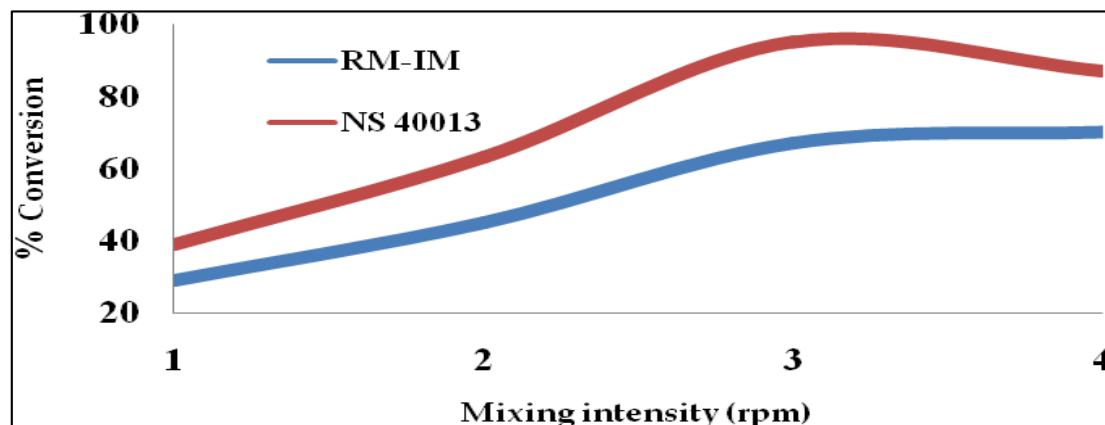


Figure 4: Enzyme efficacy w.r.t. Mixing intensity
[1→300 rpm, 2→400 rpm, 3→500 rpm, 4→600 rpm]
(Enzyme- 3%, Methanol: RBOFAD - 2:1, Temperature-60 C, Time - 4hrs)





Spectroscopic Evaluation and Calibration Technique for Different Fiber Optic Sensors

Shehab A. Kadhim¹, Nibras K.Juber¹and Firdous Sh. Ahmed^{2*}

¹Materials Research Directorate, Ministry of Science and Technology, Iraq.

²Collage of Agricultural Engineering Sciences, University of Baghdad, Iraq.

Received: 07 Oct 2018

Revised: 10 Nov 2018

Accepted: 14 Dec 2018

*Address for Correspondence

Firdous Sh. Ahmed

Collage of Agricultural Engineering Sciences,

University of Baghdad, Iraq.

E mail: firdousshakir@yahoo.com



This is an Open Access Journal / article distributed under the terms of the **Creative Commons Attribution License** (CC BY-NC-ND 3.0) which permits unrestricted use, distribution, and reproduction in any medium, provided the original work is properly cited. All rights reserved.

ABSTRACT

In this paper, the platform for evaluating and calibrating FBG sensors and optical fiber sensors is designed and constructed. Calibration is a number of measuring processes carried out under specific conditions by using instruments that are in agreement with SI system. The intention is to specify the accuracy of the sensor and decide whether it is compatible to be used or not, and this can be done by finding a relationship between the standard and measured values. This research aimed to calibrate the optical fiber sensors especially the ones used for measuring temperature and strain. It is known that the working principle of temperature and strain sensors is that, the transducer modulates wavelength and phase which in turn gives rise to a change in the characteristics of the optical signal received at high resolution detector (optical spectrum analyzer or spectrograph). Both uniform Fiber Bragg Grating (FBG) and Mach-Zehnder interferometric (MZI) sensors based on single mode fibers were implemented for comparison and investigation due to measurement of the Bragg wavelength shift. It has been shown from the results that the FBG is linearly sensitive to variations in temperature, strain. The extracted temperature distribution was characterized by two parameters of amplitude, width and the center position shift. The strain distribution was determined from the analysis of the intensity reflection spectrum. Optigrating software has been used to simulate the input parameters before and after applying heat and strain and a good agreement between the results gotten practically and by simulation.

Key Words: Optical fiber sensors, wavelength modulated fiber optic sensor, phase modulated fiber optic sensor, fiber Bragg grating sensor. Fiber optic sensor based on the Mach-Zehnder interferometer.



**Shehab A. Kadhim et al.**

INTRODUCTION

Over the past few years there have been revolutionary inventions done in the field of fiber optics. This is due to the advantages of optical transmission over electrical transmission [3]. In the field of optical fibers, lots of researches have been done; focus on suitable design of fibers. Among these researches, one of the fields is designing a sensing system based on optical fiber and optical sensors [3]. Here rises the value and need for calibrating such systems before introducing them to perform certain sensing application.

Fiber optics sensor principles

Fiber-optic sensors are fiber-based devices for sensing some quantity, typically temperature or mechanical strain [1]. The general principle of such devices is that light from a laser (often single-frequency fiber laser) is sent through an optical fiber, experiences subtle changes of its parameters either in the fiber or in one or several fiber Bragg gratings, and the light reaches a detector arrangement which measures the changes [1]. Optical fibers are used either as the sensing element (intrinsic sensors) or as a means of relaying signals from a remote sensor to the electronics that process the signals (extrinsic sensors) [2]. Depending on the application, fiber may be used because of its small size, immune to electromagnetic interference and designed to withstand high temperature as well [2].

As shown in figure one an optical fiber sensing system is composed of a light source (laser, laser diode, LED, etc.), optical fiber as transmission channel or sensing element and a detector and at the end processing devices (oscilloscope, optical spectrum analyzer, etc.) [3]. Fiber optic sensor technology offers different parameter measurements such as strain, pressure, temperature, current and many more things [3]. For that different type of sensors are used and these sensors convert these parameters to optical parameters like light intensity or phase or polarization of light [3]. These converted parameters are transmitted using an optical link over a long distance. As a result, the possibility to replace ordinary sensors like acceleration, electric and magnetic field measurement, temperature, pressure, acoustics, vibration, linear and angular position, strain, humidity, viscosity, chemical measurements and many others, should be replaced by optical sensors [3].

Optical sensor itself is efficient to monitor physical, biological, chemical changes in the object or over a process [3]. Fiber optics sensors can be classified under three categories: the sensing location, the operating principal and the applications. Depending on location of the sensor, a fiber sensor can be classified as an intrinsic or extrinsic. Based on the operating principal and demodulation technique, a fiber optic sensor can be further divided into intensity, phase, and frequency or polarization sensor. Based on application, fiber sensors can be classified in physical, chemical, bio-chemical sensors [3]. In this research an intrinsic, phase-modulated and wavelength modulated for measuring temperature and strain sensors are used as study case. A uniform (FBG) and Mach-Zehnder interferometric (MZI) sensors based on single mode fibers were implemented for comparison and investigation.

Wavelength Modulated Fiber Optic Sensors

Whenever there is a change in measuring parameter, this kind of optical sensor will make a change in their wavelength of light generation. This can be determined by the light detector at receiver side and that will make measure from the change in wavelength to change in measured parameter [3]. Bragg grating sensors are of this type.

Fiber Bragg grating sensors

Formed by constructing periodic changes in the index of refraction in the core of single mode optical fiber. This change in refractive index can be made by exposing the fiber core to an intense interference pattern of UV energy [3].





Shehab A. Kadhim *et al.*

The Bragg grating sensor operation is shown in figure 2 in which light emitted by LED source is used and center frequency is also shown in figure which is also closer to the Bragg wavelength. When light propagates through the Grating and part of signal is reflected back at the Bragg wavelength. The complimentary part of the process shows a small silver of signal removed from the total transmitted signal [3]. Fiber based on doped silica contains defects in the glass structure. When the fiber is irradiated with certain wavelengths of UV-light these defects absorb some of the radiation resulting in a permanent increase in the refractive index locally in the fiber, depending on the amount of absorbed radiation. If the irradiation along with the fiber occurs with periodically varying intensity, an FBG is produced with the characteristics of the following equation:[4]

$$\lambda_B = 2n_{\text{eff}} \Lambda$$

Phase Modulated Fiber Optics Sensors or interferometric sensors

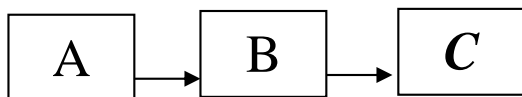
These sensors rely on the interferometric techniques. Generally the sensor employs a coherent light source such as a laser and two single mode optical fibers [4]. Light is split and coupled into both the fibers, if the measurand perturbs the optical properties of one of the fibers relative to the other, a phase shift occurs [4]. The change in phase can be measured very precisely. There are four kinds of interferometric configurations: Mach-Zender, Michelson, Sagnac interferometers – are the two beam interferometers- while in the case of Fabry-Perot interferometer occurs [4].

Fiber optic sensor based on the Mach-Zehnder interferometer:

Mach-Zehnder interferometer is commonly used in diverse sensing applications because of their flexible configurations. The interferometer has two independent arms, the reference arm and the sensing arm. The incident light is split into two arms by a fiber coupler and the recombined by another fiber coupler. For sensing applications, the reference arm is kept isolated from external variation and only the sensing arm is exposed to the variation. The variation in the sensing arm is created because of the temperature and strain change, which in return leads to the change in the optical path difference which can be detected easily by analyzing the variation in the interference signal [5].

Experimental Setup for Availability Analysis

In the field of optical fibers, lots of researches have been done, which focus on suitable design of fibers. Among these researches, one of the fields is designing a sensing system based on optical fiber and optical sensors. And here rises the need for designing a calibration platform to calibrate and evaluate the sensors before being used in optical sensing system. The experimental setup is shown in the following diagram:



An optical fiber sensing system is composed of :-

A-light source

Is a key element in many fiber optic systems. Before using the source it is very essential to know its maximum power output, the wavelength of emission, linewidth, radiation pattern and modulation bandwidth which are important when selecting a light source to achieve the best performance of the sensor. The optical sources used for sensors, range from hot filament lamps to semiconductor lasers. These sources can be placed into two groups incoherent and





Shehab A. Kadhim et al.

coherent sources. For the sensors based on interference phenomenon, coherent sources with single mode fibers are used. In a laboratory demonstration experiment, a visible laser such as He-Ne laser may be the preferred source while in commercial applications, the laser diode is preferred[5].

B-Sensing element or transducer

The light from the source is coupled into the fiber using suitable optics. The sensing action occurs either within the fiber or external to the fiber. In intrinsic sensors, the optical fibers become the active element of the sensor. The phenomenon or the parameter under investigation modifies the light propagation in the fiber[5].

C-Detectingsystem

The optical detector is another important component of optical fiber sensors. The optical detector converts the optical signal to an electrical one. The signal is then processed either to record or to display. To perform efficiently, an optical detector should be highly sensitive with a fast response time and linear relationship between current and incident energy and the signal to noise ratio should be as large as possible so that the smallest possible optical signal is detected [6].

Study case

Current researches on optical fiber temperature and strain sensing are focused on improving the accuracy, measurement range and reducing the cost as well. In many practical applications, it is required to monitor the temperature in order to achieve temperature compensation while measuring the environmental parameters. The basic concept behind the FBG sensors is the change in properties of the sensor as a response to environmental changes such as strain and temperature that alter the condition of FBG. As a result, the spectrum of both reflected and transmitted waves are changed. With the proper equipment the spectral changes can be measured and analyzed to determine the temperature and strain values, and other variables of interest. As mentioned above Calibration is a number of measuring processes carried out under specific conditions by using instruments that are in agreement with SI system. The intention is to specify the accuracy of the sensor and decide whether it is compatible to be used or not, and this can be done by finding a relationship between the standard and measured values, in this research this done by two steps. First, calibrating of the fiber Bragg grating at room temperature is carried out without being exposed to any kind of temperature/strain variation. Second, by exposed it to heat variation and study its behaviour. The Bragg grating can be described theoretically by using coupled-mode equations. Here important properties are summarized for the tightly bound single mode propagation through a uniform grating. The grating is assumed to have a sinusoidal index profile with amplitude Δn . The reflectivity, of the grating at the Bragg wavelength is expressed by the simple equation:

$$R = \tanh^2(kL)$$

Where, $k = (\pi/\lambda) \Delta n$, is the coupling coefficient and L is the length of the grating.

The reflectivity is determined by kL , and a grating with a kL greater than one is termed a strong grating whereas a weak grating has a kL less than one. Figure 3 shows the typical reflection spectra for weak and strong gratings[7, 8]. The other important property of FBGs is the reflection bandwidth. In case of weak coupling ($kL < 1$). The $\Delta\lambda_{FWHM}$ is approximated by the spectral distance from the Bragg wavelength, λ_B to the neighboring dip wavelength, λ_D .

$$\Delta\lambda_{FWHM} \approx (\lambda_D - \lambda_B) = \lambda_B^2 (2N_{eff}L)$$





Shehab A. Kadhim *et al.*

The bandwidth of a weak grating is inversely proportional to the grating length and can be very narrow for a long grating. On the other hand, in the case of strong coupling ($kL > 1$), $\Delta\lambda_{FWHM}$ is approximated by the wavelength difference between the adjacent reflection dips across the Bragg wavelength,

$$\Delta\lambda_{FWHM} = 4 \lambda_B^2 k / (\pi N_{eff}) .$$

The bandwidth of the FBG is limited by the attainable values of the index perturbation, Δn , of the photosensitivity, and several nanometers in the actual limit corresponding to $\Delta n \approx 0.001$ at wavelengths used for optical fiber sensor 1.5 μm [7]. Above the theoretical part is mentioned and now the practical part will be discussed where The FBG used for this work is manufactured by the Raysung Photonics Inc. The fiber used was SMF-28 with the core diameter of 8 μm . This fiber supports single mode at a wavelength of (1550 \pm 0.3 nm). According to the specification sheet as shown in figure (4), 99% reflection occurs from (1550 \pm 0.3 nm).

To characterize the FBG a (LPS-1550-FC) Pigtailed Laser Diodes, Single Mode Fiber, from THORLAB Inc. is used with center wavelength about (1550 nm), output power approximation 1.5 mW. A spectrum analyzer and a flexible connector are used. One FC was connected to the output of the laser source through using a (3- ports, SMF polarization independent circulator with operating wavelength 1550 \pm 20 nm, and other FC is connected to the input of the optical spectrum analyzer (OSA) wavelength range (1000- 2500) nm from THORLAB Inc. Since the FBG fiber is SMF-28, an FC with the same fiber ends was selected so as to have a good coupling. The whole experimental setup is shown in the figure (5). First, the light from a (LPS-1550-FC) Pigtailed Laser Diodes is launched into one end of the fiber containing the grating and the transmission spectrum is recorded by both optical spectrum analyzer (OSA) and monochromator / spectrograph (zolixinc.). The emission spectrum of the LD source is shown in Figure (9) which indicates an output in the wavelength range about (1548-1553) nm.

The spectral response of the FBG is experimentally noted by using the Monochromator / Spectrograph model Omni- λ Series (InGaAs Detector) from Zolix Inc. with 0.05 nm resolution, interfaced with a Data Acquisition System model DCS300PA, as an (OSA) optical spectrum analyzer system. The wavelength and the amplitude of the transmitted signal are simultaneously obtained from the (OSA). The amplitude of transmission is plotted against the wavelength to give the transmission spectrum of the wavelength range of (1547- 1554) nm. The transmission spectra are shown in the figure (10), which are in good agreement with the specification sheet.

FBG sensor simulation study concept

Optigrating 4.2.2 is powerful and user-friendly design software for modeling integrated and fiber optic devices that are assisted by optical gratings. The operation of many sensor devices is based on optical gratings which alter coupling between guided light modes. For example, waveguide, grating technology has been used in temperature and strain sensing. Once a device setup is done, then we can use the program to perform numerical simulations. Such simulations are based on solving coupled mode equations that describe the interaction of guided modes. For example, waveguide, grating technology has been used in temperature and strain sensing. Once a device setup is done, then we can use the program to perform numerical simulations. Such simulations are based on solving coupled mode equations that describe the interaction of guided modes. A grating-assisted device can be analyzed and designed by calculating light propagation, reflection and transmission spectra, the phase group delay, and the dispersion. While the calculation results depend on waveguide and grating parameters, the design task can be greatly facilitated by the use of the appropriate computer software (Optigrating 4.2.2.). The data is viewed as the reflection spectrum, which visually shows the trends and can be analyzed numerically. This research intends to reproduce the reflection spectrum using a combination of finite element analysis (FEA) software and OptiGrating. This has the potential to extend academic knowledge and be a step in the development of methods to calculate the actual strain field or temperature variation to which a sensor is subject.





Shehab A. Kadhimet al.

There are several steps and options must be processed using the FBG as a sensor. From the menu of parameters, the grating selected, to opening the grating manager dialog box, and open the grating definition dialog box and inserting the options as shown in figure (8). From the dialog box of grating definition, the sensors check box must be enabled in order to activate the define button. In the fiber Bragg grating sensor dialog box from the temperature or strain dialog box can control the default weather changes. Fiber Bragg grating dialog box contains important parameters, the first is strain optic parameter that set to photosensitivity coefficient, second parameter is thermo-optic parameter, which include thermal expansion coefficient, thermo-optic coefficient and reference temperature, the third is applied micro-strain, and the fourth is applied temperature. Both of applied micro-strain and temperature has four ways to gradient that are uniform, linear, Gaussian, and user defined. As shown in figure (9).

The second part of calibration: [6]

The Bragg wavelength is as given by: $\lambda_B = 2n_{\text{eff}} \Lambda$

Is Dependent on the refractive index and the periodicity of the FBG. Both of these values can be displaced by longitudinal forces as well as by changes in temperature. The relative sensitivity of Bragg wavelength as strain and temperature change is given by [9]:

$$\Delta \lambda_B / \lambda_B = (1 - \rho_e) \epsilon_z + (\alpha + \eta) \Delta T$$

Where α is the thermal expansion coefficient of the fiber, η is the thermo-optic coefficient representing the shift in refractive index with changes in temperature, ρ_e is the photo-elastic coefficient representing shift in refractive index due to strain and ϵ_z is the longitudinal strain over the grating. Typical values for germanium doped optical fiber cores are: $\rho_e = 0.22$, $\alpha = 0.55 \times 10^{-6} \text{ } ^\circ\text{C}^{-1}$, $\eta = 8.6 \times 10^{-6} \text{ } ^\circ\text{C}^{-1}$

Thus, theoretical values of the sensitivity of the Bragg wavelength in the range of 1550 nm due to temperature shifts and strain are, as given by [10]: $\Delta \lambda_B / \Delta T = 14.18 \text{ pm}/^\circ\text{C}$ and $\Delta \lambda_B / \Delta \epsilon = 1.2 \text{ pm}/\epsilon$

The theoretical predictions in equation make a good approximation to the respective sensitivities for fibers not exposed to any heating process. More precise values are obtained through calibration of the grating. Calibration was done by putting the grating through a known cycle of changes in the quantity that is to be measured, which for this project means that the gratings was tested for their sensitivity during shifts in temperature, and record the corresponding changes in Bragg-wavelength.

CONCLUSION

The FBG is calibrated to be used as a temperature sensor within the range (20 – 70)°C. The used fiber Bragg grating (FBG) in this work is very sensitive to the variation of the temperature degrees, the sensitivity was (1-6pm\0.1°C). The relation between the applied temperature and shifting the Bragg wavelength was linear. The sensitivity of the Bragg wavelength to temperature arises from the change in the refractive index of the optical fiber. Finally, Simulation has been carried out to analyze the spectral characteristics of the FBGs using OptiGrating software. This powerful tool for the analysis of coupling and reflection among the guided modes of optical waveguides and fibers, also has specialized modules for simulating physical conditions such as temperature and strain on the grating.

REFERENCES

1. https://www.rp-photonics.com/fiber_optic_sensors.html
2. https://en.wikipedia.org/wiki/Fiber_optic_sensor





Shehab A. Kadhim et al.

3. Ghetia, S. and Gajjar, R., (2013).Classification of Fiber Optical Sensors,International Journal of Electronics Communication and Computer Technology (IJECCCT). Vol. 3, Issue 4 .
4. Gupta, B. D.,(2006).Fiber optic sensors principles and applications.
5. Halee, B. and HoKim Y.,(2012).Interferometric fiber optic sensors",Open access, sensors,12.
6. Gagliardi,G.,Salza,M., Ferraro,P., Chehura,E., Tatam, R. P., Gangopadhyay, T. K. , Ballard,N., Paz-Soldan, D., Barnes, J. A., Loock,H.-P., Lam, T. T.-Y., Chow, J. H. and Natale,P.D. (2010).Optical Fiber Sensing Based on Reflection Laser Spectroscopy, Sensors, 10, 1823-1845; doi:10.3390/s100301823.
7. Ekestam, H. and Larsson, J.,(2015).Temperature sensor based on dual fiber Bragg gratings, report May.
8. Zichos, Saito, Smith, handbook of materials measurement methods ,Springer.
9. Hu, C. and Bai, W., (2018). High-Speed Interrogation for Large-Scale Fiber Bragg Grating Sensing, Sensors, 18, 665; doi:10.3390/s18020665.
10. Wang, Z., Wen, H.Q., Luo, Z.H.,and Dai, Y.T.,(2016).Time Division Multiplexing of 106 Weak Fiber Bragg Gratings Using a Ring Cavity Configuration, Photonic Sens., 2, 132–136.
11. Dai, Y.B.,Li, P., Liu, Y.J., Asundi, A., and Leng, J.S.,(2014).Integrated real-time monitoring system for strain/temperature distribution based on simultaneous wavelength and time division multiplexing technique,Opt. Lasers Eng. 59, 19–24.

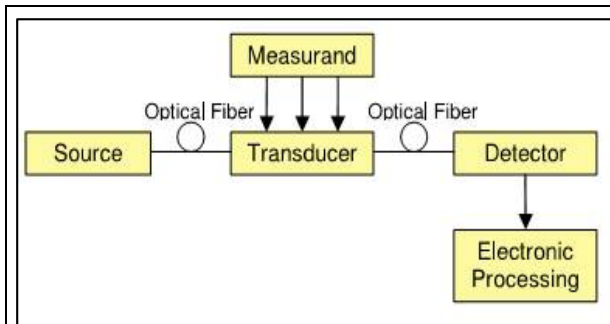


Figure 1. "basic elements of an optical fiber sensing system".

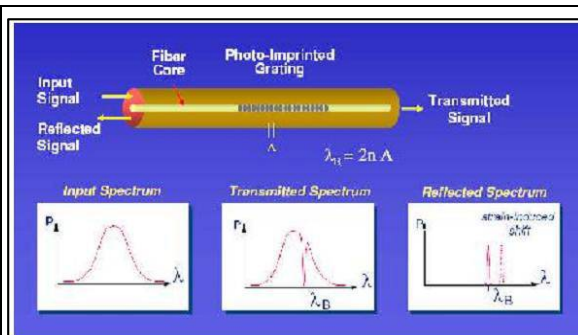


Figure 2. "Bragg Grating Responses".

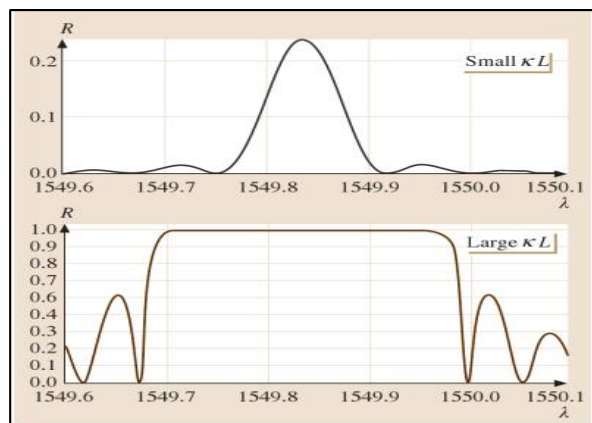


Figure 3. "Typical reflection spectra for weak and strong gratings".

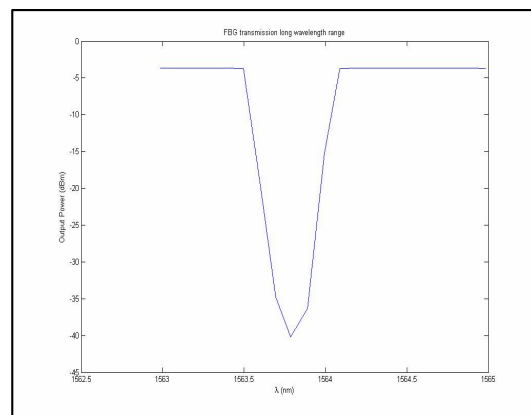


Figure 4. Manufacturer's Specification sheet of FBG.





Shehab A. Kadhim *et al.*

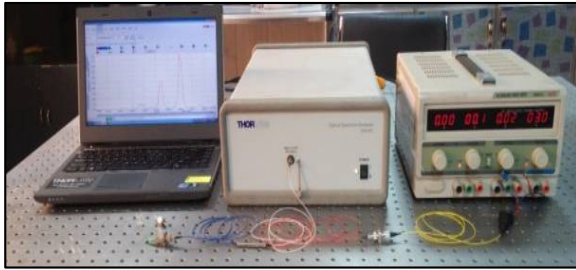


Figure 5. Experimental setup for Characterization of FBG sensor

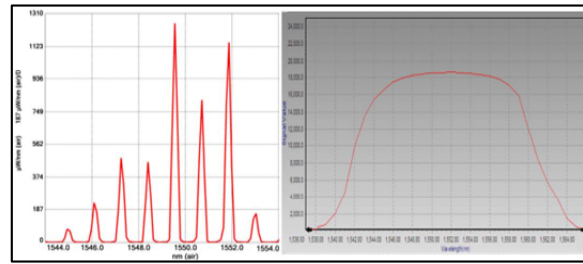


Figure 6. Characterization of LD Source spectrum using (left) Optical spectrum analyzer (right) Monochromator / Spectrograph

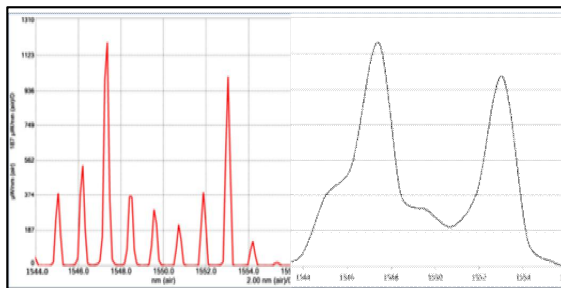


Figure 7. FBG measured Transmission Spectrum using (left) Optical spectrum analyzer (right) Monochromator / Spectrograph

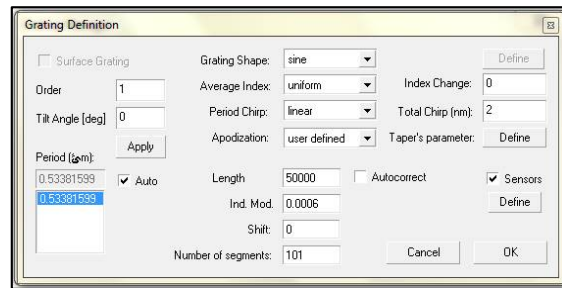


Figure 8. Grating definition dialog box

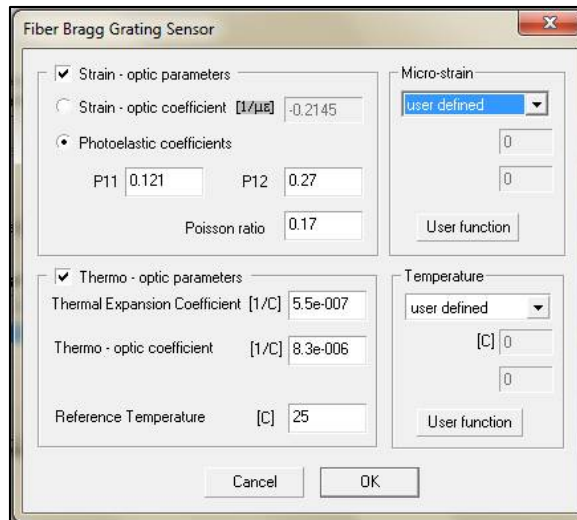


Figure 9. Fiber Bragg grating parameters.





Investigation of Bacterial and Parasitological Contamination in Buffalo's Milk Cream (Arab Cream) in Alsamawa City, Iraq

Mohenned A. Alsaadawi^{1*}, Haider S. Almnehlawi² and Ali M. Al-yasari³

¹Department of Parasitology, College of Veterinary Medicine, Al-Muthanna University, Iraq.

²Department of Environment and Pollution, College of Science, Al-Muthanna University, Iraq.

³Department of Physiology, Veterinary Medicine, Al-Muthanna University, Iraq.

Received: 25 Oct 2018

Revised: 27 Nov 2018

Accepted: 29 Dec 2018

* Address for Correspondence

Mohenned A. Alsaadawi

Department of Parasitology,
College of Veterinary Medicine,
Al-Muthanna University, Iraq.
Email: mha18@mu.edu.iq



This is an Open Access Journal / article distributed under the terms of the **Creative Commons Attribution License** (CC BY-NC-ND 3.0) which permits unrestricted use, distribution, and reproduction in any medium, provided the original work is properly cited. All rights reserved.

ABSTRACT

Milk products of buffalo are widely consumed and represent a rich environment for the microorganism growth. This kind of cream is sold by individuals and out of factories without health and environmental control. This may increase the chance of microorganism contamination. The goal of the study is to investigate the bacterial and parasitological contamination in buffalo milky cream which produced and preserved under unsanitary conditions. Forty-seven samples were collected from the cream buyers in Alsamawa city from November 2012 to February 2013 in irregular periods of time. Several parasitological and bacterial analysis were performed including plating, biochemical tests and microscopic examination. The results showed that all samples were contaminated with two bacterial genera; *Escherichia* and *Klebsiella* with proportions 74.4% and 9.3% respectively. Mixed contamination with the two bacterial genera was 18.6%. Two types of protozoa; *Cyclospora* and *Cryptosporidium*, were detected with proportion rates of 8.5% and 2.1% respectively. The proportion of contamination was higher in November compared to the other dates. There are no positive samples in December and February.

Keywords: Buffalo, milk cream, *Escherichia*, *Klebsiella*, protozoa, *Cyclospora*, *Cryptosporidium*.

INTRODUCTION

The main way for protozoan parasites is via food in many countries. These protozoa include *Cryptosporidium*, *Giardia* and *Toxoplasma* mainly. However, *Cyclospora* could be transmitted by intaking contaminated food (1). *Cyclospora* has only been documented as a significant human pathogen since the early 1990s. It has been recognized in developed countries as the causative agent of a few gastrointestinal outbreaks associated with fresh (unprocessed) food produce,



**Mohenned A. Alsaadawi et al.**

i.e. soft fruits and leafy vegetables (2). Milk products can be important source of foodborne intestinal coliforms. *Escherichia coli* is a serious problem threatening public health for being responsible for multiple instances of food poisoning as contaminating the food with *Escherichia coli* can lead to outbreak infection (3). Milk products contamination could lead to cause watery diarrhea then bloody diarrhea and might end with hemorrhagic colitis (4). Milk cream produced at homes, farms or some popular stores is not a subject to even the basic scientific health rules. The alimentary canal of dairy cattle especially buffaloes and cows could be the source of contamination. The surrounding environment is another source of raw milk contamination or processed products, especially for cream and cheese. Finally, the cream and cheeses could be contaminated during or after the manufacturing or transportation processes (5). Many studies and reports around the world have been concerned the role of milk products in transferring illness caused pathogens, especially in children and elderly. Based on the above-mentioned aim of the current study is to investigate the presence of protozoa and bacteria in the cream produced from buffalo's milk.

MATERIALS AND METHODS**Parasitology aspect**

- 1- 47 samples of the cream were collected from sellers in Alsamawa.
- 2- 10 grams of this milk product were taken and mixed well with 10 ml of sterile distilled water. The mixture was spun down at 2500 rpm for 15 min.
- 3- The sediment was carefully transferred into one or more centrifuge tubes, depending on the volume, and washed thrice with distilled water at 2500 rpm for 15 min.
- 4- The supernatant was removed. The pellets were rinsed thoroughly with a detergent solution to ensure that no sediment is discarded, and re-centrifuged at 2500 rpm for 15 min.
- 5- The pellet was suspended in an equal volume of acetoacetic buffer, pH 4.5 (i.e. if the volume of the pellet is 2 ml, add 2 ml of buffer). If the pellet is less than 2 ml, the buffer is increased up to 4 ml to ensure that there is sufficient volume of buffer above the pellet to allow the ethyl acetate layer to be poured off without resuspension of the pellet.
- 6- Add two volumes of ethyl acetate or ether (i.e. 4 ml in the above example) and mix the solution thoroughly in a vortex mixer. The sample can also be shaken by hand. This is quite acceptable if a mechanical mixer is not available.
- 7- The sample was centrifuged at 3500 rpm for 15 min. The sample was separated into three distinct phases. All the non-fatty, heavier debris, including helminth eggs, larvae, and protozoa, were deposited in the bottom. Then the buffer was above this layer and it is clear. The fatty and other material move into the ethyl acetate or ether and forms a thick dark plug at the top of the sample.
- 8- The volume of the pellet containing the eggs was recorded, and then the rest of the supernatant was poured off in one smooth action. It may be necessary to loosen the fatty plug first by running a fine needle around the side of the centrifuge tube.
- 9- The pellet was resuspended in five volumes of zinc sulfate solution, (i.e. if the volume of the pellet is 1 ml, add 5 ml of ZnSO₄). The sample was mixed thoroughly, preferably using a vortex mixer.
- 10- An aliquot with a Pasteur pipette was quickly removed and transferred to a glass slide for final examination.
- 11- Glass slides were placed on the microscope stage and examined under 10× or 40× magnification.

Bacteriology aspect

- 1- One gram of each sample was diluted by 9 ml of sterile distilled water with mixing. Diluted samples were plated on nutrient, blood and MacConkey agars then by streaking method and incubated at 37°C for 24-48 hours.
- 2- Strains were transferred on nutrient agar three times.
- 3- Gram stain was done for each strain.



**Mohenned A. Alsaadawi et al.**

4- The following biochemical tests were performed (Indol, Simmon citrate, Methyl red, and Vogus Proskeur) to identify the bacterial genera or species.

Statistical analysis was done by using Chi-square according to (6).

RESULTS

The proportion of total positive samples with protozoa was 10.6% (table 1). The highest infection rate was 8.5% with *Cyclospora* while the lowest infection rate was 2.1% with *Cryptosporidium* (table 2). The highest rate of protozoan prevalence was in November (52%) while the lowest rate was in February 3.3%. The positive samples were significantly affected by the months (table 3). The bacterial contaminant was found in all tested samples. The percentage of *E.coli* and *Klebsiella* spp presence were 74.4% and 9.3% respectively for single infection and 18.6% for mixed infection (table 5). The bacterial infection was directly related to the temperature as the rate of bacterial infection decreased with dropping of temperature. Five buffalo's cream shops were used as sources of the cream through the months of the study (table 6). The highest rate of bacterial existence was in October (11.5%), then February (8.8%) while the lowest rate was in December (3.6%). Figure 1. Cream samples were collected and were treated to get the parasitic contents as explained above. The samples were examined under the microscope (100X). A1 and A2 represent *Cryptosporidium* while B and B2 represent *Cyclospora* from two different samples. Figure (2) the collected samples were subjected for Gram stain (A) and blood agar (B) tests which showed two kinds of bacteria; *E. coli* and *Klebsella*

DISCUSSION

We found that the overall proportion rate of protozoa reached 10.6 % (table 1) while it was 100% (table 4) of bacterial existence. The reasons behind this might be the higher contamination rate which can be related to many factors. These factors could be lack the healthy ways in manufacturing of cream and storing the product in bad conditions during transportation or before selling. Contamination of the udder and the hands of owners or employees with feces of infected animals could be an important way of milk products contamination (7). The cream could also be contaminated due to the way of handling. The sellers (mainly women) do not care with the hygiene rules. They do not wear gloves when touching the cream and exposing the cream to the air and sun directly in unclean containers. In addition, the owners of animals or employees in the manufacturing of cream may be infected with bacterial diseases and which is transmitted to milk as they do not subject to regular health checking or medical examinations (8). In December and January, the absence of the existence of protozoa in cream may relate to being these months characterized by lowering of temperature thus these conditions are unsuitable to growth and existence of protozoa. Temperature plays an important role in the bacterial contamination. In November the average number of bacteria was 11.5 cell/gram while it was 3.5 cell/gram in January (table 6). These results found that the bacterial proportions directly increased with increasing of climate temperature. The suitable environmental conditions for bacterial growth are in the warm and hot seasons compared to the cold winter.

Conflict of interest

This research is a personal non-profit work and there is no conflict of interest.

Source of funding

None.





Ethical Clearance

Ethical clearance was obtained from the Faculty Scientific Committee (Department of Parasitology, College of Veterinary Medicine, Al-Muthanna University, Iraq) to Investigatethe bacterial and parasitological contamination in Buffalo's milk cream (known as Arab cream) in Alsamawacity-Iraq

REFERENCES

- (1) D. Dawson, International journal of food microbiology, 103, 207, 2005.
- (2) P. Gourabathini, M.T. Brandl, K.S. Redding, J.H. Gunderson and S.G. Berk, Applied and Environmental Microbiology, 74, 2518, 2008.
- (3) J. Durch, T. Ringhand, K. Manner, M. Barnett, S. Ahrabi-Fard, J. Davis and D. Boxrud, Morbidity and Mortality Weekly Report, 49, 911, 2000.
- (4) D. Widiasih, N. Ido, K. Omoe, S. Sugii and K. Shinagawa, Epidemiology & Infection, 132, 67, 2004.
- (5) R.J. Perla and J. Carifio, American Journal of Infectious Diseases, 1, 162, 2005.
- (6) E.C. Todd, J.D. Greig, C.A. Bartleson and B.S. Michaels, Journal of food protection, 72, 202, 2009.
- (7) J.M. Farber and P.I. Peterkin, Microbiological reviews, 55, 476, 1991.
- (8) G.L. Nichols, British medical bulletin, 56, 209, 2000.

Table 1. Number and proportion of total positive samples with Protozoa

Total examined samples	Positive samples	
	No.	%
47	5	10.6

Table 2. The prevalence of *Cyclospora* and *Cryptosporidium* in the sample population

Protozoangenera	positive samples	
	No.	%
<i>Cyclospora</i>	4	8.5
<i>Cryptosporidium</i>	1	2.1

Table 3. Effect of months on proportions of protozoa in milk cream

month	No. of Examined samples	Positive samples with <i>Cyclospora</i>		Positive samples with <i>Cryptosporidium</i>	
		No.	%	No.	%
10	9	3		0	
11	14	0		1	
12	8	0		0	
1	4	0		0	
2	12	1		0	
Total	47	4		1	





Mohenned A. Alsaadawi et al.

Table 4. number and proportion of total positive samples with Bacteria

Total examined samples	Positive samples	
	No.	%
43	43	100

Table 5. The prevalence of *Escherichia coli* and *Klebsiellasp* in the sample population

Types of Bacteria	Single infection		mixed infection	
	No.	%	No.	%
<i>Escherichia coli</i>	32	74.4	8	18.6
<i>Klebsellasp</i>	4	9.3	8	18.6

Table 6. total number of aerobic bacteria per 1 gm of buffalo’s cream multiply 10³

Sample sources	October	November	December	January	February
A	9	9	8	4	5
B	14	3	5	2	7
C	11	7	3	7	11
D	13	6	7	2	17
E	10	5	2	3	4
rate	11.5	6	5	3.6	8.8

Table 7. Bacterial biochemical test

Characteristics	<i>E. coli</i>	<i>Klepsella spp</i>
Gram Stain	Negative (-ve)	Negative (-ve)
Indol	Positive (+ve)	Negative (-ve)
Simmon Citrate	Negative (-ve)	Positive (+ve)
Methyle Red	Positive (+ve)	Negative (-ve)
VogusProskour	Negative (-ve)	Positive (+ve)

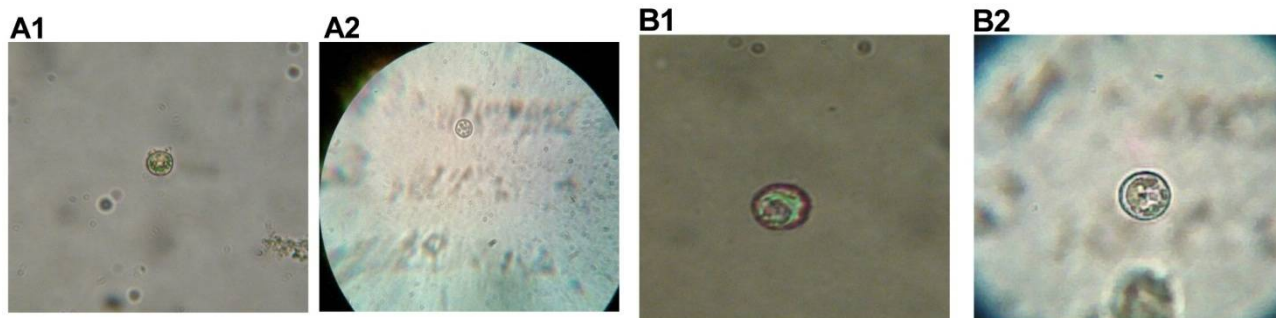


Figure 1: types of protozoa in buffalo’s cream

Cream samples were collected and were treated to get the parasitic contents as explained above. The samples were examined under the microscope (100X). A1 and A2 represent *Cryptosporidium* while B and B2 represent *Cyclospora* from two different samples.





Mohenned A. Alsaadawi et al.

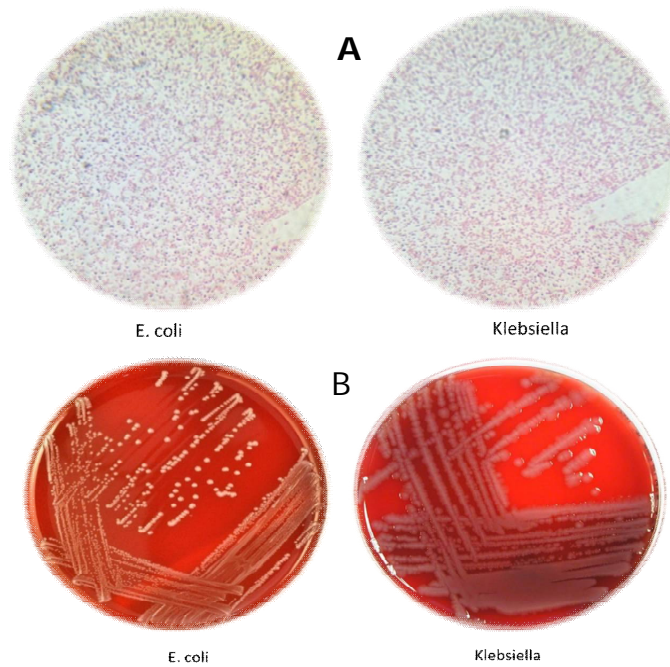


Figure 2 Gram Stain test

The collected samples were subjected for Gram stain (A) and blood agar (B) tests which showed two kinds of bacteria; *E. coli* and *Klebsiella*

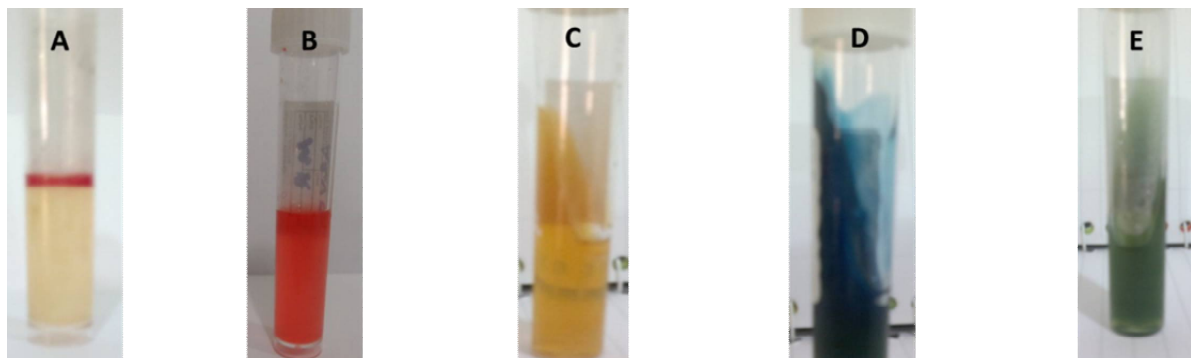


Figure 3: Results of biochemical tests A: Indol, B: Methyl red, C: Vogues Proskauer, Citrate Utilization(D: positive, E:Negative)





Investigation the Effect of Annealing on the Optical Properties of CdS Thin Films by Spin Coating Deposition (SCD)

Ghaith H. Jihad* and Hamed M. Ameen

Department of Physics, College of Science, University of Baghdad, Iraq.

Received: 13 Oct 2018

Revised: 15 Nov 2018

Accepted: 18 Dec 2018

*Address for Correspondence

Ghaith H. Jihad

Department of Physics,

College of Science,

University of Baghdad, Iraq.

E-mail: GHAITHJIHAD@scbaghdad.edu.iq



This is an Open Access Journal / article distributed under the terms of the **Creative Commons Attribution License** (CC BY-NC-ND 3.0) which permits unrestricted use, distribution, and reproduction in any medium, provided the original work is properly cited. All rights reserved.

ABSTRACT

CdS nanofilms have been produced on glass substrates by Spin Coating technique with different Temperature $T = (100^{\circ}\text{C}, 150^{\circ}\text{C}, 200^{\circ}\text{C})$. It is observed from optical properties that the films possess transition 75% in visible and near infrared region of spectrum and direct band gap values in the range of 2.2-1.6 eV at decreasing temperature, when increases Temperatures the films are more homogenate.

Key words: Spin Coating Deposition (SCD), Atomic Force Microscopic (AFM), X-Ray diffracting (XRD), CdS (Cadmium Sulfate).

INTRODUCTION

Cadmium sulfide is an II-VI compound semiconductor. Bonding in these compounds is a mixture of covalent and ionic type's. Group VI atoms are considerably more electronegative than group II atoms and this introduces ionicity. This character has the effect of binding the valence electrons rather tightly to the lattice atoms. Thus, each of these compounds has higher melting point and large band gaps than those of the covalent semiconductors of comparable atomic weights [1]. Two types of crystal structure, cubic zinc blend and hexagonal wurtzite, are observed in these compounds. Structure type of the deposited crystals depends on the substrate temperature it becomes zinc blend whereas at a high temperature one wurtzite type is seen [2]. In recent year CdS thin films has attracted wide attention as one of the most promising material for application as window layers [3,4]. in low-cost, high efficiency thin film solar cells because of its suitable band gap, high optical transparent and absorption coefficient in the visible range of solar spectrum. CdS is a direct band gap (2.42 eV) II-VI semiconductor and has been used as a vital component in different solar cell hetero-structures together with narrow band gap material such as CeTe, Cu₂S, InP, CuInSe₂ with efficiencies between 10-16% [5,6]. CdS becomes sublime at about 700 C° and melts at about 1750 C° under several atmospheric pressure. It can be deposited either from vapor phase or from high pressure liquid phase.



**Ghaith H. Jihad and Hamed M. Ameen**

Its effective permittivity (dielectric constant) is 11.6 and density is approximately 4.84 g/cm^3 . CdS does not show intrinsic behavior at room temperature, i.e. deposited CdS thin films doesn't need doping to become n-type. Formation of p-type CdS is very difficult, because of the strong self-compensation effect caused by sulfur vacancies [7,8]. Pure CdS crystals have a high resistivity about $10^{12} \Omega\text{-cm}$. polycrystalline CdS thin film's resistivity can be reduce by In, Sn, Al, Cr or Br doping or by some growth techniques. For example, $10^{-3} \Omega\text{-cm}$ resistivity was reported for the films grown by close-apace vapor transport [9]. The grain sizes of CdS films are usually around 0.3-0.5 μm . As the film thickness is increased, large crystallites are formed in the film. Annealing at high temperatures enhance the grain size and re-crystallization of CdS [10]. CdCl₂ treatment increases the effect of annealing [11].

EXPERIMENTAL METHOD

The technique has been employed in this work is Spin coating that involves adding the material on the glass slid and then rotation it to deposited the solution on the substrate then annealing it for different temperature to study the effect of the temperature on it.

Device use in my work: Balance, Oven, Magnetic-stirrer, Spin coating device

Film deposition**Spin Coating Technique**

The spin coating procedure can be effectively modeled by dividing whole process into three stages:

Deposition and spin up, spin off and film drying, during first stage: solution is allowed to fall on a rotating substrate from a micro syringe and the substrate is accelerated to the desired speed. Spreading of the solution takes place due to centrifugal force and height is reduced to critical height. During second stage (spin off), subsequent reduction in film height is dominated by the evaporation of the solvent. During final stage centrifugal outflow stops and further shrinkage is due to solvent loss. In actual practice these three stages overlap each other [12]. figure (1) shows the relation between film thickness and both spin speed and spin time.

Preparing the Chemicals

We chose the materials provided by (BDH) company with specifications given in table (1).

Synthesis of CdS/PVA nanocomposite thin film

CdS and PVA nanocomposite thin film were deposited on glass substrates by Spin Coating technique using cadmium acetate $[\text{Cd}(\text{NO}_3)_2 \cdot 4\text{H}_2\text{O}]$ as Cd⁺⁺ ion source and thiourea $[\text{CS}(\text{NO}_2)_2]$ as S⁻² ion source with cadmium to sulfur ratio: (Cd:S) 3:5 and polyvinyl alcohol (PVA) as a polymer controller matrix. The Cd:S ratio play an important role on the structure of the CdS thin film because S-excess and Cd-excess films exhibit hexagonal and cubic structure, respectively [13]. For solar cell application hexagonal films are preferable. In a typical reaction a matrix solution was prepared by adding 20 ml of 0.6 M cadmium acetate into an equal volume of 5% aqueous solution of polyvinyl alcohol (PVA) and stirred continuously for 90 minutes at 70 C°. the solution was left overnight to get transparent liquid indicating complete dissolution of cadmium acetate. To this matrix solution, 20 ml of 1M thiourea was added drop wise and the reactants were stirred continuously for 30 minutes. For the preparation of CdS,PVA nanocomposite thin film , a chemically clean glass substrates was coated with the solution by spin coating technique and then the substrate was heated in an oven at 100 °C (150 and 200 C°).within 15-20 minutes the colar of the film





Ghaith H. Jihad and Hamed M. Ameen

changed from transparent to light yellow indicating the formation of CdS,PVA nanocomposite thin film. Of course the PVA plays the role of matrix in the thin film.

RESULTS AND DISCUSSION

X-ray diffraction (XRD)

The structure properties of the spin coating CdS films have been investigated by x-ray diffraction technique use $\text{CuK}\alpha$ radiation. Fig.2, fig.3, fig.4 shows the x-ray diffraction pattern of CdS thin prepared by spin coating method and annealing at 100°C , 150°C and 200°C for 10-15 minutes. The x-ray diffraction pattern at 100, 150 and 200 $^\circ\text{C}$ annealing samples exhibit peaks at 24.16° , 20.94° and 22.000° respectively. The presence of small peaks in x-ray diffraction reveals the formation of nanocrystalline CdS films. The peaks are not sharp indicating that the average crystalline size is small. Due to size effect the peaks in the diffraction broaden and their widths became large as the particles became smaller. The obtain grain size value of the annealing CdS films are given in Table 1. It seen that crystalline size of CdS increase from 29.97 nm to 32.897 nm as the annealing temperature increase from 100C to 200 C . Table 2 comparison between grain size from XRD and Eg

Atomic force microscopy (AFM)

Fig (5, 6 & 7) show the atomic force microscopic picture for the three samples at different annealing temperature $T_a=100, 150$ and 200°C respectively. The grain size and the average diameter were listed in table 3.

Optical Measurements

The Transmittance Spectra

The experimental transmission spectrum for CdS thin film in spectrum range (300-1100) nm at room temperature as showing in fig. (8). All spectra show good transparency ($T > 85\%$). Where it is very clear and that transmission decrease with increase the annealing temperature as show in table (4)

The Optical Energy Gap

The optical energy gap values (E_g) for CdS films have been determined by using Tauc equation which is used to find the type of the optical transition by plotting the relations of $(\alpha h\nu)^2$ versus photon energy ($h\nu$) and selecting the optimum linear part. The optical energy gap decreases with increasing annealing temperature as show in the figures (9) given in Table (4).

CONCLUSIONS

In summery the CdS embedded in PVA matrix in thin films was prepare using spin coating technique. The effect of annealing on prepare films at thickness about $67.66 \mu\text{m}$ were. From the x-ray diffraction the crystal grain size increase with increase the annealing temperature .The absorption of the films and the absorption coefficient increase with increases the annealing temperature. While the transmission of the films is decrease directed with the simple annealing temperature. The energy gap for CdS thin films decrease due to increase annealing temperature.





Ghaith H. Jihad and Hamed M. Ameen

REFERENCES

1. C. Kittel "Introduction to Solid State Physics" Eight Edition, John Wiley and Sons, p.416,(2005).
2. S.M.Sze "Physics of Semiconductor Devices" John Wiley and Sons,(1981).
3. B.L.Sharma, R.K.Purohit and S.N.Mukerjee "Infrared Physics", Vol.10, pp.225-231, Pergamon Press, printed in Great Britain, (1970).
4. A.G.Milnes and D.L.Feucht, "Heterojunctions and Metal-Semiconductor Junctions", Academic Press, New York and London (1972).
5. M. S. Tyagi. "Introduction to Semiconductor Material and Devices ". John Wiley and Sons, Canada 1991.
6. N.Wenstem, G.M. Wolf and B.N. Das. Appli. Phys. Let. ,6:73 ,1965.
7. D. A. Cusano. Solid State Electron. 6:217, 1963
8. G.Mandel. Phy. Rev. ,134:A1073 ,1964
9. I. Gunal and M. parlak. J.Mater. Sci. Mater. Electron ,8:9, 1997
10. H. Chavez, M. Jordan , J. C. Mc Clure, G. Lush and V. P. Singh. J. Mater. Sci. Mater . Electron. 8:151, 1997
11. Kittel, Introduction to Solid State Physics " 8th ed. , John Wiley and Sons, Inc. New York, 2005
12. J.Pankove , " Optical Processes in Semicouductors ", London (1971).
13. J.E.Bertie , Handbook of Vibrational Spectroscopy , Univers. of Alberta , Edmonton , Canada , John Wiely & Sons , Ltd. (2001)

Table 1. the chemical parameters of the substances used in this project.

Material	atomic weight	Purity	Chemical Composition	Concentration	Company
Cadmium Nitrite	308.47	99%	Cd(NO ₃) ₂ .4H ₂ O	0.6M	BDH
Thiourea	76.12	99%	Cs(NH ₂) ₂	1M	BDH
Polyvinyl alcohol (PVA)	1400	99%			BDH

Table 2 comparison between grain size from XRD and Eg

Annealing temperature	Grain size from XRD	Energy gap
100	29.97	2.25
150	32.58	1.65
200	32.897	1.60

Table 3: Average diameter for samples grains at different Ta

Ta (°C)	Grain No	Avg. Diameter (nm)
100	52	224.45
150	45	212.86
200	81	156.23

Table 4: Calculations the Optical and structural properties at different Temperature

Parameters	T=100 C ^o	T=150 C ^o	T=200 C ^o
Grain size	29.9	32.58	32.9
Absorption of films	0.011	0.028	0.035
Transmission spectra	97.427%	93.691%	92.235%
Optical Energy Gap	2.25	1.65	1.60





Ghaith H. Jihad and Hamed M. Ameen

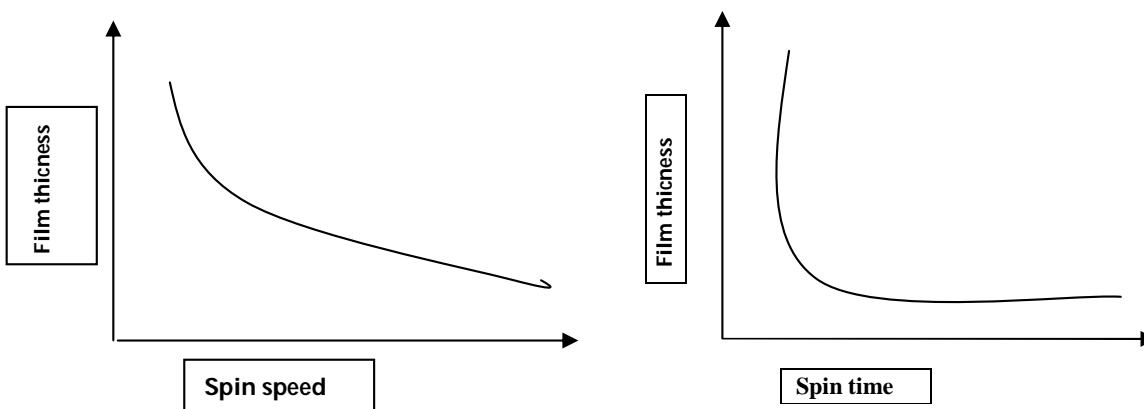


Figure 1. The relation between film thickness and both spin speed and spin time.

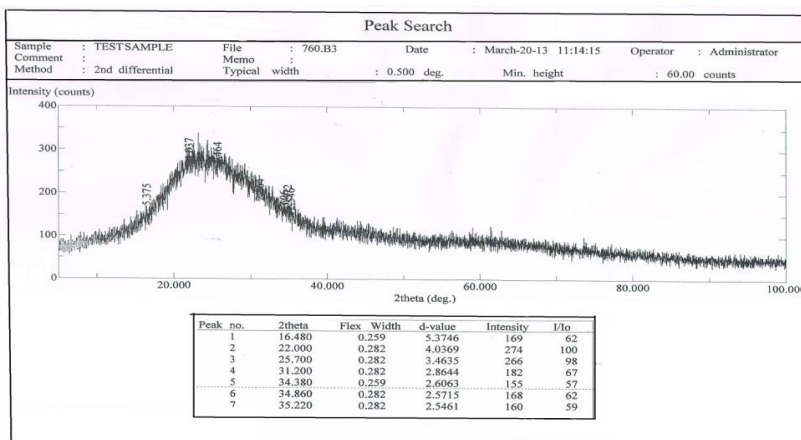


Fig.2: Shows the X-ray diffraction for CdS at 100 C°

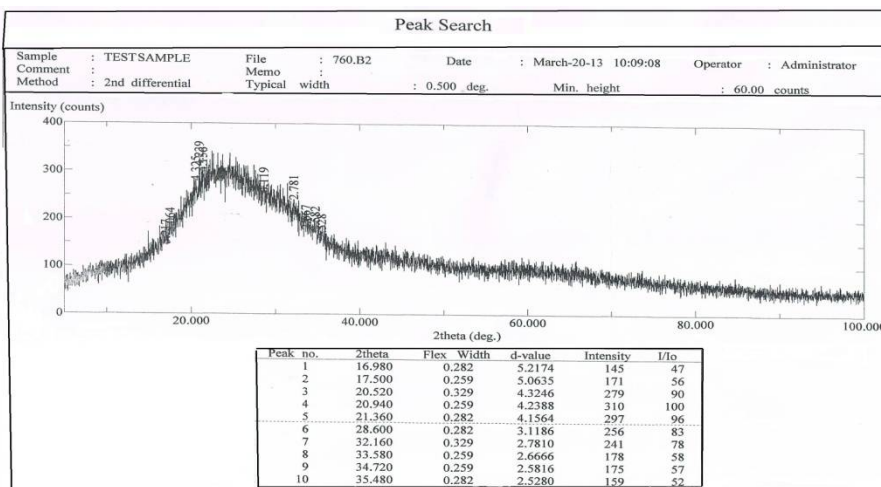


Fig.3: Shows the X-ray diffraction for CdS at 150C°





Ghaith H. Jihad and Hamed M. Ameen

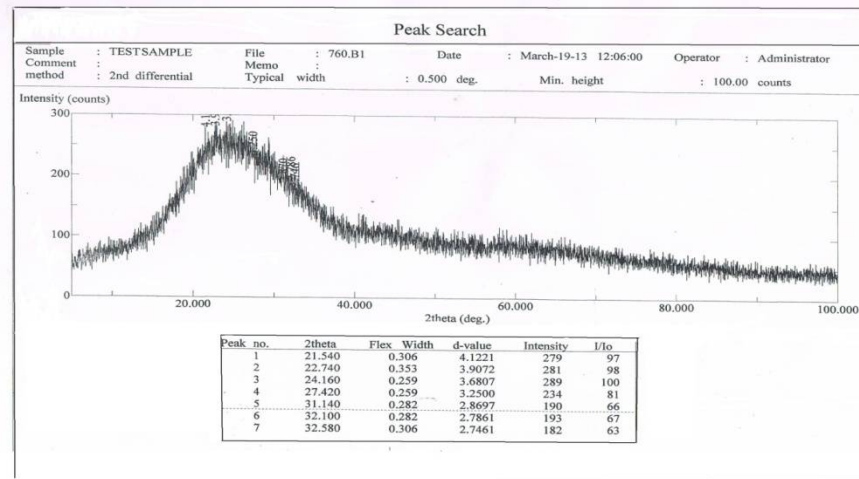
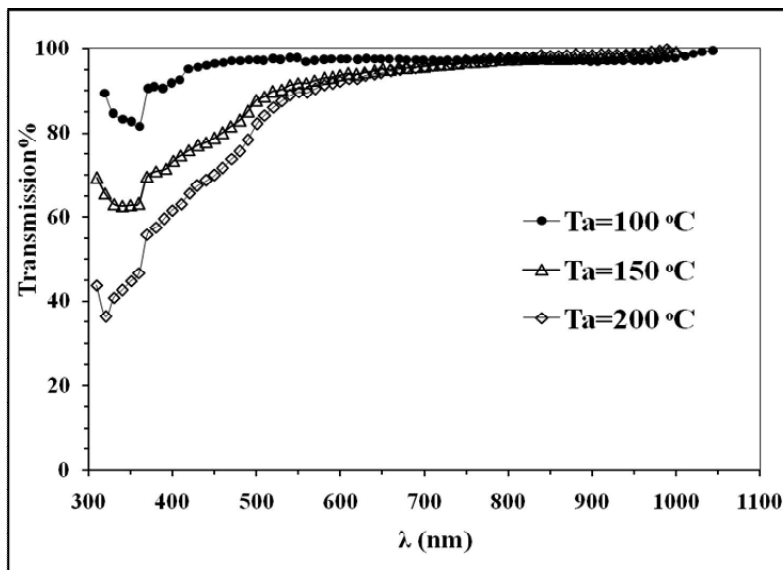
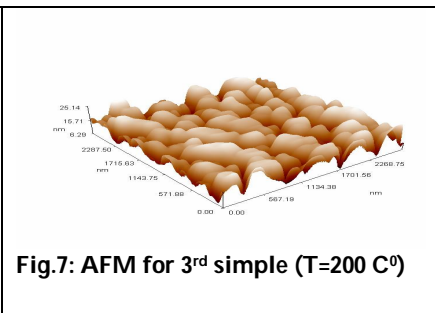
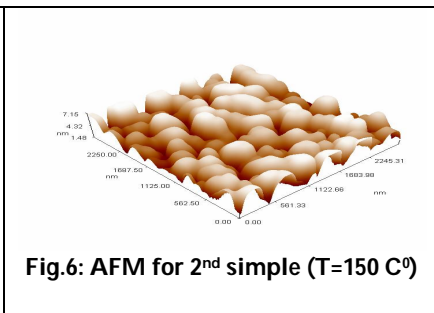
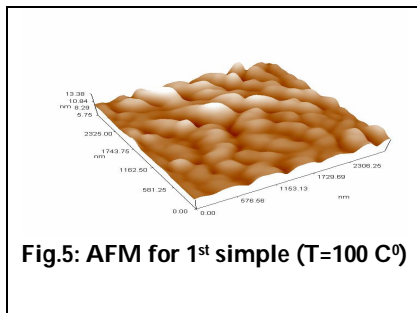


Fig.4: Shows the X-ray diffraction for CdS at 200°C





Ghaith H. Jihad and Hamed M. Ameen

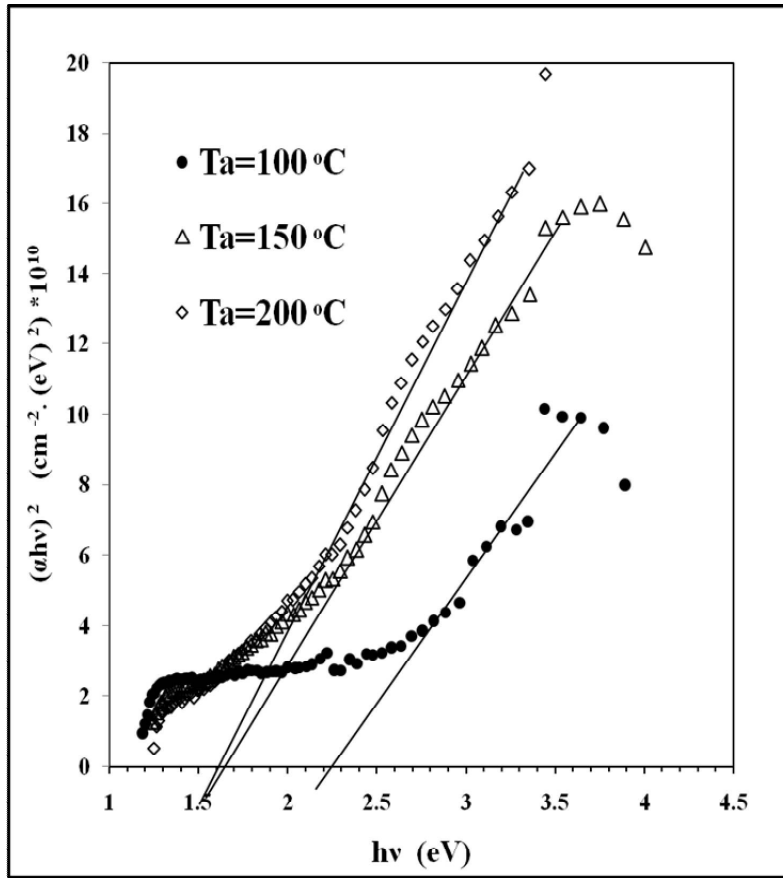


Fig.9 use Tauc equation to determine The Energy Gap for films with different T_a



Fig.10 Balance





Study the Optical and Structural Properties of (ZnO: Pb) thin Films Prepared by Laser Induced Plasma Technique

Ghaith H. Jihad

Department of Physics, College of Science, University of Baghdad, Iraq.

Received: 14 Oct 2018

Revised: 16 Nov 2018

Accepted: 18 Dec 2018

*Address for Correspondence

Ghaith H. Jihad

Department of Physics,

College of Science,

University of Baghdad, Iraq.

E-mail: GHAITHJIHAD@scbaghdad.edu.iq



This is an Open Access Journal / article distributed under the terms of the **Creative Commons Attribution License** (CC BY-NC-ND 3.0) which permits unrestricted use, distribution, and reproduction in any medium, provided the original work is properly cited. All rights reserved.

ABSTRACT

ZnO:Pb nanofilms have been produced on glass substrates by Laser induced plasma (LIPS) technique in Vacuum ($p = 2.5 \times 10^{-2}$ mbar) using Nd:YAG laser with (1064 nm) , $X=0.2$ and distance 10cm between laser and the substrate with thickness of films 108 nm. It is observed from optical properties that the films possess transition 75% in visible and near infrared region of spectrum and direct band gap values in the range of 2.2eV at $\lambda=1064\text{nm}$, when increases no. of pulse the films are more homogenate.

Key words: Laser Induced Plasma Spectroscopic (LIPS), Atomic Force Microscopic (AFM), X-Ray diffracting (XRD), Lead (Pb), Zinc mono Oxide (ZnO).

INTRODUCTION

Over the last few years, semiconductors has been widely studied due to their fundamental structural, electrical and optical properties Among them ZnS with a direct gap (3.6 eV) displays a high refractive index , and a high transmittance in the visible range making this a strong candidate for use in photo electronic devices . Tables (1-1) indicate physical, electrical properties of the basic characteristics for ZnS semiconductor.^[1,2,3] In general ZnS compound have two phase structure Cubic and Hexagonal and ZnS compound from group II-VI is white pellets has two crystalline structure which are (α wurtzite) with hexagonal structure and (β Zinc blend) with cubic structure, didn't passes in the liquid state i.e. it has low sublimation temperature, dissolves slightly in mixture of HNO_3 and H_2SO_4 but didn't dissolves in water. Also has low toxic. It was found that the small crystallite of wurtzite phase had been compound at **1273 K** i.e. Zinc blend changed to wurtzite phase at or before sublimation temperature, which affirm that the last phase is the most stable structure at high temperature. recent investigation have invoked considerable interest in ZnS thin film due to their vast potential for in thin film devices such as photoluminescent and





Ghaith H. Jihad

electroluminescent devices and more recently as n-type window layer heterojunction solar cell. Zinc sulfite has found wide range use as thin film coating in optical and micro electrical industries, it has wide wavelength pass band (9.4-13 μm). It is commonly used as filter reflector and planar waveguide. It is also the most commonly used as host material in thin film electroluminescent devices.^[1,4,5,6]

EXPERIMENTAL METHOD

Preparation of ZnO film doped with Pb under Vacuum ($P=2.5 \times 10^{-2}$ mbar) with weight $x=0.2$, using chemical mixed, Optical and Structural properties have been studied. In this study observe the crystal structure, investigate the absorbance of ZnO films with layer variation, and determine band gap energy with Pb doped variation pulsed Nd:YAG laser. ZnO thin film has been synthesized by LIPS method under Vacuum. On to the microscope glass substrates ($1 \times 25 \times 75 \text{mm}^3$) at energy value $E=600$ mJ with different number of pulses of Nd:YAG laser, then prepare ZnO:Pb films with different weight according to the following equation

$$W_{\text{ZnO}+\text{Pb}} = X * (W_{\text{Zn}} + W_{\text{O}}) + (1-X) * W_{\text{Pb}} \quad (1)$$

The results for Mixing between ZnO & Pb ($W_{\text{CuO}+\text{Pb}} = 3\text{gm}$)

The schematic arrangement of LIPS set-up is shown in Fig. (4). In which thin films are prepared under Vacuum with pressure tell to 2.5×10^{-2} mbar

RESULTS AND DISCUSSION

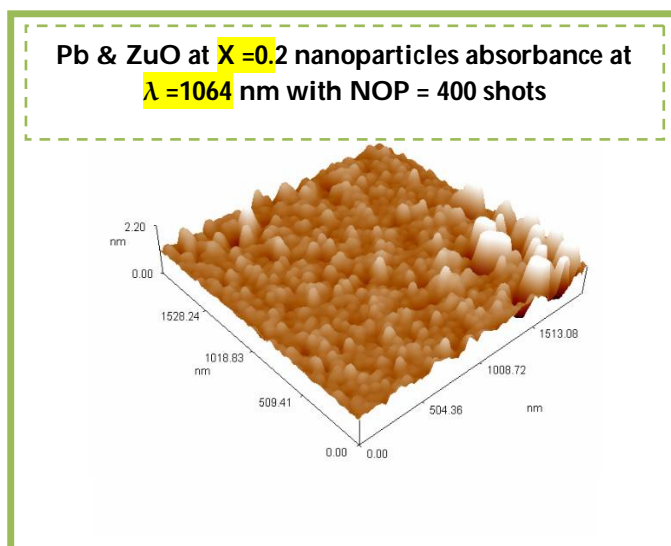
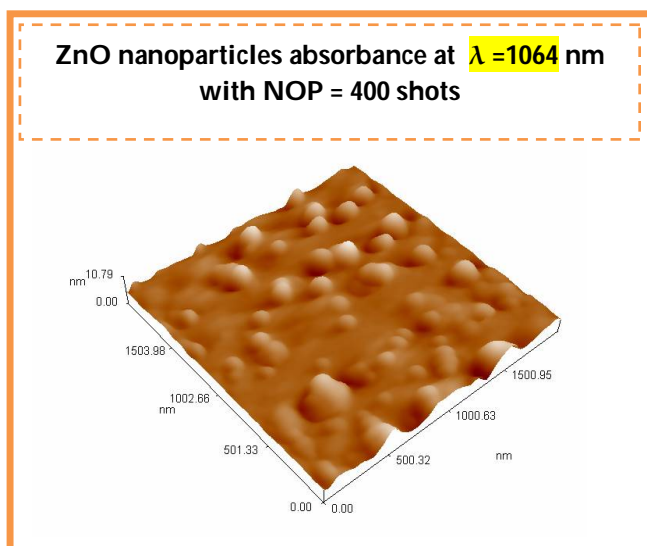
X-ray diffraction (XRD)

Figure (5) show The X-ray diffraction patterns of ZnS powder which indicated that the ZnS Compound has polycrystalline structure. From figure (5), it can be observed that the structure of ZnS powder was mixed of cubic with hexagonal system with peaks (111),(200),(220) and (311) for cubic system and (100),(101),(102),(103),(200),(112) and (201) for hexagonal system. Fig.(6) represent the X-ray diffraction pattern for ZnS thin film, the figure shows the preferred orientation (111) for pure ZnS structure as thin films at $2\theta = 28.5^\circ$. Fig.(7) show the X-ray diffraction pattern for ZnS:Pb thin film and get from the figure that the structure of ZnS after doped by Pb have the same preferred orientation by high intensity after the doping by improved structure for ZnS:Pb thin films which indicates the maker of (111) orientation between ZnS atoms and Pb atoms at 28.5° , this is a good agreement with Tran Thi Q. Hoa et al ^[4], M. Ashraf et al ^[7] and Dong Hyun Hwang et al ^[8].

Atomic force microscopy (AFM)

Atomic force microscopy AFM used to study the Morphology of the surface and crystal structure of the surface thin films precipitated, and which was calculated average grains size, Figure (8) describe three-dimensional pictures and distribution of the grains respectively for surfaces of prepared thin film. Average diameters for particles are increased with increase the doping of Pb due to transmission.





Optical Measurements

The Transmittance Spectra

The Transmittance Spectra for ZnS: Pb thin films can be shown in Fig. (8), we notes that the transmittance of ZnS: Pb thin film is zero between (200-520) nm, then the transmittance for the ZnS: Pb thin film increasing in (520-800) nm range of the wavelength. The maximum value for ZnS:Pb thin film at the wavelength (800nm), the figure shows that the properties of ZnS thin films can be change by the doped of Pb atoms when it incorporates in ZnS structure during the preparation. Direct energy gap for samples can be calculated using Tauc relation[8]:-

$$\alpha h \nu = B(h \nu - E_g)^{1/2} \quad (2)$$

Where B is a constant depends on the nature of the material, h is Planck's constant and ν is the photon frequency. The relationship between $(\alpha h \nu)^2$ and photon energy (hv) and extended straight portion of the curve to cut the photon energy axis at the point $(\alpha h \nu)^2 = 0$ we get the value of the energy gap, with thickness measured by using Fizeu Fringes is equal to 100 nm. Figures (8) show the optical energy gap for direct transmission of the copper oxide films with different number of pulses at Energy (E=900 mj) under Vacuum with $P=2.5 \times 10^{-2}$ mbar are Figure (9) show the optical energy gap of ZnS:Pb thin films, the energy gap for the ZnS thin film is 3.6 ev, this was agreement with J.P. Borah et al [2] and M. Ashraf et al [7].and the energy gap for ZnS:Pb thin film was decreases to 2 ev after annealing .

CONCLUSIONS

The Conclusion from the data which were mentioned in the previous chapter, and conclude that:-

- 1) The structure of Zn thin film is improved after the doping.
- 2) The Transmittance is zero between the region (200-500) nm after the doping, and The maximum value for ZnS: Pb thin film at the wavelength (800nm).
- 3) The energy gap for the ZnS thin film was decreasing to 2 eV after annealing with T=200k.





Ghaith H. Jihad

4) the structure of the ZnS thin film enhanced after the doped by Pb atoms and more homogeneity after annealing with T=300K.

REFERENCES

1. M.Y. NADEEM and Waqas AHMED "Optical Properties of ZnS Thin Films", Turk J Phy. Vol.24, P (651 – 659), (2000).
2. J.P. Borah and K.C. Sarma, "Optical and Optoelectronic Properties of ZnS Nanostructured Thin Film" ACTA PHYSICA POLONICA, Vol. 114, (2008) .
3. M. Ruhul Amin BHUIYAN, M. Monjarul ALAM and M. Abdul MOMIN" Effect of substrate temperature on the optical properties of thermally evaporated ZnS thin films", Turk J Phys, Vol.34, P(43 – 49),(2010).
4. Tran Thi Quynh Hoa , Ngo Duc The , Stephen McVitie , Nguyen Hoang Nama, Le Van Vu , Ta Dinh Canh , Nguyen Ngoc Long "Optical properties of Mn-doped ZnS semiconductor nanoclusters synthesized by a hydrothermal process", Optical Materials, Vol 33 ,P(308–314) ,(2011).
5. B.Ray, "II-VI Compounds", Vol, 122, P.12, (1969).
6. P.Burrous and S.Forrest, "J.Appl.Phys. ", Vol.177, P.101, (1996).
7. M. Ashraf, S.M.J. Akhtar, Z. Ali and A. Qayyum," The influence of substrate temperature on the structural and optical properties of ZnS thin films" ,Vol. 45 , P.5 .
8. Dong Hyun Hwang, Jung Hoon Ahn, Kwun Nam Hui, Kwan San Hui and Young Guk Son," Structural and optical properties of ZnS thin films deposited by RF magnetron sputtering" ,Vol .7,P.(24),(2012).

Table .1. indicate physical, electrical properties of the basic characteristics for ZnS semiconductor

Property \ Material	ZnS
Energy Gap (eV)	3.66
Type of transition	Direct
Mobility Cm ² /v	150
Effective mass	0.26
Melting point (K)	1930-2173
Color	White-yellow transparent grains
Melting point under vacuum (1 Torr)	1811 K
Density (gm/cm ³)	3.98
Molecular weight	97.44
Lattice constant (A ⁰)	5.406

Table 2 The results for Mixing between ZnO & Pb (W_{CuO+Pb} = 3gm)

X	ZnO (gm)	Pb (gm)
0.2	2.732	0.278





Ghaith H. Jihad

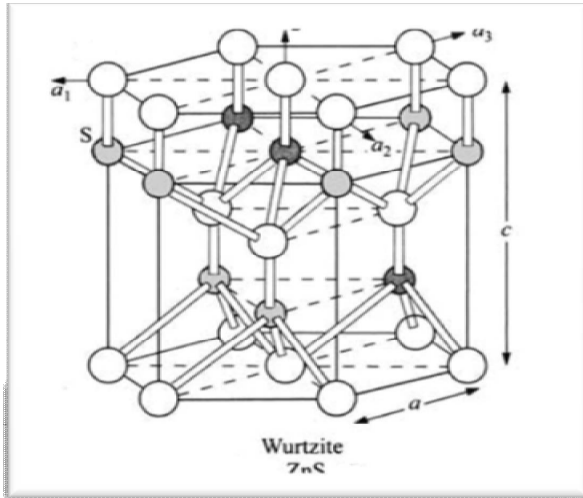


Fig. 1. Wurtzite Structure

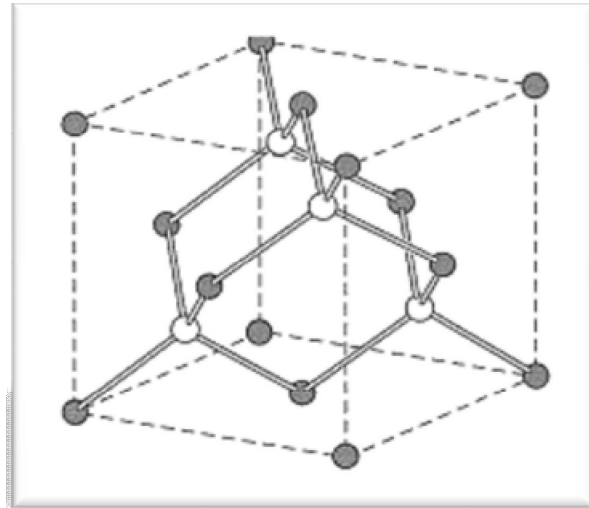


Fig. 2. Cubic Zinc Sulfide Structure

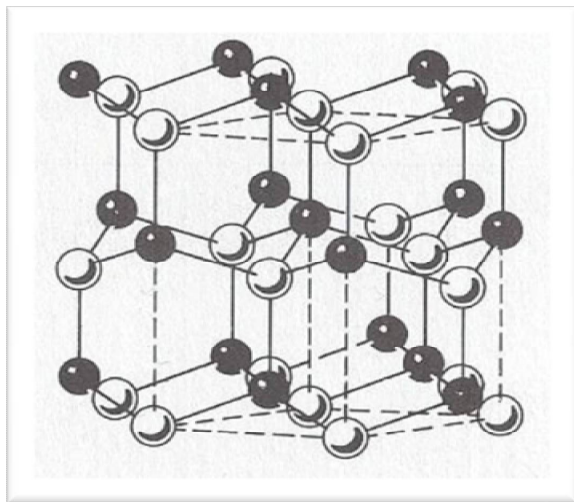


Fig. 3. Hexagonal Zinc Sulfide Structure

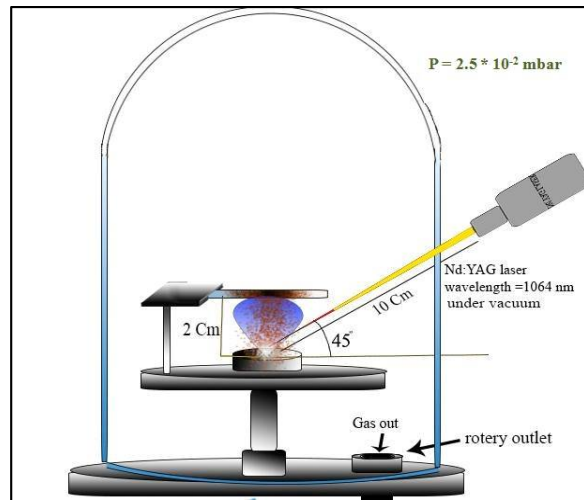


Fig. 4. ZnO:Pb films fabrications by using Laser Induced Plasma System under Vacuum with $\lambda=(1064\text{nm})$





Ghaith H. Jihad

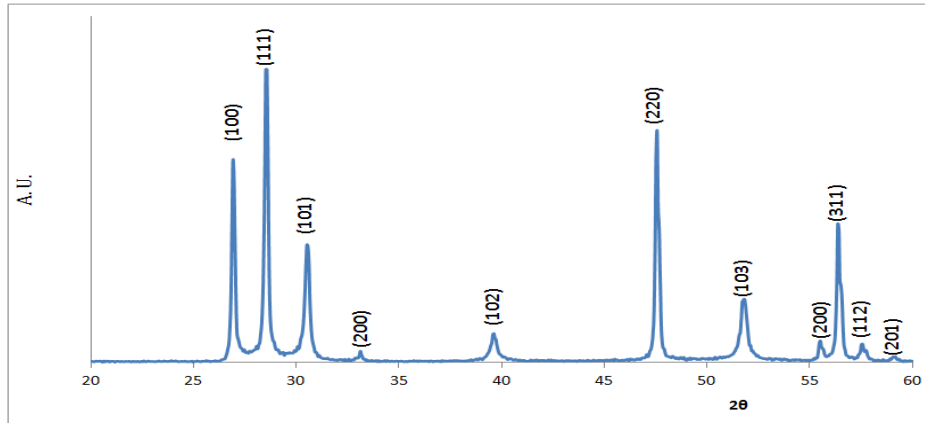


Fig. 5. X-Ray diffraction of ZnS powder

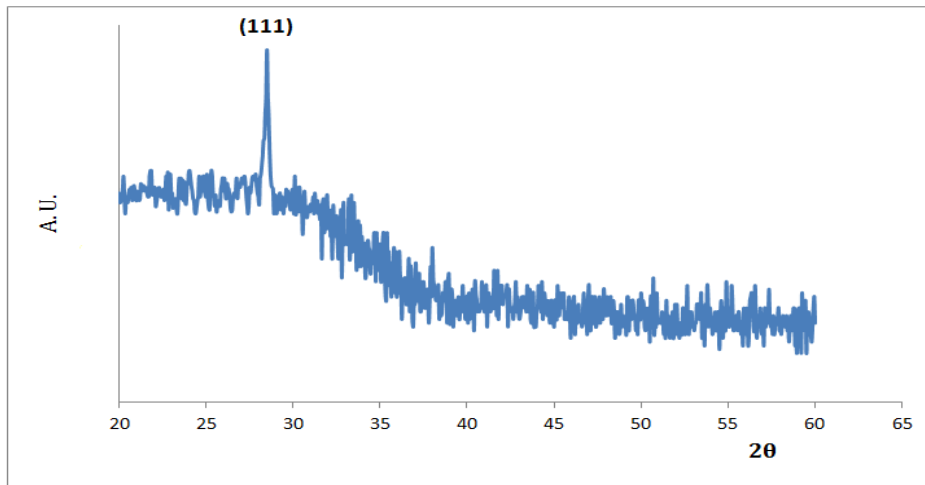


Fig.6.X-Ray diffraction of ZnS thin film

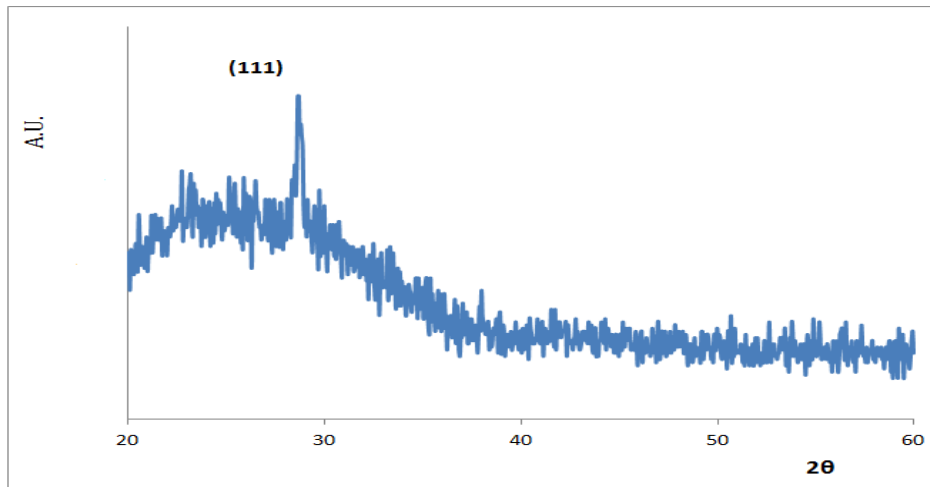


Fig.7. X-Ray diffraction of ZnS:Pb thin film





Ghaith H. Jihad

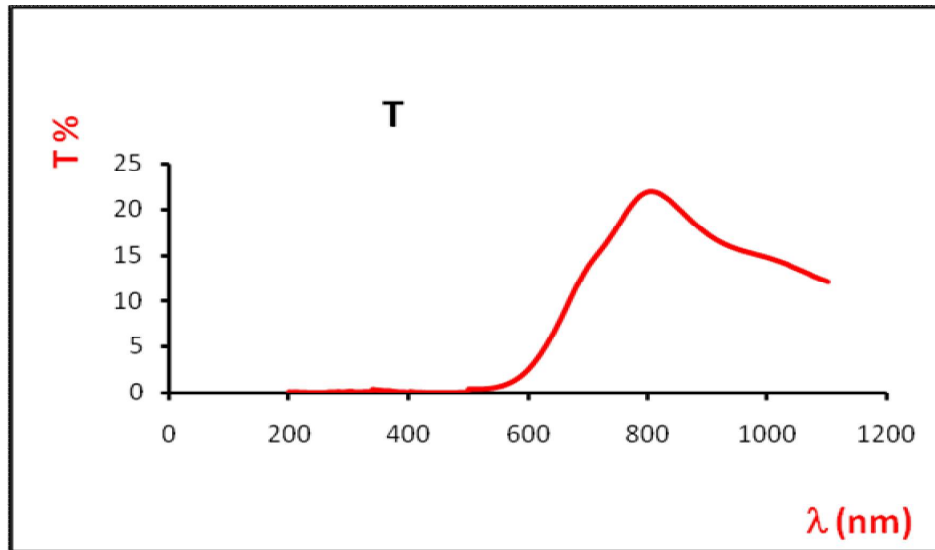


Fig.8. The Optical transmittance of ZnS:Pb thin films

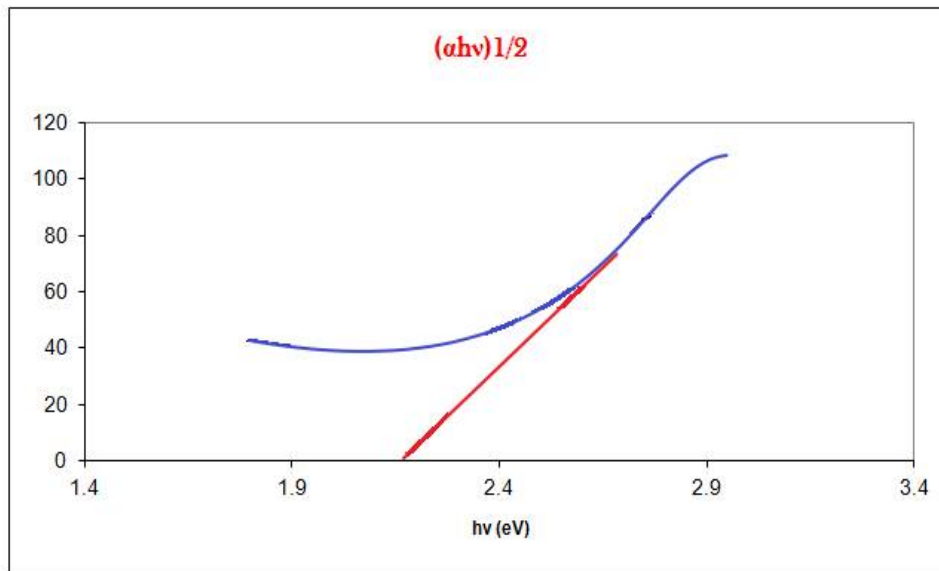


Fig.9. The Optical Energy gap ZnS: Pb thin films





Utilizing Remote Sensing Techniques to Extract the Geological Lineaments in AL-Najaf Plateau

Alaa Hassan Harif* and Laith A. Jawad

Unit of Remote Sensing, College of Sciences, University of Baghdad, Iraq.

Received: 13 Oct 2018

Revised: 15 Nov 2018

Accepted: 17 Dec 2018

*Address for Correspondence

Alaa Hassan Harif

Unit of Remote Sensing,

College of Sciences,

University of Baghdad, Iraq.

E-mail: alaaharif@ScBaghdad.edu.iq



This is an Open Access Journal / article distributed under the terms of the **Creative Commons Attribution License** (CC BY-NC-ND 3.0) which permits unrestricted use, distribution, and reproduction in any medium, provided the original work is properly cited. All rights reserved.

ABSTRACT

Iraq is one of the Arabian region countries, which considered as an arid to semi-arid area, though it has two main rivers that pass through (Tigris and Euphrates) it suffers the same problem as them (drought), only the rivers' nearby regions make use of their water for (domestic, agricultural, and industrial purposes). One of the usable solutions is to make advantage of the groundwater (especially in the desert regions). remote sensing and geographic information system is a rapid and cost effective techniques, they provide information of large and inaccessible area within short span for assessing, monitoring, and management of groundwater resources. In this work the hydrogeological unit (system) of AL-Najaf Plateau has been delineated using SRTM DEM based new rapprochements (the compaction layers, isopleth contour lines, and the profile graph) to be 2768 square kilometers, the Hillshaded DEM was adopted for geological lineaments visually extraction because of their topographic aspects (since each lineament causes fracture that yield steep slope in the earth crust). then GIS techniques has been used to identify the maximum secondary porosity and permeability locations in the plateau, which considered optimum locations for wells drilling using lineaments longitudinal density distribution map which achieved by utilizing the IDW spatial interpolation method.

Keywords: spatial interpolation, secondary permeability, longitudinal density, and topographic aspects

INTRODUCTION

Geological Lineament is a linearly, rectilinearly, or a curvilinear aspect of tectonic activity reference which can be seen in the aerial or the satellite imageries [1]. The extracting and/ or mapping method of them is essential issue for the engineering problem solving in location selecting for dams, bridges, or roads construction [2], the assessment of seismic or landslide risk [3], the exploration of mineral mines [4], and the application of hydrogeological researches



**Alaa Hassan Harif and Laith A. Jawad**

[5]. Geological lineaments usually show tone, texture, relief, linearity and curvilinearity in drainage and vegetation [6]. faults, joints, or boundaries between stratigraphic formations are examples of geologic lineaments [7]. Remotely sensed imagery is considered rapidly and costly effective modern technique for lineaments extraction, since it provide raw data / information about large and inaccessible area within short span [8]. In the field of water projects remote sensing utilizing as a multi-spectral data acquisition scheme for situation assess, observation, and project management of groundwater resources [9], and GIS techniques utilizing as tools for measuring and analyzing offer a predefined knowledge about the runoff water infiltration zones, the natural factors of the hydrogeological unit, the nature of the basin, the groundwater flow orientation, and the optimum locations for drilling wells that characterized of having a long- term stable high yield (i.e. high permeability wells in the groundwater aquifer zone) [10].

The study area

The study region is AL-Najaf plateau basin, which locates in the south -western part of Iraq country, it comprises of districts from several provinces (Najaf, Anbar, Karbala, Dewaniya, and Babil). The basin extends between the north latitudes 31° 54' to 32° 42' and east longitudes 43° 38' to 44° 33' and covers an area of 2707 square kilometers. The region is arid to semiarid with rare rain storms around the year; the surface water is absent, therefore, rainfall recharged groundwater is very essential for the drinking and agricultural purposes.

METHODOLOGY

The work of this article was partitioned into four phases, as follow:

SRTM DEM Preprocessing

The preprocessing involves restoration of the DEM image pixels with two steps:

1. -32768 value excluding (background removal).
2. Filling the "No data" pixels using the (3×3) mean filter.

After the no data pixels filling with proper values process, the (basin) option from the (hydrology) option in the spatial analyst arc tool in Arc GIS 9.3 selected to delineate all the basins in the corrected DEM as in figure (1):

As can be seen this method failed to state the recharge, discharge zones.

Delineation of Hydrogeological Unit in AL- Najaf Plateau**Delineation of Hydrogeological Unit in AL- Najaf Plateau by using Compaction Layers**

To overcome the previous failure a new (DEM depending scheme) introduced in this research by using a compaction of two transparent layers (aspect and percentage arise slope) with a non- transparent layer (the corrected hillshaded DEM), this scheme as can be seen below is succeeded to determine the recharging zones of the basin only. As in figure (2).

Delineation of Hydrogeological Unit in AL- Najaf Plateau by using DEM's Isopleth Contour Lines

An adapted contour lines approach with 90m SRTM DEM was introduced. The new idea is to add more than one (Isopleth's contour line images) then approximated them to avoid fuzzy in order to determine the recharge-discharge zones as can be illustrated in figures from (3) to (7).

The approximation step of the contour lines resulted in missing many terrain features making this method good but not optimum





Alaa Hassan Harif and Laith A. Jawad

Delineation of Hydrogeological Unit in AL- Najaf Plateau by using DEM's Profile Graph

A new method were submitted in this search again, which is the applying of the 3D analyst tools in Arc GIS 10.3 (interpolate line and create profile graph) on the corrected 90m SRTM elevation model with sufficient times as illustrated in figure (8) to recognize the recharging and discharging zones, which is a sink zone for the present area of the basin. The next step is study area extraction, which is AL-Najaf formation basin. As illustrated in figure (9). This technique simply enables the analyzers (the experts and the non-experts as well) to define the main basin's borders.

The Geological Lineaments Extraction in AL- Najaf Plateau basin

The Geological Lineaments Extraction in AL- Najaf Plateau using SRTM Hillshaded DEM.

In this study these topographic aspects has been utilized to distinguish the lineaments by using the (hillshading 3D tool in ArcGIS 10.3) with the corrected 90m Shuttle Radar Topographic Mission DEM. The lineaments main directions have been determined by changing the illumination angle and fixing the altitude of the sun as shown in figure (10). One of the Hillshaded AL-Najaf basin images is shown in figure (11). When the azimuth angle of the sun changed the relief appearance is different as can be seen with some angles of the figure (12). As can be seen the topographic aspects of the lineaments are obvious in different orientations. The Lineaments Visually Extraction in Different Orientations Using Sun Azimuth Angles (0°, 45°, 90°, and 135°) can be illustrated in figure (13). The geological Lineaments Visually Extraction in Different Orientations Using Sun Azimuth Angles (180°, 225°, 270°, and 315°) can be illustrated in figure (14). After The extraction of geo-lineaments Visually in Different Orientations Using Sun Azimuth Angles (0°, 45°, 90°, 135°, 180°, 225°, 270°, 315°), all the non-overlapping lineaments were added to create region lineaments distribution image as showed in figure (16).

The lineaments distribution image of AL-Najaf plateau basin cannot be used to state the locations of lineaments maximum longitudinal density (i.e. the locations where the secondary porosity and secondary permeability are maxima), so Inverse Distance Weighted spatial interpolation scheme has been used to create raster images that identify different longitudinal densities with different colors. In order to certify the raster accuracy, The plateau area was partitioned into squares of (2×2) km as a grid and the lineaments longitudinal density of each square has been calculated and placed in its center, then longitudinal density raster image created. Figure (17) illustrate the partitioning scheme. Using IDW, the lineaments maximum longitudinal density locations has been delineated as shown in figure (18). The red polygons are the ones with maximum secondary porosity and permeability and the best theoretically to drill wells.

CONCLUSIONS

In this work AL-Najaf plateau basin borders delineated perfectly by applying the 3D analyst tools (interpolates line and create profile graph) on the corrected 90m SRTM, also the lineaments visually extracted using their topographic aspects in the Hillshaded SRTM DEM with different orientations. AL-Najaf plateau lineaments maximum longitudinal density distribution map was obtained using the IDW interpolation scheme and the optimum locations for drilling wells that characterized of having a long-term stable high groundwater yield in AL-Najaf plateau basin with comparison to other locations was delineated using the remotely sensed information.

REFERENCES

1. Sulaksana, N. and Helman, A. (2014) The Analysis of Remote Sensing Imagery for Predicting Structural Geology in Berau Basin East Kalimantan. International Journal of Science and Research, 3, 18-21.



**Alaa Hassan Harif and Laith A. Jawad**

2. Papadaki, E.S., Mertikas, S.P. and Sarris, A. (2011) Identification of Lineaments with Possible Structural Origin Using ASTER Images and DEM Derived Products in Western Crete, Greece. EARSel eProceedings, 10, 10.
3. Melki, F., Zouaghi, T., Ben Chelbi, M., Bedir, M. and Zargouni, F. (2010) Tectono-Sedimentary Events and Geodynamic Evolution of the Mesozoic and Cenozoic Basins of the Alpine Margin, Gulf of Tunis, North-Eastern Tunisia Offshore. *Comptes Rendus Geoscience*, 342, 741-753.
4. Kacem, J. (2004) étude sismotectonique et évaluation de l'aléa sismique régional du Nord-Est de la Tunisie: Apport de la sismique réflexion dans l'identification des sources sismogéniques. Thèse de Doctorat, Université de Tunis El Manar, Tunisie.
5. Pepe, F., Sulli, A., Bertotti, G. and Catalano, R. (2005) Structural Highs Formation and Their Relationship to Sedimentary Basins in the North Sicily Continental Margin (Southern Tyrrhenian Sea): Implication for the Drepano Thrust Front. *Tectonophysics*, 409, 1-18
6. Riahi, S., Soussi, M., Boukhalifa, K., Ben Ismail Lattrache, K., Dorrik, S., Khomsi, S. and Bedir, M. (2010) Stratigraphy, Sedimentology and Structure of the Numidian Flysch Thrust Belt in Northern Tunisia. *Journal of African Earth Sciences*, 57, 109-126.
7. Chihi, L. (1995) Les fossés néogènes à quaternaires de la Tunisie et de la mer pélagienne: Etude structurale et leur signification dans le cadre géodynamique de la Méditerranée centrale. Thèse Doctorat ès Science Géologique, Université de Tunis El Manar, Tunisie.
8. Biémi, J., Gwyn, Q.H.J., Deslandes, S. and Jourda, P. (1991) Géologie et réseaux de linéaments, région du bassin versant de la Marahoué, Cote d'Ivoire: Cartographie à l'aide des données Landsat-TM et du champ magnétique total. In: Gagnon, P., Ed., *Téledétection et gestion des ressources*, Vol. 7, Association québécoise de téledétection, 134-145.
9. Demetre, A., Ourania, M., and Marianthi, S. 2000. Automatic mapping of tectonic lineaments (faults) using methods and techniques of Photointerpretation / Digital Remote Sensing and Expert Systems.
10. Semere, S., Ghebread, W. 2006. Lineament characterization and their tectonic significance using landsat TM data and field studies in the central highlands of Eritrea, *Journal of African Earth Science*, 46, pp: 315-318.

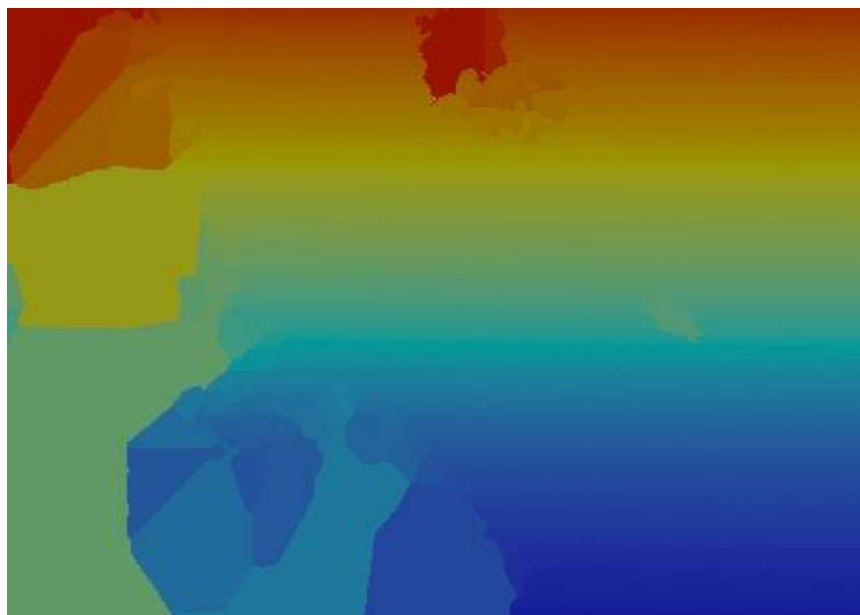


Figure 1. The Delineated Basins Using Arc Map Hydrology Tool.





Alaa Hassan Harif and Laith A. Jawad

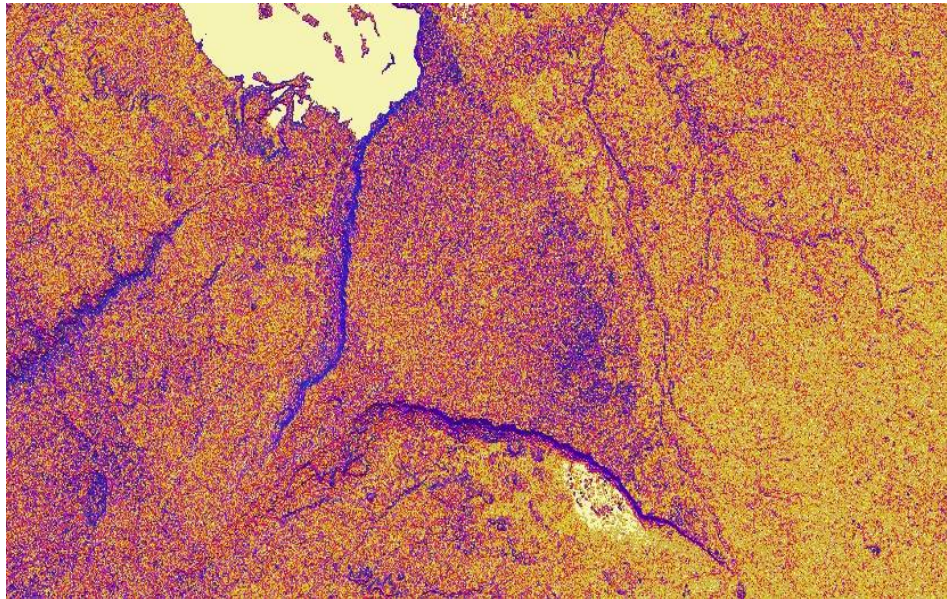


Figure 2. Basin's Recharging Zones Delineated Using a Compaction of Two Transparent Layers (Aspect and Percentage Arise Slope) with a Non- Transparent Layer (The Corrected Hillshaded DEM).

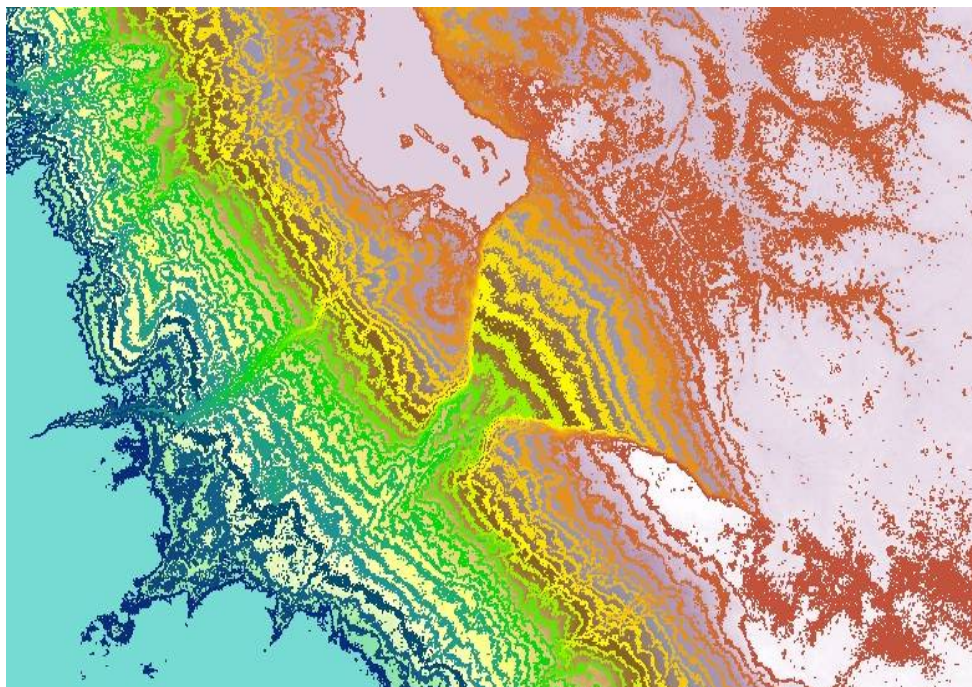


Figure 3. AL-Najaf Plateau and Surroundings 10m Isopleth's Contour Line Image.





Alaa Hassan Harif and Laith A. Jawad

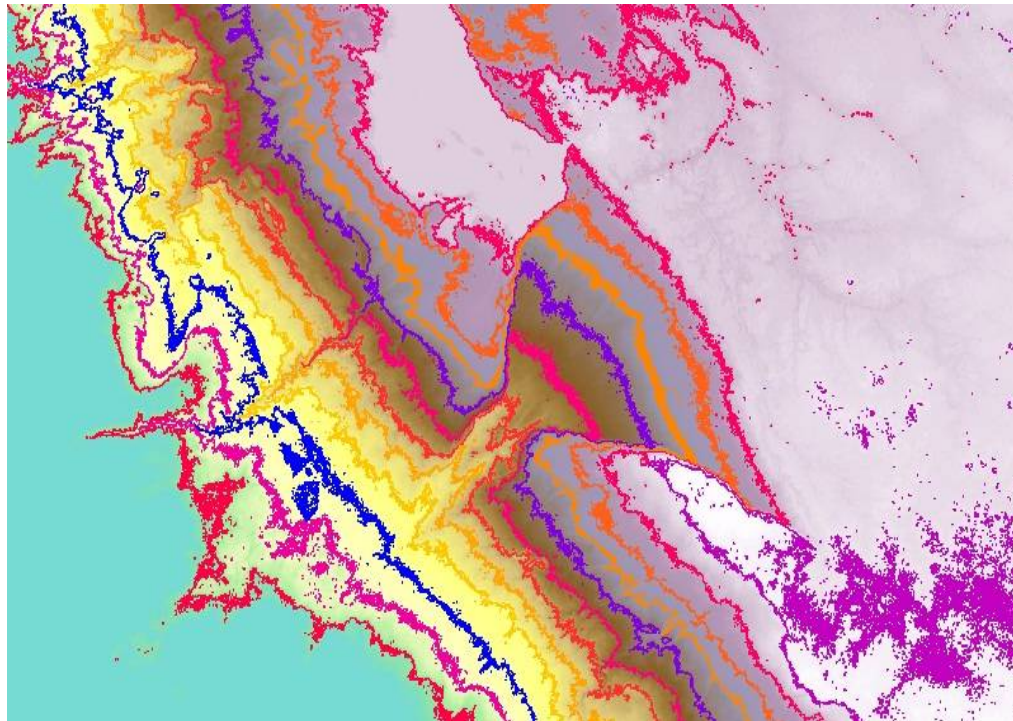


Figure 4. AL-Najaf Plateau and Surroundings 20m Isopleth's Contour Line Image.

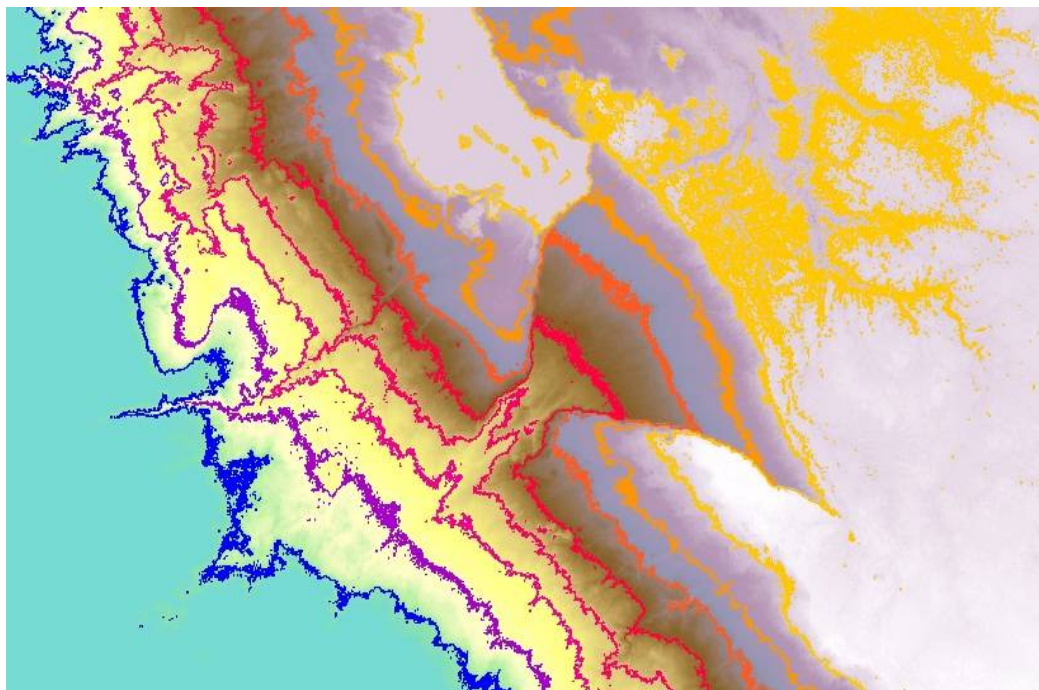


Figure 5. AL-Najaf Plateau and Surroundings 30m Isopleth's Contour Line Image.



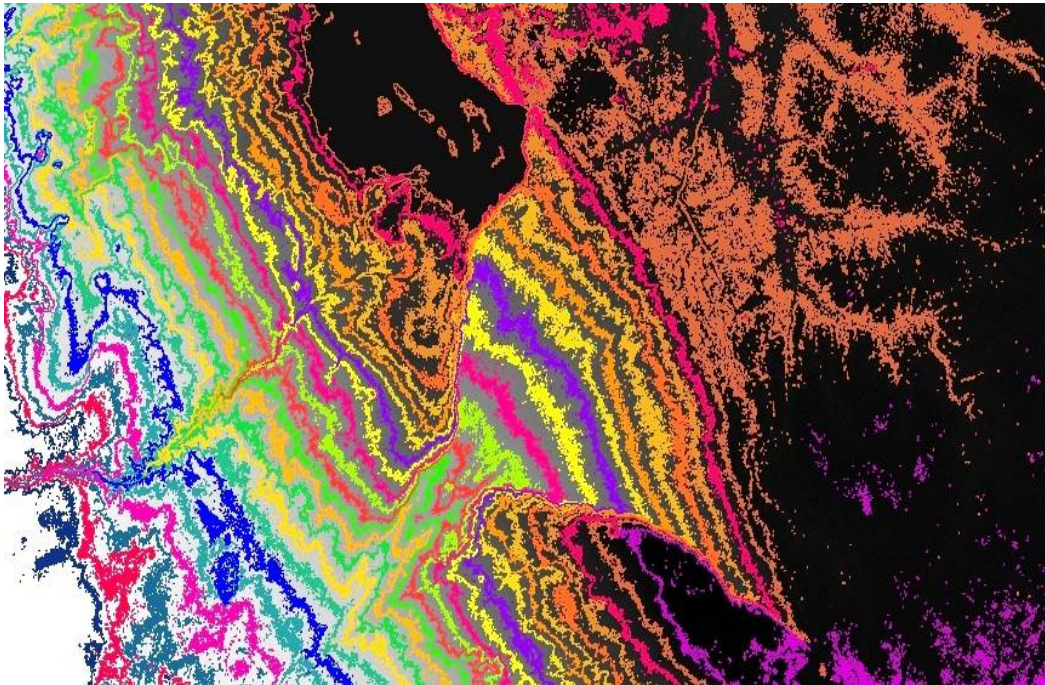


Figure 6. AL-Najaf Plateau and Surroundings (10, 20, and 30) m Isopleth's Contour Line Added Image.

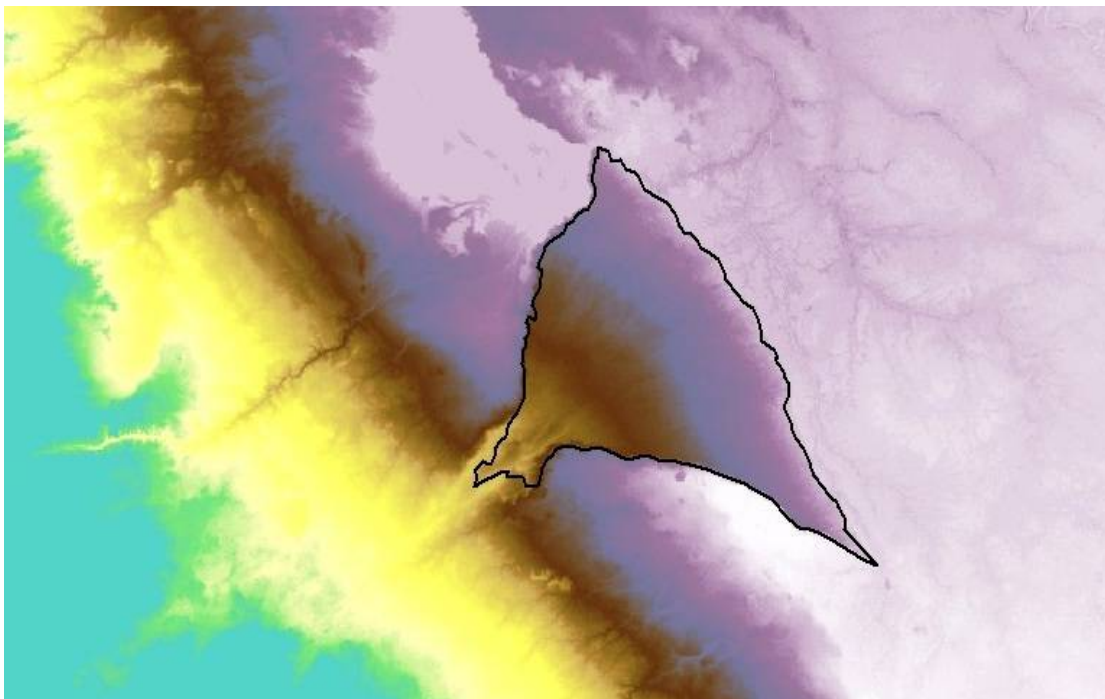


Figure 7. AL-Najaf Plateau and Surroundings Basin Using Isopleth's Contour Line Scheme.





Alaa Hassan Harif and Laith A. Jawad

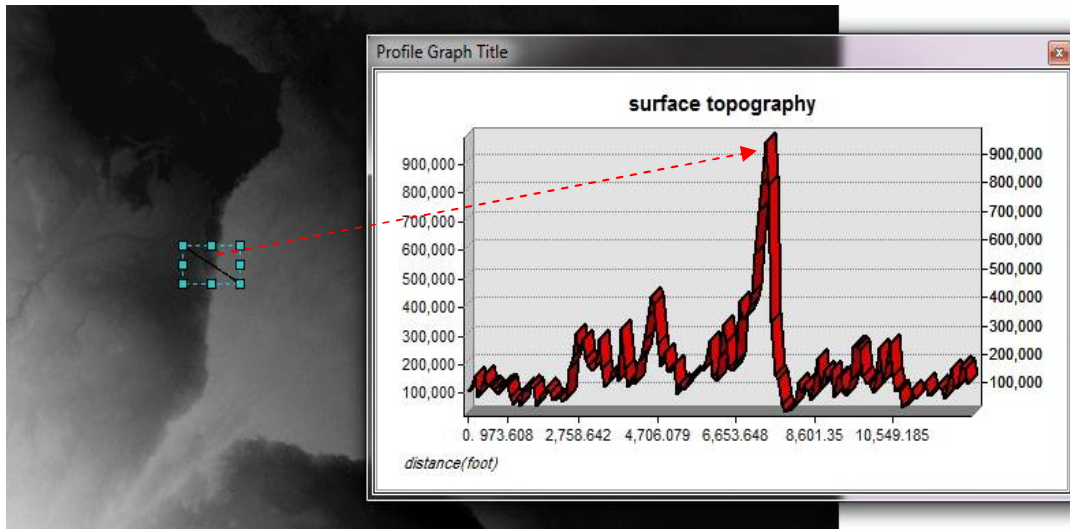


Figure 8.AL-Najaf Plateau and Surroundings Image Illustrating One of the Profile Graphs That Used to Delineate The Basin Borders.

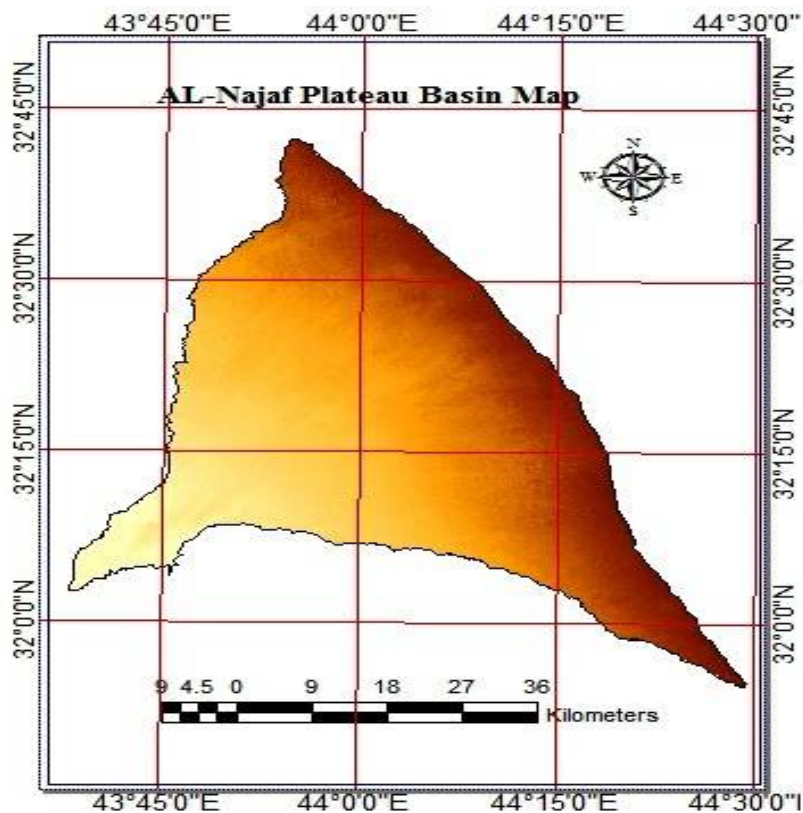


Figure 9. Corrected DEM Image of AL-Najaf Basin.





Alaa Hassan Harif and Laith A. Jawad

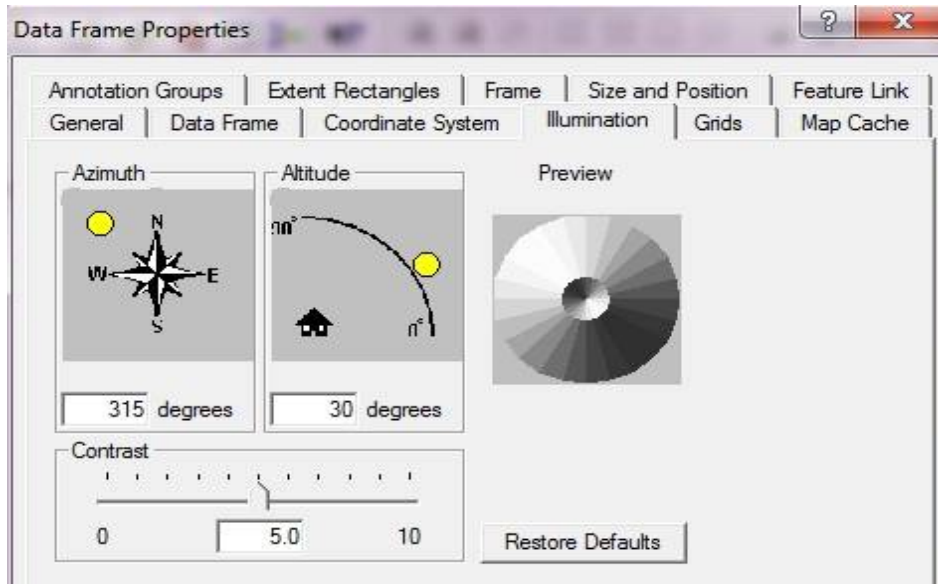


Figure 10. The Lineaments Orientation Delineation by Changing the Illumination Angle and Fixing the Altitude of the Sun.

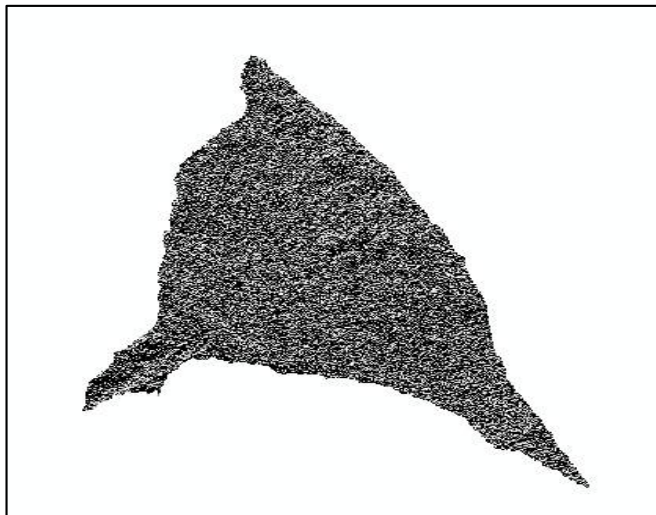


Figure 11. Hillshaded DEM of AL-Najaf Basin Image with Sun's 315° Azimuth Angle and 45° Altitude Angle.

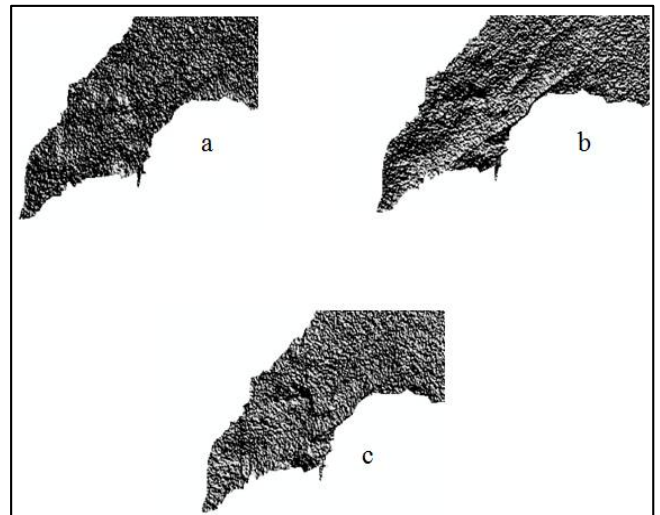


Figure 12. The Effect of Changing The Sun Azimuth Angle on The Relief Apparent in Different Orientation in AL-Najaf Basin. (a) 0° (b) 45° (c) 90°.





Alaa Hassan Harif and Laith A. Jawad

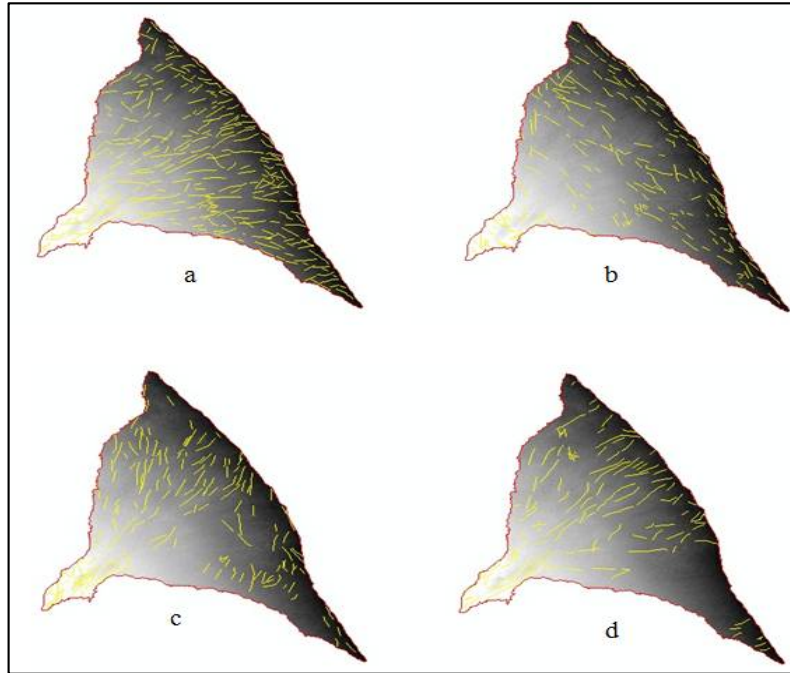


Figure 14. The geo-Lineaments Visually Extraction in Different Orientations Using Sun Azimuth Angles (a) 0° (b) 45° (c) 90° (d) 135°.

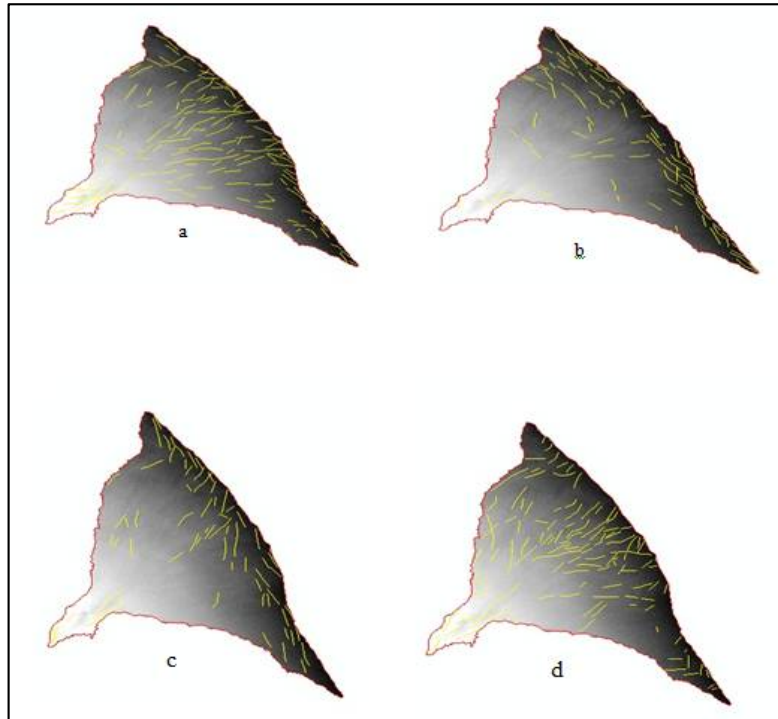


Figure 15. The lineaments Visually Extraction in Different Orientations Using Sun Azimuth Angles (a) 180° (b) 225° (c) 270° (d) 315°.





Alaa Hassan Harif and Laith A. Jawad

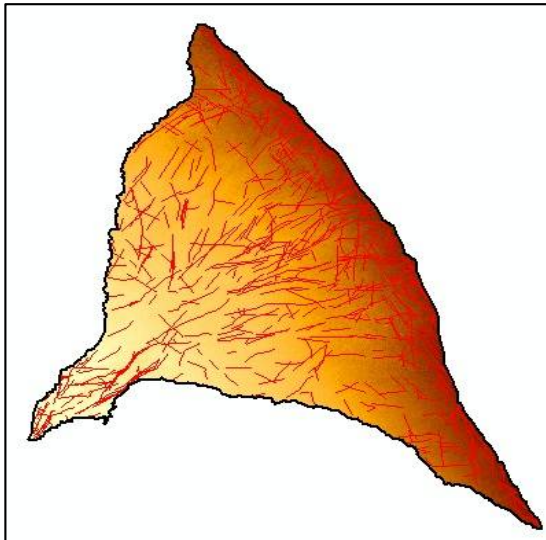


Figure 16. lineaments distribution image of AL-Najaf Basin.

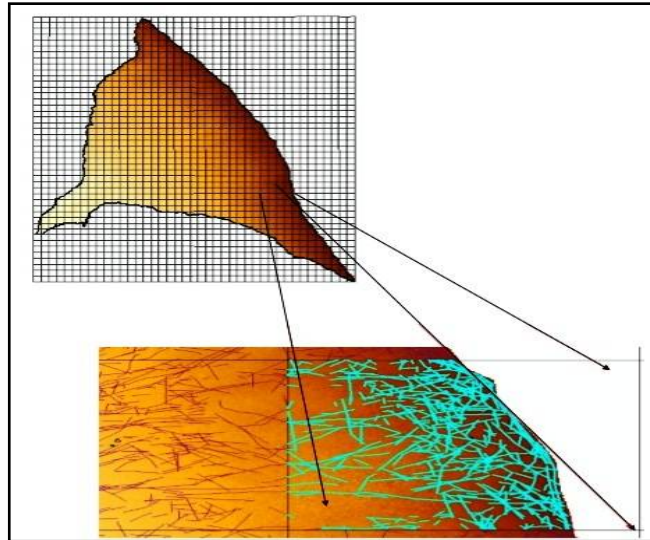


Figure 17. AL-Najaf Basin 2 km Side Length Square Grid Illustrating One of the Squares Selected Lineaments to be processed.

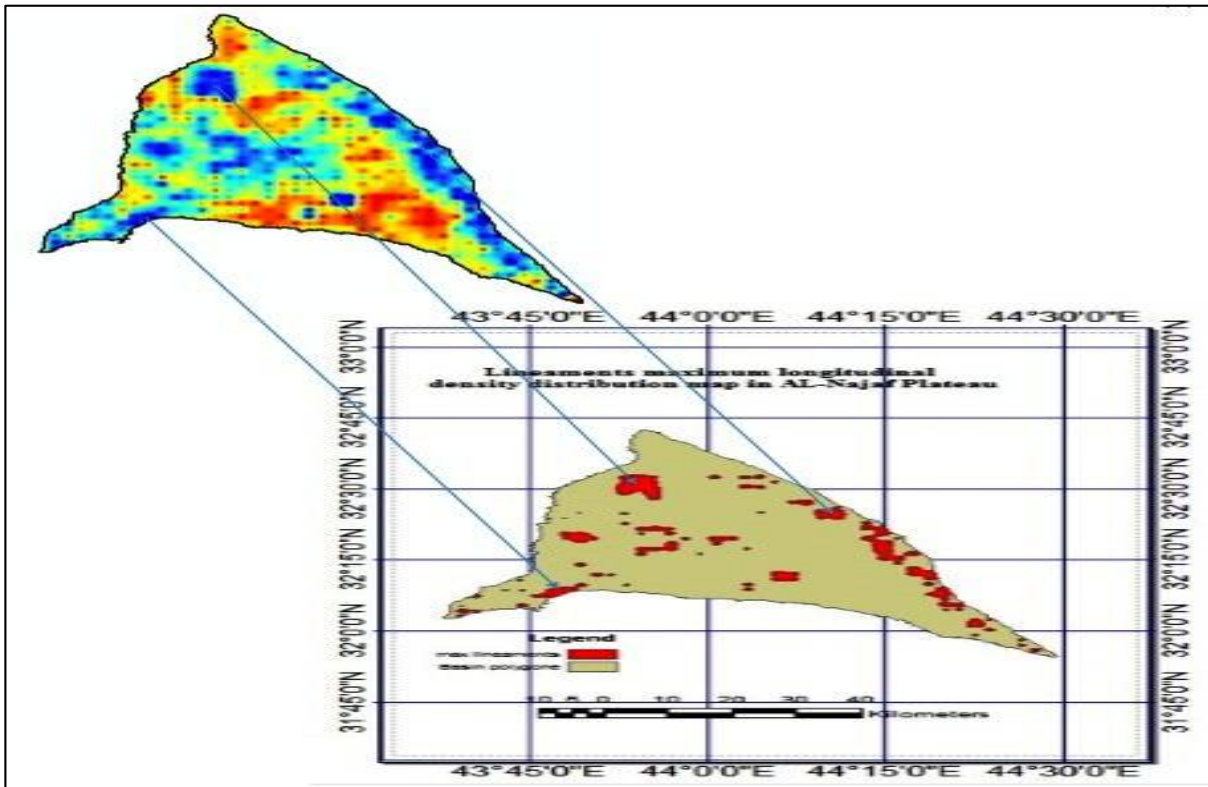


Figure 18. The Lineaments Maximum Longitudinal Density Locations of AL-Najaf Basin Delineated with red Polygons Using IDW Scheme.





Effect of the Oxygen / Argon Mixture on the Parameters of the plasma Glow Discharge Prepared by DC Magnetron Sputtering

Muhammed.Sh.Muhammed^{1*}, Mohammed.K. Khalaf² and Sabri. J. Mohammed³

¹Education Mission, Education Department, Salah al-Din, Iraq.

²Ministry of Sciences and Technology, Baghdad, Republic of Iraq.

³Physics Department, University of Tikrit , Republic of Iraq.

Received: 10 Oct 2018

Revised: 13 Nov 2018

Accepted: 18 Dec 2018

*Address for Correspondence

Muhammed.Sh.Muhammed

Education Mission,
Education Department,
Salah al-Din, Iraq.



This is an Open Access Journal / article distributed under the terms of the **Creative Commons Attribution License** (CC BY-NC-ND 3.0) which permits unrestricted use, distribution, and reproduction in any medium, provided the original work is properly cited. All rights reserved.

ABSTRACT

In this present work, we investigate the properties of reactive magnetron sputtering plasma using Vanadium target. The properties of reactive magnetron Vanadium pentoxide sputtering plasma at various discharge conditions were studied. Basically, the electron temperature is determined from the slope of Boltzmann's plot that uses the intensity of several spectral lines versus their corresponding excitation energies. We studied the changing of spectral lines intensity of (O₂/Ar) gas mixture plasma and related plasma parameter of electron temperature (T_e), electron density (n_e), with applied (660-820) V, and working pressure (0.08-0.3) mbar. A results showed that the intensity of spectral lines and electron temperature increase with increasing of applied voltage while electron density decrease as the applied voltage is increased in the range (660 – 820) Volt .on other hand , results show that the OI and OII spectral lines and electron density increase while it's electron temperature decrease according to increasing of the gas pressure . Results showed that the intensity of spectral lines and electron temperature increase with increasing of applied voltage while electron density decrease as the applied voltage is increased in the range (660 – 820) Volt.

Keywords: magnetron sputtering, electron temperate, electron density.

INTRODUCTION

Reactive sputtering technique using Vanadium metal target represents one of the simplest and most effective technique which has been used by many researchers[1][2].The Spectroscopy method for plasma diagnostics are the least perturbative, and for the evolution of the plasma Parameters, they study the emitted, absorbed or dispersed radiation[3]. Oxygen plasma has an important application in the semiconductor industry due to their ability to





Muhammed.Sh.Muhammed et al.

charge free, unlike electropositive plasma with ions and electrons. An electronegative plasma is composed of three different charges, positive ions, electrons, and negative ions, which were formed the attachment reaction of electron to the neutral of oxygen gas can significantly change the plasma characteristics, obtaining the fundamental knowledge and the experimental results about the oxygen plasmas is important in determining the optimum operating conditions with certain atoms or molecules[4]. In addition, oxygen is one of the best disinfectant agents [5]. Because only a small amount of the characteristics of the plasma[6].

Current research on plasma is focused on plasma diagnostics. Optical Emission Spectroscopy is the most popular technique to investigate glow discharges. Since it is simple and that it produces no perturbation in the plasma. All plasmas emit radiation depending on their gas composition and plasma parameters. The purpose of the optical emission spectroscopy (OES) is to measure and analyze this radiation for understanding the plasma[7]. The remarkable advantage of OES is its aggressive measurement process. By just measuring the radiation from the plasma there is no need to bring a probe system in contact with the plasma (like Langmuir-Probe or Multiple Resonance Probe) which might influence the plasma itself. Furthermore, OES enables one to investigate very small plasmas; often smaller as probes themselves. One of the most commonly used remote diagnostic methods is optical spectroscopy (OES), which is the illuminated section of general radio therapy. In OES, visible light is usually collected by a lens and focused on a spectrometer gap[3] [5]. From the information which take from optical emission spectroscopy we can measure electron temperature and electron density. Electron temperature and electron density obtained by the following equation respectively:

$$\frac{I_1}{I_2} = \left(\frac{\lambda_{n,m,z}}{\lambda_{k,i,z}} \right) \left(\frac{A_{k,i,z}}{A_{n,m,z}} \right) \left(\frac{g_{k,z}}{g_{n,z}} \right) e^{\left(\frac{-E_{k,z} - E_{n,z}}{KTe} \right)} \dots \dots \dots (1)$$

$$ne = \left(\frac{2\pi m_e K}{h^3} \right)^{3/2} \times \left(\frac{2A_{k,i,z} g_{k,i,z} \lambda_{N,M,Z} I_2}{A_{n,m,z} g_{n,m,z} \lambda_{k,i,z} I_1} \right) e^{\left(\frac{-E_{k,i} - E_{n,m}}{KTex} \right)} \times T_e^{3/2} \dots \dots \dots (2)$$

Reported by [6] the electron density increasing and electron temperature decrease with increasing gas pressure, while electron temperature increase with increasing the power. Although numerous studies have shown that due to the electrical properties of the plasma, little attention is given to the properties of the plasma spectrum[8].

EXPERIMENTAL SETUP

The plasma diagnostics in vanadium sputtering is commenced by evaluating the chamber to pressure lower than (8.6x10⁻² mbar). (90/10),(80/20),(70/30), and (50/50) of Ar/O₂ mixer was introduced into the chamber at a specified pressure. The discharges plasma spectra were measured in Ar/O₂ mixer at an applied voltage of 660 Volt and discharge current (40mA). When adding a small amount of oxygen gas causes a lot of changes in the characteristics of the light source of argon light, it is evaporated in the emission spectrometry. The effect of oxygen addition on the sputtering rate and the excitation of the analyses in the argon plasma were investigated by using argon-oxygen binary mixed gases having well-predefined compositions. Optical emission spectroscopy (OES) is often employed for diagnostics of reactive plasmas to characterize the different excitation and ionization processes of both atomic and molecular species in Ar-O₂ mixture plasma under different discharge conditions. The partial pressure of the gun, the spray time, the substrate temperature and the spray voltage, are the main parameters of determining the film properties when the VO thin films are reacted by the DC magnetron spectrometry. Among these parameters, the applied voltage and working pressure[9].

perhaps is the most accessible parameter. The VOx thin film is coated on the crystal, glass, and coated ITO glasses, a DC power source of magneto-spectrometry to subtract the target with high purity vanadium (99.95%) in argon (99.995%) and oxygen (99.995%) was used. The DC power supply is then switched on and established to the required current and cathode bias voltage. Surface finish and nature of the substrate used for depositing is very important





Muhammed.Sh.Muhammed et al.

since it influences the properties of the thin layers tremendously [10][11]. The substrates were sputtered etched in Ar/O₂ (10%,20%,30%,50%) plasma at bias voltage of 660 volts. and current 40mA for 2hours. From the figures(5,6,7,8) Indicates that each function as an O₂ function from this figure can be seen that both electron temperatures increase with an increase in the percentage of O₂ due to a decrease in energy loss by the electrons during ionizing collision with O₂ molecules as the ionization cross-section for O₂ is smaller than that of Ar. while the electron density decrease with the addition of O₂ in the ambient gas, The phenomenon is explained by the molecular gases O₂ reduce the electron density due to the high-energy losses in excitation of vibrational levels [12].

Glow discharge of both pure argon and argon-oxygen plasmas has been studied at different pressures and constant current mode equal to 40 mA. Results show that increasing the working pressure gives rise to an increase in the number of carriers of electrical current (electrons and ions) and collision frequency. It has been found that for both argon plasma and argon-pure oxygen, the electron temperature increases from the cathode to the anode, while the electron density decreases. The potential of the plasma and the floating potential of the cathode increases to the anode. On the other hand, an increase in discharge pressure leads to a decrease in the electron electron's temperature. The electronegativity of oxygen decreases the electron density which leads to decrease the floating potential and increase the plasma potential. The plasma electron temperature at these points can be observed. From the cathode to the anode, the density of electrons is decreased while their temperature is increased. With drifting from cathode to anode, electrons achieve energy from the applied electric field which leads to an increase in their temperature. By increasing the temperature the collision frequency which is inversely proportional to electron temperature is decreased. A smaller number of ionization cuts reduces electron density. After the introduction of oxygen as an electronegative gas, the electron density decreases, while the electron temperature increases as compared to the pure Ar plasma. In fact, the number of ionizing collisions is reduced. Plasma current is kept constant in both Ar and Ar/O₂ plasmas. But in Ar/O₂ plasma some electrons are bonded to oxygen atoms to make negative ions. Because plasma is quasi-neutral, the number of free electrons in Ar/O₂ plasma is less than Ar plasma decreasing the electron density leads to decreasing the collision numbers so in the case of Ar/O₂ plasma electron energy is higher [13][14][15].

CONCLUSIONS

In this paper, advances in experimental research on plasma properties were determined by determining their physical parameters using optical spectroscopy. The advances obtained in this yield have included the development of procedures that enable classical spectroscopic techniques to be applied for plasma diagnostics to the specific cases of sputtering and vacuum arc plasmas. The dependence of the values of the parameters on the experimental conditions is also a characteristic feature of these plasmas, which complicates the comparison of results of different experiments. Nevertheless, significant progress has been achieved in determining accurate values of the plasma electron density, temperature and densities of atoms.

REFERENCES

1. M. K. Sharma, B. K. Saikia, and S. Bujarbarua, "Optical emission spectroscopy of DC pulsed plasmas used for steel nitriding," *Surf. Coatings Technol.*, vol. 203, no. 3–4, pp. 229–233, Nov. 2008.
2. [S. A. Wissel, A. Zwicker, J. Ross, and S. Gershman, "The use of dc glow discharges as undergraduate educational tools," *Am. J. Phys.*, vol. 81, no. 9, pp. 663–669, Sep. 2013.
3. C. Aragón and J. A. Aguilera, "Characterization of laser induced plasmas by optical emission spectroscopy: A review of experiments and methods," *Spectrochim. Acta Part B At. Spectrosc.*, vol. 63, no. 9, pp. 893–916, Sep. 2008.
4. J.-S. Kim, G.-H. Kim, and K.-H. Kwon, "Characterization of an Oxygen Plasma by Using a Langmuir Probe in an Inductively Coupled Plasma," *J. Korean Phys. Soc.*, vol. 38, no. 3, pp. 259–263, 2001.
5. *and M. Meyyappan†† A. A. Bol'shakov,* B. A. Cruden,† R. Mogul,‡ M. V. V. S. Rao,§ S. P. Sharma,¶ B. N. Khare, "Radio-Frequency Oxygen Plasma as a Sterilization Source," *AIAA*, vol. 42, pp. 823–832, 2004.





Muhammed.Sh.Muhammed et al.

6. J. K. Rhee, D. B. Kim, S. Y. Moon, and W. Choe, "Change of the argon-based atmospheric pressure large area plasma characteristics by the helium and oxygen gas mixing," *Thin Solid Films*, vol. 515, no. 12, pp. 4909–4912, Apr. 2007.
7. A. K. Shrestha, R. Shrestha, H. B. Baniya, R. B. Tyata, D. P. Subedi, and C. S. Wong, "Influence of Discharge Voltage and Pressure on the Plasma Parameters in a Low Pressure DC Glow Discharge," *Int. J. Recent Res. Rev.*, vol. VII, no. 2, 2014.
8. F. J. Gordillo-Vázquez, M. Camero, and C. Gómez-Aleixandre, "Spectroscopic measurements of the electron temperature in low pressure radiofrequency Ar/H₂/C₂H₂ and Ar/H₂/CH₄ plasmas used for the synthesis of nanocarbon structures," *Plasma Sources Sci. Technol.*, vol. 15, no. 1, pp. 42–51, Feb. 2006.
9. M. Y. Naz, A. Ghaffar, N. U. Rehman, S. Naseer, and M. Zakaullah, "DOUBLE AND TRIPLE LANGMUIR PROBES MEASUREMENTS IN INDUCTIVELY COUPLED NITROGEN PLASMA," *Prog. Electromagn. Res.*, vol. 114, pp. 113–128, 2011.
10. T. H. Chung, Y. M. Shin, and D. C. Seo, "Comparison of Two Methods of Interpretation of Langmuir Probe Data for an Inductively Coupled Oxygen Plasma," *Contrib. to Plasma Phys.*, vol. 46, no. 5–6, pp. 348–353, Jun. 2006.
11. A. V Phelps and Z. L. Petrovic, "Cold-cathode discharges and breakdown in argon: surface and gas phase production of secondary electrons," *Plasma Sources Sci. Technol.*, vol. 8, no. 3, pp. R21–R44, Aug. 1999.
12. D. D. • M. Alizadeh, "Effect of negative oxygen ions on the characteristics of plasma in a cylindrical DC discharge," *J Theor Appl Phys*, 2014.
13. N. D. M. A. Hassouba, "A Comparative Spectroscopic Study on Emission Characteristics of DC and RF Discharges Plasma using Different Gases.," *Life Science Journal*, Vol. 11, No. 9, pp.656–666, (2014).
14. M. Barbisan, B. Zanionl, M. Cavernago, R. Pasqualotto, G. Serianni, and M. Zanini, "Electron density and temperature in NIOI RF source operated in oxygen and argon " *AIP Conference Proceedings* 1869.030031 (2017).
15. N. D. M. A. Hassouba, "A Comparative Spectroscopic Study on Emission Characteristics of DC and RF Discharges Plasma using Different Gases , " *Life Science Journal* , Vol.11.No.9 .pp. 656-666, (2014).

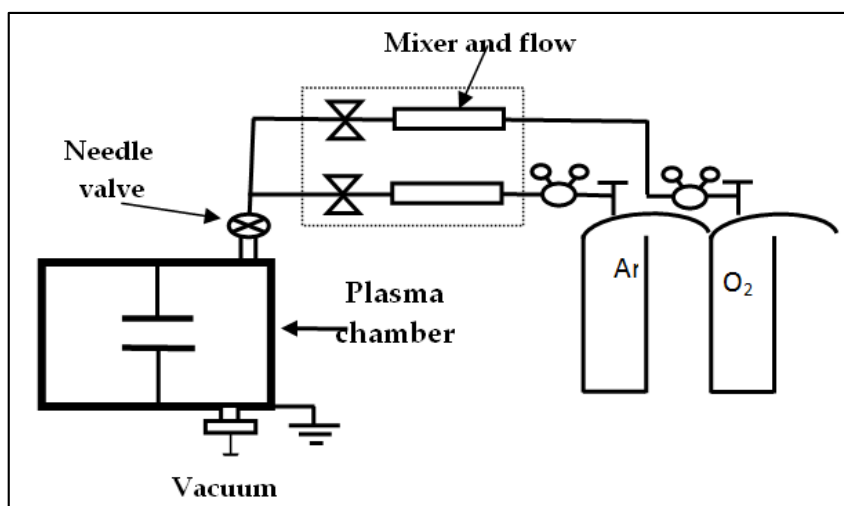


Figure 1. The main experimental set-up used in this work





Muhammed.Sh.Muhammed et al.

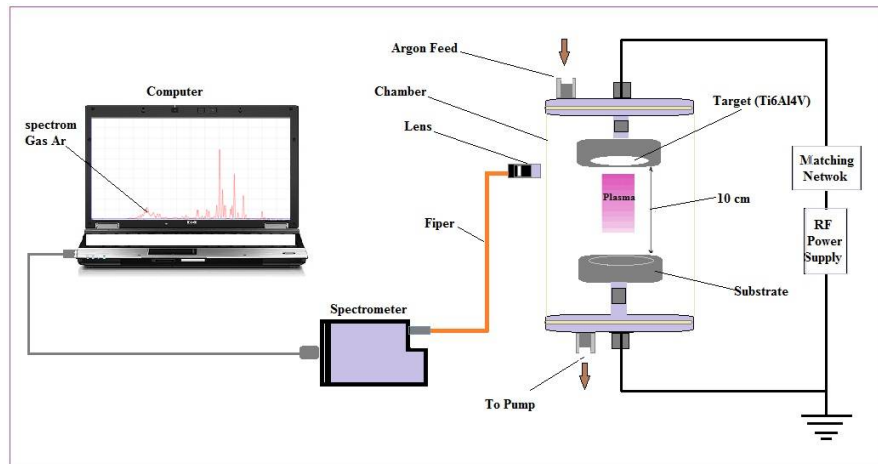


Figure 2. Optical emission spectroscopy experimental setup.

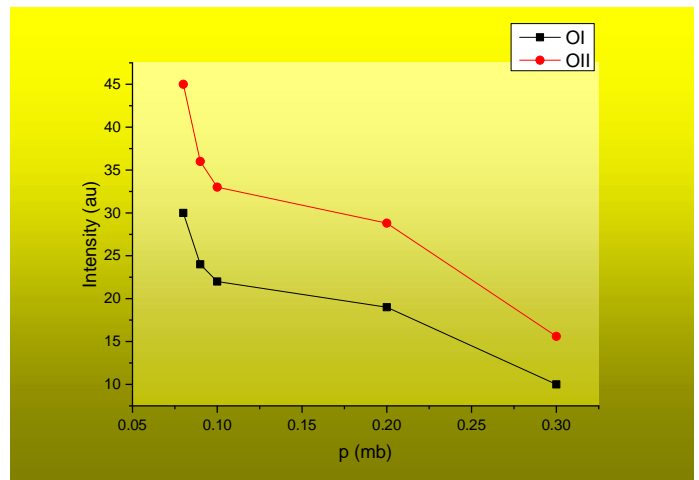
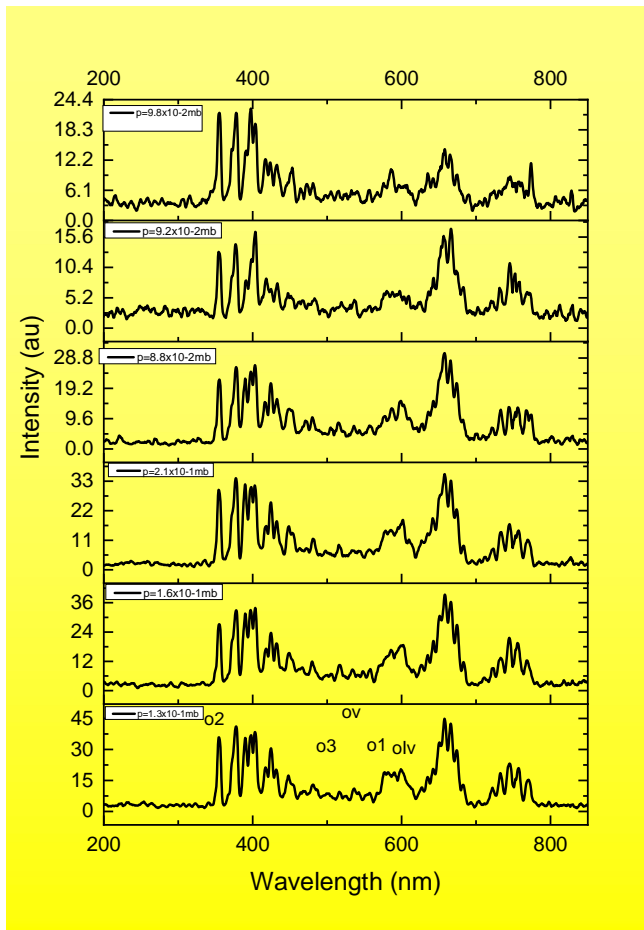


Figure 3. spectrum by using Vanadium target at different working pressure . A-The plasma intensity in different applied voltage. B-The variation of plasma intensity of OI and O II spectral lines with working pressure.





Muhammed.Sh.Muhammed et al.

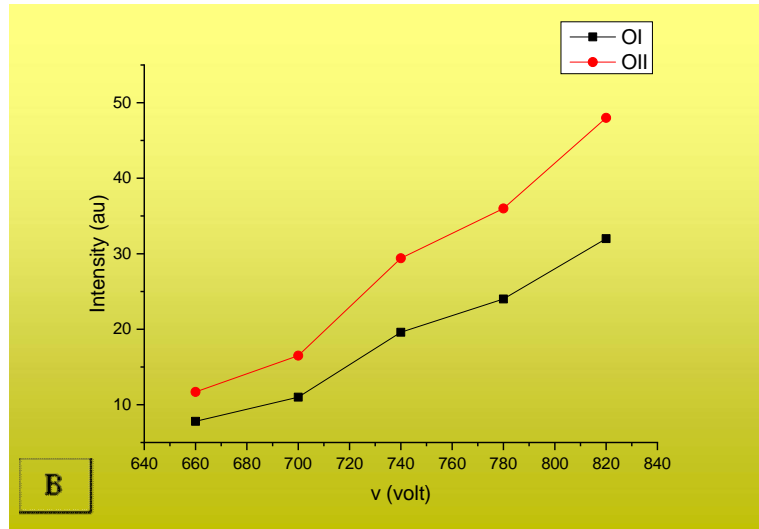
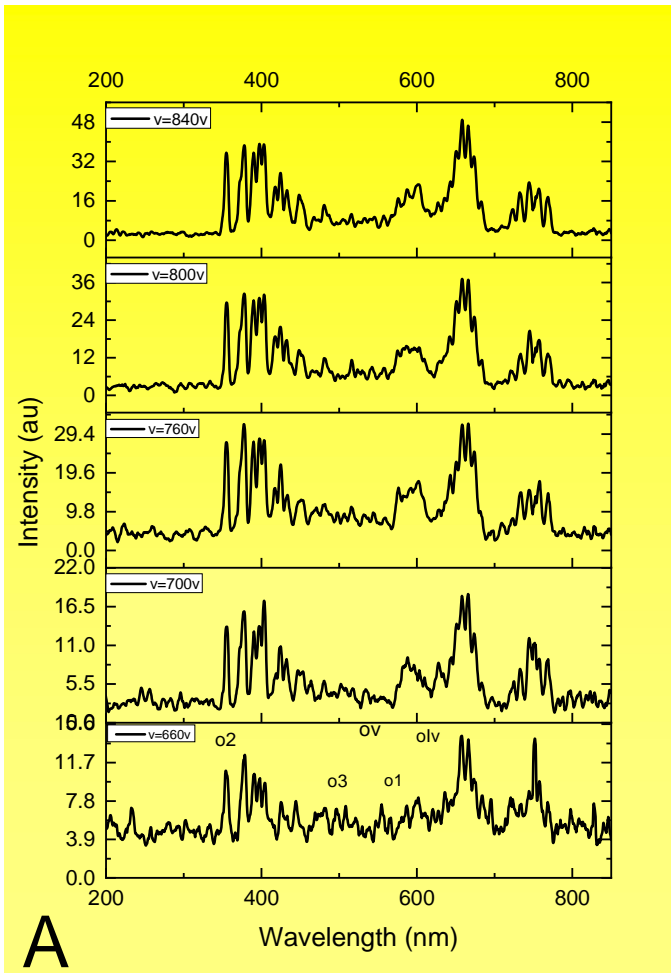


Figure 4. Spectrum by using Vanadium target at different applied voltage. A-The plasma intensity in different applied voltage. B-The variation of plasma intensity of OI and O II spectral lines with applied voltage





Muhammed.Sh.Muhammed et al.

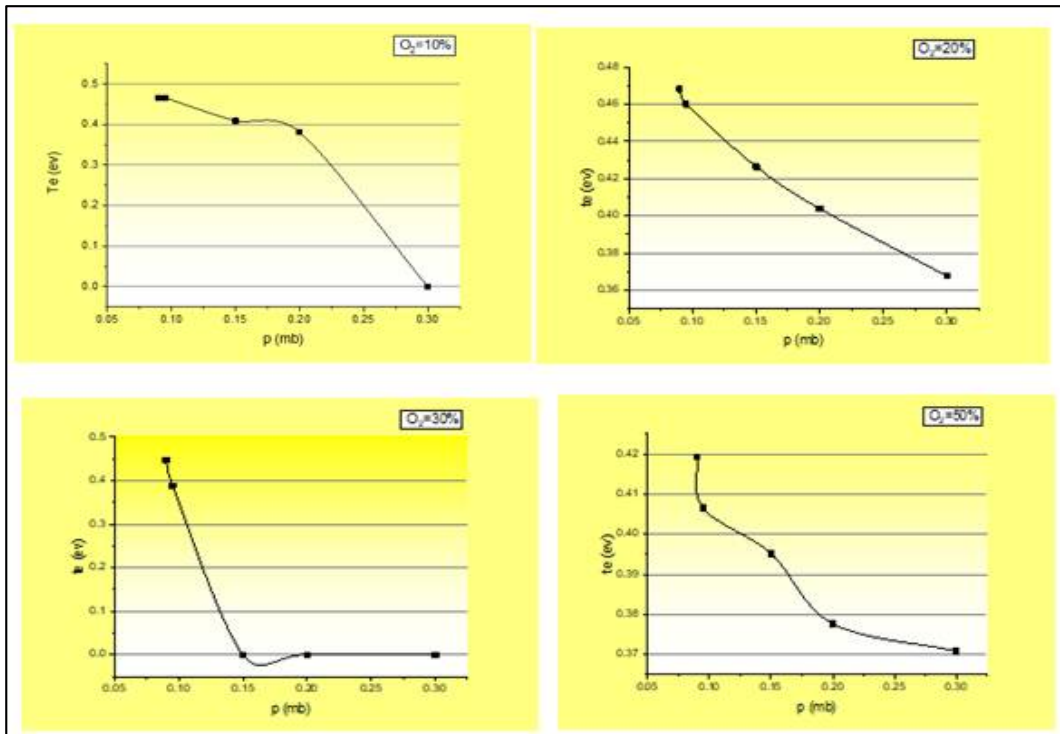


Figure 5. Shows the evolution of the electron's temperature as a function of O_2 with working pressure

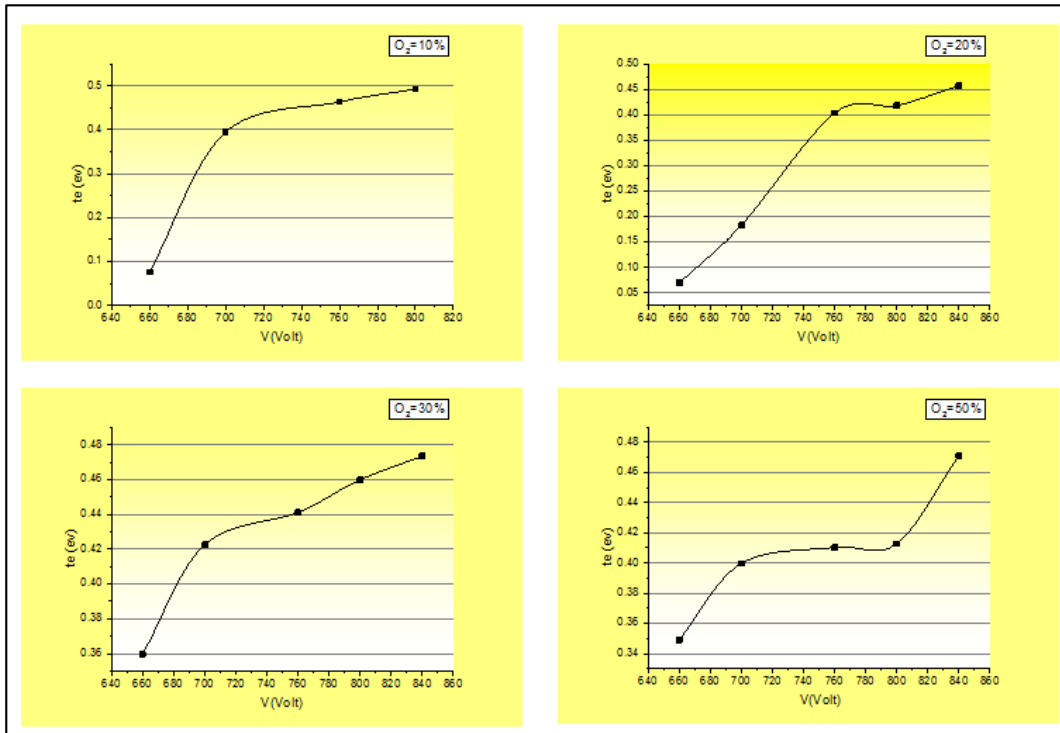


Figure 6. Shows the electron temperature and electron density as the applied voltage function



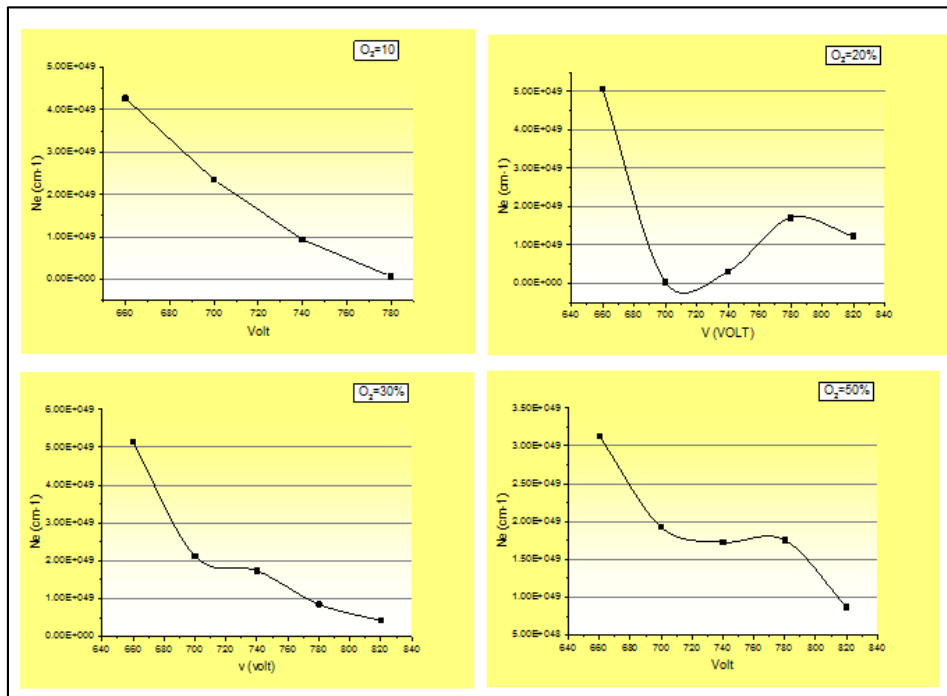


Figure 7. Shows the evolution of electron's density as a function of O₂ with working pressure

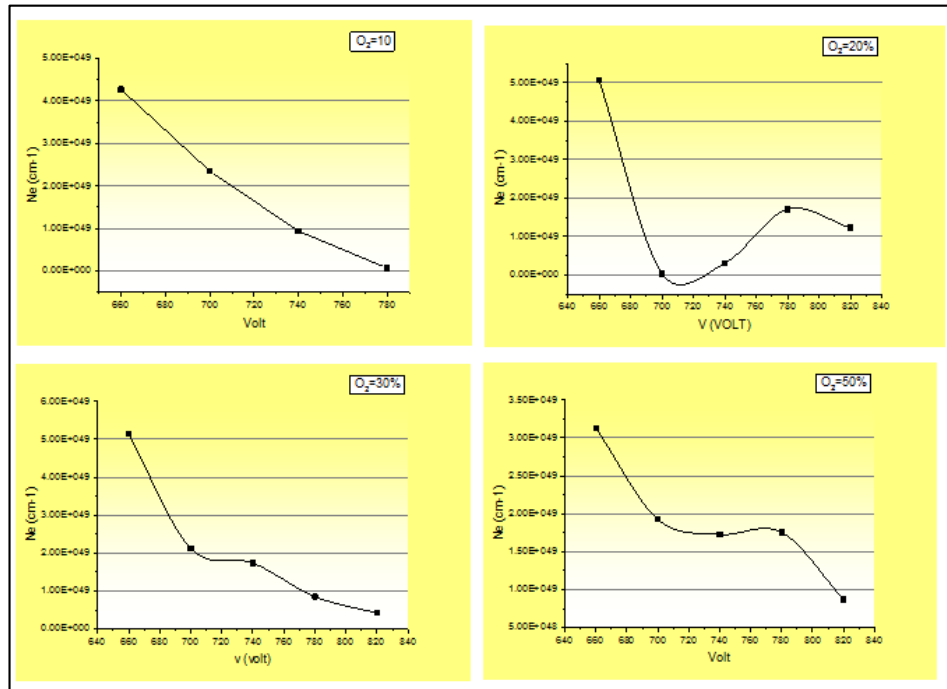


Figure 8. Shows the evolution of electron's density as a function of O₂ with voltage





Cooperation of Sonicated *Corynebacterium pseudotuberculosis* and *Pseudomonas aeruginosa* Antigens for Enhancement Cellular Immune Response in Rabbits

Ikram Abbas Aboud Al-Samarrae*

Department of Microbiology, College of Veterinary Medicine, University of Baghdad, Baghdad, Iraq.

Received: 13 Oct 2018

Revised: 16 Nov 2018

Accepted: 19 Dec 2018

*Address for Correspondence

Ikram Abbas Aboud Al-Samarrae

Department of Microbiology,
College of Veterinary Medicine,
University of Baghdad, Baghdad, Iraq.



This is an Open Access Journal / article distributed under the terms of the **Creative Commons Attribution License** (CC BY-NC-ND 3.0) which permits unrestricted use, distribution, and reproduction in any medium, provided the original work is properly cited. All rights reserved.

ABSTRACT

The objective of this study was aimed to evaluate the cooperative between *Corynebacterium pseudotuberculosis* and *Pseudomonas aeruginosa* antigens in the cellular immune response by using twelve local breed rabbits, which divided into three groups, the first group inoculated 1mg/ml killed whole cell sonicated *Corynebacterium pseudotuberculosis* antigen (KWCSAg-Cp) and 1mg/ml killed whole cell sonicated *Pseudomonas aeruginosa* antigen (KWCSAg-Pa), the second group inoculated 1mg/ml killed whole cell sonicated *Corynebacterium pseudotuberculosis* antigen (KWCSAg-Cp) and 0.5mg/ml killed whole cell sonicated *Pseudomonas aeruginosa* antigen (KWCSAg-Pa) and the third group inoculated 1mg/ml killed whole cell sonicated *Corynebacterium pseudotuberculosis* antigen (KWCSAg-Cp) subcutaneously. The results showed that the first group gave a high cellular reaction (Erythema and induration) followed by the second and finally the third group. In conclusion, there was a good cooperation between these two antigens to enhance a good cellular immune response.

Key words: *Corynebacterium*, *Pseudomonas aeruginosa*, skin test, DTH, sonicated antigen.

INTRODUCTION

Infected animals play an important role in spreading the infection through contaminated soil, water, feed and pastures by their faces, pus from rupture external abscess and respiratory secretion [1]. *Corynebacterium pseudotuberculosis* belongs to *Actinobacteria* [2], anaerobic, Gram positive, small curved facultative bacillus, causing caseous lymphadenitis (CLD), which is an important chronic disease of adult and small ruminants [3], such as cattle, goats, camels, deer and also horses, pigs, and laboratory animals [4], which causes ulcerative lymphangitis in horses [5] and infected humans particularly veterinarians and farm practitioners [6].





Ikram Abbas About Al-Samarrae

Pseudomonas aeruginosa is a Gram- negative bacillus bacterium that considered as an opportunistic pathogen which is widely spread in the environment[7] and that associated with infection in cystic fibrosis patient, burn patient and others such as undergoing chemotherapy or AIDS patients.[8] This bacteria containing several virulence factors such as LPS, exotoxins A, ribosome, flagella, pili, high molecular weight polysaccharide, alginate, outer membrane protein, DNA, protein of type III secretion system[9]. The immune response against these bacteria is complex, including both arms of immunity -cellular and humoral immune responses [10]. Due to the importance of the synergistic effects of bacterial antigens (Gram positive and Gram negative) to enhance the immune response, this study was carried by using sonicated antigens of *Corynebacterium pseudotuberculosis* and *Pseudomonas aeruginosa* and Delayed Type Hypersensitivity-Skin test in rabbits.

MATERIALS AND METHODS

Bacterial isolates

A-*Corynebacterium pseudotuberculosis* isolate was obtained from Pathology department / College of Veterinary Medicine, University of Baghdad.

B-*Pseudomonas aeruginosa* isolate was provided from Department of Microbiology, College of Veterinary Medicine, University of Baghdad.

C-Killed whole cell sonicated *Corynebacterium pseudotuberculosis* antigen (KWCSAg-Cp) was prepared with some modification according to [11], that was used to immunization of rabbits and DTH-Skin test.

D-Killed whole cell sonicated *Pseudomonas aeruginosa* antigen (KWCSAg-Pa) was prepared with some modification according to [11], that was used as cooperateto KWCSAg-Cp antigen.

E-The protein of antigens was measured by Biuret method [12].

Rabbits Immunization

Twelve [12], local breed rabbits of both sexes, (about 1.5--2Kg B.W.) were used, they were divided randomly into three groups as follow:-

A-First group (4 animals) was immunized by 1mg/ml of *Corynebacterium pseudotuberculosis* antigen (KWCSAg-Cp) and 1mg/ml of *Pseudomonas aeruginosa* antigen (KWCSAg- Pa) subcutaneously.

B-Second group (4 animals) was immunized by 1mg/ml of *Corynebacterium pseudotuberculosis* antigen (KWCSAg-Cp) and of 0.5mg/ml of *Pseudomonas aeruginosa* antigen (KWCSAg-Pa) subcutaneously.

C-Third group (4 animals) as positive control group was immunized by 1mg /ml *Corynebacterium pseudotuberculosis* antigen (KWCSAg-Cp) subcutaneously.

E-A booster dose was given at day 14 after immunization for 1st, 2nd, and 3rd groups by 1mg/ml of KWCSAg-Cp.

Delayed Type Hypersensitivity-Skin test (DTH-Skin test)

Delayed Type Hypersensitivity was done for all immunized rabbits in at day 25 after immunization [13], with some modification, by using different protein concentrations of sonicated KWCSAg-Cp, as crude antigen in doses 0.5mg/ml, 1:2 dilution (0.25mg/ml), 1:4 dilution (0.12mg/ml) and PBS (pH 7.2) as a control region by intradermal injection of immunized animals.





RESULTS

Erythema

The results showed that the erythema of the skin in all immunized groups had high significant difference ($P < 0.05$, $P < 0.01$) in diameters compared with PBS. The first group that immunized by *Corynebacterium pseudotuberculosis* 1 mg/ml with *Pseudomonus aeruginosa* 1 mg/ml gave a high diameters after 24, 48 and 72 hrs, followed by the second group that immunized by *Corynebacterium pseudotuberculosis* 1 mg/ml with *Pseudomonus aeruginosa* 0.5 mg/ml and finally the third group that immunized by *Corynebacterium pseudotuberculosis* 1 mg/ml, while within groups high diameters of immunized groups showed after 24 hrs. with significant difference ($P < 0.05$, $P < 0.01$) and decrease after 48 and 72 hrs compared with PBS. (Tables 1, 2, 3)

Induration

The results showed that the induration of the skin in all immunized groups had high significant difference ($P < 0.05$, $P < 0.01$) in diameters compared with PBS, and the first group that immunized by *Corynebacterium pseudotuberculosis* 1 mg/ml with *Pseudomonus aeruginosa* 1 mg/ml gave a high diameters after 24, 48 and 72 hrs, followed by the second group that immunized by *Corynebacterium pseudotuberculosis* 1 mg/ml with *Pseudomonus aeruginosa* 0.5 mg/ml and finally the third group that immunized by *Corynebacterium pseudotuberculosis* 1 mg/ml, while within groups high diameters of immunized groups showed after 72 hrs. with significant difference ($P < 0.05$, $P < 0.01$) and decrease after 48 and 24 hrs compared with PBS. (Tables 4, 5, 6)

DISCUSSION

Immune responses against *Corynebacterium pseudotuberculosis* are complex and including both arms of immunity, cellular and humoral immune responses (10), and the cellular immune response play an important role in the eradication [14], [15], and [16], with both non specific and specific immune responses that play an essential role in the host protection against this bacteria [17], Delayed type hypersensitivity- skin test is a simple test, which helps in the diagnosis of certain infectious diseases. This test detects cutaneous (skin) hypersensitivity to antigens, which done to find whether the individual was already exposed (sensitized) to a particular antigens [18], The cellular types and their percentage were associated with persistence or elimination of the microorganisms by the host [19], *C. pseudotuberculosis* can be aggregates polymorphonuclear cells and macrophages in the site of infection [20], due to faculties intracellular organism, cell mediated particularly Th1 producing cytokines INF- γ [21], [14], and [22], and IL2, IL12, INF- γ recorded at seventh day post infection [19], and the appearance of swelling called induration in 48 to 72 hrs., that suggests that the individual was already exposed to antigen, which were injected into the skin, that reaction initiated by the activation of CD4 T cells that activated by antigen presenting cells in the skin releasing inflammation mediators that recruit the macrophage (monocytes), CD8 cytolytic T cell and NK cells also elicit the inflammatory response to eliminate the antigen (18), that reaction explain the increase the diameter of induration synchronizing with the increase the concentration of both antigens were used, also agree with [23], who mentioned that the highest indurations were recorded after 48 hrs. then they were declined at 72 hrs.; Generally CD4⁺Th1 sub set of lymphocytes (TDTH lymphocytes) induce the DTH responses, also CD8⁺T cells induce DH responses, cytokine, TNF- α and IL1 induce expression of adhesion molecules on endothelial cells of the bloodvessels, which in turn lead to the filtration in the site by monocytes and lymphocytes from the blood stream and these cells secrete a number of cytokines and the peak of that infiltration reached at 48 to 72 hrs. On the same hand, [24], [25], [26], [27], [24] and [9] reported that the whole sonicated bacterial antigens elicit cell mediated response and the last one suggested that the whole sonicated antigens were attached by residual macrophages and dendritic cells and this interaction lead to activate them to produce





Ikram Abbas Aboud Al-Samarrae

cluster of cytokines such as IL1 ,IL2 and TNF- α ,as well as processing and presenting these antigens with expressed a small peptides to naïve CD4⁺ T cells ,which proliferation and differentiation into Th cells and may be might important role in the non specific resistance. *Pseudomonas aeruginosa* has extra and intracellular stages in their course of infection, which elicit both immunological responses (Humoral and cellular) against bacterial infection [29] It has multivalent virulence factors (somatic and secretor antigens) such as pili, exotoxins A ,ribosome and high molecular weight polysaccharides, alginate ,flagella , outer membrane proteins ,...etc , they are suitable candidate for vaccine production and there was no significant difference in induced immunization between route of injections subcutaneous ,intraperitoneal and intramuscular [7] Major outer membrane proteins interact with and mitogenically stimulate B lymphocytes [8] and [30] referred by Immunoelectrophoresis 36 different antigens were demonstrated in sonicated *P. aeruginosa* , antibodies against the outer membrane antigens were detected and antigenic reactivity of outer membrane antigens. Also the bacterial antigens being presented to the humoral immune system will be those preserved on the bacterial cell surface [31] with high levels of antibody response to most of the antigens of this bacteria [32] ,they were detected 7 days post infection [33]. In conclusion, we concluded that the use of both sonicated bacterial (Gram positive and Gram negative)antigens induce, enhance and cooperation of the cellular immune response rather than a single antigen and these response synchronize with the concentration of antigens.

CONCLUSION

In conclusion, there was a good cooperation between these two antigens to enhance a good cellular immune response.

REFERENCES

1. Zaid, M.K.; Jin, Z.M.; Jesse, F.F.; Saharee, A.A.; Sabri, J.; Xusoff, R. and Haron, A.W. (2016). Relationship between the *Corynebacterium pseudotuberculosis* phospholipase D inoculation and the fertility characteristics of crossbred Boer Bucks livestock. Sci., (191) :12-21.
2. AdzaRina, M.N.; Zamri-Saad, M.; Jesse, F.F.; Saharee, A.A.; Haron, A.W. and Shahirudin, S. (2013). Clinical inoculated *Corynebacterium pseudotuberculosis* by intradermal, intranasal and oral route Open J. Vet. Med., (17) :73-81.
3. Moussa, I.M.; Ali, M.S.; Hessain, A.M. and Kabli, S.A. (2016). Vaccination against *Corynebacterium pseudotuberculosis* infections controlling caseous lymphadenitis (CLA) and edematous skin disease. Saudi J. Biol. Sci., 23(6):718-723.
4. Moore, R.; Miyoshi, A.; Pacheco, L.G.C.; Seyffert, N. and Azevedo, V. (2010). *Corynebacterium* and *Arcanobacterium* in pathogenesis of bacterial infections in animals (4thed.) Blackwell Publishing, Iowa.
5. Rafeal, A.; Barauna, C.; Rommel, T.; Ramos, T.; Ramos, J.; Adonney, A.; Veras, D.; Pablo, H.; desa, C.G.; Luis, R.; Carneiro, R.; J udy, M.; Edman, M.; Sharon, J.; Spier, V.A. and Silva, A. (2017). Genomic analysis of four stains of *Corynebacterium pseudotuberculosis* bv *equi* .Isolated from horse showing distinct signs of infection standard in Genomic. Sci., (12):16.
6. Ruiz, J.C.; D Afonseca, V.; Silva, A.; Ali, A. and Pinto, A.C. (2011). Evidence for reductive genome evolution and lateral acquisition of virulence functions in two *Corynebacterium pseudotuberculosis* strains. PLoS ONE 6: (4).e18551.
7. Benam, S.R.; Tanomand, A. and Jafari, B. (2018). Immunogenic properties of sonicated multivalent antigen of *Pseudomonas aeruginosa* Crescent J. Med. Biol. Sci., 5(1)40-44.
8. Chen, T.Y.; Lin, C.P.; Loa, C.C. *et al.* (1999). Anontoxic *Pseudomonas* exotoxins A induces active immunity and passive protective antibody against *Pseudomonas* exotoxins A intoxication. J. Biomed Sci., 6(5):357-363.
9. Alwan, M.J.; Al-Khafaji, M.A.; Al-Najjar, S.S. and Al-Kutbi, S.H. (2010). Study of the immunological induced by *Pseudomonas aeruginosa* in mice treated with alcoholic *Apium*- greveolense extract and immunized with whole sonicated *Salmonella typhimurium*. Al-anbar J. Vet. Sci., 3 (1):43-55.
10. Prescott, J.F.; Menzies, P.I. and Hwang, Y.T. (2002). Aninterferon-gamma assay for diagnosis of *Corynebacterium pseudotuberculosis* infection in adult sheep from a research flock. Vet. Microbiol., (88):287-297.





Ikram Abbas About Al-Samarrae

11. Motiva ,I.;Denchen,V.andLinda,K.(1992).Humoral and mediated immunity in mice after immunization with live oral vaccine of *Salmonella typhimurium*: auxotrophic mutant with two attenuating markers. *Vacc. Microbiol.*, (10):61-66.
12. Henry,R.;Cannon,D.and Winkelman,J.(1974) .*ClinicalChemistry, Principles and Techniques*, Harper and Row,2th ed LivingStone Pup.
13. Hudson,L. and Hay,F.C. (1980).*PracticalImmunology*. 3rd ed. Blackwell Science Publications,Oxford. Landon:359.
14. El-Enbaawy,M.I.; Saad,M.M.andSelim,S.A.(2005).Humoral and cellular immune responses of a murine model against*Corynebacterium pseudotuberculosis* antigens.Egyp. *J.Immun.*, (12):13-20.
15. DeSouza,A.P.;Vale,V.L.C.;Silva,M.C.;Araujo,I.B.O.;Trindade,S.C.and Moura-Costa,L.F.(2014).MAPK involvement in cytokinein response to *Corynebacterium pseudotuberculosis*infection,*BACMicrobiol.*, (14):230.
16. Vale,V.L.C.;Silva,M.D.C.;DeSouza,A.P.; Trindade,S.C.;Moura-Coasta, L.F.;Santos-Lima,E.K.N.and Nascimento,R.J.M..(2016).Humoral and cellular immune response in mice against secreted and somatic antigens from a *Corynebacterium pseudotuberculosis* attenuated strain:immune response against*Corynebacterium pseudotuberculosis* strain.*BMC Vet. Res.*, 12:195.
17. Batey,R.G.(1986).Factors affecting the yield of viable cell of *Corynebacterium pseudotuberculosis* in aliquid medium. *Vet. Microbiol.* , (11):145-152.
18. Jayapal,V.(2007).TypeIV hypersensitivity; *Fundamental Medical Immunology*, 1st ed.;JaypeeBrothers,Med.Pub.LTD, NewDelhi:181-183.
19. Pepin,M.;Paton,M.andHodgson,A.L.(1994).Pathogenesis and epidemiology of *Corynebacterium pseudotuberculosis* infection in sheep.*Current Top. Vet. Res.*, (1):63-82.
20. Paton,M.W.(2010).The epidemiology and control of caseous lymphadenitis in Australian sheep flocks. PhD.Thesis Murdach University.
21. Paule,B.J.A.;Azevedo,V. and Regis, L.F.(2003).Experimental*Corynebacterium pseudotuberculosis* primary infection in goats: Kinetics of IgG and interferon- γ production, IgGavidity and antigen recognition by western blotting.*Vet. Immunol. Immunopathol.*, (96):129-139.
22. Reboucas, M.F.;Portela,R.W.;Lima,D.D.;Loureiro,D.andBastos,B.I.(2011).*Corynebacterium pseudotuberculosis* secreted antigen induced specific gamma- interferon production by peripheral blood leukocytes,potential diagnostic marker for caseouslymphadenitis in sheep and goats.*J.Vet. Diag. Invest.*, (23):213-220.
23. 23-Tizard,I.R.(2009).*Veterinary immunology an introduction*.8thed.Saunders Elsevier:55-380.24
24. Lyczak,C.L.;Canon,J.B.and Pier,G.B.(2000).Establishment of *Pseudomonas aeruginosa* infection.Lesions from aversatile opportunist. *Microbiol. Infect.*,2:101-107.
25. Murphy,E. A.; Bladwin, C.H.;Zoa,B.and Palant,M.T.(2001).Generation of cytotoxic T lymphocyte response using *Salmonella* antigen delivery system.*Mol.Microbiol.*,4:21111-21114.
26. McSorly,S.J.;Brad,T.C.andMaarc,K.(2002).Characterization of CD⁴Tcell response during natural infection with *Salmonella typhimurium*. *Immunol. J.*, 164:986-993.
27. Kolls,J.K.and Linden,A.(2004).Interleukin17 family members and inflammation.*Immunity*,21:467-476.
28. AL-Khafaji,M.A.(2008).The study of synergistic effect of whole *Salmonella* sonicated antigen and alcoholic celery extract on the immunopathological changes in mice infected with *Salmonella typhimurium*.MSc Thesis, Collegeof Veterinary Medicine University of Baghdad.
29. Gregory,P.P.;Bring,M.M.; Hatano,K.;Coleman, F.T.;Pier,G.B.and Goldberg,T.B.(2002).Constructional characterization of a live attenuated ADeleonmutant of *Pseudomonas aeruginosa* asacaudicate intranasal vaccine. *Infect. Immun.*,70:1507-1517.
30. Lam,J.S.;Mutharia,L.M.;Hancock,R.E.W.;Hoiby,N.;Lam,K.;Baek,L.and Costerton,J.W.(1983).Immunogenicity of *Pseudomonas aeruginosa* outer membrane antigens examined by crossed Immunoelectrophoresis.*Infect. Immun.*,42(1):88-98.
31. Garvey,J.S.;Cramer,N.E. and Sussdorf,D.H.(1977).In *Methods in Immunology*.3rd ed.W.A. Benjamin Inc.Reading Mass: 149-152.





Ikram Abbas Aboud Al-Samarrae

32. Hoiby,N.(1977).*Pseudomonas aeruginosa* infection in cystic fibrosis. Diagnostic and prognostic significance of *Pseudomonas aeruginosa* precipitins determined by means of crossed Immunoelectrophoresis.A survey. ActaPathol.Microbiol. Scand, suppl., 262:93-96.
33. Fernandes,P. B.;Kim,C.;Cudy,K.R. and Huang,N.N.(1981).Antibodies to cell envelope proteins of *Pseudomonas aeruginosa* in cystic fibrosis patients. Infect. Immun., 33:527-532.

Table 1. Erythema of delayed type hypersensitivity-skin test with crude antigen of *Corynebacterium pseudotuberculosis* in rabbits.

Antigens	Mean ± SE(mm)/ Time (hours)		
	24	48	72
Cp 1mg/ml & Ca 1 mg/ml	8.5 ± 0.5 a** A**	7.4 ± 0.4 a* A**	5.0 ± 0.4 b A**
Cp 1mg/ml & Pa 0.5 mg/ml	7.0 ± 0.47 a* A**	5.5 ± 0.64 ac A**	5.0 ± 0.4 bc A**
Cp 1mg/ml	6.7 ± 0.47 a A**	6.0 ± 0.4 a A**	5.5 ± 0.28 a A**
PBS	1.7 ± 0.47 a B	1.7 ± 0.47 a B	1.2 ± 0.25 a B

Cp:*Corynebacterium pseudotuberculosis* Pa: *Pseudomonas aeruginosa**P< 0.05 **P<0.01

Capital letters mean a significant difference between groups

Small letters mean a significant difference within groups

Table 2. Erythema of delayed type hypersensitivity-skin test with 1:2 antigen of *Corynebacterium pseudotuberculosis* in rabbits

Antigens	Mean ± SE(mm) / Time (hours)		
	24	48	72
Cp 1mg/ml & Ca 1 mg/ml	7.0 ± 0.4 a** A**	7.5 ± 0.47 a** A**	4.2 ± 0.47 b A**
Cp 1mg/ml & Pa 0.5 mg/ml	5.5 ± 0.64 a A**	4.2 ± 0.47 a A*	4.0 ± 0.4 a A**
Cp 1mg/ml	5.5 ± 0.64 a A**	4.7 ± 0.47 a A**	4.2 ± 0.47 a A**
PBS	1.7 ± 0.47 a B	1.7 ± 0.47 a B	1.2 ± 0.25 a B

Cp:*Corynebacterium pseudotuberculosis* Pa: *Pseudomonas aeruginosa**P< 0.05 **P<0.01

Capital letters mean a significant difference between groups

Small letters mean a significant difference within groups





Ikram Abbas About Al-Samarrae

Table 3. Erythema of delayed type hypersensitivity - skin test with 1:4 antigen of *Corynebacterium pseudotuberculosis* in rabbits

Antigens	Mean ± SE(mm)(Time hours)		
	24	48	72
Cp 1mg/ml & Ca 1 mg/ml	5.0 ± 0.4 a* A**	4.5 ± 0.28 ac A**	3.5 ± 0.28 bc A**
Cp 1mg/ml & Pa 0.5 mg/ml	4.7 ± 0.47 A* A**	3.5 ± 0.28 ac A*	3.2 ± 0.4 bc A**
Cp 1mg/ml	5.0 ± 0.4 a* A**	3.7 ± 0.47 ac A*	3.2 ± 0.25 bc A**
PBS	1.7 ± 0.47 a B	1.7 ± 0.47 a B	1.2 ± 0.25 a B

Cp: *Corynebacterium pseudotuberculosis* Pa: *Pseudomonus aeruginosa* *P< 0.05 **P<0.01

Capital letters mean a significant difference between groups

Small letters mean a significant difference within groups

Table (4): Induration of delayed type hypersensitivity-skin test with crude antigen of *Corynebacterium pseudotuberculosis* in rabbits.

Antigens	Mean ± SE(mm)(Time hours)		
	24	48	72
Cp 1mg/ml & Ca 1 mg/ml	5.2 ± 0.47 a** A**	6.2 ± 0.47 ac A	7.5 ± 0.25 bc A**
Cp 1mg/ml & Pa 0.5 mg/ml	4.5 ± 0.28 a A	7.5 ± 0.25 b* A*	4.5 ± 0.28 a B
Cp 1mg/ml	5.0 ± 0.4 a* A	7.5 ± 0.47 b A	4.1 ± 0.25 a** B
PBS	1.2 ± 0.25 a B**	0.7 ± 0.25 a B**	0.7 ± 0.25 a C

Cp: *Corynebacterium pseudotuberculosis* Pa: *Pseudomonus aeruginosa* *P< 0.05 **P<0.01

Capital letters mean a significant difference between groups

Small letters mean a significant difference within groups

Table (5): Induration of delayed type hypersensitivity - skin test with 1:2 antigen of *Corynebacterium pseudotuberculosis* in rabbits.

Antigens	Mean ± SE(mm)(Time hours)		
	24	48	72
Cp 1mg/ml & Ca 1 mg/ml	4.2 ± 0.47 a** A	5.2 ± 0.25 a* A	6.5 ± 0.28 b A**
Cp 1mg/ml & Pa 0.5 mg/ml	4.0 ± 0.4 a A	5.0 ± 0.4 a A	3.7 ± 0.47 a B
Cp 1mg/ml	4.0 ± 0.4 a A	5.0 ± 0.4 ac* A	3.5 ± 0.25 ab B
PBS	1.2 ± 0.25 a B**	0.7 ± 0.25 a B**	0.7 ± 0.25 a C

Cp: *Corynebacterium pseudotuberculosis* Pa: *Pseudomonus aeruginosa* *P< 0.05 **P<0.01

Capital letters main a significant difference between groups

Small letters main a significant difference within groups





Ikram Abbas Aboud Al-Samarrae

Table (6): Induration of delayed type hypersensitivity - skin test with 1:4 antigen of *Corynebacterium pseudotuberculosis* in rabbits.

Antigens	Mean \pm SE(mm)(Time hours)		
	24	48	72
Cp 1mg/ml & Ca 1 mg/ml	3.5 \pm 0.28 a A	4.5 \pm 0.28 a A	3.7 \pm 0.47 a A
Cp 1mg/ml & Pa 0.5 mg/ml	3.2 \pm 0.4 a A	4.0 \pm 0.4 a A	3.2 \pm 0.25 a A
Cp 1mg/ml	3.2 \pm 0.25 a A	3.7 \pm 0.47 a A	3.0 \pm 0.00 aA
PBS	1.2 \pm 0.25 a B**	0.7 \pm 0.25 a B**	0.7 \pm 0.25 aB**

Cp: *Corynebacterium pseudotuberculosis* Pa: *Pseudomonas aeruginosa* *P < 0.05

**P < 0.01

Capital letters mean a significant difference between groups

Small letters mean a significant difference within groups





Evaluation of Groundwater Quality in AL-Hilla District by Comparing of Two Deterministic Interpolation Methods in GIS

Kadhim Naief Kadhim* and Noor Sabah Abbas

Faculty of Engineering, University of Babylon, Babil, Iraq.

Received: 17 Oct 2018

Revised: 19 Nov 2018

Accepted: 21 Dec 2018

*Address for Correspondence

Kadhim Naief Kadhim

Faculty of Engineering,

University of Babylon,

Babil, Iraq.

Email:altaeekadhim@gmail.com



This is an Open Access Journal / article distributed under the terms of the **Creative Commons Attribution License** (CC BY-NC-ND 3.0) which permits unrestricted use, distribution, and reproduction in any medium, provided the original work is properly cited. All rights reserved.

ABSTRACT

Surface interpolation techniques are unit unremarkably used for making continuous information from a distributed set of data points over a geographical region. in this paper, the comparison between 2 spatial interpolation techniques ordinary kriging (ok) and Inverse Distance weight (IDW)) is done. The goal is to see that technique creates the simplest real illustration of measured well water quality in AL-Hilla district counting on root mean square (RMS). Ground water prediction map was obtained for every technique by using average well water measured at thirty two wells within the study area. These maps show spatial variety inside the groundwater and that they are unit quite completely different. Ordinary kriging technique results a drum sander map and lesser error than IDW technique for all parameters except (CL) which IDW was the best.

Keywords: Groundwater, Spatial Distribution, GIS, Geostatistics, Semivariogram.

INTRODUCTION

Water is an imperative information not just for the human presence, anyway additionally for all improvements. Interest for water has swelled incredibly as of late as a result of the make, urbanization, populace increment, and extraordinary. a few urban areas and urban communities in Al-Iraq get water through region organize and from individual bore wells. Henceforth, data of hydrochemistry is crucial to survey the base water quality in any space in the midst of which the base water is used for drinking needs. The water quality examination could give clear data with respect to the sub surface land conditions in the midst of which the water presents[1].Groundwater quality depends upon the parameters of vivified water, barometrical precipitation, and land surface water on submerged geochemical frames.Time delicate fluctuations inside the supply and constitution of the resuscitated water, hydrologic and social components could result discontinuous changes in water quality parameters.The employments





Kadhim Naief Kadhim and Noor Sabah Abbas

of present physico-manufactured substances parameters like pH , Cl, HCO₃,TDS don't change prosperity at bound stages however may have an effect on the quality of drinking groundwater. Groundwater has considered the biggest natural resources within the kind of groundwater and surface water. Groundwater makes up in regards to 2%of the world's H₂O asset that is in regards to 0.61% of the aggregate world's water, with seas and perpetual snow. Crumbling of groundwater quality because of phylogeny exercises.[2]The assessment of groundwater quality is thought of as a vital index for socio-economic growth and development[3].The most objective of this analysis was to produce an summary of gift groundwater quality for parameters like pH,TDS,EC,CL and sulfates (SO₄) and electrical physical phenomenon (EC) within the Mehran plain victimization GIS and geostatistical techniques.

Study Area

The study zone is found might be a city in focal of Al-Iraq on the Hilla part of the Euphrates River,100 kilometer south of Baghdad. The populace is quantifiable at970,000 in 2015. it's the capital of city and is discovered neighboring the old town of city and close to the conventional urban communities of Borsipa and Sumer. it's situated in a dominantly agrarian area that is broadly inundated with water given by the Hilla waterway, producing a substantial differ of harvests, products of the soil. The waterway runs definitely inside the center of the city, and it's surrounded by Phoenix dactylifera trees and diverse styles of vegetation upgrading the climate and diminishing the destructive effect of mud and in this way the desert winds. it's a region of 5432 Km². It comprises around two of Iraq's aggregate zone. Its topographical territory stretches out between longitudes (424000m-464000m) and scopes (3570000m-360000m) by the UTM framework [4]. It is bordered by Baghdad Governorate from North, AL-Anbar and Karbala Governorates from the west and southwest,Najaf Governorate from South, Diwaniyah Governorate from the southeast and Waist Governorate from East ,figure(1)

MATERIALS AND METHODS

A sum of thirty two groundwater tests territory unit gathered from wells. within the completely acid-washed synthetic resin bottle of 1liter. all through inspecting investigation and transportation of water tests to the research facility, every single vital insurance [5].The groundwater tests were broke down for parameters that incorporate hydrogen particle focus, EC, TDS, cl and sulfates utilizing standard conventions and in this way the nature of the information was guaranteed through watchful institutionalization. examined groundwater tests for the investigation zone.. it's hold on in standout format and coupled with the abstraction information by be part of possibility in Arc Map. The abstraction and therefore the non-spatial info shaped integrated for the generation of reflection dispersion maps of the water quality parameters. For spatial introduction Inverse Distance Weighted (IDW) approach in GIS has been utilized in the present study to outline the locational conveyance of groundwater poisons. Also, Other spatial introduction strategies incorporate Kriging. In this examination we utilize a GIS programming ArcGIS 10.2.The contrasts among anticipated and watched values are outlined utilizing root mean square blunder (RMSE) which is figured from the accompanying condition[6].

$$RMSE = \sqrt{\frac{1}{N} \sum_{i=1}^N (Z(X_i) - \hat{Z}(X_i))^2} \dots \dots \dots (1)$$

where Z(X_i) is the anticipated esteem, Z(x_i) is the watched esteem, and N is the aggregate number of information.

RESULTS AND DISCUSSION

The water quality parameters are assessed by comparing the test results with both Iraqi Drinking Water Standard [7]and World Health Organizationguidelines for drinking water quality [8].The examined centralizations of various





Kadhim Naief Kadhim and Noor Sabah Abbas

water quality parameters are introduced in the table 1. The pH values of 32 samples were found to be within standard values, The hydraulic conductivity (EC) values of 32 samples were found to be without standard values, TDS also unsuitable to drink in the most of wells according to [7] and WHO, CL values of 32 samples were suitable to drink by (47%) according to WHO and 56% according to Iraqi standard and SO₄ unsuitable to drink. The spatial distribution of different groundwater quality parameters were carried out through GIS geo-statistical technique using ordinary Kriging and IDW AND comparing with them and chose the best. More quantitative comparison of these two techniques is obtained by comparing RMSE statistics as shown in Table 2. The best model is chosen dependent on the smallest root mean square expectation blunder (RMSE). The spatial distribution Map of pH, EC, TDS, CL and sulfates are shown in Fig2 to Fig 6.

Drinking- groundwater quality map

Figure(7) shows the ultimate drinkable quality map was made by integration five thematic grid maps of PH, EC, CL and sulfates by overlay technique. The spatial coordination for groundwater quality mapping was distributed using ArcGIS spatial Analyst extension. It will within the final drinkable quality map that space on the north-western, the south-western and tiny a part of east of the study area has water unsuitable to drink and the other parts of the study area which were represented by blue color, suitable to drink.

CONCLUSION

After the overlay of basic parameters for appropriate and unacceptable zones in AL-Hilla district, the last Groundwater Quality Map (Figure 7) showed the north-western, the south-western and small part of east of the study area has water unsuitable to drink and the other parts of the study area which were represented by blue color, suitable to drink. As can be seen from the map numerous districts have groundwater that is consumable simply after treatment. In this inadmissible zone the five parameters that are examined are above most extreme allowable limits of confinement for larger part of the example wells. The Cl focus for a large portion of the examples is above 250 mg/L and the minimum value and the maximum values observed are 134 and 352 mg/L respectively. The maximum permissible level for chloride is 250mg/L according to WHO standards. The maximum and minimum value of EC observed are 2644.9 and 1657.8 mg/L respectively. The maximum permissible level for this parameter is 1500 mg/L in WHO standards. There are alarming levels of TDS in this unsuitable zone of AL-Hilla district with almost all the wells showing well above 1000 mg/L, most values of SO₄ was exceed allowable value (250) according to WHO, where the minimum and maximum value of sulfates 718 and 1051 mg/L respectively. There are good levels of PH in this suitable zone of AL-Hilla district with all the wells. Present status of groundwater necessitates for the continuous monitoring and necessary groundwater quality improvement methodologies implementation.

As will be seen from the map several districts have groundwater that is suitable solely once correct treatment. During this unsuitable zone the 5 parameters that are studied are on top of most permissible limits confinement for larger part of the example wells. The Cl concentration for many of the samples is on top of 250 mg/L and therefore the minimum value and therefore the most values determined 134 and 352 mg/L severally. the most permissible value for chloride is 250mg/L according to World Health Organization standards. the most and minimum value of international organization determined are 2644.9 and 1657.8 mg/L respectively. the most permissible value for this parameter is 1500 mg/L according World Health Organization standards. There are horrifying values of TDS during this unsuitable zone of AL-Hilla district with the majority the wells showing well on top of one 1000 mg/L, most values of SO₄ was exceed allowable value (250) according to World Health Organization, wherever the minimum and most values of sulfates 718 and 1051 mg/L severally. There are smart values of pH during this appropriate zone of AL-Hilla district with all the wells. Present status of groundwater necessitates for the continual observance and necessary groundwater quality improvement methodologies implementation.





Kadhim Naief Kadhim and Noor Sabah Abbas

Recommendations

- Quantifying the household sewerage that goes into the distinctive water bodies settled inside the city, can encourage in structuring for viable sewerage treatment plant and limiting groundwater contamination by sewerage.
- Identification of groundwater stimulating areas and structures. For this reason, Geographical system (GIS) with the predetermined unique and non-spatial data will be utilized great on the grounds that the instrument. thinking of energizing structures is to be finished. Continuous monitoring of groundwater quality along quality study will minimize the chances of further deterioration. Continuous perception of groundwater table dimension close by quality investigation can limit the probabilities of any disintegration.

REFERENCES

1. Srinivas, Y., Oliver, D. H., Raj, A. S., & Chandrasekar, N. (2013). Evaluation of groundwater quality in and around Nagercoil town, Tamilnadu, India: an integrated geochemical and GIS approach. *Applied Water Science*, 3(3), PP. 631-651, [Online] Available: <https://link.springer.com/article/10.1007/s13201-013-0109-y>
2. Pande, C. B., & Moharir, K. (2018). Spatial analysis of groundwater quality mapping in hard rock area in the Akola and Buldhana districts of Maharashtra, India. *Applied Water Science*, 8(4), PP.1-17, [Online] Available: <https://link.springer.com/article/10.1007/s13201-018-0754-2>
3. Khosravi, H., Karimi, K., & Mesbahzadeh, T. (2016). Investigation of spatial structure of groundwater quality using geostatistical approach in Mehran Plain, Iran. *Pollution*, 2(1), PP.57-65, [Online] Available: https://jpoll.ut.ac.ir/article_55878.html
4. Al-Abody, A.A. (2016). Geotechnical Maps for the Soil of Babylon Governorate Using Geographic Information System(GIS)", M.Sc. thesis, University of Babylon, Babil , Iraq.
5. Brown, E., Skougstad, M. W., & Fishman, M. J. (1970). Methods for collection and analysis of water samples for dissolved minerals and gases., [Online] Available: <https://www.osti.gov/biblio/5138356>
6. Al-Taee, M. H., Al-Adilli, A., & Sivakugan, N. (2017). Comparison of Two Deterministic Interpolation Methods for Predicting Ground Water Level in Baghdad. *Journal of University of Babylon*, 25(5), 1787-1796, [Online] Available: <https://www.iasj.net/iasj?func=article&ald=132305>
7. Iraqi Standards for Drinking Water , No. 417, 2001
8. World Health Organization (WHO). (2006). Guidelines for Drinking water Quality ,Vol.4 ed Vol.1,Recommendation.





Kadhim Naief Kadhim and Noor Sabah Abbas

Table 1. Concentrations of Groundwater quality Parameters

ID	City	Year	PH	EC	TDS	CL	SO4
W1	Hilla	2017.00	7.90	2007.81	1285.00	241.00	897.00
W2	Hilla	2017.00	7.80	1732.81	1109.00	315.00	897.00
W3	Hilla	2017.00	7.90	1840.63	1178.00	341.00	904.00
W4	Hilla	2017.00	7.80	1876.56	1201.00	337.00	889.00
W5	Hilla	2017.00	7.90	1754.69	1123.00	226.00	851.00
W6	Hilla	2017.00	7.90	2646.88	1694.00	342.00	927.00
W7	Hilla	2017.00	7.80	2642.19	1691.00	340.00	931.00
W8	Hilla	2016.00	7.90	1657.81	1061.00	213.00	870.00
W9	Hilla	2016.00	7.90	1964.06	1257.00	184.00	763.00
W10	Hilla	2016.00	7.90	1840.63	1178.00	272.00	863.00
W11	Hilla	2016.00	7.80	1951.56	1249.00	192.00	821.00
W12	Hilla	2015.00	7.90	1862.50	1192.00	258.00	1031.00
W13	Hilla	2015.00	7.90	1767.19	1131.00	228.00	1017.00
W14	Hilla	2015.00	7.80	1737.50	1112.00	238.00	972.00
W15	Hilla	2015.00	7.90	1789.06	1145.00	286.00	1023.00
W16	Hilla	2015.00	7.80	1784.38	1142.00	288.00	1022.00
W17	Hilla	2015.00	7.90	1792.19	1147.00	285.00	1026.00
W18	Hilla	2015.00	7.80	1728.13	1106.00	227.00	981.00
W19	Hilla	2015.00	7.90	1748.44	1119.00	232.00	988.00
W20	Hilla	2015.00	7.80	1762.50	1128.00	236.00	994.00
W21	Hilla	2015.00	7.80	1998.44	1279.00	337.00	1026.00
W22	Hilla	2015.00	7.90	2004.69	1283.00	341.00	1030.00
W23	Hilla	2015.00	7.90	1981.25	1268.00	328.00	1034.00
W24	Hilla	2015.00	7.90	1964.06	1257.00	331.00	1035.00
W25	Hilla	2015.00	7.80	2420.31	1549.00	134.00	718.00
W26	Hilla	2015.00	7.90	2579.69	1651.00	164.00	758.00
W27	Hilla	2014.00	7.90	1989.06	1273.00	321.00	1028.00
W28	Hilla	2014.00	7.80	1979.69	1267.00	342.00	1035.00
W29	Hilla	2014.00	7.80	1981.25	1268.00	341.00	1051.00
W30	Hilla	2014.00	7.80	1985.94	1271.00	338.00	1049.00
W31	Hilla	2014.00	7.80	1995.31	1277.00	352.00	1039.00
W32	Hilla	2014.00	7.80	2407.81	1541.00	287.00	982.00

Table 2: RMSE for ground water quality for Kriging and IDW interpolation method.

method	parameter	RMS
IDW	Ph	0.06
IDW	TDS	161.15
IDW	EC	251.79
IDW	CL	52.06
IDW	SO4	94.10
Ordinary kriging	Ph	0.05
Ordinary kriging	TDS	145.41
Ordinary kriging	EC	227.20
Ordinary kriging	SO4	83.66
Ordinary kriging	CL	54.58





Kadhim Naief Kadhim and Noor Sabah Abbas

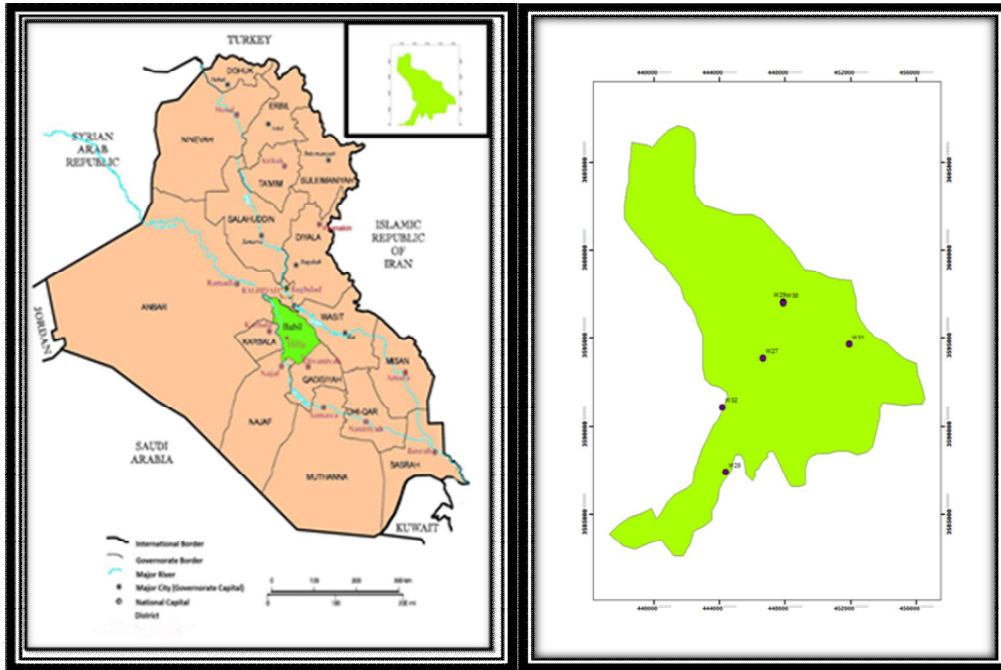


Figure 1. Study Area and Location of Sampling Points

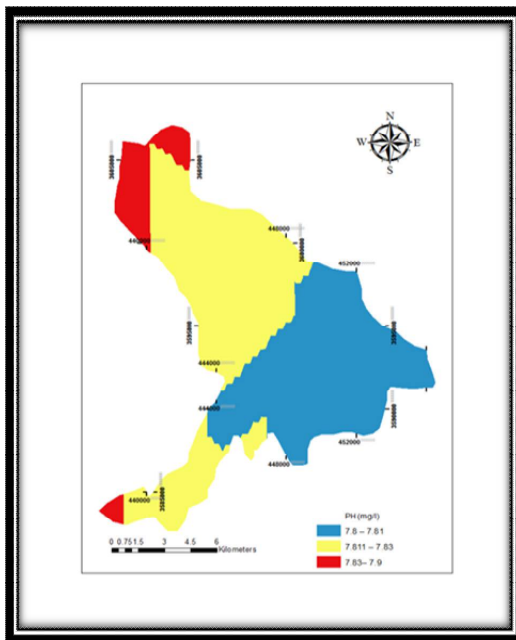


Fig 2. Spatial Distribution Map of Groundwater Quality of pH by using ordinary Kriging

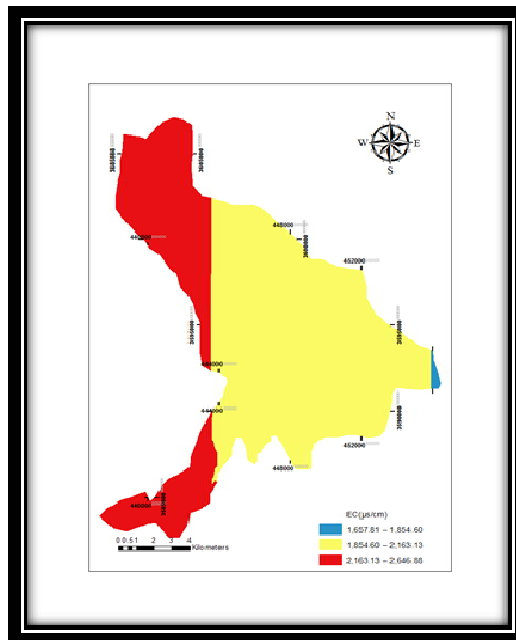


Fig 3. Spatial Distribution Map of Groundwater Quality of EC by using ordinary Kriging)



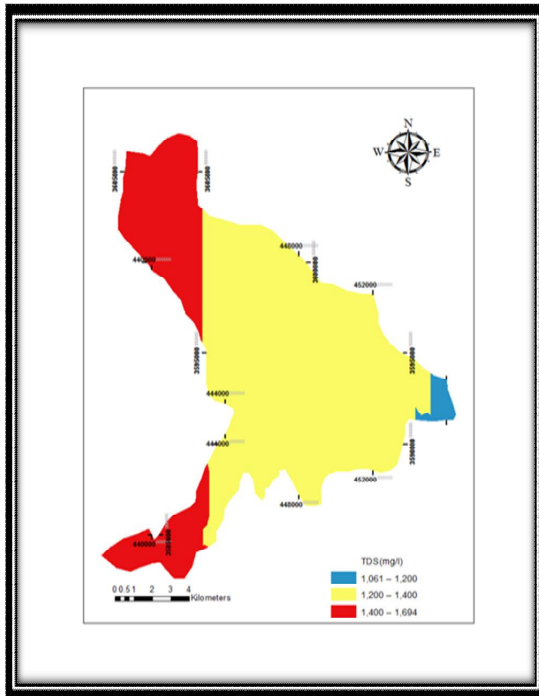


Fig. 4. Spatial Distribution Map of Groundwater Quality of TDS by using ordinary Kriging

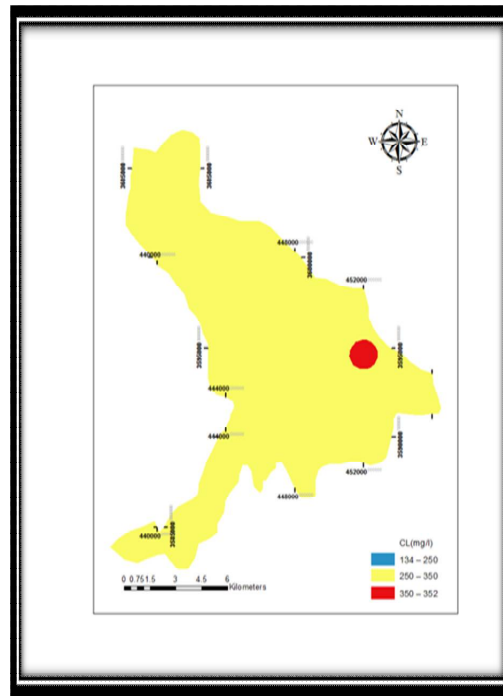


Fig. 5. Spatial Distribution Map of Groundwater Quality of CL by using IDW

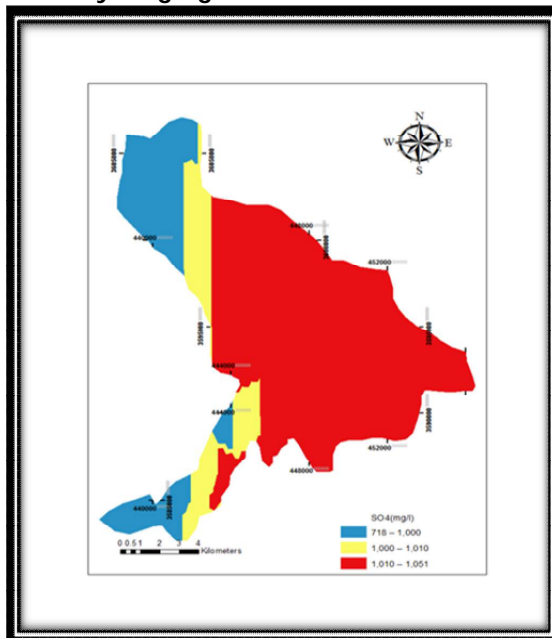


Fig. 6. Spatial Distribution Map of Groundwater Quality of CL by using ordinary Kriging



Fig. 7. Drinking- groundwater quality zone map.





The First Speckled Pigeon *Columba guinea* (Aves, Columbidae) in Iraq

Mudhafar A. Salim¹, Salwan Ali Abed^{2*}, and Wameedh S. Yassir³

¹Arab Regional Center for World Heritage, Manama, Kingdom of Bahrain

²College of Science, University of Al-Qadisiyah, P.O.Box.1895, Diwaniyah, Iraq

³The Iraqi Organization for Conservation of Nature (IOCN), Iraq

Received: 12 Jan 2019

Revised: 20 Jan 2019

Accepted: 22 Jan 2019

* Address for Correspondence

Salwan Ali Abed

College of Science,

University of Al-Qadisiyah,

P.O.Box.1895, Diwaniyah, Iraq

Email:salwan.abed@qu.edu.iq



This is an Open Access Journal / article distributed under the terms of the **Creative Commons Attribution License** (CC BY-NC-ND 3.0) which permits unrestricted use, distribution, and reproduction in any medium, provided the original work is properly cited. All rights reserved.

ABSTRACT

Speckled Pigeon *Columba guinea* is a bird species of the Order: Columbiformes, Family: Columbidae that includes Pigeons and Doves and allies. This species is common bird through its natural range in Africa which inhabits the sub-Sahara, arid lands, and even close to the farms and human settlements. Over the period 2014 – 2019, the Speckled Pigeon *Columba guinea* was observed for three times in Iraq, of which one of them was in-captivity and two were in the field. This report provides the first confirmed record of this species in Iraq, along with the habitats description in Iraq.

Keywords: Iraq, Speckled Pigeon, *Columba guinea*, Middle Euphrates, Samawa, Dalmaj.

INTRODUCTION

The Speckled Pigeon *Columba guinea* is the most conspicuous member of the Columbidae Family (Goodwin, 1964). The Speckled Pigeon (*Columba guinea*) is an African species, dweller to sub-Saharan Africa (Urban, *et.al*, 1986), including southern Africa (Colahan, 1997). It lives on mountains cliffs, rocky gorges and hills, urban and rural buildings (Hockey, *et.al.*, 2006) and feeds on a wide range of seeds, fruits and leaves (Hargreaves, 1992; Little, 1994; Pepler & Pepler 1991). The Speckled (or African rock) Pigeon is about the size of a feral pigeon. Speckled pigeons are usually seen in pairs but may congregate to large flocks of several hundred during the non-breeding seasons. The global population size of the species has not been quantified, but the species is described as common throughout most of its natural range (Gibbs, *et. al.*, 2001).

Speckled Pigeon *Columba guinea* is one of the common Columbids in the Zaria area of the Nigerian northern guinea savanna (Fry, 1965). It seems that the habit of the Speckled Pigeon *Columba guinea* and its dependence on human activities for food predisposes the bird to be easily trapped or killed, as it is widely sold or traded in





Mudhafar A. Salim et al.

most Nigerian markets to augment income (Rowan, 1983). It is a species of culinary interest and its wide acceptability as a cheap substitute to other animal protein sources, perhaps explains why the increasing demand for this bird (Adang, 1999), although the bird is not an endangered species and classified as a least concern according to the IUCN Redlist (IUCN, 2017 ; BirdLife International, 2017). The geographic range of the Speckled Pigeon *Columba guinea* concentrates mainly to Africa; it is native to Angola; Benin; Botswana; Burkina Faso; Burundi; Cameroon; Central African Republic; Chad; Congo, The Democratic Republic of the; Côte d'Ivoire; Djibouti; Eritrea; Ethiopia; Gambia; Ghana; Guinea; Guinea-Bissau; Kenya; Lesotho; Mali; Mauritania; Namibia; Niger; Nigeria; Rwanda; Senegal; Somalia; South Africa; South Sudan; Swaziland; Tanzania, United Republic of; Togo; Uganda; Zimbabwe; also extant (breeding) Malawi; Sierra Leone and also in Sudan, however, the species also recorded as an Extant & Vagrant (Non breeding) in Yemen (IUCN, 2017).

The observations of the Speckled Pigeon *Columba guinea* in Iraq

The Speckled Pigeon *Columba guinea* has been observed for three times in Iraq so far. The first observation was for an individual male found in a cage in a market in Diwaniya District, Southern Iraq at the 18th of September 2014. The bird was spotted by a member for the Iraqi Organization for Conservation of Nature (IOCN) during one of their regular checking of the cage-birds in Iraq as one of the activities adopted by the IOCN under the project: Sustainable Hunting Project in Iraq. The observed male was in a cage along with some birds (Collared Dove *Streptopelia decaocto*, and Laughing Dove *Spilopelia senegalensis*) where only one individual of the Speckled Pigeon *Columba guinea* was found among this group of doves (Yassir, W., IOCN internal correspondences 2014).

The second observation for the Speckled Pigeon *Columba guinea* in Iraq was for a bird in the wild in an arid land with shrubs and scattered small thorny trees in the desert region of Dalmaj area, Middle Euphrates, Iraq. The observation was made by a member for the IOCN during one of the regular biodiversity surveys in this area at the 22nd of October 2015. The individual bird was perching on a branch of thorny tree and was very shy where it was first observed with a 12x45 binoculars. Due to the shyness of the bird, the observer was not able to photograph it and it flew away once the observer has pointed the camera towards it (IOCN, internal report, 2015). Following the protocol of recording the new bird species in Iraq (that necessitates providing clear photo for the new species), this observation was not published at that time, and only written description was documented as the first Speckled Pigeon *Columba guinea* found in the wild in Iraq. The area to the east where this individual was observed at was well-known breeding ground for the newly-expanded the African Namaqua Dove *Oenacapensis* that was recorded for the first time for Iraq and got expanding breeding range recently in Iraq (Salim, 2008; and Ararat, *et al.*, 2011), in addition to some other Dove species that were in the same area.

The third observation for the Speckled Pigeon *Columba guinea* in Iraq was after showing some photos of a bird that was shot by a hunter in an agricultural area in Rumeitha sub-district, Samawa district at the 7th of Jan, 2019. The source of the information has been immediately contacted by IOCN, and he has provided more information regarding the presence of the hunted bird during the phone-interview. The researchers have checked out the habitat where the bird was hunted in order to acquire better understanding of the habitat requirements of the Speckled Pigeon *Columba guinea* in Iraq. Due to the available data from the second and third observations in addition to the habitat-description (mentioned above), the team have found that there are shared features of the habitat components in the two locations where the hunted individuals of the Speckled Pigeon *Columba guinea* were found at. The key features of the habitats and the observations conditions were as follows:

- Both areas were in relatively low altitude (ranges between 15-25m asl.);
- Both areas were relatively well-vegetated;
- Both areas include trees, however, scattered and thin;
- The first observed bird was alone, however, some Doves were nearby, while the second observation was for a bird mixed with Wood Pigeon *Columba palumbus* group;





Mudhafar A. Salim et al.

Neither the recent comprehensive references on the avifauna of Iraq (Salim, 2006; Porter, et.al., 2010; and Salim, 2012), nor any other literatures in Iraq have mention the Speckled Pigeon *Columba guinea* as an Iraqi bird species. It was not mentioned also by Porter and Aspinall, that covered the birds in the Middle East region, as a bird species recorded in Iraq (Porter &Aspinall, 2010). Being observed in confirmed way for more than one time in Iraq, the researchers have thought that it would be valuable to be added to the checklist of the birds of Iraq, with keeping an eye on its future status in case more observations will be made or when it get in expanding its range just like the case with the Laughing Dove and the Namaqua Dove in Iraq.

ACKNOWLEDGEMENTS

The authors would like to thank the Iraqi Organization for Conservation of Nature (IOC/N) for providing the old data and documents regarding the new species in Iraq. We would like to extend our thanks to the Arab Regional Center for World Heritage (ARC-WH) for their continuous support and encouraging the scientific research regarding the natural heritage in the Arab Region countries. We would also like to thank Mr. Abdul-Razzaq A. Mutar for his cooperation in providing the information regarding the third recording of this species.

REFERENCES

1. Adang, K. L. 1999. Some aspects of the biology of four Columbidae species in Zaria, Nigeria. Unpublished M. Sc. Thesis. Department of Biological Sciences, Ahmadu Bello University, Zaria, Nigeria.
2. Ararat, K., O Fadhel, RF. Porter & M. Salim. 2011. Breeding birds in Iraq: important new discoveries. *Sandgrouse* 33: 12–33.
3. BirdLife International 2017. *Columba guinea* (amended version of 2017 assessment). The IUCN Red List of Threatened Species 2017: e. T22690080A118855992. <http://dx.doi.org/10.2305/IUCN.UK.2017-3.RLTS.T22690080A118855992.en>.
4. Colahan, B.D., 1997, 'Rock pigeon', in J.A. Harrison, D.G. Allan, L.G. Underhill, M. Herremans, A.J. Tree, V. Parker et al. (eds.), The atlas of Southern African birds, vol. 1, pp. 502–503, BirdLife International, Johannesburg.
5. Fry, C. H. 1965. The birds of Zaria. i. African migrants, ii. Palaearctic migrants, iii. Residents, Vagrants and checklist (nonpasserines) iv. Residents, Vagrants and checklist (Passerines). *Bulletin of the Nigerian Ornithological Society*, 2: 9-17, 35-44, 68- 79 and 91-101.
6. Gibbs, D.; Barnes, E.; Cox, J. 2001. Pigeons and doves: a guide to the pigeons and doves of the world. Pica Press, Robertsbridge, U.K.
7. Goodwind, 1956. Remarks on the Rock and Speckled Pigeons. *Bull. Br. Ornithol. Club* 76: 6-9.
8. Hargreaves, B.J. 1992. 'A spurge *Jatropha zeyheri* eaten by rock pigeon (*Columba guinea*), Botswana', *Babbler* 23, 43–45.
9. Hockey, P.A.R., Dean, W.R.J. & Ryan, P.G. (eds.), 2006, *Roberts birds of South Africa*, 7thedn., The Trustees of the John Voelcker Bird Book Fund, Cape Town.
10. IUCN, 2017. The IUCN Red List of Threatened Species. Version 2017-1. Available at: www.iucnredlist.org. (Accessed: 27 April 2017).
11. Little, R.M. 1994. 'Marked dietary differences between sympatric feral rock doves and rock pigeons', *South African Journal of Zoology* 29, 33–35.
12. Pepler, D. & Pepler, C. 1991. 'Food of rock pigeon in the Karoo', *Promerops* 199, 9–10.
13. Porter, R & S Aspinall. 2010. *Birds of the Middle East*. Christopher Helm, London.
14. Porter, RF., M. Salim, K. Ararat & O.Fadel. 2010. A provisional checklist of the birds of Iraq. *Marsh Bulletin* 5(1): 56–95.
15. Rowan, M. K. 1983. The Doves, Parrots, Louries and Cuckoos of Southern Africa, Academic Press, London.
16. Salim, M. A., O. F. Al-Shekhly, K. A. Majeed, and R. E. Porter. 2012. "An Annotated Checklist of the Birds of Iraq." *Sandgrouse* 34:3–44.





Mudhafar A. Salim et al.

17. Salim, M. A, R Porter, P Schiermacker-Hansen, S Christensen & S Al- Jbour. 2006. [Field guide to the birds of Iraq]. NI/BirdLife International, Baghdad.
18. Salim, M. A. 2008. The first Namaqua Dove in Iraq. *Sandgrouse* 30: 100–101.
19. Urban, E.K., Fry, C.H. & Keith, S. (eds.). 1986. The birds of Africa, vol. 2, Academic Press, London.



Fig.1.Photo of the habitat of the second observation of the Speckled Pigeon *Columba guinea* For Iraq.©IOCN.



Fig.2.Photo of the third observation of the Speckled Pigeon *Columba guinea* in Iraq. ©Abdul-Razzaq A. Mutar.





Three Topological Structures of Fuzzy Bitopological Spaces

Amer Himza Almyaly*

Department of Mathematics, The College of Science, AL Muthanna University, Iraq.

Received: 17 Oct 2018

Revised: 20 Nov 2018

Accepted: 22 Dec 2018

*Address for Correspondence

Amer Himza Almyaly

Department of Mathematics,

The College of Science,

AL Muthanna University, Iraq.

Email:ameer_almyaly@yahoo.com



This is an Open Access Journal / article distributed under the terms of the **Creative Commons Attribution License** (CC BY-NC-ND 3.0) which permits unrestricted use, distribution, and reproduction in any medium, provided the original work is properly cited. All rights reserved.

ABSTRACT

In this paper the families τ_1 and τ_2 are fuzzy topologies on a nonempty set X , τ_s is supra fuzzy topology on X generated by τ_1 and τ_2 , and τ_l is the least upper fuzzy topology on X generated by τ_1 and τ_2 . We study and compare among the concepts (compactness of fuzzy topologies and continuity, closeness and openness of mapping) of fuzzy Bitopology, Supra fuzzy topology and Least fuzzy topology.

Key words: Fuzzy Bitopology; Supra fuzzy topology and least fuzzy topology.

INTRODUCTION

Kandil and his colleagues [1] and [2] introduced the concept of fuzzy Bitopological space, but they defined the compactness of fuzzy Topological space and the continuity, closeness and openness of mapping on the associated Supra fuzzy topological space, we will show the reason for this. In this study, we divide the topological structures fuzzy Bitopological space into three parts, namely, a "fuzzy Bitopology structure", a "Supra fuzzy topology structure" and a "Least fuzzy topology structure". Then we show that our concepts can be given in terms of these structures. Also, we generalized some concepts based on the references [3], [4] and [5]. Last, I^X will point to the set of all fuzzy sets in X , and the set of all fuzzy points p_x^z is denoted by $pt(I^X)$.

Preliminaries

Definition1.1, [1]: Let X be any set and let τ_1 and τ_2 be two fuzzy topologies on X . The triple (X, τ_1, τ_2) is called a fuzzy bitopological space fpts.

Definition1.2, [1]: A family $\eta \subseteq I^X$ is called Supra fuzzy topology if it is closed under arbitrary union and contains X . The space (X, η) is called Supra fuzzy topological space sfts. There more, if we have τ_1 and τ_2 are fuzzy





Amer Himza Almyaly

topologies on X and generated the family which is a supra fuzzy topology on X then (X, τ_2) is called the associated Supra fuzzy topological space of the space (X, τ_1, τ_2) .

Definition1.3, [1]: Let X be any set and let τ_1 and τ_2 be two fuzzy topologies on X . Let $\tau_1 = \tau_1 \vee \tau_2$ is the least upper fuzzy topology generated by τ_1 and τ_2 then (X, τ_1) is called the Least upper fuzzy topological space of the space (X, τ_1, τ_2) .

Bitopology Structure of a fbts.

Definition2.1: Let (X, τ_1, τ_2) be a fbts, then:

- 1) A fuzzy set $\mu \in I^X$ is fuzzy open (shr. open) in fbts if $\mu \in \tau_1 \cup \tau_2$.
- 2) A fuzzy set $\mu \in I^X$ is fuzzy closed (shr. closed) in fbts if $\mu' \in \tau_1 \cup \tau_2$.

Definition2.2: Let (X, τ_1, τ_2) be a fbts and $\mu \in I^X$, then:

- 1) The family $\gamma = \{\eta_s : s \in S\} \subseteq \tau_1 \cup \tau_2$ is called open cover of $\mu \in I^X$ (resp. X) iff for each $p_x^f \in \mu$ ($p_x^f \in pt(I^X)$) there exist $s_0 \in S$ such that $p_x^f \in \eta_{s_0}$.
- 2) $\mu \in I^X$ (resp. X) is called fuzzy $\tau_1 - \tau_2$ compact set (fuzzy $\tau_1 - \tau_2$ compact space) in fbts (X, τ_1, τ_2) if every open cover of μ (resp. X) has finite subcover.

Remark2.1: The reason to define the compactness as in above its the union of two elements of $\tau_1 \cup \tau_2$ is not necessary belong to $\tau_1 \cup \tau_2$.

Theorem2.1: If fbts (X, τ_1, τ_2) is fuzzy $\tau_1 - \tau_2$ compact space then (X, τ_1) and (X, τ_2) are fuzzy compact space.

Remark2.2: The reverse of the theorem 2.1 is not true ingeneral. i.e., if (X, τ_1) , (X, τ_2) or both are fuzzy compact spaces then is not necessary (X, τ_1, τ_2) is fuzzy $\tau_1 - \tau_2$ compact space as following examples:

Example2.1: Let X be infinite set. Let (X, τ_1) is indiscrete fuzzy top. space and (X, τ_2) is discrete fuzzy top. space, then (X, τ_1) is fuzzy compact space and (X, τ_2) is not fuzzy compact space and so (X, τ_1, τ_2) is not fuzzy $\tau_1 - \tau_2$ compact space.

Example2.2: Let X infinite set and τ_1, τ_2 are fuzzy topologies on X define as following: let $x, y \in X$ be a fixed points:

$$\tau_1 = \{\mu \in I^X : \mu(x) \neq 1\}$$

$$\tau_2 = \{\mu \in I^X : \mu(y) \neq 1\}$$

Then (X, τ_1) and (X, τ_2) are fuzzy compact spaces, but (X, τ_1, τ_2) is not fuzzy $\tau_1 - \tau_2$ compact space.

Definition2.3: A fuzzy cotopology is a family τ' of fuzzy sets in X which satisfy the following conditions:

1. $\emptyset, X \in \tau'$.





Amer Himza Almyaly

2. If $\eta_s, \eta_k \in \tau'$ then $\eta_s \cup \eta_k \in \tau'$.
3. If $\eta_s \in \tau'$ for each $s \in S$, then $\bigcap_s \eta_s \in \tau'$.

τ' is call a fuzzy cotopology on X , and the pair (X, τ') is a fuzzy cotopological space or fcts.

Definition2.4: A fuzzy bicotopological space (fbcts) is a triple (X, τ'_1, τ'_2) , such that τ'_1 and τ'_2 are arbitrary fuzzy cotopologies on X .

If (X, τ_1, τ_2) is fbcts then (X, τ'_1, τ'_2) is fbcts whenever τ'_1 and τ'_2 are complete of τ_1 and τ_2 , respectively. Conversely, if (X, τ'_1, τ'_2) is fbcts then (X, τ_1, τ_2) is fbcts whenever τ_1 and τ_2 are complete of τ'_1 and τ'_2 , respectively. For given fuzzy topologies τ_1 and τ_2 , we take into consideration from now the fuzzy cotopologies on X are τ'_1 and τ'_2 , where τ'_1 and τ'_2 are complement of τ_1 and τ_2 , respectively.

Definition2.5: Let $f: (X, \tau_1, \tau_2) \rightarrow (Y, \gamma_1, \gamma_2)$ be a function wherever τ_1 and τ_2 are ft on X and γ_1 and γ_2 are ft on Y . This function is called "fuzzy bitopology continuous function (fb continuous)" iff for each $A \in \gamma_1 \cup \gamma_2 \Rightarrow f^{-1}(A) \in \tau_1 \cup \tau_2$.

Proposition2.1: A function $f: (X, \tau_1, \tau_2) \rightarrow (Y, \gamma_1, \gamma_2)$ is fb continuous iff $\forall U \in \gamma'_1 \cup \gamma'_2 \Rightarrow f^{-1}(U) \in \tau'_1 \cup \tau'_2$.

Proof: We can get proof through definitions 2.4 and 2.5.

Proposition2.2: Let (X, τ_1, τ_2) , (Y, γ_1, γ_2) and (Z, σ_1, σ_2) be three fbcts, if the function $f: (X, \tau_1, \tau_2) \rightarrow (Y, \gamma_1, \gamma_2)$ and $g: (Y, \gamma_1, \gamma_2) \rightarrow (Z, \sigma_1, \sigma_2)$ are fb continuous, then $g \circ f: (X, \tau_1, \tau_2) \rightarrow (Z, \sigma_1, \sigma_2)$ is fb continuous.

Definition2.6: A function $f: (X, \tau_1, \tau_2) \rightarrow (Y, \gamma_1, \gamma_2)$ is called "fuzzy Bitopology open (fb open) (resp., fuzzy Bitopology closed (fb closed)) function" iff for each $U \in \tau_1 \cup \tau_2 \Rightarrow f(U) \in \gamma_1 \cup \gamma_2$ (resp., $U \subset \tau'_1 \cup \tau'_2 \Rightarrow f(U) \subset \gamma'_1 \cup \gamma'_2$).

Proposition2.3: Let $f: (X, \tau_1, \tau_2) \rightarrow (Y, \gamma_1, \gamma_2)$ be a surjective and fb continuous. If the fbcts (X, τ_1, τ_2) is fuzzy $\tau_1 - \tau_2$ compact space then so is (Y, γ_1, γ_2) .

Proof: Let (X, τ_1, τ_2) is fuzzy $\tau_1 - \tau_2$ compact space. Let $\lambda = \{\xi_s : s \in S\} \subseteq \gamma_1 \cup \gamma_2$ is open cover for Y . $\forall p_x^s \in pt(I^X)$ then $p_{f(x)}^s \in pt(I^Y)$. Since λ is open cover for $Y \Rightarrow \exists s_0 \in S$ s.t. $p_{f(x)}^s \in \xi_{s_0} \Rightarrow p_x^s \in f^{-1}(\xi_{s_0})$, but f is fb continuous $\Rightarrow \{f^{-1}(\xi_s) : s \in S\}$ is open cover for X and X fuzzy $\tau_1 - \tau_2$ compact space $\Rightarrow \exists S' \subseteq S$ is finite s.t. $\{f^{-1}(\xi_{s'}) : s' \in S'\}$ is finite subcover for X . Now, $\forall p_y^r \in pt(I^Y)$ then $p_{f^{-1}(y)}^r \in f^{-1}(\xi_{s_0})$, $s_0 \in S' \Rightarrow p_y^r \in \xi_{s_0} \Rightarrow \{\xi_{s'} : s' \in S'\}$ is finite subcover for $Y \Rightarrow Y$ is fuzzy $\tau_1 - \tau_2$ compact space.





Amer Himza Almyaly

Supra structure in fpts.

Definition3.1: A Supra fuzzy cotopology $\tau_s' \subseteq I^X$ is family closed under arbitrary intersection and contains X . The space (X, τ_s') is called a Supra fuzzy cotopological space. It easily seen that $\tau_s' = \{\mu \in I^X : \mu^c \in \tau_s\}$ and $\tau_s = \{\mu \in I^X : \mu^c \in \tau_s'\}$. i.e. τ_s' is complement of τ_s on X and vice versa.

Definition3.2: Let τ_s and σ_s two sfts on X and Y , respectively. A function $f: (X, \tau_s) \rightarrow (Y, \sigma_s)$ is called " $\tau_s - \sigma_s$ Supra continuous" iff, for each $U \subset I^Y, U \in \sigma_s \Rightarrow f^{-1}(U) \in \tau_s$.

Proposition3.1: A function $f: (X, \tau_s) \rightarrow (Y, \sigma_s)$ is $\tau_s - \sigma_s$ Supra continuous wherever τ_s and σ_s be sft on X and Y , respectively, iff $\forall U \in I^Y, U \in \sigma_s' \Rightarrow f^{-1}(U) \in \tau_s'$.

Proposition3.2: Let τ_s, σ_s and γ_s be three sft on X, Y and Z , respectively. If the function $f: (X, \tau_s) \rightarrow (Y, \sigma_s)$ and $g: (Y, \sigma_s) \rightarrow (Z, \gamma_s)$ are $\tau_s - \sigma_s$ Supra continuous and $\sigma_s - \gamma_s$ Supra continuous, respectively, then the function $g \circ f: (X, \tau_s) \rightarrow (Z, \gamma_s)$ is Supra continuous.

Definition3.3: A function $f: (X, \tau_s) \rightarrow (Y, \sigma_s)$ where τ_s and σ_s are sft on X and Y , respectively, is called a "Supra open map (resp., Supra closed map)" iff $\forall U \in I^X, U \in \tau_s \Rightarrow f(U) \in \sigma_s$ (resp., $U \in I^X, U \in \tau_s' \Rightarrow f(U) \in \sigma_s'$).

Definition3.4: Let (X, τ_s) be sfts. The family $\gamma = \{\eta_\ell : \ell \in L\} \subseteq I^X$ is called cover for X iff $X = \bigcup_{\ell \in L} \eta_\ell$ and open cover if γ is cover for X and $\eta_\ell \in \tau_s, \forall \ell \in L$.

Definition3.5: The sfts (X, τ_s) is Supra compact iff for all covering of X has a finite subcover.

Proposition3.6: Let $f: (X, \tau_s) \rightarrow (Y, \sigma_s)$ be a surjective and $\tau_s - \sigma_s$ Supra continuous function. If the sfts (X, τ_s) is Supra compact then (Y, σ_s) is so.

Definition3.6, [1]: Let (X, τ_1, τ_2) be fpts. Then (X, τ_s) is called the associated Supra fuzzy topology of the space (X, τ_1, τ_2) . i.e., $\forall U \in \tau_s$ then $U \in \tau_1, U \in \tau_2$ or U is union elements of τ_1 and τ_2 .

Remark3.1:

1. τ_s may not be closed under finite intersection.
2. τ_s' may not be closed under finite union.
3. If (X, τ_1, τ_2) is fpts, then $\tau_1 \cup \tau_2 \subset \tau_s$ and may be $\tau_1 \cup \tau_2 \neq \tau_s$.
4. If (X, τ_1', τ_2') is fcbts, then $\tau_1' \cup \tau_2' \subset \tau_s'$ and may be $\tau_1' \cup \tau_2' \neq \tau_s'$.

Example3.1: Let $X = \{a, b, c\}$, and let τ_1 and τ_2 are fuzzy topologies on X defined as follows:

- 1) $\tau_1 = \{X, \emptyset, \{p_a^1\}, \{p_b^1, p_c^1\}\} = \tau_1'$
- 2) $\tau_2 = \{X, \emptyset, \{p_b^1\}, \{p_a^1, p_c^1\}\} = \tau_2'$





Amer Himza Almyaly

Then $\tau_1 \cup \tau_2 = \{X, \emptyset, \{p_a^1\}, \{p_b^1\}, \{p_b^1, p_c^1\}, \{p_a^1, p_c^1\}\} = \tau_1' \cup \tau_2'$.

$\tau_s = \{X, \emptyset, \{p_a^1\}, \{p_b^1\}, \{p_b^1, p_c^1\}, \{p_a^1, p_c^1\}, \{p_a^1, p_b^1\}\}$ and

$\tau_s' = \{X, \emptyset, \{p_a^1\}, \{p_b^1\}, \{p_c^1\}, \{p_b^1, p_c^1\}, \{p_a^1, p_c^1\}\}$

Furthermore;

- τ_s is not closed under finite intersection since $\{p_b^1, p_c^1\} \cap \{p_a^1, p_c^1\} = \{p_c^1\} \notin \tau_s$.
- τ_s' is not closed under finite union since $\{p_a^1\} \cup \{p_b^1\} = \{p_a^1, p_b^1\} \notin \tau_s'$.
- It's clear $\tau_1 \cup \tau_2 \subset \tau_s$ but $\tau_1 \cup \tau_2 \neq \tau_s$
- It's clear $\tau_1' \cup \tau_2' \subset \tau_s'$ but $\tau_1' \cup \tau_2' \neq \tau_s'$

Theorem3.1: Let (X, τ_s) associated Supra fuzzy topology of the space (X, τ_1, τ_2) . The sfts (X, τ_s) is compact space iff fbts (X, τ_1, τ_2) is compact space.

Proof: Let (X, τ_s) be supra compact space. Let $\gamma = \{\eta_\ell; \ell \in L\} \subseteq I^X$ is open cover for X in $\tau_1 \cup \tau_2$ then γ is open cover for X in τ_s , but (X, τ_s) is supra compact $\Rightarrow \gamma$ has finite subcover for X in τ_s , hence γ has finite subcover for X in $\tau_1 \cup \tau_2$.

Conversely: Let (X, τ_1, τ_2) is compact space. Let $\gamma = \{\eta_\ell; \ell \in L\}$ is open cover for X in τ_s . Since $\forall \eta_\ell \subset \gamma, \eta_\ell \subset \tau_1, \tau_2$ or union elements of τ_1 and τ_2 then we form the family

$$\gamma^* = \begin{cases} \eta_\ell & \text{if } \eta_\ell \in \tau_1 \text{ or } \tau_2 \\ \zeta_{\ell, \sigma} & \text{if } \eta_\ell = \bigcup_{\sigma} \zeta_{\ell, \sigma} \text{ and } \zeta_{\ell, \sigma} \in \tau_1, \tau_2 \text{ or both} \end{cases}$$

Then this family is open cover for X in $\tau_1 \cup \tau_2$. But $\tau_1 \cup \tau_2$ is compact $\Rightarrow \gamma^*$ has finite subcover γ^{**} for X in $\tau_1 \cup \tau_2$. Therefore, we choose η_ℓ which belong to τ_1, τ_2 or correspond $\zeta_{\ell, \sigma}$ in $\gamma^{**} \Rightarrow \gamma$ has finite subcover for X in τ_s .

least topology structure in fbts.

Remark4.1: Since τ_ℓ is fuzzy topology, then the concepts which have introduced in sections 3 and 4 are defined with respect to τ_ℓ .

Remark4.2

- 1- If (X, τ_1, τ_2) is fbts and (X, τ_s) is associated sfts then $\tau_s \subset \tau_\ell$ and may be $\tau_s \neq \tau_\ell$.
- 2- If (X, τ_1', τ_2') is fbts and (X, τ_s') is associated sfts then $\tau_s' \subset \tau_\ell'$ and may be $\tau_s' \neq \tau_\ell'$.





Amer Himza Almyaly

Example4.1: In example 3.1, then

- 1- $\tau_\ell = \{X, \emptyset, \{p_a^1\}, \{p_b^1\}, \{p_c^1\}, \{p_b^1, p_c^1\}, \{p_a^1, p_c^1\}, \{p_a^1, p_b^1\}\}$ such that $\tau_\ell \neq \tau_\ell'$.
- 2- $\tau_\ell' = \{X, \emptyset, \{p_a^1\}, \{p_b^1\}, \{p_c^1\}, \{p_b^1, p_c^1\}, \{p_a^1, p_c^1\}, \{p_a^1, p_b^1\}\}$ such that $\tau_\ell \neq \tau_\ell'$.

Theorem4.1: Let (X, τ_α) associated Supra fuzzy topology of the space (X, τ_1, τ_2) and let (X, τ_ℓ) least upper fuzzy topological space of τ_1 and τ_2 , then (X, τ_α) is compact space iff (X, τ_ℓ) is compact space.

Proof: \Rightarrow the proof is easily as in theorem 3.1.

\Leftarrow Let (X, τ_α) is compact space. Let $\gamma = \{\eta_\ell : \ell \in L\}$ is open cover for X in τ_ℓ , then every η_ℓ in γ belong to τ_α or finite intersection elements of τ_α , therefore we form the family

$$\gamma^* = \left\{ \zeta_c \text{ if } \eta_\ell = \bigcap_c \zeta_c \text{ and } \zeta_c \in \tau_\ell \text{ for any } c \right.$$

Then γ^* is open cover for X in τ_α , but τ_α is compact $\Rightarrow \gamma^*$ has finite subcover γ^{**} for X in τ_α . Therefore, we choose η_ℓ which belong to τ_1, τ_2 or corresponds ζ_c in $\gamma^{**} \Rightarrow \gamma$ has finite subcover for X in τ_ℓ .

CONCLUSION

1. From theorems 3.1 and 4.1 the definitions of compactness are equivalent in Bitopology, associated Supra topology and Least upper topology.
2. $\tau_1 \cup \tau_2 \subseteq \tau_\alpha \subseteq \tau_\ell$ [1].
3. $\tau_1' \cup \tau_2' \subseteq \tau_\alpha' \subseteq \tau_\ell'$
4. Let (X, τ_1, τ_2) be fbts. Let (X, τ_α) is associated supra topology and $A \subseteq X$ then
 - i. $A^\circ = \cup \{L \in \tau_1 \cup \tau_2 : L \subseteq A\}$
 - ii. $\bar{A} = \cap \{K \in \tau_1' \cup \tau_2' : A \subseteq K\}$

Proof

i. $A^\circ \subseteq A$, then $A^\circ \in \tau_1 \cup \tau_2$ or A° is union elements $L \in \tau_1 \cup \tau_2$ and $L \subseteq A$ and in both cases then $A^\circ \subseteq \cup \{L \in \tau_1 \cup \tau_2 : L \subseteq A\}$. On other hand, for each $L \in \tau_1 \cup \tau_2$ such that $L \subseteq A \Rightarrow L \subseteq A^\circ \Rightarrow \cup \{L \in \tau_1 \cup \tau_2 : L \subseteq A\} \subseteq A^\circ$. Hence the equality is satisfying. ii. $A \subseteq \bar{A}$, then $\bar{A} \in \tau_1' \cup \tau_2'$ or \bar{A} is intersection elements $K \in \tau_1' \cup \tau_2'$ and $A \subseteq K$ and in both cases then $\cap \{K \in \tau_1' \cup \tau_2' : A \subseteq K\} \subseteq \bar{A}$. On the other hand, $\forall K \in \tau_1' \cup \tau_2'$ such that $A \subseteq K \rightarrow \bar{A} \subseteq K \rightarrow \bar{A} \subseteq \cap \{K \in \tau_1' \cup \tau_2' : A \subseteq K\}$. Hence the equality is satisfying.





Amer Himza Almyaly

5. In 4, this is not satisfy on (X, τ_f) , from examples 3.1 and 4.1 then:

- i. $\{p_\tau^1\}^* = \emptyset$ in (X, τ_α) but $\{p_\tau^1\}^* = \{p_\tau^1\}$ in (X, τ_f) .
- ii. $\overline{\{a, b\}} = X$ in (X, τ_α) but $\overline{\{a, b\}} = \{a, b\}$.

REFERENCES

- [1] A. Kandil, A. A. Nouh and S. A. El-Sheikh, "On Fuzzy Bitopological Spaces", Fuzzy Sets and Systems; Vol. 74, PP. 353-363, (1995).
- [2] A. Kandil, A. A. Nouh and S. A. El-Sheikh, "Strong and Ultra Separation Axioms On Fuzzy Bitopological Spaces", Fuzzy Sets and Systems; Vol. 105, PP. 459-467, (1999).
- [3] B. P. Dvalishvili, "Bitopological Spaces: Theory, Relations with Generalized Algebraic Structures, and Applications", Printed in the Nerber Lands, Third edition, (2005).
- [4] Hong Wang, "Separation Axioms of Fuzzy Bitopological Spaces", International Journal of Computer Science and Network Security, Vol. 13, No. 10, PP. 21-25, (2013).
- [5] M. Demirci, "Three Topological Structure of Smooth Topological Spaces", Fuzzy Sets and Systems, Vol.101, PP.185-190, (1999).





Co-doping Effect (Pb and Nd) on Mechanical Properties of BSCCO System

Firas Salim Abed* and Amal K. Jassim

Physics Department, College of Science, University of Baghdad, Iraq.

Received: 16 Oct 2018

Revised: 19 Nov 2018

Accepted: 22 Dec 2018

*Address for Correspondence

Firas Salim Abed

Physics Department,

College of Science,

University of Baghdad, Iraq.

Email: amelalmalki1974@yahoo.com



This is an Open Access Journal / article distributed under the terms of the **Creative Commons Attribution License** (CC BY-NC-ND 3.0) which permits unrestricted use, distribution, and reproduction in any medium, provided the original work is properly cited. All rights reserved.

ABSTRACT

To study the Lead and Neodymium doping effects on mechanical properties of BSCCO superconducting system, bulk samples with the general formula $\text{Bi}_{2-x}(\text{Pb}, \text{Nd})_x\text{Sr}_2\text{Ca}_2\text{Cu}_3\text{O}_{10+\delta}$ ($x = 0.0, 0.1, 0.2, 0.3, 0.4, 0.5$ and 0.6) were prepared by solid-state reaction method. The results showed that the values of Vickers microhardness (Hv), Young's modulus (E) and yield strength (Y) change randomly with increasing (Pb, Nd) concentration. On the other side an increase of the applied load caused a decrease in mechanical properties.

Keywords: Bi-2223; Superconductor; Mechanical Properties.

INTRODUCTION

The most common mechanical properties which are used in order to classify and identify material are hardness (Hv), yield strength (y) and young's modulus (E). Hardness is a measure of the resistance of a material to deformation, and is measured by forcing an indenter into the surface of a material. The material that composes the indenter must be harder than the material being tested. Therefore, for ceramics, it is common to use diamond indenters. The indentation is measured and then fitted to a correlation specific to the indenter being used. Macrohardness testing methods require large sample sizes and many repeated sample tests, requiring a great deal of bulk materials. Therefore, macro-hardness cannot be measured in small samples. Instead, microhardness is measured. Microhardness is a mechanical parameter related to the structure and composition of the material. This testing gives insight into mechanical properties such as Young's modulus, yield strength, and Fracture toughness [1]. Microhardness is more or less constant with load, and is influenced by solid solution effects connected with the chemical nature of atoms, defect aggregates and amorphous regions, and point defects that hinder the motion of dislocations [2]. During microhardness testing, the indentation made by the indenter is on the micrometer scale, and therefore cannot be seen without the aid of an optical microscope. The ratio between tensile stress to tensile strain in





Firas Salim Abed and Amal K.Jassim

the linear elastic range is called modulus of elasticity and is a characteristic of the metal type [3]. Therefore, Young modulus describes the resistance of the body to mechanical action, can be represented as a force applied to the sample. The elastic modulus of crystal depends only on the type of atom and their relative position and it is a measure of the atomic binding forces in the crystal lattice [4]. On the other side, Yield strength, is one of the material property, particularly in ductile materials. It not only represents the change from a recoverable, elastic response to a plastic response and the accompanying permanent deformation but also represents an important design parameter in materials selection. As a result, the yield strength may be an even more important mechanical property than the modulus for certain applications [5]. However, more investigations are needed to study the mechanical properties of Bi-2223 superconductors Thus in this work we're trying to prepare and investigate the mechanical properties of Bi_{2-x}(Pb, Nd)_xSr₂Ca₂Cu₃O_{10+δ} system.

EXPERIMENTAL

Starting materials of high- purity powders (99.9%) of (Bi₂O₃, Pb₃O₄, Sr(NO₃)₂, CaO,CuO and Nd₂O₃) were used to prepare the system Bi_{2-x}(Pb,Nd)_xSr₂Ca₂Cu₃O_{10+δ} with (0≤x≤0.6). Then pressed the mixture into pellets under pressures 0.7 GPa using hydraulic press type (Specac). The samples were sintered at 850° C for 160 hr. The Vickers hardness tester (Model THV-30D Digital Vickers (test uses a square-base diamond pyramid as the indenter and an angle of 136 degrees between opposite faces subjected. The Two diagonals of indentation left in the surface of the material after removal of the load are measured using a microscope and their average calculated .The area of the sloping surface of the indentation is calculate

RESULTS AND DISCUSSION

For the sake of industrial application of high temperature oxide superconductors, it is important to know and measure the mechanical properties such as Vickers microhardness (Hv) ,Young's modulus (E) and yield strength (Y). All samples were polished prior to being tested using a Vickers pyramidal indenter with different loads (0.490, 0.980, 1.960, and 2.940) N, the waste of time was 20 second to measure the diagonals of indentation, at different locations on the surface of the samples, was calculated the average value of the Vickers micro hardness for each load. The (Hv), (E) and (Y) at different applied loads have been calculated by equations (1), (2) and (3) [6,7,8] and illustrated in Figs. (1), (2) and (3) for each sample.

$$Hv = \frac{2F \sin \frac{136}{2}}{d^2} = 0.001854 \cdot F/d^2 \dots\dots\dots (1) \text{ Where } F \text{ is the indenter load and } d \text{ is the length of the diagonal}$$

$$E = 81.96 \cdot Hv \dots\dots\dots(2) \quad Y = Hv / 3 \dots\dots\dots(3)$$

It is found from these figures that the mechanical properties of the samples was observed to be load dependent. In general, the curves in the figures show that Hv, E and Y values decreased non- linearly as the applied load increased, this decrease is attributed to the presence of weak grain boundaries of the superconductor ceramics. Similar behavior were reported by [9&10]. Another features has also been observed, the values of Hv , E and Y change randomly with increase of x value Figs.(4), (5) and (6) with notes that there a high decreasing at x=0.2. Hardness is a property that can be understood in terms of resistance offered to dislocation motion and bonding force between the atoms. Changes in the hardness of the BSCCO ceramic material depending on doping or substitution concentration. The general contribution to the resistance is mainly of two types [11]: (1) The intrinsic resistance. (2) The resistance due to imperfections .In our case, change in values of Hv , E and Y of BSCCO samples with x values may be due to both





Firas Salim Abed and Amal K.Jassim

pinning of dislocations at the impurity sites and other defects caused by the presence of impurity atoms in the crystal, and also to variation in the magnitude of the bond forces in the crystal containing impurities [12]. The results are summarized in Table (1).

CONCLUSIONS

Codoping with (Pb,Nd) altered the mechanical properties of superconductor samples, a remarkable decrease, in the mechanical resistance of the samples was observed with the increase of the (Pb,Nd) up to 0.2. On the other hand the Hv, E and Y values decreased non- linearly as the applied load increased.

REFERENCES

1. P. Kaur, K. K. Sharma, R. Pandit, R. Kumar, R. K. Kotnala, and J. Shah, "Temperature dependent dielectric and magnetic properties of GdFe_{1-x}Ni_xO₃(0.0 ≤ x ≤ 0.3) orthoferrites," *J. Appl. Phys.*, vol. 115, no. 22, pp. 0–7, 2014.
2. K. K. Bamzai, P. N. Kotru, and B. M. Wanklyn, "Fracture mechanics, crack propagation and microhardness studies on flux grown ErAlO₃ single crystals," *J. Mater. Sci. Technol.*, vol. 16, pp. 405–410, 2000.
3. L. H. Van Vlack, *Elements of Materials Science and Engineering*, Sixth edit. Addison-Wesley, 1989.
4. D. W. Budworth, *An introduction to ceramic*. Elsevier, 2016.
5. B. S. Mitchell, *An Introduction to Materials Engineering and Science for Chemical and Materials Engineers*. John Wiley & Sons, 2004.
6. I. J. McColm, *Ceramic Hardness*. Springer Science & Business Media, 2013.
7. B. Özkurt, M. A. Madre, A. Sotelo, and J. C. Diez, "Structural, superconducting and mechanical properties of molybdenum substituted Bi_{1.8}Sr₂Ca_{1.1}Cu_{2.1}O_y," *J. Mater. Sci. Mater. Electron.*, vol. 24, no. 4, pp. 1158–1167, 2013.
8. M. Yilmazlar, O. Ozturk, H. Aydin, M. Akdoğan, and C. Terzioglu, "The Effect of Sm→Ca Substitution on Mechanical Properties of BSCCO Superconductors," *Chinese J. Phys.*, vol. 45, pp. 128–134, 2007.
9. A. K. Jassim and A. A. Hussien, "Effect of Co substitution on the mechanical properties of Bi₂Pb_{0.3}Sr₂Ca₂Cu_{3-x}CoxO_{10+δ} system," *AARJMD.*, vol. 3, no.4 April, 2016.
10. H. A. Cetinkara, M. Yilmazlar, O. Ozturk, M. Nursoy, and C. Terzioglu, "The influence of cooling rates on microstructure and mechanical properties of Bi_{1.6}Pb_{0.4}Sr₂Ca₂Cu₃O_y superconductors," *J. Phys. Conf. Ser.*, vol. 153, no. March, 2009.
11. S. M. Khalil, "Effects of optimum annealing time on superconducting properties of Bi_{2-x}PbxSr₂Ca₂Cu₃O_y system," *Phys. status solidi a*, vol. 178, no. 2, pp. 731–744, 2000.
12. U. Kölemen, O. Uzun, M. Yilmazlar, N. Güçlü, and E. Yanmaz, "Hardness and microstructural analysis of Bi_{1.6}Pb_{0.4}Sr₂Ca_{2-x}Sm_xCu₃O_y polycrystalline superconductors," *J. Alloys Compd.*, vol. 415, no. 1–2, pp. 300–306, 2006.

Table (1): Vickers microhardness (Hv) , Young's modulus (E) and yield strength (Y) for different load with x=0, 0.0 , 0.1, 0.2, 0.3, 0.4, 0.5, and 0.6

X	F (N)	HV (GPa)	E (GPa)	Y (GPa)	F (N)	HV (GPa)	E (GPa)	Y (GPa)
0	0.49	1.533	125.64	0.511	0.98	1.37	112.94	0.459
0.1		1.26	103.26	0.420		1.18	96.71	0.393
0.2		1.01	82.77	0.336		0.98	80.32	0.326
0.3		1.74	142.61	0.580		1.40	114.74	0.466
0.4		1.61	131.95	0.536		1.42	116.38	0.473
0.5		1.51	123.75	0.503		1.48	121.30	0.493
0.6		1.16	95.07	0.386		1.09	89.33	0.363
X	F (N)	HV (GPa)	E (GPa)	Y (GPa)	F (N)	HV (GPa)	E (GPa)	Y (GPa)





Firas Salim Abed and Amal K.Jassim

0	1.96	1.11	91.38	0.371	2.94	1.04	85.56	0.348
0.1		0.98	80.32	0.326		0.88	72.12	0.293
0.2		0.95	77.86	0.316		0.63	51.63	0.21
0.3		1.32	108.18	0.440		0.86	70.48	0.286
0.4		1.12	91.79	0.373		1.00	81.96	0.333
0.5		1.07	87.69	0.356		0.87	71.30	0.290
0.6		1.08	88.51	0.360		0.96	78.68	0.320

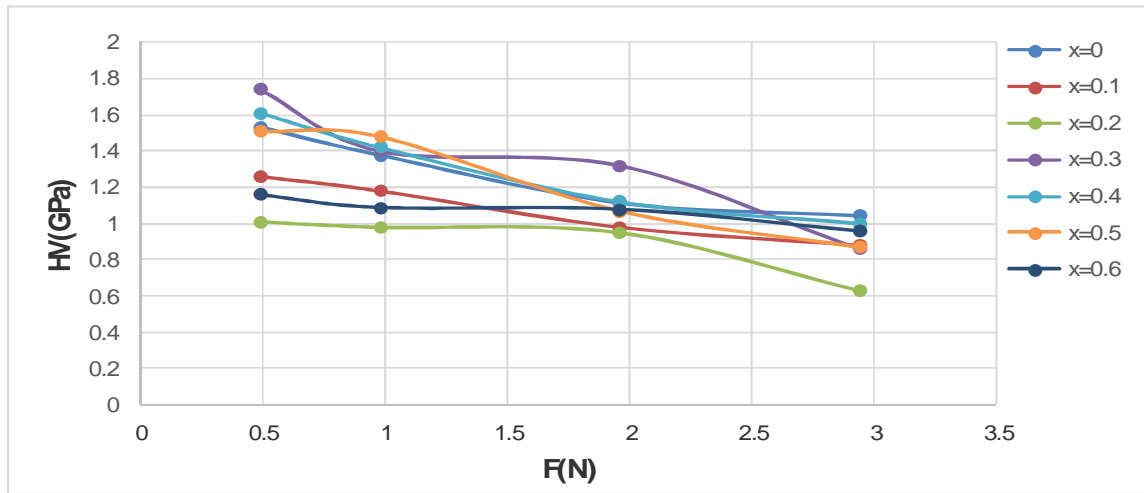


Fig. 1. variation of Vickers microhardness with applied load for different nominal compositions of $Bi_{2-x}(Pb,Nd)_xSr_2Ca_2Cu_3O_{10+\delta}$

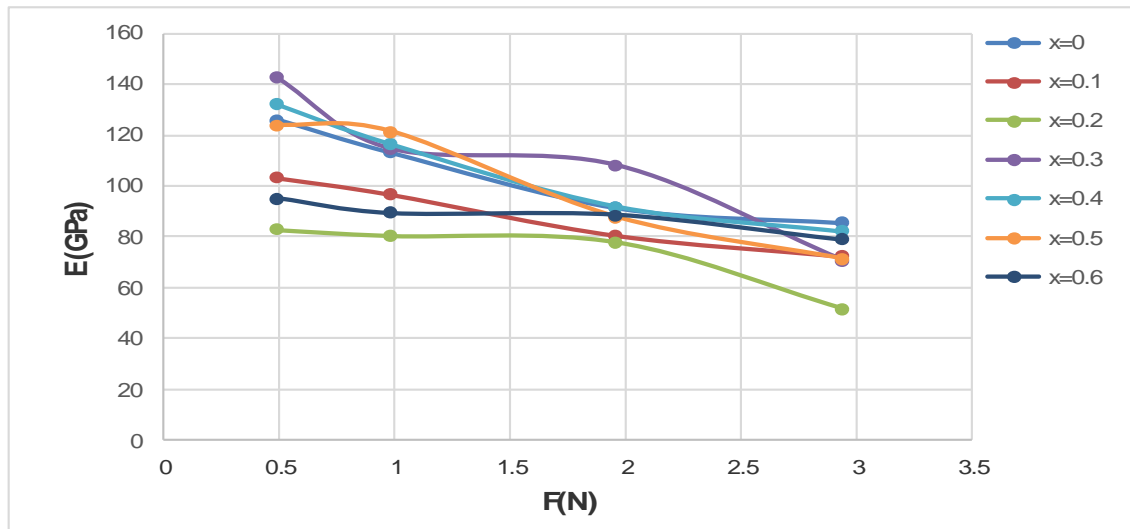


Fig.2 variation of Young modulus with applied load for different nominal compositions of $Bi_{2-x}(Pb,Nd)_xSr_2Ca_2Cu_3O_{10+\delta}$





Firas Salim Abed and Amal K.Jassim

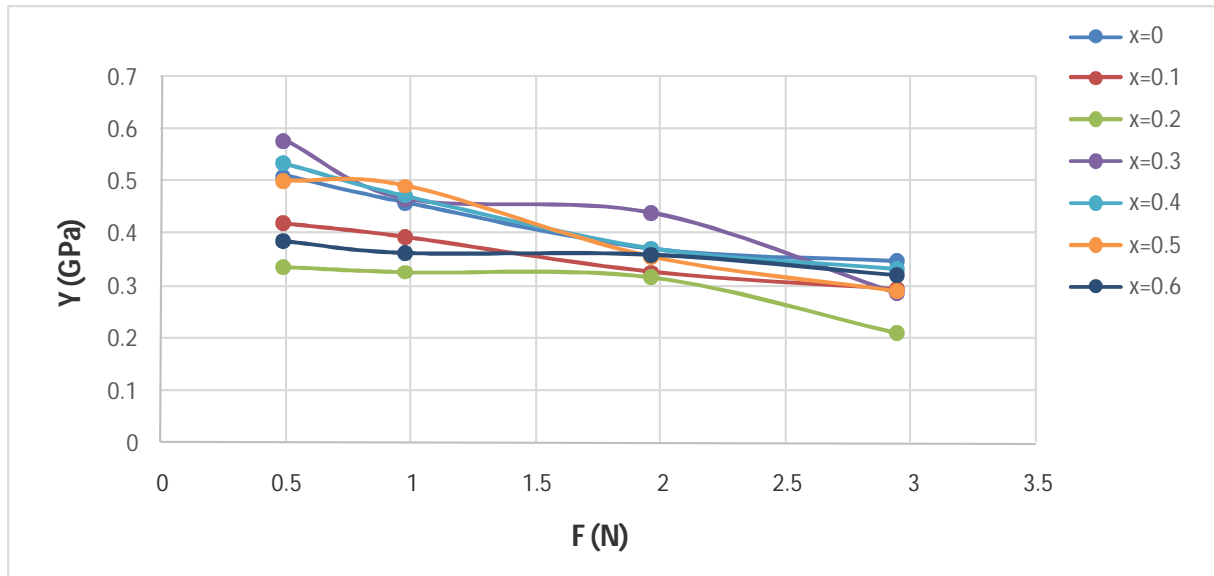


Fig.3. variation of yield strength with applied load for different nominal compositions of $Bi_{2-x}(Pb,Nd)_xSr_2Ca_2Cu_3O_{10+\delta}$

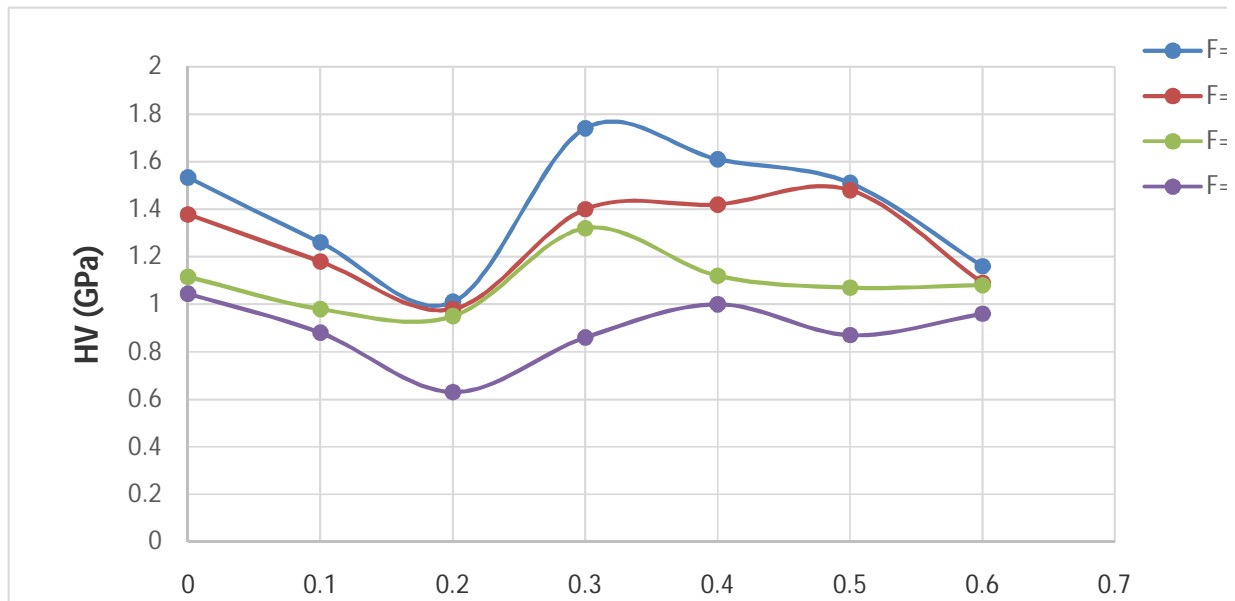


Fig.4. variation of microhardness Hv as a function of (Pb,Nd) content for different loads.





Firas Salim Abed and Amal K.Jassim

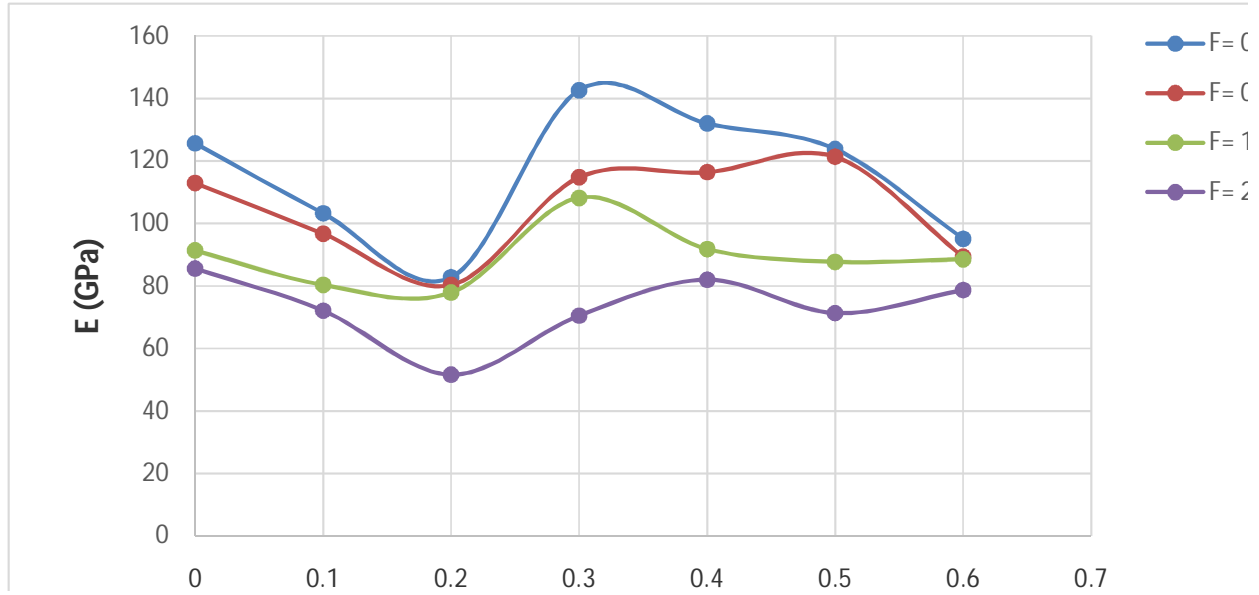


Fig.5. variation of Young modulus as a function of (Pb, Nd) content for different loads.

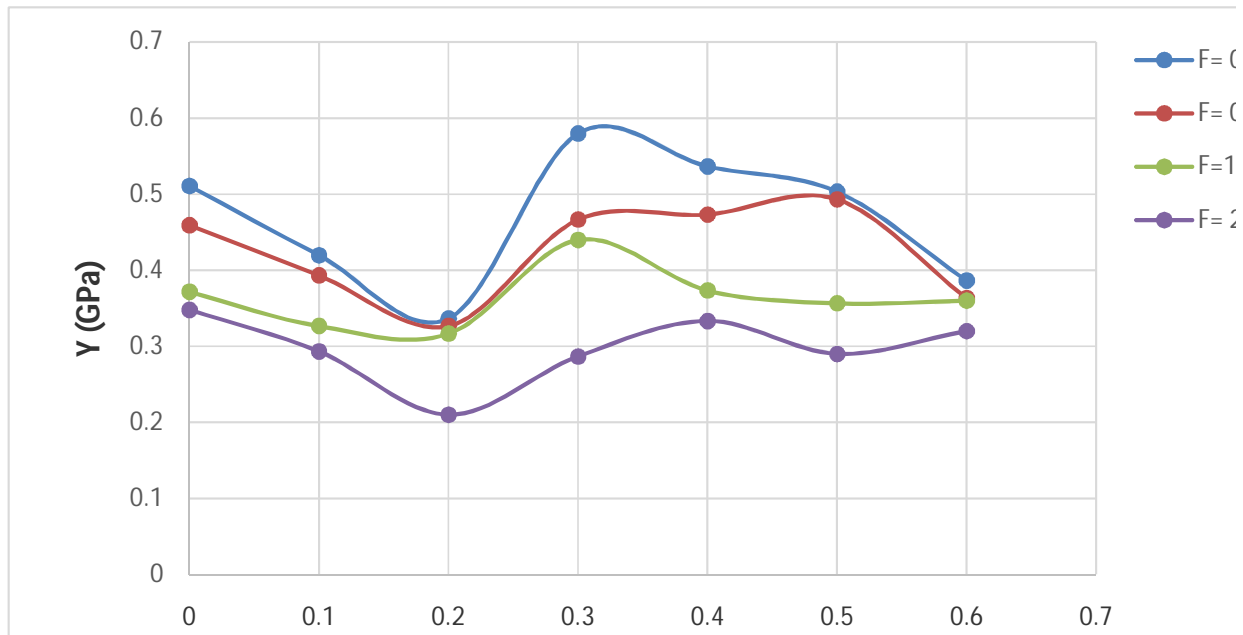


Fig. 6. variation of the yield strength as a function of (Pb,Nd) content for different





The Installation of Three Meter Small Radio Telescope in University of Baghdad

Mohammed R. Hoobi* and Kamal M. Abood

Department of Astronomy and Space, College of Science, University of Baghdad, Baghdad, Iraq.

Received: 20 Oct 2018

Revised: 23 Nov 2018

Accepted: 25 Dec 2018

*Address for Correspondence

Mohammed R. Hoobi

Department of Astronomy and Space,
College of Science,
University of Baghdad, Baghdad, Iraq.



This is an Open Access Journal / article distributed under the terms of the **Creative Commons Attribution License** (CC BY-NC-ND 3.0) which permits unrestricted use, distribution, and reproduction in any medium, provided the original work is properly cited. All rights reserved.

ABSTRACT

In this work, the installation of a radio telescope with parabolic three meter antenna over the building of the department of Astronomy and Space, College of Science in Baghdad University at latitude ($33^{\circ} 16' 28''$ N) and longitude ($44^{\circ} 22' 50''$ E), at time zone +3, Which can detect radio sources emission at frequency range (1.3 GHz – 1.5 GHz), and at central frequency is 1.42 GHz, 21 cm Hydrogen Emission Line.

Key Words: Radio Telescope, 21 cm Hydrogen Emission Line, Radio Telescope Control Units (RTCS), Radio Telescope Receiver Units (RTRS).

INTRODUCTION

The purpose of this paper is to construct a radio telescope that will detect hydrogen emission at 21 cm, 1.42 GHz in frequency, over the building of the department of Astronomy and Space, College of Science in Baghdad University at latitude ($33^{\circ} 16' 28''$ N) and longitude ($44^{\circ} 22' 50''$ E), at time zone +3. A radio telescope is an astronomical instrument consisting of a radio receiver and some sort of antenna. The radio telescope works by detecting radio-frequency radiation which is emitted by extraterrestrial sources. Begin the construction of the process of building a radio telescope and in the long run it should be able to map out the outer space.

Some Small Radio Telescope in the World

Haystack Small Radio Telescope

A small radio telescope used for research and education. Located at Bosscha Observatory, Massachusetts Institute of Technology (MIT), which has altitude of 1310 m. It consists of a receiver, low noise amplifier, feed horn, noise diode calibrator, and 2.3 m parabolic dish and focal length of 95.8 cm with an alt-azimuthal mount controlled by software





Mohammed R. Hoobi and Kamal M. Abood

written in JAVA. The antenna is mounted in a meteorological tower at the Bosscha Observatory to get all the sky coverage above horizon. The receiver can cover frequency range of (1.4 GHz - 1.44 GHz), at this range the telescope is very convenient to conduct spectral line observations at the neutral hydrogen (HI) 1.42 GHz frequency (21 cm Line Wavelength) [1].

Indlebe Radio Telescope (IRT)

Indlebe radio telescope Located in the Durban University of Technology (DUT), the IRT is to provide a real world platform for project work for students within the department of electronic engineering. Although science was not an initial goal of the IRT, it has demonstrated the potential to conduct useful astronomical observations; the radio telescope uses a 5m parabolic reflector antenna construct and tests a radio telescope operating at the hydrogen line frequency of 1.42 GHz [2].

Hydrogen Line Spectrum (21 cm)

In spectral line observation, radio receivers are used for studying the interstellar medium. The most studied spectral line in radio astronomy is the HI-line; it comes from neutral hydrogen, which can be detected in 1.42 GHz [3]. One of the reasons is that the emissions of the sky that are observed by radio astronomers are not the light from the stars, but radio waves from the gas and dust clouds that are remnants of supernova or star explosions. The 21cm hydrogen emission line used to chart the structure of our galaxy, known as the Milky Way. The 21cm hydrogen emission line is in fact one of the most accurate measured physical properties [4][5]. The hydrogen atom consists of one proton and one electron, orbits around the nucleus. Most of the hydrogen in space is in ground state. The electron moving around the proton have a spin in the same direction as the proton's spin (parallel) or spin in opposite direction (anti-parallel). The energy state of an electron spinning anti-parallel is lower than the energy state of the parallel spin. The atoms always want to be in the lowest energy state possible, the electron will ultimately flip to the anti-parallel spin direction if it were in the parallel spin. The energy carried by the atom in the parallel spin is greater than the energy in the anti-parallel spin. Therefore, when the spin state flips from parallel to the anti-parallel, the energy difference is very small, so it's emitted at a radio wavelength of 21 cm. This 21 cm correspond the radio spectral line at frequency of 1.42 GHz, and then hydrogen atom can wait a few million years before this transition [6].

Three Meter Baghdad University Radio Telescope (BURT) Setup

The best performance can be achieved by selecting the best location for the antenna in Baghdad University at latitude ($33^{\circ} 16' 28''$ N) and longitude ($44^{\circ} 22' 50''$ E), over the building of the department of Astronomy and Space in College of Science. The selection of this location follows these guidelines for choosing the installation location.

1. The telescope location should be far from the large microwave sources to reduce the signal affection.
2. The telescope location should be far from anything that prevents the electromagnetic wave, such as trees or buildings.
3. The antenna location should be relatively flat.
4. The supported base should be installed away from buried cables or pipes. BURT radio telescope consists of two parts (Hardware and Software).

Setup the Radio Telescope Hardware

At first, the setup location is prepared on a suitable platform (Concrete Base) with square shape with dimensions (160 cm long, 160 cm width, 30 cm height), as in figure (2): Then the antenna parabolic stand is connected to the base, as in figure (3) The antenna mount type is Elevation/Azimuth for ensuring antenna pointing range being Az 0° ~ 360° or El 0° ~ 90° . Then connect the motors: Azimuth motor (Az), and Elevation motor (El) to the stand and then connect the motors by cables to the control system, as in figure (4):





Mohammed R. Hoobi and Kamal M. Abood

Then connect the 3-meter rugged parabolic antenna to the stand, as in figure (5). The antenna is rugged and reliable that will operate at L-band or any other bands up to 18 GHz, and consists of reflector, sub-reflector, feed assembly complete with feed horn, mount, foundation model, foundation screw, stainless steel standard part. Then connect the feed horn which acts like a collecting funnel, it collects electromagnetic wave flux at 1.42 GHz. And low noise amplifier (LNA) which acts as a preamplifier at frequency band (1.3 GHz – 1.5 GHz). The LNA is directly connected to the feed horn, which is mounted over radio dish antenna. Thus the signal collected by feed horn gets amplified by LNA, as in figure (6): And finally, connect the whole system to the Telescope Computer in the lab, as in figure (7):

The telescope computer is consists of two parts

Radio Telescope Control Units (RTCS) is consists of two parts: Antenna Control Unit (ACU), Antenna Derive Unit (ADU), are the devices which is controls the antenna positions motors, and it's a RS-232 base connector and it be communicate with the computer through a USB to serial port adapter cable.

1. Radio Telescope Receiver Units (RTRS) is the device which is receives the signals and displayed it as a spectrum, and it can be connected to the computer by a USB cable directly.

Computer Radio Telescope Software

The Radio Telescope Software (RTC v_6.3.0) is used for control and data acquisition of a professional radio telescope. RTC is able to control the antenna for scanning an area in the sky, track the radio astronomy sources and also show the object positions in the equatorial and horizontal coordinate system. 60 strong radio astronomical sources with their position and intensity are presented by RTC. This software connects to devices such as Radio Telescope Control System (RTCS), and Radio Telescope Receiver System (RTRS). RTC contains a main common window with five major parts, including Setup, Spectral Line Observation, Continuum Observation, Functions and Help, as in figure (8).

The Radio Observation of Cassiopeia-A Results

The study and the observe of the supernova remnant Cas-A in the constellation Cassiopeia, because it has a high flux density in 1420 MHz (2477 Jy), and it has a stationary position in the celestial sphere and it's not set or rises, so we can observe it at day and night, to see the difference in spectrum when we observe it at night (Date: 10/1/2018, Time: 07:06:02 PM) and at day (Date:11/1/2018, Time: 10:35:28 AM) and to be sure that the telescope is working well. As in figure (9) the spectrum of Cas-A at night after applying the noise elimination average technique, and we notice the two sided peaks in each spectrum, these peaks represent the interference noise from ground stations in the telescope location area. And the peak of Cas-A is should appear between the frequency range (1395 MHz – 1425 MHz). Then take the data between this range of frequencies (1395 MHz – 1425 MHz) to see the probability of appearing the peak of Cas-A, as in figure (10): As in figure (11) the spectrum of Cas-A at day after applying the noise elimination average technique, and we notice the two sided peaks also. But we see a different shape of the spectrum differs from the night, and the spectrum at day is much noisy than at night. So this gives an indication of the effect of the sun on the observation, because its interferes with the signal of Cas- A. Then we found that the peak is between the ranges of frequencies (1395 MHz – 1407 MHz), as in figure (12)

CONCLUSIONS

The high frequency radio telescope along with antenna system and setup over the building of the department of Astronomy and Space, College of Science in Baghdad University at latitude ($33^{\circ} 16' 28''$ N) and longitude ($44^{\circ} 22' 50''$ E), at time zone +3, which is operating at 21 cm Hydrogen Line (1.42 GHz). A radio telescope system is used for





Mohammed R. Hoobi and Kamal M. Abood

educational purposes. The system has a basic tracking capability, and is control by commanded through computer interface software. By rotating and pointing of dish antenna it observes the radio radiations from the astronomical objects. Limitation of this radio telescope is by using a single telescope which is cannot form image, for image formation it requires interferometer array or more than one radio telescope

REFERENCES

1. T. Hidayat, M. Irfan, B. Dermawan, A.B. Suksmono, P.Mahasena, D.Herdiwijaya, 2009. Development of Radio Astronomy at the Bosscha Observatory. Proceeding of the Conference of Indonesia Astronomy and Astrophysics PP: 29-31.
2. Janse V., Ajith D., 2015. The Development of Scada Control and Remote Access for the Indlebe Radio Telescope. Master thesis. Department of Electronic Engineering in the Faculty of Engineering and the Built Environment, Durban University of Technology PP: 2-10.
3. Petri Kirves, 2011. Radio Frequency interference in Radio Astronomy. Master Thesis. Department of Radio Science and Engineering, AALTO University School of Electrical Engineering PP: 6-8.
4. Antti Kuhlberg, 2014. Assembling and Exploring a Small Radio Telescope. Bachelor of Engineering Thesis. Helsinki Metropolia University of Applied Sciences PP: 3-4.
5. K. Rohlfs and T. L. Wilson, 2004. Tools of Radio Astronomy. 4th Edition, Springer, New York PP: 406-409.
6. Surajit Paul , Suklima Guha Niyogi, 2004. Setting up A 21-cm Hydrogen Line Radio Telescope and Receiver /Spectrometer. Master's Thesis. Department of Physics, University of Pune PP: 7.
7. <https://astronomylog.wordpress.com/radio-astronomy/milkyway-in-21cm/>
8. POAM ELECTRONICS. Radio Telescope Software RTC v_6.0.0, User Manual-2015

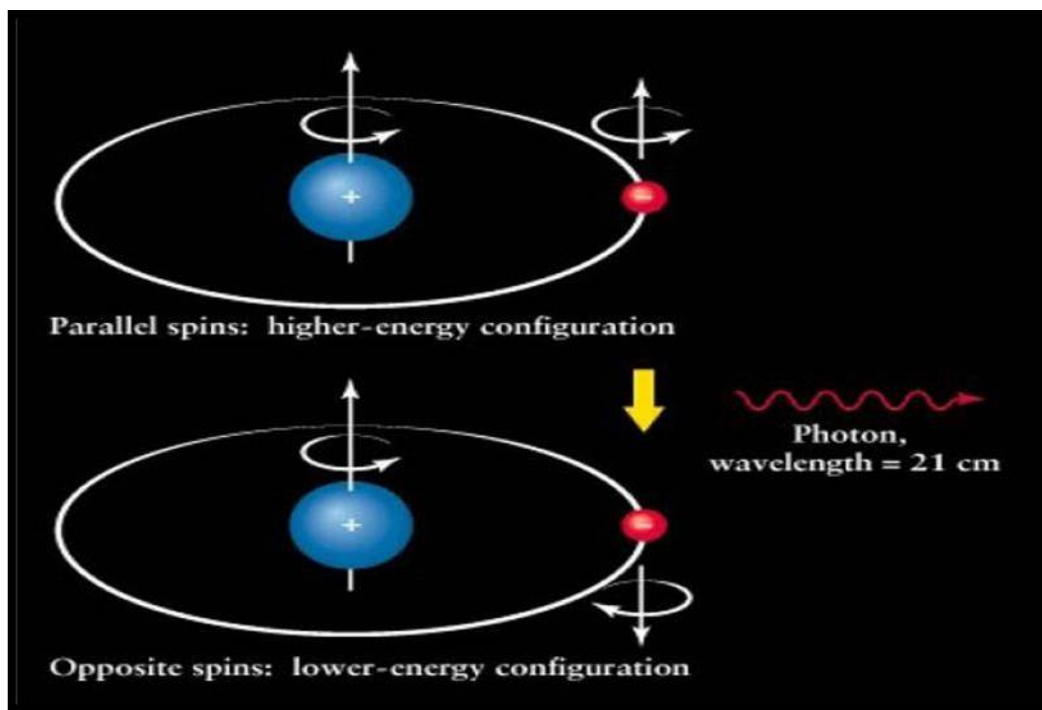


Figure 1. 21 cm transition of the hydrogen atom [7]





Mohammed R. Hoobi and Kamal M. Abood



Figure 2. The base of 3-meter parabolic antenna



Figure 3. The stand of the parabolic antenna



Figure 4. a- 3-Phase Az motor



b- 3-Phase EI motor





Mohammed R. Hoobi and Kamal M. Abood



Figure 5. The 3 meter parabolic antenna of the telescope



Figure 6. a- Feed horn b- Low noise amplifier LNA



Figure 7. Radio Telescope Receiver Unit (RTRS), Antenna Control Unit (ACU), Antenna Drive Unit (ADU)





Mohammed R. Hoobi and Kamal M. Abood



Figure 8. Software main window

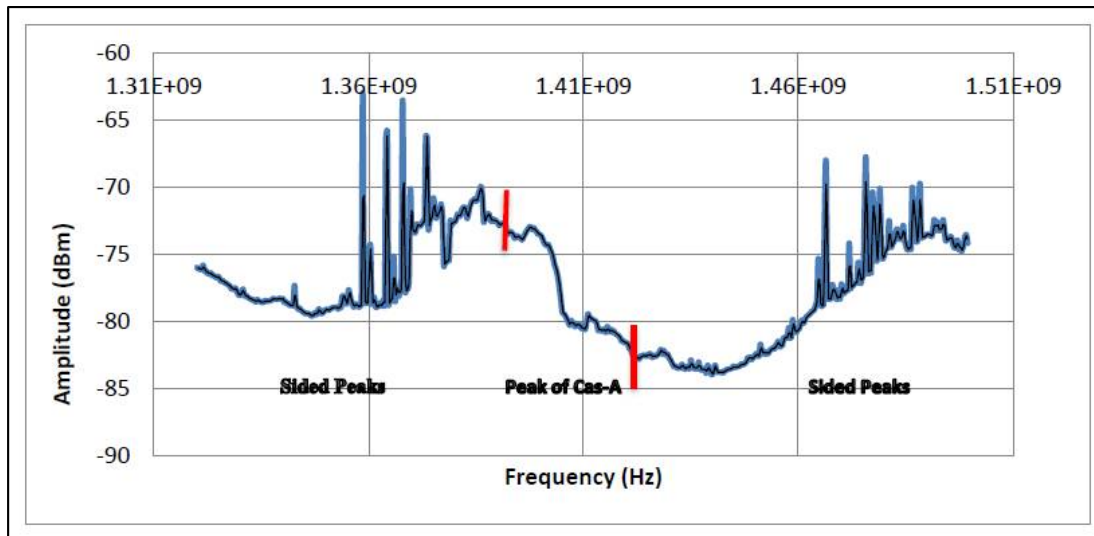


Figure 9. The spectrum of Cas-A at night after applying the noise elimination average technique





Mohammed R. Hoobi and Kamal M. Abood

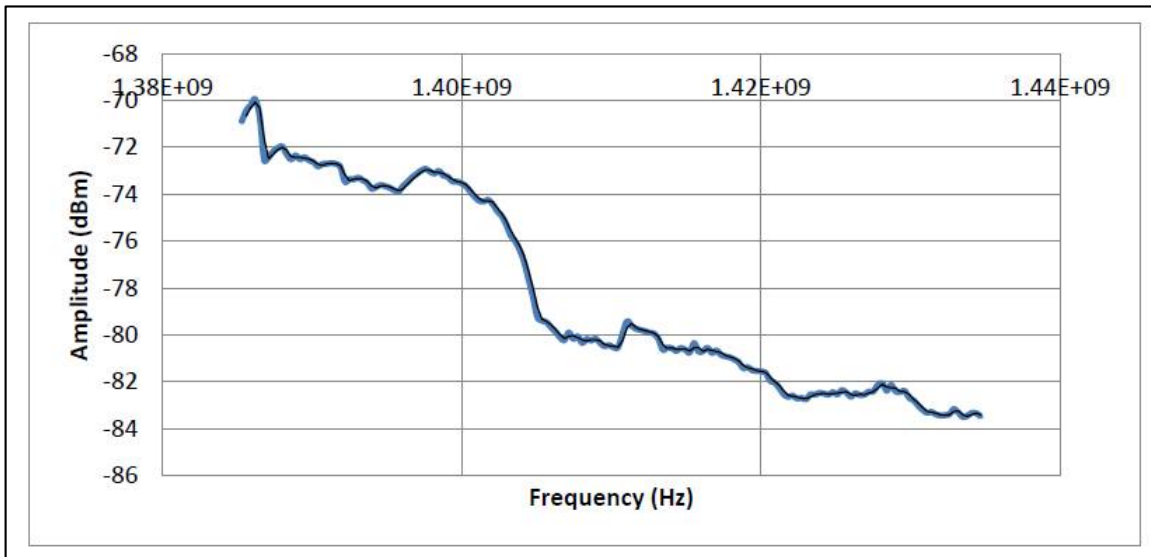


Figure 10. The frequency range of Cas-A spectrum at night

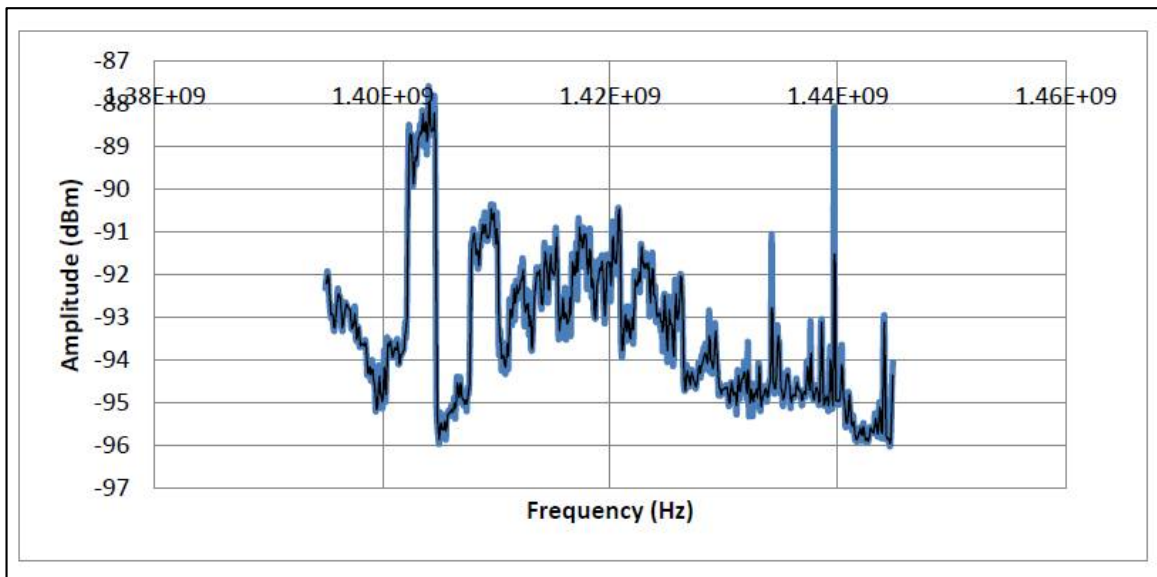


Figure 11. The spectrum of Cas-A at night after applying the noise elimination average technique





Mohammed R. Hoobi and Kamal M. Abood

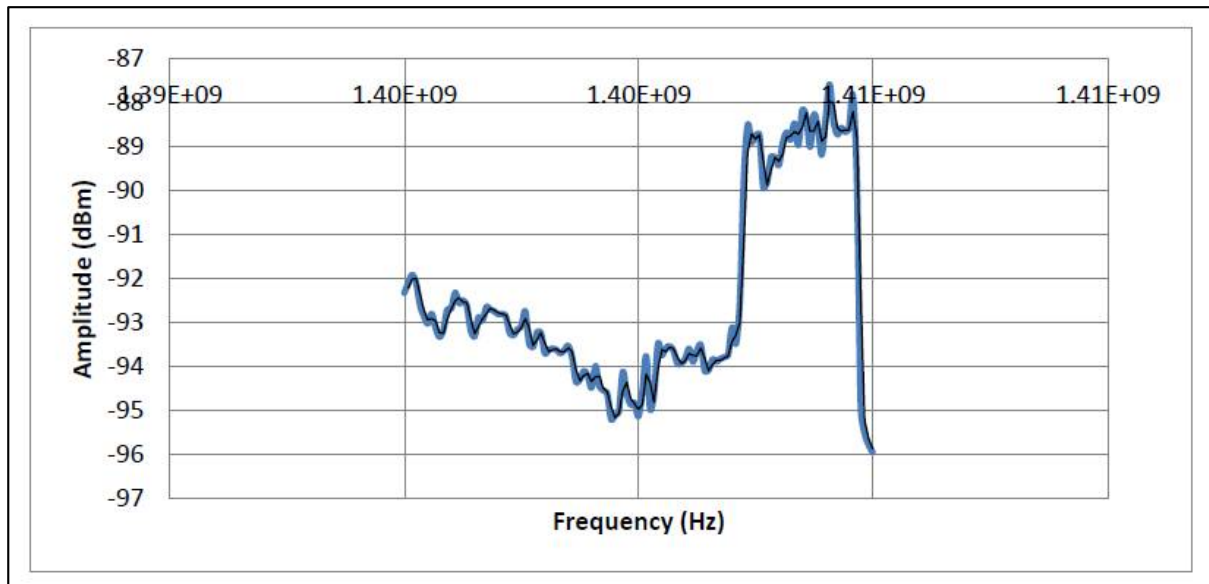


Figure 12. The frequency range of Cas-A at day





Spectral Investigations for the Explanation the Nature of Interstellar Matter

Haydar Al-baqir*

Department of Astronomy and Space, College of Science, University of Baghdad, Baghdad, Iraq.

Received: 18 Oct 2018

Revised: 21 Nov 2018

Accepted: 25 Dec 2018

*Address for Correspondence

Haydar Al-baqir

Department of Astronomy and Space,
College of Science,
University of Baghdad,
Baghdad, Iraq.
Email: hayderhussenx1@gmail.com



This is an Open Access Journal / article distributed under the terms of the **Creative Commons Attribution License** (CC BY-NC-ND 3.0) which permits unrestricted use, distribution, and reproduction in any medium, provided the original work is properly cited. All rights reserved.

ABSTRACT

The interstellar matter nature has been discussed by using an experimental model contain a mixture of organic and inorganic materials in the wavelength range (8.5-12.5) μm . The FTIR spectrometer device were used to obtain spectral results for prepared sample, these sample contain various ratio of organic and inorganic materials, the spectral results were compared with observation data of Trapezium nebula in the e wavelengths range (8.5-12.5) μm . The best molecule mixture model found to fit with observation data was contain: 40.1 % (Silicon dioxide (SiO_2)) + 12.2 % (Meteorite material) + 17.7 % (Glycine amino acid) + 30 % (Tyrosine amino acid), this are done using summation technique.

Keywords: interstellar matter, extinction, spectroscopy, organic, inorganic.

INTRODUCTION

Stars are born out of massive clouds of gas that float between the stars, known as the interstellar medium (ISM). These clouds can contain matter that coalesced directly out of the big bang, and/or they can contain matter that has been processed and expelled back into the ISM through stellar wind and explosive events like supernovae. This material, the remnants of old stars long gone and pure matter from the beginning of the universe is the mixture that forms stars [1]. The interstellar medium (ISM), material in the space between stars, consists of gas and dust that represent 20-30% of the mass of our Galaxy. The ISM consists of:

1. Gas (99%): about 90% hydrogen, 10% helium, and trace amounts of other elements, especially oxygen, carbon, and nitrogen.
2. Solid particles (1%): These are typically smaller than 1 μm (a millionth of a meter) and have a carbonaceous or silicate-based core surrounded by an icy mantle of (H_2O), carbon dioxide (CO_2), or ammonia (NH_3) [2].





Haydar Al-baqir

The extinction of starlight was happen due to the two processes absorbance and scattering of energy that caused by the material in the interstellar medium. The degree and wavelength dependence of the interstellar extinction curve is affected by the grain size, composition, and morphology of the dust between the source of the starlight and the observer [3]. The chemical composition of interstellar matter (IM) dust grains remains an unsolved problem in astrophysics. Astronomers tried through these investigations to identify the chemical composition of IM, through two principle methods, these are [4]:

1. Modeling of the broadband extinction and polarization curve using Mie theory.
2. Identification of discrete spectral features attributed to grain materials using infrared, visual and ultraviolet spectroscopic techniques.

The study of interstellar dust has led to several dust models that are compared with the average extinction curve obtained from observations of stars through interstellar clouds. The extinction curve is separates the light spectrum into three parts: Infrared –visible; Ultraviolet (hump signature at 2200 Å hump), and the far- Ultraviolet region [5].

Experimental work of parts

The following tools have been used:

- 1- Mortar. 2- Mini hand press. 3- Sensitive balances. 4- Oven. 5- Fourier transforms infrared spectroscopy (FTIR) device.

Material used

Inorganic and biological materials were used as follow:

- a- Inorganic materials: Silicon dioxide (SiO_2), Magnesium oxide (MgO), Iron (III) oxide or ferric oxide (Fe_2O_3), Carbon (C) and Diatom silica (98% pure silica).
- b- Biological materials Tyrosine amino acid, Glycine amino acid and Tryptophan amino acid

Sample preparation

Every material mixed with Potassium Bromide (KBr) at mass ratio 1/10 to make the samples. The samples were kept in the oven for 12 hours at a temperature of (80 K° - 90 K°) to get rid of the humidity and keep it dry. The samples were pressed by Mini hand press to produce the disks. Each disk examined by FTIR spectrophotometer device to measure the transmittance as a function of wave number of each material. Spectra were produced and further investigation will be applied on these spectra. Spectra sample is shown in figure-1.

Calculations and results

Experimental measurements produced transmittance (T) which is related to the optical depth (τ) by the equation [6]:

$$\tau = -\ln T \dots \dots \dots (1)$$

This equation used to calculate the optical depth for all experimental results.

The flux density of each sample can be calculated by using the following equation [32]:

$$F(\lambda) = \tau \cdot B(\lambda) \cdot A \dots \dots \dots (2) \text{Where:}$$

B (λ): Planck function which is given by:





Haydar Al-baqir

$$B(\lambda) = \frac{2hc^2}{\lambda^5} \times \frac{1}{e^{(hc/\lambda kT)} - 1} \dots\dots\dots (3)$$

Where:

h: Planck's constant = 6.63×10^{-27} erg. Sec

C: Light velocity = 3×10^{10} cm .Sec⁻¹

λ : Wavelength in μm

k: Boltzmann's constant = 1.38×10^{-16} erg.k⁻¹

T: Temperature in kelvin (K°)

A: Normalization constant

The flux density as a function of wavelength for all samples has been calculated using the above equations. The experimental data converted into flux density for samples as a function of wavelengths in micrometer in order to fit these data to get the models. Many tests were done including changing the materials in the mixture and its ratios for many times until achieved a best fit with observation data of Trapezium region. Table-1, is a list of best-fit data obtained matching the observation [7]. Figure-2 shows the comparison between the proposed model and observation data for Trapezium region. This fitting has been done applying the summation technique, obtaining accurate results for matching with observational data.

DISCUSSION AND CONCLUSION

The constituent of interstellar matter could be explained by organic or inorganic or both, by trying different mixture with the achievement of best fitting through wavelength range, depending on the size nature of interstellar dust grains. The model proposed in this work found to fit with observation for data Trapezium region in the wavelength ranges (8.5-12.5) μm , consisting of inorganic and organic materials (chosen from the multi choice trial material) with different percentages contribution used. This result indicated that the contribution of organic materials represents almost 47% of the sample prepared, the majority of it is the Tyrosine and Glycine amino-acids, while inorganic contributed only 52% of the sample. It can conclude therefore, that interstellar matter consists of amount of organic material that biological formation is fairly possible and inorganic material.

REFERENCES

1. Torres J. and Olenick R., (2004), "Data Analysis of the T Tauri Star V1331 Cyg", University of Dallas.
2. <http://www.ifa.hawaii.edu/UHNAI/article3.htm>.
3. Nuth J. A. III, Charnley S. B. and Johnson N. M., (2006), "Chemical Processes in the Interstellar Medium: Source of the Gas and Dust in the Primitive Solar Nebula", Meteorites and the Early Solar System II, University of Arizona Press, Tucson, 943, pp.147-167.
4. Whittet D. C. B., (1981), "The Gas-To-Dust Ratio In The Rho Ophiuchi Cloud", Monthly Notices of the Royal Astronomical Society, Vol. 196, pp. 469-472.
5. Zagury F., (2002), "The Incompatibilities between the Standard Theory of Interstellar Extinction and Observations", New Astronomy, Vol. 7, Issue 4, pp. 185-189.
6. Hoyle F. and Wickramasinghe N. C., (1996), "Biofluorescence and the Extended Red Emission in Astrophysical Sources", Astrophysics and Space Science, Volume 235, Issue 2, pp.343-347.
7. Layth M Karim, Nadhem H Hyder, Haydar R Al-Baqir, 2014, Molecules mixture model to explain the nature of interstellar matter, Iraqi Journal of Science, Vol.55, Issue: 1 Pages: 251-257.





Haydar Al-baqir

Table -1 Flux density values as function of wavelength for proposed model

Wavelength(μm)	Flux density ($\text{w}/\text{cm}^2 / \text{s}$)	Wavelength(μm)	Flux density ($\text{w}/\text{cm}^2 / \text{s}$)
8.60	4.71E-16	10.11	5.76E-16
8.69	4.87E-16	10.22	5.77E-16
8.84	5.08E-16	10.31	5.55E-16
8.97	5.24E-16	10.45	5.35E-16
9.12	5.34E-16	10.54	5.14E-16
9.32	5.40E-16	10.69	4.92E-16
9.45	5.56E-16	10.80	4.69E-16
9.60	5.64E-16	10.95	4.44E-16
9.82	5.69E-16	11.06	4.21E-16
10.00	5.74E-16	11.28	3.97E-16

Table -2: best fit model of inorganic and organic material.

inorganic material	%	organic material	%
Silicon dioxide (SiO_2)	40.1 %	(Glycine amino acid)	17.7 %
(Meteorite material)	12.2 %	(Tyrosine amino acid)	30 %

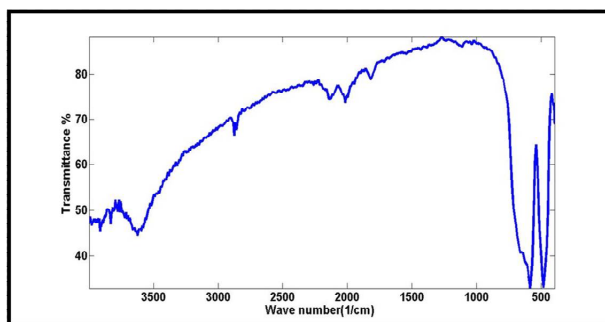


Figure -1: The transmittance (T) produced as a function of wave number in (1/cm) for one of prepared sample (Magnetite (Fe_3O_4))

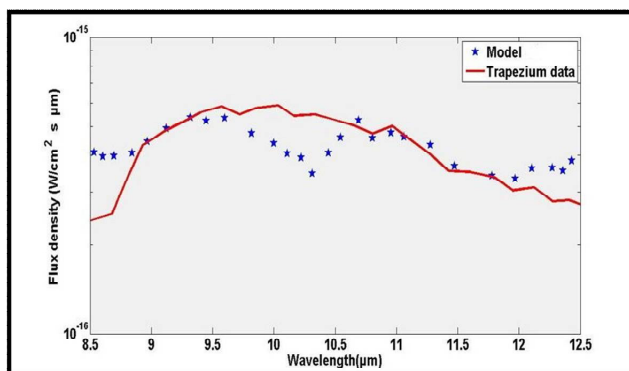


Figure -2 The flux density as a function of wavelength of the proposed model consist of 40.1 % (Silicon dioxide (SiO_2)) + 12.2 % (Meteorite material) + 17.7 % (Glycine amino acid) +30 % (Tyrosine amino acid), this are done using summation technique, Compared with observational data for trapezium region





Utilizing Air-Gap of the Mach-Zehnder Interferometer as Acetone Vapor Sensor

Dhuha Nihad Issa* and Hanan J. Taher

Institute of Laser for Postgraduate Studies, University of Baghdad, Baghdad, Iraq.

Received: 21 Oct 2018

Revised: 25 Nov 2018

Accepted: 27 Dec 2018

*Address for Correspondence

Dhuha Nihad Issa

Institute of Laser for Postgraduate Studies,

University of Baghdad,

Baghdad, Iraq.

Email:duha93nihad@gmail.com



This is an Open Access Journal / article distributed under the terms of the **Creative Commons Attribution License** (CC BY-NC-ND 3.0) which permits unrestricted use, distribution, and reproduction in any medium, provided the original work is properly cited. All rights reserved.

ABSTRACT

The proposed of this study is to demonstrate a simple high sensitivity vapor sensor for acetone (CH_3COOH). A free space gap is employed in two arms of a Mach-Zehnder interferometer (MZI) to serve as the sensing mechanism by adding acetone volume (0.2, 0.4, 0.6, 0.8, and 1) ml and to set the phase reference with a physical spacing of (0.5, 1, 1.5, and 2) mm. The propagation constant of transmitted light in the MZI's gap changes due to the small variation that will further shift the optical phase of the signal. Experimental results indicate that has highest sensitivity of acetone is about 0.0285 nm/ml for spacing 0.5 mm.

KeywordsMach-Zehnder interferometer, acetone vapor sensor, highsensitivity, wavelength shift.

INTRODUCTION

Environmental sensor has recent global research the optical fiber sensors are being employed for various sensing applications, e.g. optical fiber sensors are used for detecting the presence of air pollutants in the atmosphere [1, 2, 3], as well as being employed in the biomedical field [4, 5]. Since1980, a lot of research in optical fibers has been devoted to sensing, and then found applications in chemicalfield [6]. Chemical sensing technology has become important in a wide variety of areas, including industrial plants, research labs, the home, and various military applications [7, 8]. A chemical transducer and an optical fiber are the two components that constitute an optical fiber chemical sensor. The optical fiber is the medium which propagates the light from the source to the chemical transducer and guides the light again from the transducer to the photo detector. A chemical parameter is then measured in the form of light modified by the transducer [9]. A chemical sensor can be defined as a portable miniaturized analytical device which can deliver real-time on-line information on the presence of specific compounds or ions in complex samples [10]. In this work, a kind of Mach-Zehnder interferometer of acetone vapor sensor is fabricated based on air gap using optical fiber coupler (3 dB). The system is designed for 1550 nm wavelength regime, as this is a common wavelength with





Dhuha Nihad Issa and Hanan J. Taher

easily available and low cost components. The optical transmission of the proposed sensor is observed and then measured the sensitivity of acetone for different volumes and different spacing.

EXPERIMENTAL SETUP

Figure 1 displays the set-up of proposed system utilizing light source which is a diode laser with wavelength of 1550 nm, two optical coupler (3 dB) types of single mode fiber, two chambers are a Parallel Rectangle-shape sealed chambers, fabricated from Polyvinyl chloride (PVC) plastic, and finally optical spectrum analyzer (OSA). The MZI is fabricated using 3dB couplers, with the common port of one 3 dB coupler connected to the diode laser and the common port of the other 3 dB coupler joined to the OSA (YOKOKAWA, Ando AQ6370). In this paper, a created MZI with different distance of air gap (0.5, 1, 1.5, and 2) mm that under controlled conditions, the length of both arms are the same. Acetone liquid volumes (0.2, 0.4, 0.6, 0.8, and 1) ml is injected in sensing chamber while the reference arm is contained air only. The sensor of the two MZI arms causes the phase shift when change the length of spacing of air gap for arms and injected the acetone volumes in the sensing arm therefore the variation in the refractive index inside the chemical chamber causes a phase disparity in the MZI, due to the dissimilar phase velocities. Since the phase velocities and the phase deference are wavelength dependent, the propagating wavelength along the two different arms of the MZI creates a superposition pattern. The separation in between two peaks in a two-mode interferometer is defined as:-

$$\Delta\lambda = \lambda^2 / L \Delta n_e \quad (1)$$

where λ represents the wavelength, L is the MZI length and Δn_e is the effective difference in the refractive index between the two MZI arms. The changes in the RI in the MZI's sensing arm can now be defined as:-

$$\Delta\phi = \Delta\beta \cdot L = K \Delta n_e \quad (2)$$

where $\Delta\beta$ is the difference between the travelling signal's initial and instant propagation constant, which is taken before as well as after the change in the RI occurs respectively.

RESULTS AND DISCUSSION

Fig. 2 shows the relationship between the wavelength and power of the transmission spectrum which is measured by OSA for different air-gap distances of MZI. The black color line was refer to air in air-gap region and the red, blue, pink, green, and indigo color lines were refer to liquid volume (0.2, 0.4, 0.6, 0.8, and 1) ml in air-gap region respectively. The transmission spectrum displacement was increased when acetone liquid volumes increased. The wavelength shift increased toward the blue region, because the refractive index of acetone was 1.35 while the refractive index of air was 1. The refractive index is inversely proportion with the wavelength as shown equation 1. Therefore acetone liquid with higher refractive index will show the wavelength shift in the blue region. The sensitivity of acetone was calculated by the experimental measured of the wavelength shifting response to the acetone liquid volumes as shown in the figure 3. It observed that air-gap distance at 0.5 mm show the higher sensitivity (0.0285 nm/ml) compare with air-gap distances at different acetone liquid volumes. The relationship between the wavelength shift and acetone volume was linear when the liquid volume increase the sensitivity will be increase too. To calculate the changes in effective refractive index, propagation constant, and the phase shift can be done by using equations 1 and 2. It was indicated in the table 1

The numerical results of effective refractive index change of acetone was show the inverse proportion with wavelength shift, the wavelength shift increased with decreased the effective refractive index change when the air-gap distances were changed. The effective change in refractive index (Δn_e) was due to the alteration in the





Dhuha Nihad Issa and Hanan J. Taher

propagation constant (β) of the transmitted light in the MZI's gap. The relationship between the propagation constant with the effective refractive index was the linear. The instant propagation constant increases as the ambient RI increase. The refractive index variation produces linear change in the phase shift as equation 2. As illustrated in fig.4 for acetone. The black, red, blue, and pink lines were referred to the air-gap distance at (0.5, 1, 1.5, and 2) mm respectively.

CONCLUSION

In this work, a simple, novel, and high sensitivity single mode MZI acetone vapor sensor is proposed. The experimental results of acetone vapor show the blue shift of transmission spectrum with increasing for each distance of air gap. The value of shift is increasing with increased of acetone volumes. Improved the sensitivity could be achieved in distance 0.5 mm is 0.0285 nm/ml.

REFERENCES

- [1] Wolfbeis, O.S. "Fiber-Optic Chemical Sensors"; CRC Press: Boca Raton, FL, USA, 1991; Volume 1–2.
- [2] Wolfbeis, O.S.; Posch, H.E. "Fiber optic fluorescing sensor for ammonia". Anal. Chim. Acta 1986,11, 185–321.
- [3] Rowe-Taitt CA, Ligler FS. "Optical fiber Biosensors. Handbook of optical fiber sensing technology" Edited by J. M. Lopez-Higuera, John Wiley & Sons Ltd 2001:687-700
- [4] Tubb, A.J.C.; Payne, F.P.; Millington, R.B.; Lowe, C.R. "Single-Mode Optical Fiber Surface Plasma Wave Chemical Sensor". Sens. Actuators B Chem. 1997, 41, 71–79.
- [5] Rhines, T.D.; Arnold, M.A. "Fiber-Optic Biosensor for Urea Based on Sensing of Ammonia Gas". Anal. Chim. Acta 1989, 227, 387–396.
- [6] Wolfbeis. "Optical fiber chemical sensors and biosensors". CRC Press, Boca Raton, Florida: 1991, 1992: Vol1 &2.
- [7] D. Kohl, "Function and applications of gas sensors", J. Phys. D. Appl. Phys. 34 (2001) 125–149.
- [8] X. Liu, S. Cheng, H. Liu, S. Hu, D. Zhang, H. Ning, "A survey on gas sensing technology", Sensors (Switzerland). 12 (2012) 9635–9665.
- [9] B.H. Timmer, K.M.v. Delft, R.P. Otjes, W. Olthuis, A.v.d. Berg, " A miniaturized measurement system for Ammonia in air", Anal. Chim. Acta 507 (1), 2004, 139–145.
- [10] D. Marcuse, "Theory of Dielectric Optical Waveguides", Academic Press, New York, 1974.

Table 1. The numerical calculation of acetone.

Air gap distance	Liquid volume (ml)	$\Delta\lambda$ (nm)	Δn_e	$\Delta\beta$ (nm ⁻¹) $\times 10^3$	$\Delta\phi^\circ \times 10^3$
0.5 mm	0.2	0.003	0.396	2.093	1.658
	0.4	0.009	0.132	0.697	0.184
	0.6	0.015	0.079	0.418	0.066
	0.8	0.02	0.0595	0.314	0.037
	1	0.026	0.045	0.241	0.021
1 mm	Liquid volume (ml)	$\Delta\lambda$ (nm)	Δn_e	$\Delta\beta$ (nm ⁻¹) $\times 10^3$	$\Delta\phi^\circ \times 10^3$
	0.2	0.007	0.169	0.897	0.303
	0.4	0.035	0.033	0.179	0.011
	0.6	0.0652	0.018	0.096	0.003
	0.8	0.102	0.011	0.061	0.0013
1	0.129	0.009	0.048	0.0008	
1.5 mm	Liquid volume (ml)	$\Delta\lambda$ (nm)	Δn_e	$\Delta\beta$ (nm ⁻¹) $\times 10^3$	$\Delta\phi^\circ \times 10^3$
	0.2	0.016	0.074	0.392	0.058
	0.4	0.0274	0.043	0.229	0.019





Dhuha Nihad Issa and Hanan J. Taher

	0.6	0.0350	0.033	0.179	0.011
	0.8	0.046	0.025	0.136	0.006
	1	0.055	0.021	0.114	0.004
2 mm	Liquid volume (ml)	$\Delta\lambda$ (nm)	Δn_e	$\Delta\beta$ (nm ⁻¹) $\times 10^3$	$\Delta\phi^\circ \times 10^3$
	0.2	0.0516	0.022	0.121	0.0053
	0.4	0.0601	0.019	0.104	0.003
	0.6	0.0726	0.016	0.086	0.0027
	0.8	0.0816	0.014	0.076	0.0021
	1	0.0911	0.012	0.068	0.0016

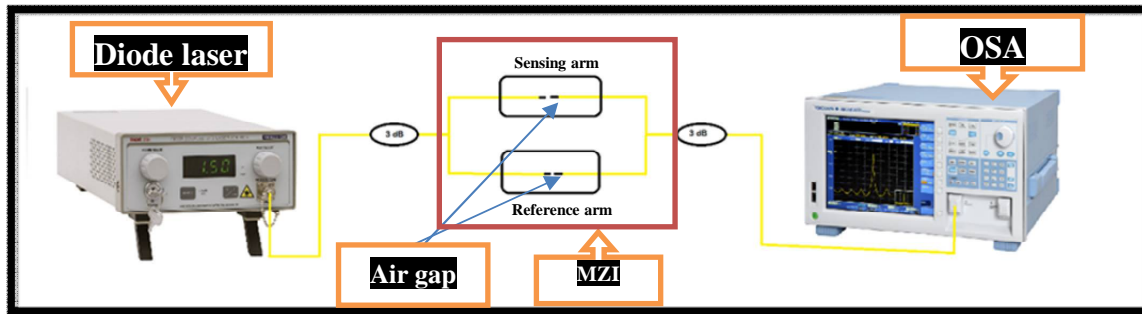


Figure 1. Experimental set-up for acetonevapor sensor using MZI

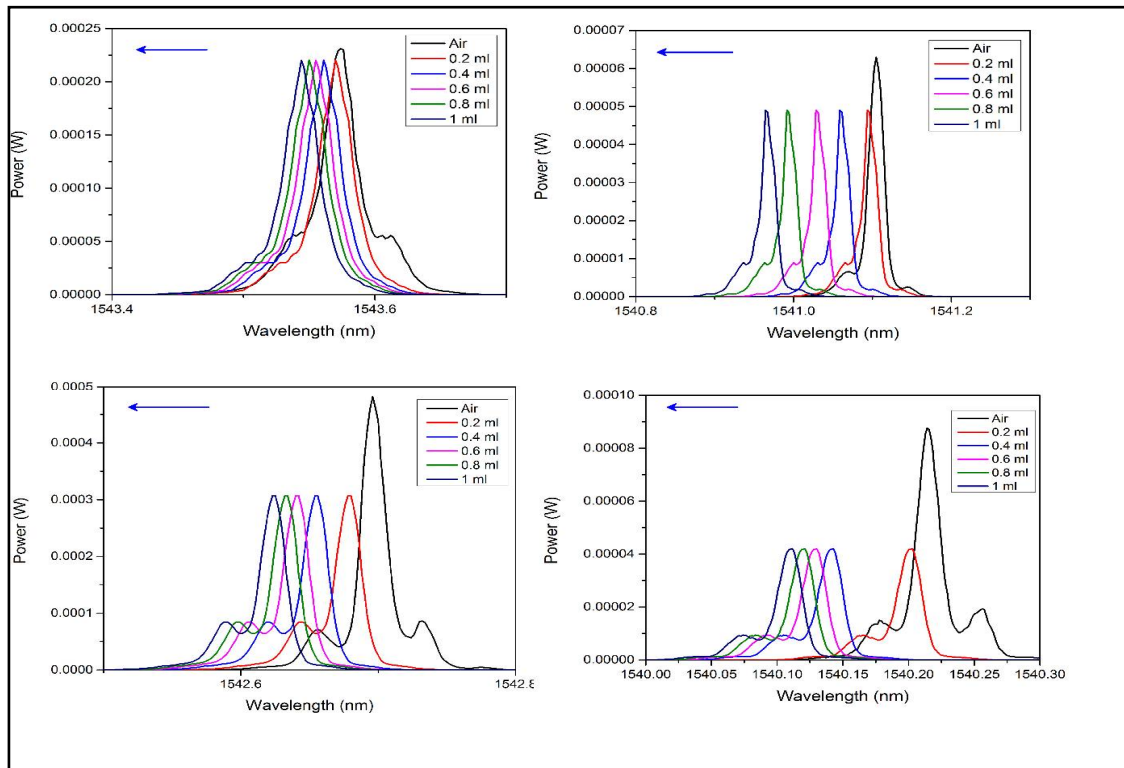


Figure 2. (a), (b), (c), (d) Transmission spectrum of air-gap at different (0.5, 1, 1.5, 2) respectively





Dhuha Nihad Issa and Hanan J. Taher

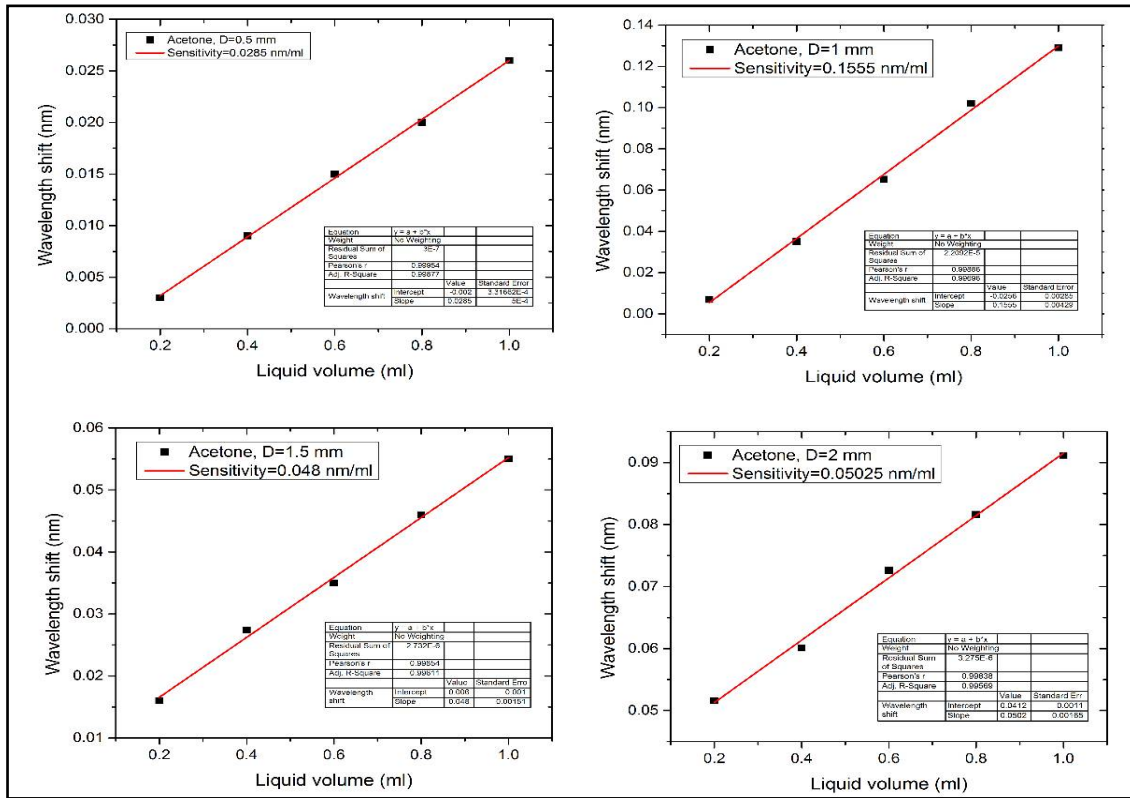
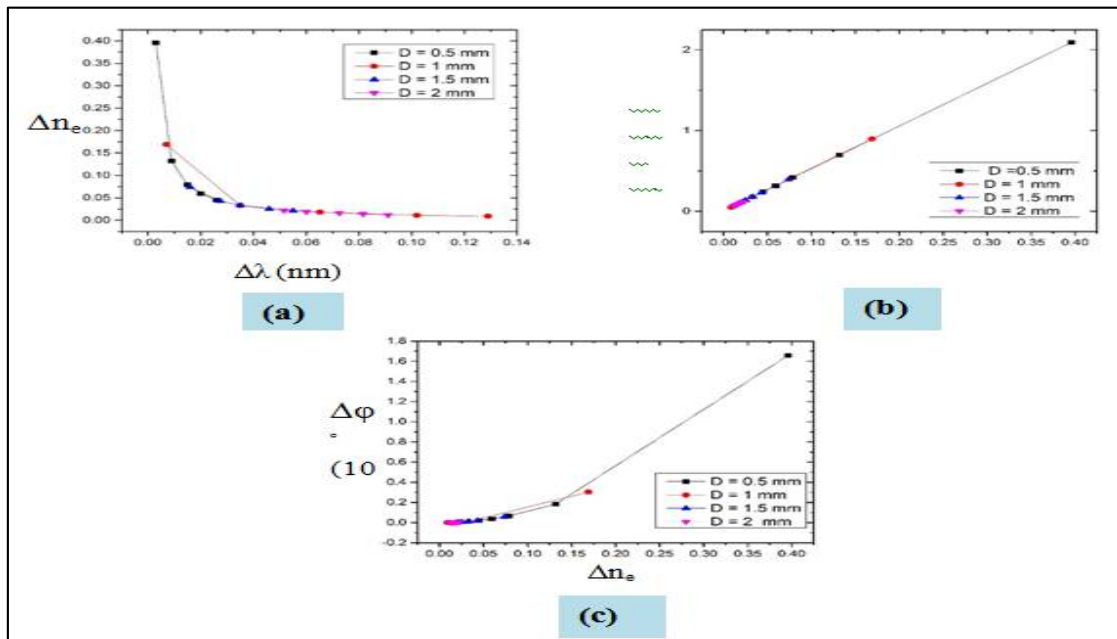


Figure 3. Sensitivity of acetone vapor sensor for different distances



Figure(4): The numerical calculations of acetone for relationship between (a) Wavelength shift with effective change in refractive index. (b) Effective change in refractive index with propagation constant change. (c) Effective change in refractive index with phase shift change.





Economic Efficiency of Dietary Supplementation of Rumen Bypass Fat in Crossbred Cows

Ani S. Das^{1*}, Metilda Joseph², Shibu Simon², Shyama K², Manoj M², and Muhammad Aslam M.K².

¹Associate Professor, Communication Centre, Kerala Agricultural University, Mannuthy, Thrissur, Kerala – 680651, India

²Department of Animal Reproduction, Gynaecology and Obstetrics, College of Veterinary and Animal Sciences, Mannuthy – 680651, Kerala, India.

Received: 20 Nov 2018

Revised: 24 Dec 2018

Accepted: 26 Jan 2019

*Address for Correspondence

Ani S. Das

Associate Professor,
Communication Centre,
Kerala Agricultural University,
Mannuthy, Thrissur,
Kerala – 680651, India
E-mail: anisdas@gmail.com



This is an Open Access Journal / article distributed under the terms of the **Creative Commons Attribution License** (CC BY-NC-ND 3.0) which permits unrestricted use, distribution, and reproduction in any medium, provided the original work is properly cited. All rights reserved.

ABSTRACT

Postpartum infertility due to negative energy balance is a major problem among the high producing cows of Kerala, incurring huge economic loss. The present study was aimed to evaluate the economic benefits of supplementation of bypass fat in high yielding crossbred cows with or without postpartum hormonal induction of estrus. The trial was conducted with four experimental groups of six cows each (GI – control, GII- 200 g bypass fat, GIII – 200g bypass fat daily + Ovsynch protocol, GIV – Ovsynch protocol alone). The techno-economic analysis showed that the expenditure incurred for bypass feeding was considerably less compared to the savings on increase in conception rate and decrease in calving to conception interval. Moreover, the cost of milk additionally produced added to the savings as it was observed that the day of achievement of peak yield in GII and GIII was significantly lower than that of group GI and GIV. The benefits in terms of higher pregnancy rate itself outweighed the cost of bypass feeding and it is more effective than hormonal treatment in terms of reproductive performance and productive performance. The results proved that bypass fat supplementation is a financially viable, eco-friendly and socially acceptable method for improving the production and reproduction parameters of the cows, thereby augmenting the farm income.

Keywords: Techno-economics, Bypass fat, Reproductive efficiency, Hormonal therapy.



**Ani S. Das et al.**

INTRODUCTION

The annual milk production of Kerala was recorded as 2.65 MMT (2015-16). The annual growth rate of milk production in Kerala was far below than the national average with less than 2.5 percent for the last few years and we contributed only 1.7 percent of the annual milk production of the country (Economic Review, 2016). Even though the average productivity of the crossbred cows in Kerala is high comparing to national average, the production in the state is lagging behind the actual domestic requirement. Hence the Govt. of Kerala is targeting to achieve self-sufficiency in milk production in the state in coming two years and implementing integrated schemes in the dairy sector to ensure fair returns to dairy farmers (The Hindu, 2017). To achieve this goal, improving the reproductive efficiency of available female cattle population is of utmost importance. To enhance the reproductive performance, optimizing the genotypes to production environment coupled with suitable management practices is necessary so that the inter-calving periods are shortened and the conception rates are high. The infertility will in turn force the farmers to distress sale of their crossbred high producing animals for meat purpose which lead to the loss of superior germplasm and reduction in the number of high yielding crossbred animals. So treating infertility and bringing more animals in to milking is of paramount importance (Draft Agricultural Policy, Kerala 2013).

Anoestrus and repeat breeding are two of the major reproductive problems affecting 30 to 40 per cent of total cattle and buffalo population of India. In Kerala, the incidence was reported to be even higher (61%) and this is mostly attributed to the negative energy balance in high producing cows during the postpartum period (Kutty and Ramachandran, 2003). It is reported that reproductive efficiency of dairy cows had improved by the supplementation of bypass fat, by increasing the conception rate and reducing the days open (Sklan et al., 1994, Naik et al., 2009). But these studies were preliminary in nature and did not provide any concrete confirmation about the mechanism of action and the exact benefit of its supplementation. Preliminary studies on effect of supplementation of bypass fat on production have been carried out in the Department of Animal Nutrition, College of Veterinary and Animal Sciences, Mannuthy and observed to be beneficial in improving the production and reproduction efficiency. But, any strategy will work in the field if it is economically viable and affordable to the dairy farmers. Thus, the economic efficiency of various strategies adopted for improving the reproductive efficiency of dairy cattle also needs to be studied in detail. Hence the present study analysed the techno-economic efficiency of bypass fat feeding in post-parted crossbred cows of Kerala.

MATERIALS AND METHODS

A total of 24 apparently healthy normally calved, crossbred cattle of similar age and parity with a body score of 3 to 3.5 out of 5 were selected from University Livestock Farm and Fodder Research Station, Mannuthy for the study. The animals were randomly allotted to four groups of six cows each. All the animals in these four groups were fed as per standard feeding practices based on ICAR recommendations. Animals in Group I was not given any supplementation and kept as control. The animals in Group II were fed with 200 g bypass fat per day (Calcium salt of long chain fatty acid, supplied by National Dairy Development Board) from 5 days after calving till 90th day along with compounded cattle feed, every morning. The animals in Group III were fed 200 g of bypass fat per day from 5th day of calving till 90th day along with compounded cattle feed every morning. In addition, they were subjected to Ovsynch protocol as described earlier (Hagen et al., 2015). Briefly, 10 µg of GnRH analogue (Buserelin acetate - Receptal, Intervet, India) were administered intramuscularly (i/m) on Day 45 postpartum followed by 500 µg Cloprostenol (Pragma, Neovet, India) i/m on day 52 postpartum. A second dose of GnRH analogue, 10 µg, i/m on Day 54 was also administered, followed by timed artificial insemination at 16 h after second dose of GnRH. Animals in Group IV were not supplemented with bypass fat. But they were subjected to Ovsynch protocol on Day 45 postpartum. All the animals in Groups I and II were inseminated during natural oestrus exhibited after Day 45 postpartum. Animals in Groups III and IV were subjected for timed AI and observed for induced oestrus.



**Ani S. Das et al.**

Data pertaining to cost of feeding, hormonal treatments, days open, total milk and production, were calculated and the techno economic impact of bypass fat supplementation by virtue of improvement on reproductive performance and date of attainment of peak yield were analysed. The economic advantages of different treatments were compared taking the non-fat fed, non-hormonal treated group (GI) as standard. For estimating different cost benefit factors, the following values were considered. Cost of bypass fat – Rs. 240 per Kg; Cost of 5 ml GnRH – Rs. 350; Cost of 2 ml PGF_{2α} – Rs. 160; Professional charges for one visit – Rs. 200; Cost of milk – Rs. 43 per Kg; Savings on conception – Rs. 5000 per animal if conceived within study period. (Kumaresan et al. 2013, Madkar et al.2018). The total lactation yield of the animals was predicted by using the regression formula by multiplying with a factor 215.5 (KVASU, 2015). The data recorded were analyzed statistically using statistical software SPSS (SPSS, Version 14, USA).

RESULTS AND DISCUSSION

The peak yield and total lactation milk yield estimated based on the regression formula developed by KVASU are presented in Table 1. The days of achieving peak yield of animals in GI, GII, GIII and GIV were 40.50 ± 3.60 , 18.17 ± 3.32 , 28.17 ± 5.02 and 32.17 ± 3.77 respectively. The total lactation milk yield estimated using the regression formula developed by KVASU indicated that bypass fat feeding was beneficial in terms of total milk production. The total cost incurred and the benefits of feeding bypass fat are summarized in Table 2. The relative benefit of fat feeding in GII, GIII, and GIV compared to GI were Rs. 15650.04, 19261.83 and 4449.9 respectively. The relative advantage per animal were 2608.34, 3210.31, and 741.65 in animals belonging to GII, GIII and GIV respectively, compared to the control group (GI). From the table, it can be seen that feeding bypass fat has a financial advantage over the other group. Same time it was also observed that feeding bypass fat alone is comparable to that combined with hormonal treatment in an economical point of view. On the other hand, the animals in group IV, which had undergone hormonal treatment alone, did not yield considerable economic benefit.

On analyzing the techno economics of bypass fat feeding, it can be seen that feeding bypass fat along with hormonal treatment has a financial advantage over the other groups. Same time it is also observed that feeding bypass fat alone is comparable to combination of bypass fat and hormonal treatment in an economical point of view. On the other hand, the animals in group IV, which had undergone hormonal treatment alone, did not yield considerable economic benefit. These results are in concomitant with earlier study reports of Yadav et al. (2015) and (Mane et al., 2017) who observed better economic benefits from feeding bypass fat to dairy animals. The results of the present study indicate that bypass fat feeding improves the productive and reproductive performance of postpartum dairy animals. It can be concluded that bypass fat feeding is an economical and environment-friendly recommendation for improving the reproductive efficiency of high producing crossbred cows.

CONCLUSIONS

It was observed that bypass fat feeding is financially viable, eco-friendly and socially acceptable alternative to hormonal therapy for improving the reproductive efficiency of crossbred cows.

REFERENCES

1. Draft Agricultural Policy, Kerala. 2013. Department of Agriculture, Govt. of Kerala.
2. Economic Review, 2016. Ministry of finance, Govt. of Kerala
3. Kutty, C. I. and Ramachandran, K. 2003. Bovine infertility, a field oriented categorisation based on investigation among crossbred cattle in a district of Kerala. *Indian Journal of Animal Sciences*, **73**:155-157.
4. KVASU, 2015. Package of Practices Recommendations, Kerala Veterinary and Animal Sciences University, Pookod, Wayanad, Kerala.





Ani S. Das et al.

5. Mane S.H., Mandakmale S.D., Nimbalkar C.A., Kankhare D.H. and Lokhande A.T. 2017. Economics of feeding protected protein and protected fat on crossbred cattle. *Indian Journal of Animal Research*, **51**(6): 1080-1085
6. Naik, P.K., Saijpaul, S., Sirohi, A.S. and Raquib, M. 2009. Lactation response of cross bred dairy cows fed indigenously prepared rumen protected fat - A field trial. *Indian J. Animal Sci.*, **79**: 1045-1049.
7. Sklan, D., Kaim, M., Moallam, U. and Folman, Y. 1994. Effect of dietary calcium soaps on milk yield, body weight, reproductive hormones, and fertility in first parity and older cows. *J. Dairy Sci.*, **77**:1652-1660.
8. The Hindu. 2017. 17% increase in milk production: Raju. *The Hindu News Paper*, Accessed on 30.06.2017 from <https://www.thehindu.com/todays-paper/tp-national/tp-kerala/17-increase-in-milk-production-raju/article19584887.ece>
9. Yadav, G., Roy, A. and Singh, M. 2015. Effect of Prilled Fat Supplementation on Milk Production Performance of Crossbred Cows. *Indian J. Anim. Nutr.*, **32**:133-138.

Table1. Milk production parameters of crossbred cows

S. No.	Group (n=6)	Day of achieving peak yield (Mean ± SE)	Peak yield obtained (Kg) (Mean ± SE)	Total Lactation Milk Yield* (Kg)
1	I	40.50 ± 3.60 ^a	14.08 ± 1.77	3034.24
2	II	18.17 ± 3.32 ^b	15.13 ± 1.34	3260.52
3	III	28.17 ± 5.02 ^{bc}	15.10 ± 1.28	3254.05
4	IV	32.17 ± 3.77 ^{ac}	14.68 ± 1.07	3163.54

Values bearing different superscripts differ significantly ($p < 0.05$); *Calculated based on the regression formula as per KVASU package of practices

Table2. The relative cost benefit analysis of feeding bypass fat in cows belonging to different groups

S. No.	Item	GI	GII	GIII	GIV
I	Relative cost incurred (GI as standard)				
a	Cost of bypass fat (85 days @ 200 g daily - Rs. 240 per Kg)	0	4080	4080	0
b	Cost of Hormones (GnRH and PGF2 α)	0	0	510	510
c	Professional charges (3 visits)	0	0	600	600
	Total relative cost	0	4080	5190	1110
II	Relative Savings (GI as standard)				
a	Savings on conception (In GI – 5000; GII- 15000; GIII- 20000; GIV – 5000)	0	10000	15000	0
b	Savings from extra milk yield (Groups without fat feeding were taken as standard and the extra yield (Kg) in GII – 226.28; GIII – 219.81; GIV – 129.3)	0	9730.04	9451.83	5559.9
	Total savings	0	19730.04	24451.83	5559.9
III	Relative benefit of fat feeding (II-I)	0	15650.04	19261.83	4449.9
IV	Relative benefit of fat feeding (Per Animal)	0	2608.34	3210.31	741.65





Deployment of OSPFv3 and IPv6 on Simulated and Geographically Separated Sites

Mohammed Aldagdoog*, Sadeq Hilal Alzaghir and Raheeq Abd Mohammed AIKhafaji

Information Technology Department, Directorate of Education in Babylon, Ministry of Education, Iraq.

Received: 24 Oct 2018

Revised: 26 Nov 2018

Accepted: 28 Dec 2018

*Address for Correspondence

Mohammed Aldagdoog

Information Technology Department,
Directorate of Education in Babylon,
Ministry of Education, Babil, Iraq.
Email:mo85th@gmail.com



This is an Open Access Journal / article distributed under the terms of the **Creative Commons Attribution License** (CC BY-NC-ND 3.0) which permits unrestricted use, distribution, and reproduction in any medium, provided the original work is properly cited. All rights reserved.

ABSTRACT

As IPv4 is running out, the need for changing to IP next generation, IPv6, is obvious because the number of people and devices that connect to networks increases every day. Not only does IPv6 give us enormous addresses (3.4×10^{38} = definitely enough), but there are many other features built into this version that make it well worth the cost, time, and effort required to migrate to it. However, the use of Classless Inter-Domain Routing (CIDR) and Network Address Translation (NAT) has helped to extend the shortage of addresses, but we will run out of them, and it is going to happen within a few years. This study aims to describe the benefits of applying IPv6 dynamic routing protocol in the campus of the university of Turkish aeronautical association. In this work, a simulated network represents the campus of the university by using Graphical Network Simulator (GNS3) to deploy OSPF on three geographically separated campuses armed with IPv6. Going deep inside some packets to analyze OSPF performance over the campus by using tool of network sniffing Wireshark.

Keywords: Internet Protocol version 6; Dynamic Routing Protocol OSPF; Graphical Network Simulator version 3; Wireshark.

INTRODUCTION

Undoubtedly, one of the elements of life nowadays is information technology. Computer technologies and architectures are used in all areas. PCs need to provide an infrastructure to ensure the communication with each other. The world is provided by infrastructure and companies that are providing this communication all over the Internet. Currently, the standard protocol used in the Internet communication is Internet Protocol Version 4 (IPv4). To be addressed with IPv4 by providing end-to-end communication between computers and similar devices, the work has continued with some improvements made in a good way as to be seamless. Internet technology on mobile



**Mohammed Aldagdoog et al.**

devices, security systems, remote access to work in the desired systems, and electronic devices at businesses or homes are not even used in small electronic appliances. In short, both commercial and social use the Internet very often, this need has led to further growth every day. The biggest problem in the process of technological development is the limit capacity of the IPv4 address that can be used for this system. 4,294,967,296 IPv4 addresses cannot be used efficiently due to the huge growth in number of devices that use the Internet these days [2].

Rapid depletion of IPv4 has led to the start using the mechanism of the NAT and CIDR. Network Address Translation allows multiple devices to share one public IP address [4]. Classless Inter-Domain routing eliminates the concept of class from the IP address [3]. Despite these improvements, the enormous increase in Internet usage, high mobility, multimedia, strong security, end-to-end access, etc. have been increasing the inability to meet the demand in a good way. For these reasons, new solutions were proposed by the Internet Engineering Task Force (IETF) and other relevant institutions and organizations who are responsible for the Internet protocols. The most important study is Internet Protocol Version 6 (IPv6). The using of the Internet, mobile phone development, smart home applications, new technologies and Voice over Internet Protocol (VoIP) applications, such as anytime access, are growing faster than expected, This growing led to lay the foundation of IPv6 in the early 1990s [5]. A new development of IP protocol working group was established in the early 1990s by the IETF, after a series of studies, in 1995 December, the first IPv6 Requests for Comments (RFC) 1883 (and others) was officially launched to announce IPv6. The main purpose is to provide mobility between the Internet Protocol networks. IPv6 has more capabilities than IPv4. The most basic feature that distinguishes IPv6 from IPv4 is extended with a 128-bit address space. This theoretical number of the expanded addressable nodes will provide 2128 (340, 282, 366, 920, 938, 463, 463, 374, 607, 431,768,211,456) IP addresses [6]. This tremendous number of IPv6's address space solves the problem of IPv4's shortage and the quick growth of different applications on the Internet.

With the currently available IPv4, the Internet address of each device in the management of IP mechanisms needs to be confirmed manually. In IPv6, this administrative burden is reduced by automatically addressing mechanism. In addition, IPv6 offers stability in commercial transactions such as scalability, availability, end-to-end access, quality of service (QoS), VoIP and IP-based TV (IPTV). IPv6 is coming with a feature of having more flexible structure than IPv4. To compare between the two protocols, there are some changes with the structure of the headers of both v6 and v4, the major one is adding the extension to the header of IPv6. From security wise, built in IPsec is developed in IPv6, whereas in IPv4 security faces difficulty due to NAT usage [1]. This work is intended to apply IPv6 to the University of Turkish aeronautical association with OSPFv3 and link the tree campuses of that university in simulated environment by using Graphical Network Simulator GNS3 since it is too difficult to work on real world campus environment.

LITERATURE REVIEW

There are many works that tried to deploy IPv6 to a campus network in Turkey and we will demonstrate three of them as follows: In the M.S. thesis [7], the main objective was to pass the necessary examinations of Muğla University campus network, apply IPv6 on a server and reduce to a minimum the possible problems of other hardware and software by preparing the ground to smooth transition. There is a transition from IPv4 to IPv6 by assigning IPv6 to each department based on the IPv4 subnet as a first step. Full IPv6 support process of dual stack is to Install IPv6 service. Then make a separate VLAN with an IPv6 address can also be provided to operate only with IPv6. The author of [8] has developed (by using OPNET) a simulated environment network in order to measure the throughput of the routing performance analysis in current, transition period and finally IPv6 native networks. His major focuses include:

1. Significant differences, proposed superiorities and advantages of IPv6 to IPv4.
2. Measurement-based comparison, especially transaction mechanism, of IPv6 – IPv4 routing and IPv6 gains on a simulated test-bed environment (OPNET).



**Mohammed Aldagdoog et al.**

Another study about applying IPv6 on a campus environment has been done in Ege University. After a close examination of the studies, the basic information about the transition to IPv6 and the transition mechanisms are given and some of the studies made about the transition to IPv6 in the world and also in Turkey are presented. In this context, the level of the current operating status for IPv6 in Ege University is also presented. In addition to the studies made, some steps to facilitate the transition to IPv6 and to optimize performance of IPv6 networks are also given in this thesis scope [9]. The difference between the three works mentioned above and our work is that we built our three campuses initially with IPv6 without any transition or adaptation to the existing IPv6 in addition to applying one of dynamic routing protocols, which is OSPF to share the routing information between all campuses of the university of Turkish aeronautical associations.

METHODOLOGY

Our network environment is virtualized by using GNS3 (Graphical Network Simulator) that is an open source emulation tool in which we can create our campus network. GNS3 allows us to add different kinds of network devices, connect them all together and configure the devices with Command Line Interface (CLI) that is very similar to Cisco IOS or other network vendors. In addition, GNS3 gives us the opportunity to connect our simulated topology to the Internet directly because it supports all features that exist on Cisco devices [10]. The University of Turkish Aeronautical Association has three geographically separated campuses with the one in Ankara as the main one, the second one is in İzmir and the third campus is in Eskişehir. The first campus we will cover is the Ankara one, since it is our campus and we will consider them as the same when it comes design and layout. We will try to apply Cisco campus hierarchy on the current campus with IPv6 as the layer 3 addressing carrier. To be able to grasp the final structure of the network, we need to divide it into two components the physical layout of the building and the virtual network and the mapping between them. The campus has many buildings but not all of them will need a wired network (as the cafeterias, the restaurant and the gym), that will leave us with five main buildings to be included in the master design: Engineering building: it consists of two floors where the first floor has two labs with 40 computers each, and a couple of administration offices so in total this floor needs around 86 ports which is 4 layer two switches to cover (as each switch has 24 ports). The second floor is exactly the same story with four switches also. English language building: it has two floors as the first one has classrooms with almost 90 ports to cover them, which make it needs 4 switches. The second floor has faculty offices and needs around 160 port to cover which means seven switches to cover.

Administration building: it has two floors as well, the first one of them has beside a lab two classrooms and offices with around 84 port which means four switches to cover. The second floor has only offices with four switches to cover. Aeronautics and Astronautics engineering building: it has three floors that share the same layout with around 80 ports to cover each of them, which means four switches in each floor. Library: it is a one floor building with one switch to cover. In total, we will have 40 switches that will make the backbone of our access layer and each of them will have two type of connection: the first connection is the Ethernet connection through STP (Shielded Twisted Pair) cables as CAT6 and this connection will cover the side between the access switch and the end user. The second connection will be a single mode fiber connection, since it is the most popular form of fiber connection to connect the access layer switch from all over the campus with the core switch. We will end up having the topology elucidated in Figure 1 to represent the campus of Ankara. Starting from the top down, the router R1 is to connect our campus to the ISP as well as to İzmir and Eskişehir campuses respectively. We configured it as “Router on a Stick” that enables a trunk between the router and the core switch in order to send all VLAN traffic by dividing one physical interface on the router into sub interfaces as the same number as the VLANs. This interface must be fast Ethernet or faster to be able to carry a lot of traffic comes in and out. The core switch is connected to the router from one side, and to the access switches from the other. Every access switch represents one floor per building.





Mohammed Aldagdoog et al.

Virtual Network

The virtual structure of the network will consist of a group of networks or VLANs that will span through the geographical boundaries, the reason of dividing them into different VLANs instead of having only one VLAN is to have more control over our network and it will be easier to manage, manipulate and traffic engineering. The reason behind VLANs is to logically segment our network into small groups of users. The list of the VLANs in our network for Ankara campus will be as shown in table 1. Wireless VLAN: this VLAN will be dedicated for wireless coverage and will cover all buildings that need a wireless connection. The range of the of IPv6 that will be used for this VLAN will be 2001:0000:0000:0002::/64 Administration VLAN: will be used by the administration officers and the faculty wherever it needed. The range of the of IPv6 that will be used for this VLAN will be 2001:0000:0000:0003::/64

Labs VLAN: this VLAN will be used by the students in the Labs that exist in three buildings. The range of the of IPv6 that will be used for this VLAN will be 2001:0000:0000:0004::/64 Management VLAN: this VLAN will be used to manage all the devices in the network including the switches and routers. The range of the of IPv6 that will be used for this VLAN will be 2001:0000:0000:0005::/64 Flight Simulator VLAN: this VLAN will be dedicated to the flight simulator since it is a highly sensitive device and need to a high level of security. The range of the of IPv6 that will be used for this VLAN will be 2001:0000:0000:0006::/64 After creating the VLANs on the core switch, we can see them by the command show vlan as illustrated in figure 2. VLANs on İzmir and Eskişehir campuses are created in the same ways of Ankara campus. These VLANs need to be created and deployed on all the 40 switches of the campus, which makes it a very hard and inefficient process to deploy or update. Therefore, to solve this problem, we will use VTP (Virtual Trunking Protocol) [11] that allows us to choose one of our devices as a server. We create all VLANs on the server then this switch will pass these VLANs through to all other switches that will be deployed as clients. This means that the client switches cannot create VLANs by themselves and they only receive their database copy from the server.

We will need a Trunk port on each switch to share VLANs of our network between all devices, otherwise without Trunk ports we would get separate VLANs that could not communicate because Trunk sends all VLANs traffic across the network. The range of the IPv6 addresses that connect the core with the access layer switches is addressed in a way that all starts with 2001:0:0:xy::z where x always has a value of 1 referring to the core. y is the access switch number starting from 1 which is the first access switch in the network (ENG-GF) and so on until we reach the last switch which is Library-SW. z value is 1 on the core side and 2 on the access switch. For example the IPv6 of the core switch in Ankara's campus that is directly connected to the ENG-GF is 2001:0:0:11::1 (where x is 1 representing the core, y is representing the very first switch that is ENG-GF, z is 1 because it is on the core side), while the IPv6 of ENG-GF in the same campus is 2001:0:0:11::2. The above addressing is for Ankara campus only while İzmir campus range is 2001:0:1:xy::z and the values of x, y and z are the same. The third and last campus is Eskişehir with the IPv6 range of 2001:0:2:xy::z.

After all the campus connections, VLANs and addressing are done and the connectivity inside the campus been tested. The next step will be adding the connectivity among the campuses where in our case both İzmir and Eskişehir campuses will have a connection to the router of the Ankara campus so this router will work as the core of whole university with all of its campuses. The addressing that will be used to connect the cores will be as following: 2001:0:12:12::x/64 between Ankara router (router 1) and İzmir router (router 2) where x will have the value of 1 on Ankara side and the value of 2 on the İzmir side. 2001:0:13:13::x/64 is the IPv6 address that is used between Ankara router and Eskişehir router (router 3) where x will have the value of 1 on Ankara side and the value of 2 on the Eskişehir side. After having all the intra-campus and inter-campus networks, testing within campus network connectivity and testing the direct connectivity between the cores it is the time to deploy the OSPFv3 as our routing protocol, after having the OSPFv3 deployed, we should have a full connectivity all over the three campuses and among them.



**Mohammed Aldagdoog et al.**

With OSPF, we divided our workspace into 3 areas as OSPF uses the concept of areas. Area 0 (the backbone area; figure 3) contains all devices of Ankara campus in addition to the links on İzmir and Eskişehir router that connect them to Ankara router. Area 1 (figure 4) has all the devices of İzmir campus except the link between İzmir router and Ankara router. And area 2 (figure 5) that all Eskişehir campus devices within, note that one link of the main router of area 2 is out that area: After deploying OSPF, all devices of the three campuses share their information between each other in a way that make all devices can reach and have connection to all. We will use some show commands to reveal facts about OSPF besides WireShark, which allows us to capture, sniff, and analyze traffic packets between the connected devices. We made İzmir router connected to different areas, which are area 0, and area1 of OSPF and RIP from another side in order to see almost all the LSA types such as in figure 6. In this bidirectional redistribution, İzmir router (R2) will take the routes from RIP and redistribute them into OSPF to see external LSA. We will take the routes from OSPF and redistribute them into RIP in a way RIP routes can see the entire topology and we can test the connectivity. From İzmir router's view, it can run two routing protocols as clarified in figure 7. We can see that İzmir router can run two routing protocols, OSPF redistributing RIP and vice versa.

Now we have full connectivity across the entire network as Eskişehir router sees it (figure 8). OE2 is external route from outside OSPF 2001:0:3:1::/64 injected it to the whole network where 2001:0:3:1::/64 is the link of İzmir router with RIP, figure 9 shows the subnet between all the routers in the topology. OI means inter routes coming from other areas (area 0 and area 1, since Eskişehir router is within area 2). O is intra area routes coming from devices that are inside the area the router belongs to (directly connected).

Assigning Ports to VLAN

We are going to connect Windows 7 host to the Management VLAN at Ankara campus at the Administration building ground floor in order to manage our entire network (figure 10). This PC will have IPv6 from the range of that VLAN 2001:0:0:5::/64, the Windows 7 PC will have 2001:0:0:5::10/64 IPv6. From another side of the campus we will use VPCS (virtual PC simulator) on GNS3 and then test the connectivity between these two PCs by using the command ping and running WireShark to capture the packet. VPCS is a lightweight application that we cannot assign an IP address to. It can simulate computers from a single command line interface. However, it will not be on a specific VLAN because it gets IPv6 by using autoconfiguration feature of IPv6 from an access port on an access switch (figure 11). It gets this IPv6 from the range of its default gateway 2001:0:1:1::/64 and by using the method of EUI (Extended Unique Identifier) as shown in figure 12. Although we assigned IPv6 address to the Windows 7 PC within the range of VALN 5 but it did not use it to ping the PC at İzmir side of the topology. It used the EUI IPv6 it made up for itself. In addition, we can see the successful of that ping request using WireShark capture packet containing the source and the destination addresses such as in figure 13. By now, all the devices can reach each other thanks to deploying OSPF on our campus and we can assign ports on access switches to supply our end users with the service. Either we can assign these ports to VLANs or to be access ports that serve the Internet to every one connects his /her PC to these access ports.

RESULTS

Checking Routing Tables

Before we started to describe the statistical results of IPv6 and OSPFv3, we checked the routing table of Ankara router before we booting up all other devices. It has 14 entries that came from the six VLANs we created on the sub interfaces to make this router as Router on a Stick. In addition to "made up" link local address for each of our 6 VLANs, that's 12 entries. The other remaining two are multicast and link-local respectively as illustrated in figure 14.





Mohammed Aldagdoog et al.

After almost 50 seconds of booting all other devices up, the routing table of Ankara router became with 31 entries, the same old 14, 12 from inter OSPF which are advertisements of VLSNs from İzmir (6 VLANs) and Eskişehir (6 VLANs too), 1 external OSPF which is RIP area connected to İzmir router and 2 connections to İzmir and Eskişehir routers with their made up link local (figure 15).

Packet Capturing

We captured these packets at the same time we booted all the devices up. This capture was on the link between Ankara and İzmir routers by using the protocol analyzer Wireshark with High-Level Data Link Control network protocol created by Cisco Systems, Inc. for exactly 300.006708 seconds. Within that period of time we gained 24050 packets with different sizes, 34010080 bytes in total as in figure 16.

Average of packets per second is 80.165

Average of packet size is 1414

Average of bytes per second is 113364.399

Average of Mega bit per second is 0.907

Protocol Tree

In this capture, the connection used Cisco DHLC protocol to define each frame between the devices. The smallest percentage of HDLC went to Cisco Discovery Protocol (CDP) 0.05 % with 13 packets. The second smallest portion was to Cisco Serial Line Address Resolution Protocol (SLARP) .025 % with 60 packets. Moreover, the biggest piece of DHLC went to IPv6 99.70 % with 23977 packets. IPv6 packets is divided between Internet Control Message Protocol (ICMPv6) 7.68 % 1846 packets, Open Shortest Path First (OSPFv3) 1.21 % with 291 packets and the Data 90.81 % with 21840 packets as figure 17 shows.

Conversation between Ankara and İzmir Routers

It is the traffic between the two devices with a lot of information on tabs but just the IPv6 tab is activated because we used it to send 14 traffics from Ankara router to İzmir router and vice versa (figure 18). We will take a look at two packets example. Address A: FE80::C802:EFF:FEF4 is the Extended Unique Identifier (EUI) of İzmir router. FE80::C802:EFF:FEF4 sent 89 packets (12084 bytes) to all routers that are running OSPF on the same link by using FF02::5 as address B. we can see also Rel Start with the value of 18.808146 seconds "Rel Start is the time in seconds between the start of the capture (packet #1) and the start of the conversation" while the Duration was 280.0413 seconds "Duration" is the time in seconds between the first and last packet of the conversation". We have another FF02::5 connection from address A with the EUI of FE80::C801:7FF:FE8C which is Ankara router to all OSPF routers FF02::5. This connection was 202 packets (28640 bytes) with Rel Start of 22.133652 seconds and Duration of 277.1956 seconds. Ankara router sent 826.56 bits per second during this connection. Therefore, we have 291 packets of FF02::5 type with 40724 bytes in total.

Packet Lengths

During the connection between Ankara and İzmir routers, the two devices sent various lengths of packets to each other (figure 19). We will discuss the largest ones sent, that are between 1280 – 2559 bytes. These were the maximum number of packets transmitted in that capture connection with the Count of 21840 packets and percentage 90.81 %. The maximum and minimum lengths were equal with 1500 bytes each to give us an average of 1500 bytes too. Burst Rate is the maximum number of packets sent per interval of time and Burst Start is the time when the maximum number of packets sent occurred.





Mohammed Aldagdoog et al.

I/O Graph

This graph has two axis:

X Axis: consists of the following:

Tick interval: 1 second interval in our case.

Pixels per tick: we used 2 pixels per tick interval

Y Axis

Unit: In this capture, the unit for the y direction was Packets/Tick.

As we can see the graph below, from time interval 0 – 96 there were small packets sending bidirectionally represented by ICMP Neighbor Solicitation and Advertisement, CDP packets and OSPF Hello Message and LSAs to complete the routing tables for all devices. Then Ankara router started to send traffic to İzmir router until second 134 with almost over 150 packets per second. However, the maximum throughput was between the period of time from 223.9 to 257 when the two devices started to send packets back and forth to each other simultaneously with more than 300 packets per second as elucidated in figure 20.

CONCLUSION

In this research we tried to build the campus of the University of Turkish Aeronautical Association by following typical Cisco hierarchy, deploy IPv6 as layer 3 addressing protocol, and use dynamic routing protocol for the inter and intra-campus connections, OSPFv3 as our routing protocol to apply it on the three geographically separated campuses on a simulated environment. The significance we have acquired from applying dynamic routing protocol (OSPFv3 is our case study) is represented by getting rid of old method of routing (static routing) and automatically updating of routing table entries for the changes in network topology. The routing tables at our campus are maintained and built automatically through ongoing communication. Devices of our topology have become dynamic that use routing OSPF to facilitate the ongoing communication and dynamic updating of routing tables. At our university, we use private addressing because we have a shortage of internet addresses and we do not want to pay to assign public address to all of our computers. However, in IPv6 we have enough IP addresses to give every device an IP address in the campus for years and years to come. We do not have shortage anymore, therefore, this whole concept of private IP address is gone away. This has been done by using one kind of addressing which is called GLOBAL SCOPE or what people are calling the internet 2. Global scopes are addresses that are alive on the internet. Now, the good news is that our university is now able to have internet addressing for every device that is available within the campus.

REFERENCES

1. Kozierok, Charles M. The TCP/IP guide: a comprehensive, illustrated Internet protocols reference. No Starch Press, 2005, pp. 1616.
2. Huston, Geoff. Considerations on the IPv6 Host Density Metric. No. RFC 4692. 2006, pp. 17.
3. Silva, Pedro Miguel, Jaime Dias, and Manuel Ricardo. CIDRarchy: CIDR-based ns-3 routing protocol for large scale network simulation. 2015.
4. Chen, Yaw-Chung, and Wen-Kang Jia. Challenge and Solutions of NAT Traversal for Ubiquitous and Pervasive Applications on the Internet. Journal of Systems and Software, 82 (10), 2009, pp. 1620–1626.
5. Feldner, Benjamin, and Paula Herber. A Qualitative Evaluation of IPv6 for the Industrial Internet of Things. Procedia Computer Science 134, 2018, pp. 377-384.
6. Turiel, Avi. IPv6: new technology, new threats. Network security 2011 (8), 2011, pp. 13-15.





Mohammed Aldagdoog et al.

7. Ahmet Demiröz, Adaptation of IPv6 to a campus network: Mugla University case, Master Thesis. 2011, pp. 103.
8. DursunTuranÜstündağ, January, Comparative Routing Performance Analysis of IPv4 and IPv6, Master Thesis. 2009, pp. 122
9. SuleemanKhateeb, Developing Computer’s Networks by Moving from IPv4 to IPv6 and Works Done to Improve Performance in IPv6 and IPv4 Networks, Master Thesis. 2013, pp. 153.
10. Welsh, Chris. GNS3 network simulation guide. Packt Publ., 2013, pp. 155.
11. Al-Zaghir, Sadeq, Sibel T. Ozyer, and Mohammed Al-Dagdoog. "Recruitment of security features for securing VTP3 domain in campus environment." 2017 International Conference on Computer Science and Engineering (UBMK). IEEE, 2017.

Table 1 The VLANs at Ankara campus

VLAN Name	VLAN No.	IPv6 Address Range
Wireless VLAN	2	2001:0000:0000:0002::/64
Administration VLAN	3	2001:0000:0000:0003::/64
Labs VLAN	4	2001:0000:0000:0004::/64
Management VLAN	5	2001:0000:0000:0005::/64
Simulator VLAN	6	2001:0000:0000:0006::/64

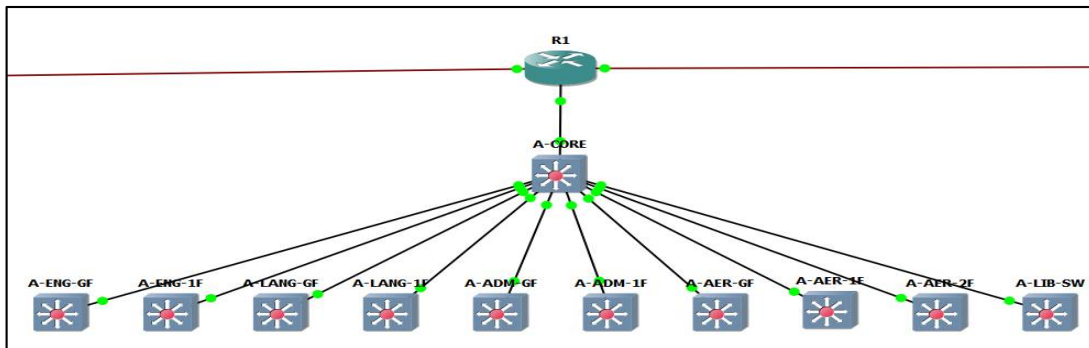


Figure 1. Ankara campus topology

```

A-CORE#show vlan
-----
VLAN Name         Status      Ports
-----
1    default         active     Et0/1, Et0/2, Et0/3, Et1/0
                Et1/1
2    WIRELESS        active
3    ADMINISTRATION  active
4    LAB'S           active
5    MANAGEMENT      active
6    SIMULATOR       active
1002 fddi-default    act/unsup
1003 trcrf-default  act/unsup
1004 fddinet-default act/unsup
1005 trbrf-default  act/unsup

VLAN Type  SAID      MTU   Parent  RingNo BridgeNo  Stp  BrdgMode  Trans1  Trans2
-----
1    enet   100001    1500   -       -       -       -       0         0
2    enet   100002    1500   -       -       -       -       0         0
3    enet   100003    1500   -       -       -       -       0         0
4    enet   100004    1500   -       -       -       -       0         0
5    enet   100005    1500   -       -       -       -       0         0
6    enet   100006    1500   -       -       -       -       0         0

VLAN Type  SAID      MTU   Parent  RingNo BridgeNo  Stp  BrdgMode  Trans1  Trans2
-----
1002 fddi   101002    1500   1005   3276   -       -       srb       0         0
1003 trcrf  101003    4472   -       -       -       -       -       0         0
1004 fddnet 101004    1500   -       -       -       -       -       0         0
1005 trbrf  101005    4472   -       -       15      -       ibm       0         0

VLAN AREHops STEHops Backup CRF
-----
1003 7           7         off

Primary Secondary Type          Ports
-----
    
```

Figure 2. Show VLAN command on the core switch





Mohammed Aldagdoog et al.

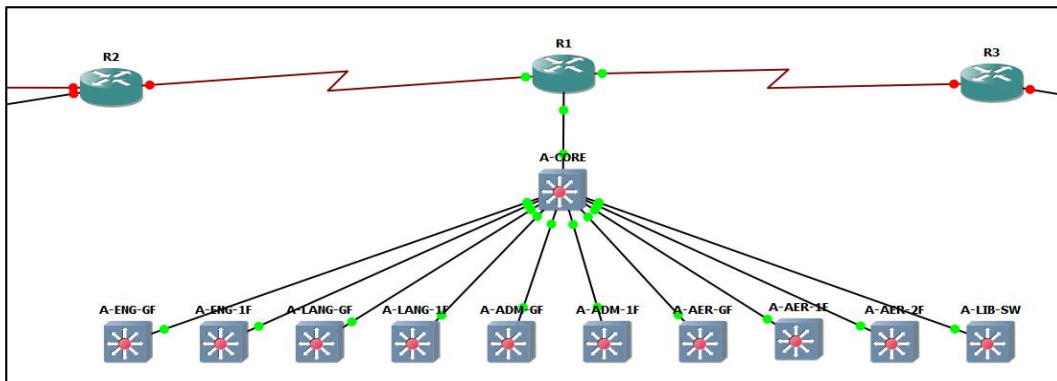


Figure 3 Area 0

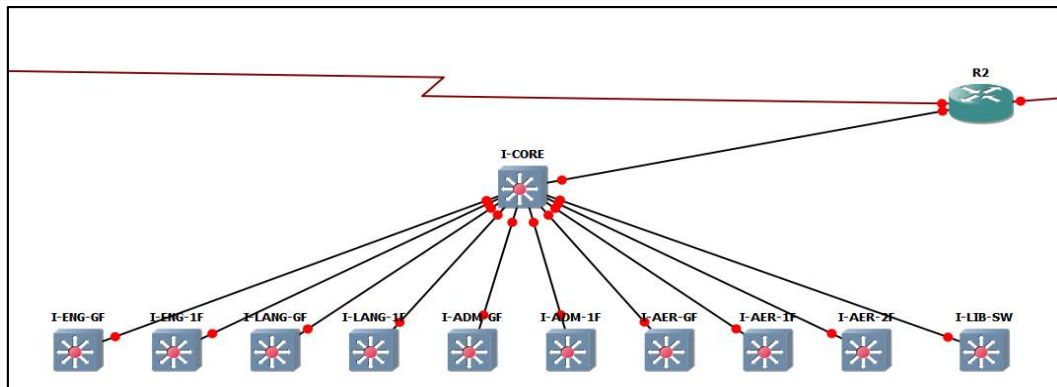


Figure 4 Area 1

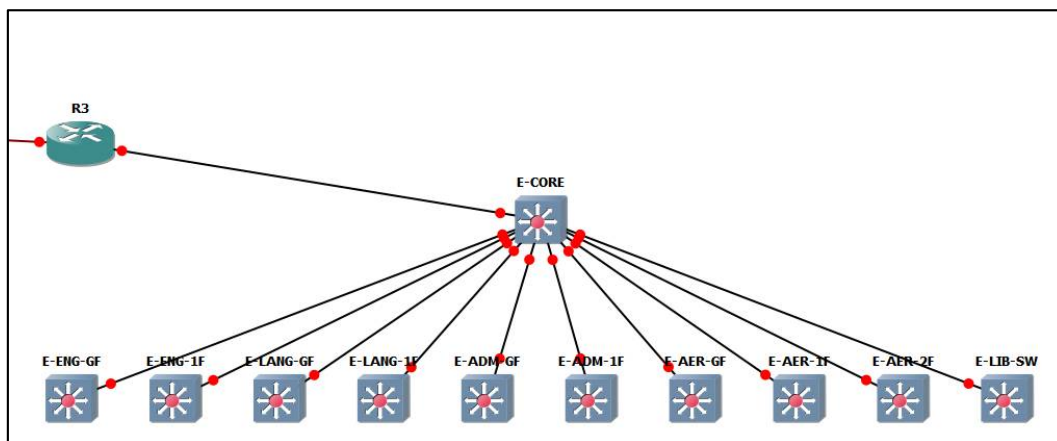


Figure 5 Area 2





Mohammed Aldagdoog et al.

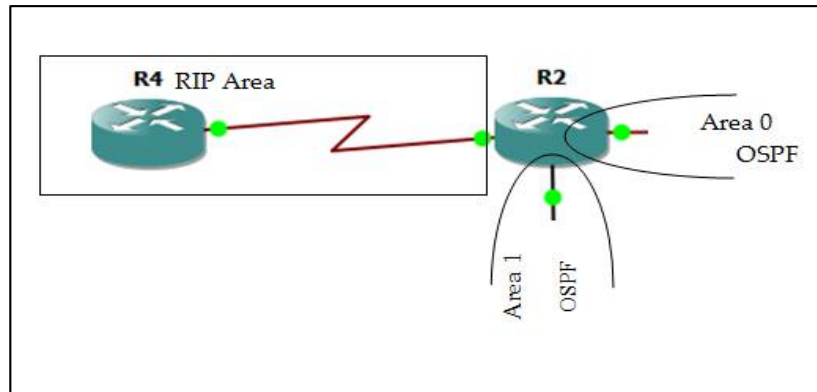


Figure 6 İzmir router links

```
I-ROUTER#show ipv6 protocols
IPv6 Routing Protocol is "connected"
IPv6 Routing Protocol is "static"
IPv6 Routing Protocol is "ospf 1"
  Interfaces (Area 0):
    Serial1/0
  Interfaces (Area 1):
    FastEthernet0/0.6
    FastEthernet0/0.5
    FastEthernet0/0.4
    FastEthernet0/0.3
    FastEthernet0/0.2
    FastEthernet0/0
  Redistribution:
    Redistributing protocol rip mo with metric 88 include-connected
IPv6 Routing Protocol is "rip mo"
  Interfaces:
    Serial1/1
  Redistribution:
    Redistributing protocol ospf 1 with metric 5 include-connected
```

Figure 7show IPv6 protocols command on İzmir router

```
E-ROUTER#show ipv6 route ospf
IPv6 Routing Table - 30 entries
Codes: C - Connected, L - Local, S - Static, R - RIP, B - BGP
        U - Per-user Static route
        I1 - ISIS L1, I2 - ISIS L2, IA - ISIS interarea, IS - ISIS summary
        O - OSPF intra, OI - OSPF inter, OE1 - OSPF ext 1, OE2 - OSPF ext 2
        ON1 - OSPF NSSA ext 1, ON2 - OSPF NSSA ext 2
O  2001:0:0:1::/64 [110/65]
   via FE80::C801:7FF:FE8C:0, Serial1/1
O  2001:0:0:2::/64 [110/65]
   via FE80::C801:7FF:FE8C:0, Serial1/1
O  2001:0:0:3::/64 [110/65]
   via FE80::C801:7FF:FE8C:0, Serial1/1
O  2001:0:0:4::/64 [110/65]
   via FE80::C801:7FF:FE8C:0, Serial1/1
O  2001:0:0:5::/64 [110/65]
   via FE80::C801:7FF:FE8C:0, Serial1/1
O  2001:0:0:6::/64 [110/65]
   via FE80::C801:7FF:FE8C:0, Serial1/1
OI 2001:0:1:1::/64 [110/129]
   via FE80::C801:7FF:FE8C:0, Serial1/1
OI 2001:0:1:2::/64 [110/129]
   via FE80::C801:7FF:FE8C:0, Serial1/1
OI 2001:0:1:3::/64 [110/129]
   via FE80::C801:7FF:FE8C:0, Serial1/1
OI 2001:0:1:4::/64 [110/129]
   via FE80::C801:7FF:FE8C:0, Serial1/1
OI 2001:0:1:5::/64 [110/129]
   via FE80::C801:7FF:FE8C:0, Serial1/1
OI 2001:0:1:6::/64 [110/129]
   via FE80::C801:7FF:FE8C:0, Serial1/1
OE2 2001:0:3:1::/64 [110/88]
   via FE80::C801:7FF:FE8C:0, Serial1/1
O  2001:0:12:12::/64 [110/128]
   via FE80::C801:7FF:FE8C:0, Serial1/1
```

Figure 8 show IPv6 route OSPF command on Eskişehir router (R3)





Mohammed Aldagdoog et al.

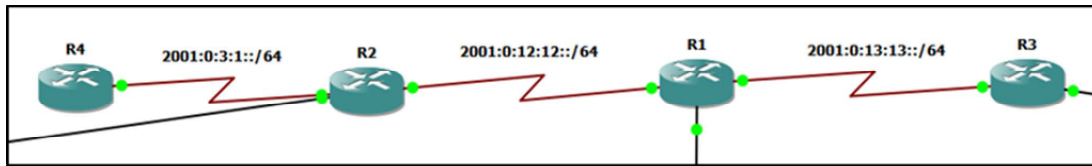


Figure 9 the subnet between routers

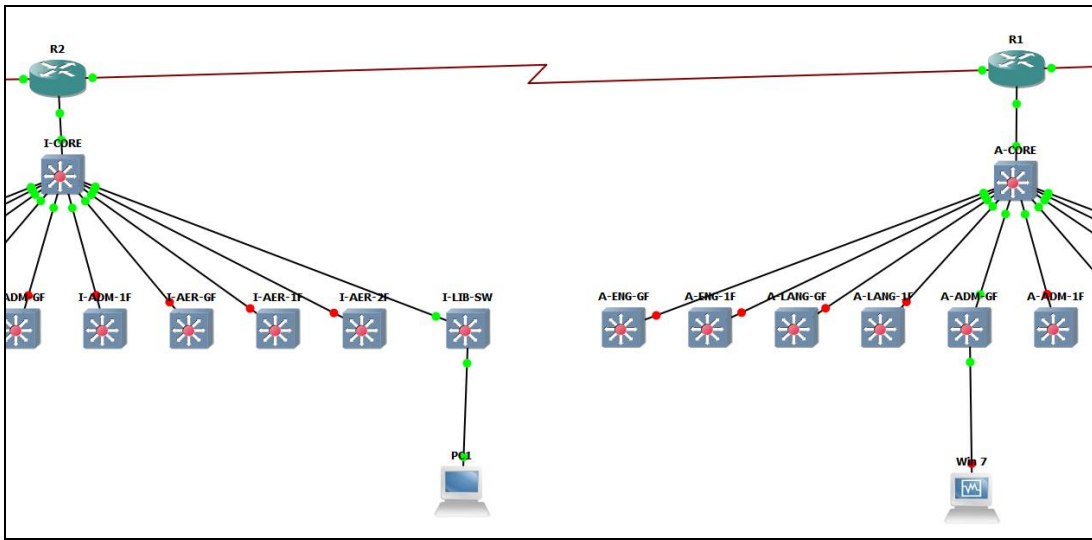


Figure 10 Adding PCs to the topology

```
PC1> ip auto
GLOBAL SCOPE      : 2001:0:1:1:2050:79ff:fe66:6801/64
ROUTER LINK-LAYER : ca:02:0e:f4:00:00
```

Figure 11 IPv6 Autoconfiguration

```
C:\Users\Moha>ipconfig
Windows IP Configuration

Ethernet adapter Local Area Connection:

Connection-specific DNS Suffix . . . :
IPv6 Address. . . . . : 2001:0:0:5::10
IPv6 Address. . . . . : 2001::5:8469:ef8d:212:2459
Temporary IPv6 Address. . . . . : 2001::5:dd98:761e:f966:25d6
Link-local IPv6 Address . . . . . : fe80::8469:ef8d:212:2459%11
Autoconfiguration IPv4 Address. . . : 169.254.36.89
Subnet Mask . . . . . : 255.255.0.0
Default Gateway . . . . . : fe80::a8bb:ccff:fe80:600%11
                          fe80::a8bb:ccff:fe80:100%11
                          fe80::c801:7ff:fe8c:0%11
```

Figure 12 IPv6 on Windows 7 host





Mohammed Aldagdoog et al.

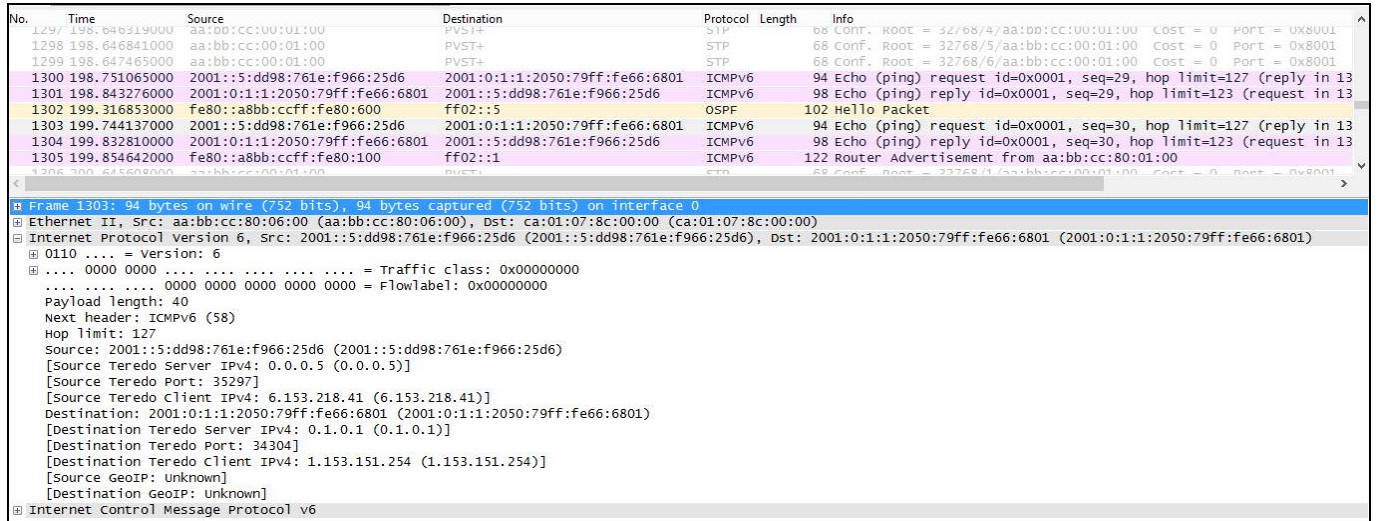


Figure 13 ping request on WireShark

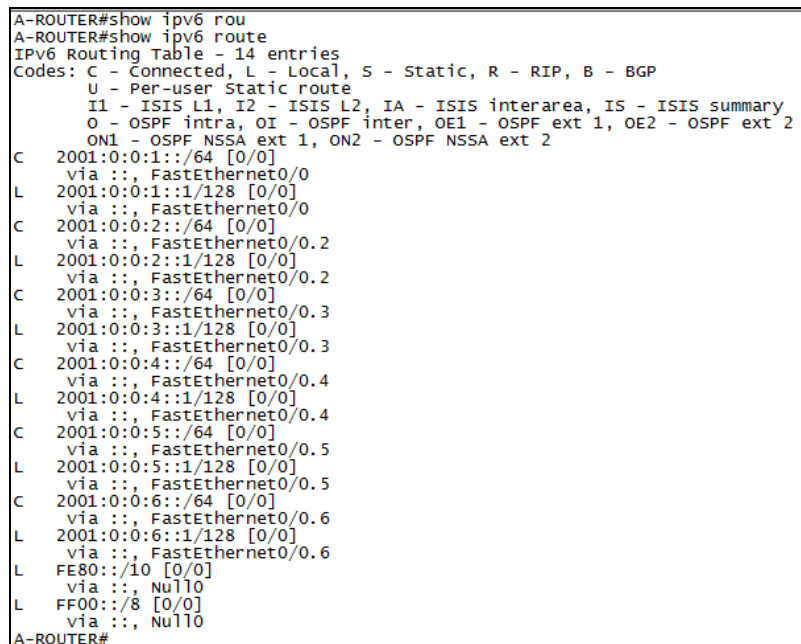


Figure 14 Routing table of Ankara router before OSPF





Mohammed Aldagdoog et al.

```
A-ROUTER#show ipv6 route
IPv6 Routing Table - 31 entries
Codes: C - Connected, L - Local, S - Static, R - RIP, B - BGP
       U - Per-user Static route
       I1 - ISIS L1, I2 - ISIS L2, IA - ISIS interarea, IS - ISIS summary
       O - OSPF intra, OI - OSPF inter, OE1 - OSPF ext 1, OE2 - OSPF ext 2
       ON1 - OSPF NSSA ext 1, ON2 - OSPF NSSA ext 2
C 2001:0:0:1::/64 [0/0]
  via ::, FastEthernet0/0
L 2001:0:0:1::1/128 [0/0]
  via ::, FastEthernet0/0
C 2001:0:0:2::/64 [0/0]
  via ::, FastEthernet0/0.2
L 2001:0:0:2::1/128 [0/0]
  via ::, FastEthernet0/0.2
C 2001:0:0:3::/64 [0/0]
  via ::, FastEthernet0/0.3
L 2001:0:0:3::1/128 [0/0]
  via ::, FastEthernet0/0.3
C 2001:0:0:4::/64 [0/0]
  via ::, FastEthernet0/0.4
L 2001:0:0:4::1/128 [0/0]
  via ::, FastEthernet0/0.4
C 2001:0:0:5::/64 [0/0]
  via ::, FastEthernet0/0.5
L 2001:0:0:5::1/128 [0/0]
  via ::, FastEthernet0/0.5
C 2001:0:0:6::/64 [0/0]
  via ::, FastEthernet0/0.6
L 2001:0:0:6::1/128 [0/0]
  via ::, FastEthernet0/0.6
OI 2001:0:1:1::/64 [110/65]
  via FE80::C802:EFF:FEF4:0, Serial1/0
OI 2001:0:1:2::/64 [110/65]
  via FE80::C802:EFF:FEF4:0, Serial1/0
OI 2001:0:1:3::/64 [110/65]
  via FE80::C802:EFF:FEF4:0, Serial1/0
OI 2001:0:1:4::/64 [110/65]
  via FE80::C802:EFF:FEF4:0, Serial1/0
OI 2001:0:1:5::/64 [110/65]
  via FE80::C802:EFF:FEF4:0, Serial1/0
OI 2001:0:1:6::/64 [110/65]
  via FE80::C802:EFF:FEF4:0, Serial1/0
OI 2001:0:2:1::/64 [110/65]
  via FE80::C803:9FF:FE8C:0, Serial1/1
OI 2001:0:2:2::/64 [110/65]
  via FE80::C803:9FF:FE8C:0, Serial1/1
OI 2001:0:2:3::/64 [110/65]
  via FE80::C803:9FF:FE8C:0, Serial1/1
OI 2001:0:2:4::/64 [110/65]
  via FE80::C803:9FF:FE8C:0, Serial1/1
OI 2001:0:2:5::/64 [110/65]
  via FE80::C803:9FF:FE8C:0, Serial1/1
OI 2001:0:2:6::/64 [110/65]
  via FE80::C803:9FF:FE8C:0, Serial1/1
OE2 2001:0:3:1::/64 [110/88]
  via FE80::C802:EFF:FEF4:0, Serial1/0
C 2001:0:12:12::/64 [0/0]
  via ::, Serial1/0
L 2001:0:12:12::1/128 [0/0]
  via ::, Serial1/0
C 2001:0:13:13::/64 [0/0]
  via ::, Serial1/1
L 2001:0:13:13::1/128 [0/0]
  via ::, Serial1/1
L FE80::/10 [0/0]
```

Figure 14 Routing table of Ankara router after OSPF

Traffic	◀ Captured	◀ Displayed	◀ Displayed %	◀ Marked	◀ Marked %
Packets	24050	24050	100.000%	0	0.000%
Between first and last packet	300.007 sec				
Avg. packets/sec	80.165				
Avg. packet size	1414 bytes				
Bytes	34010080	34010080	100.000%	0	0.000%
Avg. bytes/sec	113364.399				
Avg. MBit/sec	0.907				

Figure 16 Summary of booting up all devices





Mohammed Aldagdoog et al.

Protocol	% Packets	Packets	% Bytes	Bytes	Mbit/s	End Packets	End Bytes	End Mbit/s
Frame	100.00 %	24050	100.00 %	34010080	0.907	0	0	0.000
Cisco HDLC	100.00 %	24050	100.00 %	34010080	0.907	0	0	0.000
Cisco SLARP	0.25 %	60	0.00 %	1440	0.000	60	1440	0.000
Internet Protocol Version 6	99.70 %	23977	99.98 %	34003908	0.907	0	0	0.000
Internet Control Message Protocol v6	7.68 %	1846	3.54 %	1203184	0.032	1846	1203184	0.032
Open Shortest Path First	1.21 %	291	0.12 %	40724	0.001	291	40724	0.001
Data	90.81 %	21840	96.32 %	32760000	0.874	21840	32760000	0.874
Cisco Discovery Protocol	0.05 %	13	0.01 %	4732	0.000	13	4732	0.000

Figure 17 Protocols Hierarchy

IPv6 Conversations											
Address A	Address B	Packets	Bytes	Packets A-B	Bytes A-B	Packets A-B	Bytes A-B	Rel Start	Duration	bps A-B	bps A-B
::	ff02::1:fff4:0	1	68	1	68	0	0	14.814686000	0.0000	N/A	N/A
::	ff02::16	2	160	2	160	0	0	14.837863000	0.0001	11962616.82	N/A
fe80::c802:eff:fe4:0	ff02::1	1	68	1	68	0	0	16.113883000	0.0000	N/A	N/A
fe80::c802:eff:fe4:0	ff02::16	8	640	8	640	0	0	16.135396000	3.3997	1506.02	N/A
::	ff02::1:ff00:2	1	68	1	68	0	0	16.146227000	0.0000	N/A	N/A
2001:0:12:12::2	ff02::1	1	68	1	68	0	0	16.995690000	0.0000	N/A	N/A
fe80::c802:eff:fe4:0	ff02::5	89	12 084	89	12 084	0	0	18.808146000	280.0413	345.21	N/A
::	ff02::1:ff8c:0	1	68	1	68	0	0	21.097427000	0.0000	N/A	N/A
fe80::c801:7ff:fe8c:0	ff02::1	1	68	1	68	0	0	22.038897000	0.0000	N/A	N/A
fe80::c801:7ff:fe8c:0	ff02::16	8	640	8	640	0	0	22.079724000	0.9308	5500.50	N/A
::	ff02::1:ff00:1	1	68	1	68	0	0	22.119160000	0.0000	N/A	N/A
fe80::c801:7ff:fe8c:0	ff02::5	202	28 640	202	28 640	0	0	22.133652000	277.1956	826.56	N/A
2001:0:12:12::1	ff02::1	1	68	1	68	0	0	23.021307000	0.0000	N/A	N/A
2001:0:12:12::1	2001:0:12:12::2	23 660	33 961 200	11 830	16 980 600	11 830	16 980 600	97.586293000	188.8395	719366.58	719366.58

Figure 18 Traffic between Ankara and İzmir routers

Topic / Item	Count	Average	Min val	Max val	Rate (ms)	Percent	Burst rate	Burst start
Packet Lengths	24050	2828.28	24	1500	0.0802	100%	0.4100	226.711
0-19	0	-	-	-	0.0000	0.00%	-	-
20-39	60	24.00	24	24	0.0002	0.25%	0.0100	0.000
40-79	13	69.54	68	72	0.0000	0.05%	0.0400	28.800
80-159	206	97.65	80	152	0.0007	0.86%	0.0500	22.080
160-319	91	207.52	160	300	0.0003	0.38%	0.0300	28.863
320-639	20	376.80	336	572	0.0001	0.08%	0.0300	21.024
640-1279	1820	660.00	660	660	0.0061	7.57%	0.0400	223.441
1280-2559	21840	1500.00	1500	1500	0.0728	90.81%	0.3800	226.711
2560-5119	0	-	-	-	0.0000	0.00%	-	-
5120-4294967295	0	-	-	-	0.0000	0.00%	-	-

Figure 19 Packet Lengths

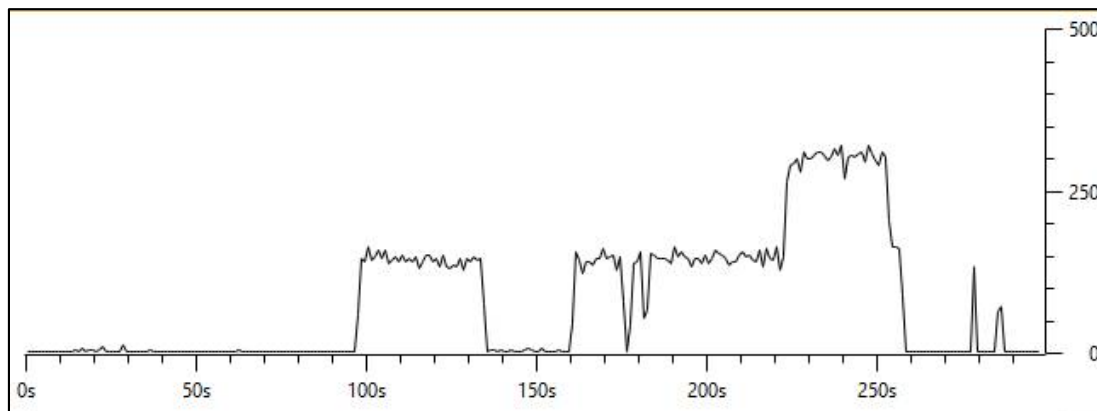


Figure 20 I/O Graph





Comparison of Body Weight Estimated using Body Measurements with Live Weight of Crossbred Cattle

S.K. George^{1,2*}, M.T. Dipu², Muhammad Aslam M K² and Lalu K²

¹Assistant Professor, Base Farm, Kolahalamedu, Kerala, India.

²Kerala Veterinary & Animal Sciences University, Pookode, Wayanad, Kerala, India.

Received: 18 Nov 2018

Revised: 20 Dec 2018

Accepted: 26 Jan 2019

* Address for Correspondence

S.K. George

Assistant Professor,

Base Farm, Kolahalamedu,

Kerala, India.

Email: skgeorge31@gmail.com



This is an Open Access Journal / article distributed under the terms of the **Creative Commons Attribution License** (CC BY-NC-ND 3.0) which permits unrestricted use, distribution, and reproduction in any medium, provided the original work is properly cited. All rights reserved.

ABSTRACT

The milk production potential of a farm has relationship with growth rate of calves/heifers and body weight changes of adult animals. Measurement of body weight is a routine need in farms as well as in field conditions. Considering the difficulty to record body weight using a weighing balance, most often it is determined by body measurements. Schaeffer's formula is commonly employed for estimating body weight in such cases. The application of Schaeffer's formula for estimating the body weight of crossbred cattle of Kerala needs examination. Therefore, the present study was conducted to compare body weight estimated using body measurements with live weight of crossbred cattle determined using a digital balance. For estimating the body weight, forty animals were selected randomly and were kept off feed and water for 12 hours prior to measurement. While comparing the two methods, Pearson's product moment correlation value of 0.97 indicates the strength of the linear relationship between two variables. However, results of paired t-test showed significant ($P < 0.05$) difference between the methods. The lower limit of the 95% confidence interval of the intraclass correlation is 0.975 which indicates how strongly units in the same group resemble each other. Hence it can be concluded that body measurements can be used to estimate body weight in crossbred cattle in conditions where the use of a weighing balance is practically difficult.

Keywords: production, farm, Measurement, body weight, animals, live





INTRODUCTION

Kerala is located in southern India between the Arabian Sea in the west and the Western Ghats in the east. Cattle farming was practiced in the state during the past, mainly to assist agricultural operations and this resulted in development of a disease resistant cattle variety tolerant to hot and humid climatic conditions. However this variety of cattle had very low milk yield. Therefore, as a measure to improve the milk production, artificial insemination was initiated in the state by introduction of germplasm of exotic milch breeds. This technology was welcomed by farmers, and hence the majority of cattle in the state was gradually transformed as crossbreds with medium body weights and better milk yield. The milk production potential of a farm is related with growth rate of calves/heifers and body weight changes of adult animals. Measurement of body weight is a routine need in farms as well as in field conditions. Most often it is difficult to record body weight using a weighing balance. Weighing scale, although accurate, it is cumbersome, costly (Heinrichs et al., 1992) and is stressful to the animals (Brandl and Jorgensen, 1996). Therefore, body weight is usually estimated by body measurements including chest girth and body length (Wangchuk et al., 2017). Schaeffer's formula is commonly employed for estimating body weight in such cases. The application of Schaeffer's formula for estimating the body weight of crossbred cattle of Kerala needs examination. Therefore, the present study was conducted to compare body weight estimated using body measurements with live weight of crossbred cattle estimated with a digital balance.

METHODOLOGY

The investigation was undertaken in an instructional cattle farm at Kolahalamedu, Peerumedu Taluk of Idukki District. The area is located at a latitude of 9.5760° N and longitude of 77.0255° E, the altitude range is from 1100 m above sea level, with an annual rainfall of 2295 mm. The cattle of the farm are cross breeds having the mixed germplasm of native breeds along with that of exotic breeds such as Brown Swiss, Holstein Friesian and Jersey. Similar animals are popular and reared by farmers through out the state. For estimating the body weight, forty animals were selected randomly and were kept off feed and water for 12 hours prior to measurement as described below.

- i) Animal weighing digital balance: Animals were made to enter directly on the platform and was allowed to stand for 20 seconds to record the weight accurately.
- ii) Schaeffer's formula: Body weight (BW) was calculated as per the equation below:
$$BW = (L \times G^2) / 300$$
where BW is body weight in pounds, L is length of animal from point of shoulder to pin bone in inches and G is the chest girth in inches i.e. circumference of chest, just behind foreleg.

Statistical analysis

The relationship between body weight estimated using body measurements with live weight obtained in the weighing balance was assessed by the estimation of Pearson's product moment correlation and intraclass correlation (Snedecor and Cochran, 1994). Similarity of the means obtained was compared using the paired t-test (Snedecor and Cochran, 1994)

RESULTS AND DISCUSSION

The mean body weight of cattle estimated using the Schaeffer's formula and the digital weighing balance is shown in Table 1. For measuring a quantitative variable such as body weight, Pearson's product moment correlation can be used as an index of equivalence while comparing two methods. Pearson's product moment correlation value of 0.97 (Table 1) indicates the strength of the linear relationship between two variables. However, statistical analysis by the





S.K. George et al.

paired t-test (Table 1) showed that the means are statistically different ($P < 0.05$). According to Lee *et al.* (1989), intraclass correlation is the correct statistic for measuring agreement and consistency between two methods i.e. the lower limit of the 95% confidence interval of the intraclass correlation should be at least 0.75. The results of comparison (Table 2) describes how strongly units in the same group resemble each other.

SUMMARY

It can be concluded that body measurements can be used to estimate body weight in crossbred cattle in conditions where the use of a weighing balance is practically difficult.

REFERENCES

1. Brandl, N and Jorgensen, E. 1996. Determination of live weight of pigs from dimensions measured using image analysis. *Comput Electron Agric*, 15: 57-72.
2. Heinrichs A.J., Rogers, G.W. and Cooper, J.B. 1992. Predicting body weight and wither height in Holstein heifers using body measurements. *J. Dairy Sci*, 75: 3576-358.
3. Lee, J., Koh, D. and Ong, C.N. 1989. Statistical evaluation of agreement between two methods for measuring a quantitative variable. *Computers in Biology and Medicine*, 19: 61-70.
4. Snedecor, G.W. and Cochran, W.G. 1994. *Statistical methods*. 8th edn. Iowa State University, Iowa, USA.
5. Wangchuk, K, Wangdi, J and Mindu, M. 2018. Comparison and reliability of techniques to estimate live cattle body weight. *J. Appl. Anim. Res*: 46. 349-352.

Table 1. Comparison between body weight estimated by body measurements with that estimated using a digital weighing balance

Parameter	Schaeffer's formula	Digital Balance	t value	P value	Pearson's correlation
Body weight (Kg)	367.3±67.18	374±70.36	2.67	0.011	0.97

Table 2. Lower (r_1) and upper limits (r_2) of the 95% confidence interval of intraclass correlation (r) between body weight estimated by body measurements with that determined using digital weighing balance

Parameters	r_1	r_2	r
Body weight (Kg)	0.975	0.993	0.987





Electron Scattering with Sigma Meson Exchange Particle as a Residual Interaction to Calculate C2 Form Factors in ^{44}Ca Nucleus

Sadeq S. Mashaan^{1*} and Firas Z. Majeed²

¹Department of Computer, Al-Musaib Technical College, Al-Furat Al-Awsat Technical University, Babylon, Iraq.

²Department of Physics, College of Science, University of Baghdad, Baghdad, Iraq.

Received: 25 Oct 2018

Revised: 27 Nov 2018

Accepted: 29 Dec 2018

* Address for Correspondence

Sadeq S. Mashaan

Department of Computer,
Al-Musaib Technical College,
Al-Furat Al-Awsat Technical University,
Babylon, Iraq.
Email:sadeq278@ymail.com



This is an Open Access Journal / article distributed under the terms of the **Creative Commons Attribution License** (CC BY-NC-ND 3.0) which permits unrestricted use, distribution, and reproduction in any medium, provided the original work is properly cited. All rights reserved.

ABSTRACT

Inelastic longitudinal electron scattering C2 form factor in ^{44}Ca has been utilized to study the effects of fitting parameters on the sigma meson exchange type potentials as a residual interaction. A model space wave vectors are generated in full fp-shell model with FPD6 as effective interaction with mixing configuration technique and harmonic oscillator as a single particle wave function. By coupling the core particles with model space particle, where the latter used as an active part of residual interaction in the so called core polarization process, it is included as a correction with first order perturbation theory to the main calculation of model space, and the excitation energy (with calculate the form factors in the states 2_1^+ , 2_2^+ , 2_3^+ , 2_4^+ and 2_5^+ with $E_x=1.561$ MeV, 3.084 MeV, 4.647 MeV, 5.540 MeV and 6.275 MeV respectively) has been carried out with $(2\hbar\omega)$. Theoretical results has been not compared with experimental data because we nautical that the theoretical results has been compared with each other's. Harmonic Oscillator potential is used to generate single particle wave functions in fp-shell and considering ^{40}Ca as an inert core. The cod OXBASH computer programing is used to generate the two body matrix elements process of this study.

Keywords: sigma meson exchange, ^{44}Ca , electron scattering, fitting parameters.





Sadeq S. Mashaan and Firas Z. Majeed

INTRODUCTION

Electron scattering form factors give the most precise information about nuclear size and charge distribution [1]. The electromagnetic theory agree with experimental observations, and Quantum Electrodynamics success in giving a well-defined description of the interaction deeply insight[2,3]. **Mott** first derived The scattering cross section which described the electron scattering and included the effect due to the electron spin. "**Nuclear form factor**" depends on the charge and magnetization distribution in the target nuclei and we can determine the form factor by the ratio of the measured cross section to the Mott cross section. The form factors can be found experimentally as a function of the momentum transfer \vec{q} by knowing the energies of the incident and scattered electron and the scattering angle[4]. Backward-angle resolution inelastic electron scattering on $^{40,42,44,48}\text{Ca}$ have been carried out by Steffen et al[5], they observed a very strong magnetic dipole ground state transition in Ca isotopes. Monopole transitions from the 1^+_0 ground states to 2^+_0 excited states with 1.837 MeV for ^{42}Ca , 1.884 MeV for ^{44}Ca and 4.272 MeV for ^{48}Ca had been investigated by Gräf et al[6] with high resolution inelastic electron scattering (FWHM \approx 30 keV) at low momentum transfer ($0.29 < q < 0.53 \text{ fm}^{-1}$).

Zheag and Zamick[7] studied the relations between Polarized-Proton-Nucleus and un polarized-transverse-electron-nucleus scattering and their application in ^{42}Ca . The electron scattering form factors have been measured by Itoh et al[8], for 2^+ , 3^- and 5^- states up to 7 MeV excitation in ^{42}Ca and ^{44}Ca , the range of the incident electron energy were 62.5–250 MeV. The derivation of Core Polarization (CP) effects with higher configuration in the first order perturbation theory and the two-body matrix elements of three parts of the realistic interaction: central, spin orbit and tensor force which are belong to realistic (M3Y) interaction and the detection of meson exchange current for every channel of interaction in a separate pictures will be introduced in the present work, harmonic oscillator single-particle basis have been used

THEORY

Through microscopic theory, the core polarization effect on the form factor combines shell-model wave functions and configurations with higher energy as first order perturbations; these are called "**core-polarization effects**"[9]. Shell-model theory showed that the true space might be divided into three separated spaces which are: model space, inert core and higher configurations. Higher orbits might be included or excluded according to the choice of the researcher and the model use, but core orbits as have been proved[9], have an active contribution in the calculation of form factors. The main problem is that the inclusion of core orbits makes the space (Hilbert Space) very vast so, we must separate between the two spaces (a core part and a valence part) to express the interaction between the core and the valence particles, and that among the valence particles. In the shell-model, we are unable to solve Schrodinger equation in the full Hilbert space, because of the huge number of configurations, so we must truncate it to a smaller part of the configurations with finite dimensions Hilbert space. This is called the shell model-space or simply the model space. For this reason, we must use effective interactions and operators. The effective interaction is used to give the nuclear properties microscopically, starting with realistic NN interaction using quantum mechanical many-body theory. For light nuclei, there are different effective interactions such as the FPD6[10],

For a selected operator Γ_{JT}^η the reduced matrix elements are written as the sum of the product of the one-body transition density matrix elements (OBDM) times the single-particle transition matrix elements:

$$\langle \Gamma_f \| \hat{T}_{JT}^\eta \| \Gamma_i \rangle = \sum_{\alpha, \beta} OBDM(\Gamma_i, \Gamma_f, \alpha, \beta) \langle \alpha \| \hat{T}_{JT}^\eta \| \beta \rangle \dots\dots\dots (1)$$





Sadeq S. Mashaan and Firas Z. Majeed

where $\Lambda = JT$ is the multi-polarity and the states $\Gamma_i = J_i J_i$ and $\Gamma_f = J_f J_f$ are initial and final states of the nucleus. While α and β denote the final and initial single-particle states, respectively (isospin is included). The reduced matrix element of the electron scattering operator \hat{T}_Λ^η consist of two parts, one is for the "Model space" matrix elements, and the other is for the " Core-polarization" matrix elements are given by[9]:

$$\langle \Gamma_f \| \hat{T}_\Lambda^\eta \| \Gamma_i \rangle = \langle \Gamma_f \| \hat{T}_\Lambda^\eta \| \Gamma_i \rangle_{MS} + \langle \Gamma_f \| \delta \hat{T}_\Lambda^\eta \| \Gamma_i \rangle_{CP} \quad \dots\dots\dots (2)$$

where, $\langle \Gamma_f \| \hat{T}_\Lambda^\eta \| \Gamma_i \rangle_{MS}$ are the model-space matrix elements ,

and, $\langle \Gamma_f \| \delta T_\Lambda^\eta \| \Gamma_i \rangle_{CP}$ are the core-polarization matrix elements.

The $|\Gamma_i\rangle$ and $|\Gamma_f\rangle$ are described by the model-space wave functions.

The core-polarization matrix elements can be written as[9]:

$$\langle \Gamma_f \| \delta \hat{T}_\Lambda^\eta \| \Gamma_i \rangle_{CP} = \sum_{\alpha, \beta} OBDM(\alpha, \beta) \langle \alpha \| \delta \hat{T}_\Lambda^\eta \| \beta \rangle_{CP} \quad \dots\dots\dots (3)$$

The first order perturbation theory says that the single-particle matrix element for the higher-energy configurations can be expressed as[11]:

$$\langle \alpha | \delta \hat{T}_J^\eta | \beta \rangle = \langle \alpha | V_{res} \frac{Q}{E - H^{(0)}} \hat{T}_J^\eta | \beta \rangle + \langle \alpha | \hat{T}_J^\eta \frac{Q}{E - H^{(0)}} V_{res} | \beta \rangle \quad \dots\dots\dots (4)$$

The single-particle energies are calculated according to [11]:

$$e_{nlj} = (2n + l - \frac{1}{2})\hbar\omega + \begin{cases} -\frac{1}{2}(l+1)\langle f(r) \rangle_{nl} & \text{for } j=l-\frac{1}{2} \\ \frac{1}{2}l\langle f(r) \rangle_{nl} & \text{for } j=l+\frac{1}{2} \end{cases} \quad \dots\dots\dots (5)$$

with: $\langle f(r) \rangle_{nl} \approx -20A^{-2/3} MeV$ (6)
 $\hbar\omega = 45A^{-1/3} - 25A^{-2/3}$

A computer program written in FORTRAN 90 language is used by Radhi to include realistic interaction M3Y, is modified to receive new fitting parameters which calculate meson part of interaction.

For the two-body matrix elements of the residual interaction $\langle \alpha\alpha_1 | V_{res} | \beta\alpha_2 \rangle_\Gamma$ and $\langle \alpha\alpha_2 | V_{res} | \beta\alpha_1 \rangle_\Gamma$, which appear in equation (4), the Michigan sum of three range Yukawa potential (M3Y) interaction of Nakada[12] is adopted. This interaction is a modified version of M3Y interaction of Berstch et al[13].this interaction containing terms like those





Sadeq S. Mashaan and Firas Z. Majeed

were given in LS-coupling and tensor effects, and density dependence part which calculates the zero range term. A transformation of the wave function from jj to LS coupling must be done to get the relation between the two-body shell model matrix elements and the relative and centre of mass coordinates, using the harmonic oscillator radial wave functions with Talmi-Moshinsky transformation. The realistic M3Y effective NN-interaction, which is used in electron scattering ($V_{res}=v_{12}$) is expressed as a sum of the central potential parts ($v_{12}^{(c)}$) as follows[10]:

$$v_{12}^{(c)} = \sum_n t_n^{(SE)} P_{SE} f_n^{(C)}(r_{12}) \dots\dots\dots(7)$$

$$v_{12}(\delta) = t_1^{SE} P_{SE} \frac{e^{-\left(\frac{r_{12}}{R_{112}}\right)}}{\frac{r_{12}}{R_{112}}} + t_2^{SE} P_{SE} \frac{e^{-\left(\frac{r_{12}}{R_{212}}\right)}}{\frac{r_{12}}{R_{212}}} + t_3^{SE} P_{SE} \frac{e^{-\left(\frac{r_{12}}{R_{312}}\right)}}{\frac{r_{12}}{R_{312}}} \dots\dots\dots(8)$$

The values of the best fit to the potential parameters (t_n^{SE}) are shown in table (1).

In this part we will focus attention in Ca isotope, ^{44}Ca , where there is a closed core ^{40}Ca and four neutrons freely distributed in fp-shell model space. We have chooses FPD6 as a model space effective interaction to generate the model space wave functions and OBDM. The total C2 form factor is calculated, from the core contribution only, and indicated the model space has no contribution, because the neutrons do not contribute to the charge form factor, because they are neutral particles, so the core protons will play this role. In general, the total results are in a good agreement.

RESULTS AND DISCUSSION

The core-polarization effects have been included in order to account for the contribution of configurations from outside of the model space in the transition. The nucleus ^{44}Ca is the lightest doubly magic nucleus with a neutron excess. It is known to be a good shell-model nucleus and thus provides an excellent testing ground of nuclear models. In fact, the nucleus ^{44}Ca is more inert than ^{40}Ca , ^{48}Ni and ^{56}Ni because of the closed sub shell neutron $1f_{7/2}$ so that it is an interesting one in fp shell nuclei. We use the single particle wave functions of the harmonic oscillator (HO) with size parameter ($b= 1.988$ fm). The interaction equation for sigma meson (δ) when $T=0, S=0$, which is expressed as (t^{SE}), which represents fitting parameter for nucleon interaction in this channel and be the interaction equation as follows[16]:

$$v_{12}(\delta) = \sum_{n=1}^3 t_n^{(SE)} P_{SE} \frac{e^{-\left(\frac{r_{12}}{R_{n12}}\right)}}{\frac{r_{12}}{R_{n12}}} \dots\dots\dots(9)$$

$$v_{12}(\delta) = t_1^{SE} P_{SE} \frac{e^{-\left(\frac{r_{12}}{R_{112}}\right)}}{\frac{r_{12}}{R_{112}}} + t_2^{SE} P_{SE} \frac{e^{-\left(\frac{r_{12}}{R_{212}}\right)}}{\frac{r_{12}}{R_{212}}} + t_3^{SE} P_{SE} \frac{e^{-\left(\frac{r_{12}}{R_{312}}\right)}}{\frac{r_{12}}{R_{312}}} \dots\dots\dots(8)$$





Sadeq S. Mashaan and Firas Z. Majeed

Note: The sum process of the fitting parameter ($t_1^{SE} + t_2^{SE}$) and negligence (t_3^{SE}) to their small value and equal to the value of all the interactions we find at the time of the collection process ($t_1^{SE} + t_2^{SE}$) devolve descending and digital output as follows: $P_0=7910\text{MeV}>E=6853\text{MeV}>P_3=P_4=5390\text{MeV}>P_5=5377\text{MeV}>P_2=5147\text{MeV}>P_1=5043.5\text{MeV}$ Clearly, all Figs. shown that nuclear force effective in the distance range (0.5-2.0 fm), so the maximum value of square form factor is equal one, that mean the probability of finding in this range equal 100%. In outer the range (0.5-2.0 fm), there are meaner of form factor values because of named tunnel effective, so it is vanishing with more of 3 fm.

The C2 Charge For Factor For 2^+ state

Charge form factors for 2_1^+ state at $E_x=1.561$ MeV.

Inelastic longitudinal form factors (C2) have calculated by using M3Y (including the OBDM elements as table(2)) as shown in Fig (1); in this figure the calculated form factors using M3Y($E, P_0, P_1, P_2, P_3, P_4$ and P_5) shows the behavior of results as two peaks.

where $P_0 > P_1 > E > P_3 > P_5 > P_4 > P_2$ (the first peak)

$P_0 > E > P_4 > P_2 > P_1 > P_5 = P_3$ (second peak)

Charge form factors for 2_2^+ state at $E_x=3.084$ MeV.

The quadruple C2 charge form factor for ^{44}Ca in 1f-2p shell model space is illustrated in Fig (2), as a residual interactions. Using M3Y (including the OBDM elements as table(3)) gave good agreement in results, which shifted than it in all region of (q).

In the region $q = (0-1.5)\text{fm}^{-1}$ $P_0 > P_1 > P_3 = P_5 > E > P_4 > P_2$

In the region $q = (1.5-3)\text{fm}^{-1}$ $P_0 > E > P_2 = P_4 > P_1 > P_3 = P_5$

Charge form factors for 2_3^+ state at $E_x=4.647$ MeV

The quadruple C2 charge form factor for ^{44}Ca in 1f-2p shell model space is illustrated in Fig (3), as a residual interactions. Using M3Y (including the OBDM elements as table(4)) gave good agreement in results, which shifted than it in all region of (q).

In the region $q = (0-0.6)\text{fm}^{-1}$ $P_1 > P_3 = P_5 > P_0 > E > P_2 = P_4$

In the region $q = (0.6-1.6)\text{fm}^{-1}$ $P_0 > E > P_1 > P_3 = P_5 > P_4 > P_2$

In the region $q = (1.6-3)\text{fm}^{-1}$ $P_0 > E > P_4 > P_2 > P_1 > P_3 = P_5$

Charge form factors for 2_4^+ state at $E_x=5.540$ MeV.

The quadruple C2 charge form factor for ^{44}Ca in 1f-2p shell model space is illustrated in Fig (4), as a residual interactions. Using M3Y (including the OBDM elements as table(5)) gave good agreement in results, which shifted than it in all region of (q).

In the region $q = (0-0.6)\text{fm}^{-1}$ $P_0 > P_1 > E > P_3 = P_5 > P_4 > P_2$ (first peak)

In the region $q = (0.6-2)\text{fm}^{-1}$ $P_0 > E > P_1 > P_2 = P_3 = P_4 = P_5$ (first peak)

In the region $q = (2-2.8)\text{fm}^{-1}$ $P_0 > P_1 > E > P_3 = P_5 > P_4 > P_2$ (second peak)





Sadeq S. Mashaan and Firas Z. Majeed

Charge form factors for 2_s^+ state at $E_x=6.275$ MeV.

The quadruple C2 charge form factor for ^{44}Ca in 1f-2p shell model space is illustrated in Fig (5), as a residual interactions. Using M3Y (including the OBDM elements as table (6)) gave good agreement in results, which shifted than it in all region of (q).

In the region $q = (0-0.8) \text{ fm}^{-1}$ $P1 > P3 = P5 > P0 > P4 = P2 > E$ (first peak)

In the region $q = (0.8-2) \text{ fm}^{-1}$ $P0 > E > P1 > P3 = P5 > P4 = P2$

In the region $q = (2-3) \text{ fm}^{-1}$ $P0 > E > P4 = P2 > P1 > P3 = P5$ (second peak)

ACKNOWLEDGEMENTS

The Authors are very grateful to Prof. Raad A. Radhi to his assistance to provide the original copy of his two codes of calculation of form factors and residual interaction and they also thanks Dr. Radhi for his assistance in the production of OBDM files from OXBASH code of B. A. Brown [13].

CONCLUSIONS

The amplitude of any channel for two body matrix elements coupling core particles to model space one does not the main responsible factor to the amplitudes of electron scattering form factors as a results of quantum tail of interactions, especially in the regions of momentum transfer (q larger than 2.1 fm^{-1}) as a results of repulsive force of short range meson sigma type and attractive force of medium range of the same meson type with a different mass and fitting parameters values.

REFERENCES

1. Walecka, J. D. 2004. " *Electron Scattering for Nuclear and Nucleon Structure*" Cambridge monographs on physics, Nuclear physics and cosmology, London-England.
2. Richter, W. A. Van der Merwe, M. G. Julies, R. E. and Brown, B. A 1994. " *Magnetic Dipole Strength and the T= 0 Proton--Neutron Residual Interaction*" Nucl. Phys. A577, 585.
3. Alder K. and Steffen, R.M. 1975. " *spectroscopy*", North-Holland, 1.
4. Mott, N.F. Proc. Roy, 1929. " *An Introduction to Particle Physics and the Standard Model*" Soci. Ser, A124, 425.
5. Steffen, V. Graf, H. D. Gross, W. Meuer, D. Richter, A. Spamer, E. Titze, O. and Knipfer, W. 1978, " *Analysis of Data From an Admissions Test With Item Models*" Phys. Lett. B95, 23.
6. Gräf, H. D. Manakos, H. Richter, P. A. Spamer, E. and Strottman, D. Nucl, 1978. " *Electro-Excitation of the 0+ 2 State in ^{48}Ca* " Phys. A295, 319.
7. Zheng C. and Zamick L. 1989. " *Effects of isoscalar admixtures on the combined analysis*" Phys. Rev. C40, 1120.
8. Itoh K., Shin Y. M., Gerace W. J. and Torizuka Y, 1989. " *Longitudinal Electroexcitation of the Low-Lying States in ^{42}Ca and ^{44}Ca* " Nucl. Phys. A492, 426 .
9. Radhi R. A., Bouchebak A. 2003. " *Perturbative role in the inelastic electron scattering from ^{29}Si* " Nucl. Phys. A716, 87 .
10. Poves, J. Sanchez-Solano, Caurier E., and Nowacki F. 2001. " *Shell model study of the isobaric chains A=50, A=51 and A=52*" Nucl. Phys. A694, 157 .
11. Brussaard P.J. and Glademans P. W. M. 1977. " *Shell-model Application in Nuclear Spectroscopy*", North-Holland Publishing Company, Amsterdam .
12. Berstch G., Borysowicz J., McManus H. and Love W. G. 1977. " *Interactions for inelastic scattering derived from realistic potentials*" Nucl. Phys. A284, 399 .





Sadeq S. Mashaan and Firas Z. Majeed

13. Brown A., Radhi R., and Wildenthal B.H. **1983**. "Energy Levels of Light Nuclei A=10" Phys. Lett. **B133**, 5-8 .Nakada H. **2008**. "Mean-field approach to nuclear structure with semi-realistic nucleon-nucleon interactions" phys.Rev. **C78**, 054301.
 14. Heisenberg J. and Blok H. P. Ann. **1983**. "constituents of matter" Rev. of Nucl. and Part. Sci. 33, 569 .
 15. Brown A. 1998." Population of superdeformed bands at extreme angular momenta" Phys. Rev. C58, 220 .

Table 1. The value of the best fit to the potential parameters[14].

Parameters	Unit	M3Y-P0	M3Y- P1	M3Y-P2	M3Y-P3	M3Y- P4	M3Y-P5	M3Y- E
R ₁ (c)	fm	0.25	0.25	0.25	0.25	0.25	0.25	0.25
t ₁ (SE)	MeV	11466	8599.5	8027	8027	8027	8027	9958
R ₂ (c)	fm	0.40	0.40	0.40	0.40	0.40	0.40	0.40
t ₂ (SE)	MeV	-3556	-3556	-2880	-2637	-2637	-2650	-3105
R ₃ (c)	fm	1.414	1.414	1.414	1.414	1.414	1.414	1.414
t ₃ (SE)	MeV	-10.463	-10.463	-10.463	-10.463	-10.463	-10.463	-10.463

Table 2. The OBDM elements for the 2₁⁺ transition obtained by FPD6 interaction in ⁴⁴Ca.

J _i	J _f	OBDM (ΔT=0)	OBDM (ΔT=1)
7/2	7/2	1.24184	0.87812
7/2	3/2	0.04643	0.03283
7/2	5/2	0.07465	0.05278
3/2	7/2	0.19414	0.13728
3/2	3/2	0.00922	0.00652
3/2	5/2	0.01195	0.00845
3/2	1/2	0.00276	0.00195
5/2	7/2	-0.06572	-0.04647
5/2	3/2	-0.00674	-0.00477
5/2	5/2	0.00585	0.00413
5/2	1/2	0.00193	0.00137
1/2	3/2	0.00323-	0.00228-
1/2	5/2	0.00372	0.00263

Table 3. The OBDM elements for the 2₂⁺ transition obtained by FPD6 interaction in ⁴⁴Ca.

J _i	J _f	OBDM (ΔT=0)	OBDM (ΔT=1)
7/2	7/2	0.08096	0.05725
7/2	3/2	0.04875-	0.03447-
7/2	5/2	0.02684	0.01898
3/2	7/2	0.10123-	0.07158-
3/2	3/2	0.00005	0.00004
3/2	5/2	0.01750-	0.01238-
3/2	1/2	-0.00100	-0.00071
5/2	7/2	-0.02467	-0.01744
5/2	3/2	0.00322	0.00228
5/2	5/2	-0.00186	-0.00132
5/2	1/2	-0.00099	-0.00070
1/2	3/2	0.00357	0.00253
1/2	5/2	-0.00267	-0.00189





Sadeq S. Mashaan and Firas Z. Majeed

Table 4. The OBDM elements for the 2_3^+ transition obtained by FPD6 interaction in ^{44}Ca .

J_i	J_f	OBDM ($\Delta T=0$)	OBDM ($\Delta T=1$)
7/2	7/2	0.19650	0.13895
7/2	3/2	0.15759-	0.11143-
7/2	5/2	0.00414-	0.00293-
3/2	7/2	1.04588-	0.73955-
3/2	3/2	0.02761-	0.01952-
3/2	5/2	0.00381-	0.00270-
3/2	1/2	0.01201-	0.00849-
5/2	7/2	0.01649	0.01166
5/2	3/2	0.01444	0.01021
5/2	5/2	0.00489	0.00346
5/2	1/2	-0.00921	-0.00651
1/2	3/2	0.02094	0.01481
1/2	5/2	-0.01275	-0.00902

Table 5. The OBDM elements for the 2_4^+ transition obtained by FPD6 interaction in ^{44}Ca .

J_i	J_f	OBDM ($\Delta T=0$)	OBDM ($\Delta T=1$)
7/2	7/2	-0.13813	-0.09767
7/2	3/2	0.02040	0.01443
7/2	5/2	-0.00304	-0.00215
3/2	7/2	0.02507	0.01772
3/2	3/2	0.00202	0.00143
3/2	5/2	0.06987	0.04940
3/2	1/2	0.00252	0.00178
5/2	7/2	-0.00606	-0.00429
5/2	3/2	-0.01455	-0.01029
5/2	5/2	-0.00150	-0.00106
5/2	1/2	0.00158	0.00112
1/2	3/2	0.00105	0.00074
1/2	5/2	-0.00076	-0.00053





Sadeq S. Mashaan and Firas Z. Majeed

Table 6. The OBDM elements for the 2_5^+ transition obtained by FPD6 interaction in ^{44}Ca .

J_i	J_f	OBDM ($\Delta T=0$)	OBDM ($\Delta T=1$)
7/2	7/2	0.15692-	0.11096-
7/2	3/2	0.00129	0.00092
7/2	5/2	0.02377	0.01681
3/2	7/2	0.02417	0.01709
3/2	3/2	0.05081	0.03593
3/2	5/2	0.01805	0.01276
3/2	1/2	0.00151	0.00107
5/2	7/2	0.09851-	0.06965-
5/2	3/2	0.00877-	0.00620-
5/2	5/2	0.00150-	0.00106-
5/2	1/2	0.00344	0.00243
1/2	3/2	-0.00290	-0.00205
1/2	5/2	0.01344	0.00950

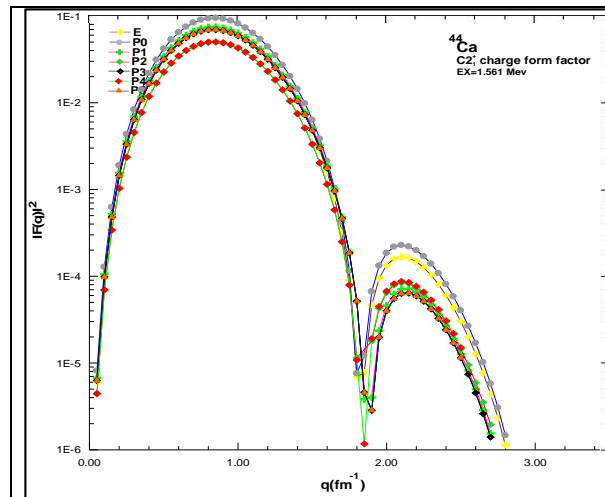


Fig.1. Charge form factor for the state 2_1^+ in ^{44}Ca using $E_x=7.319$ MeV.

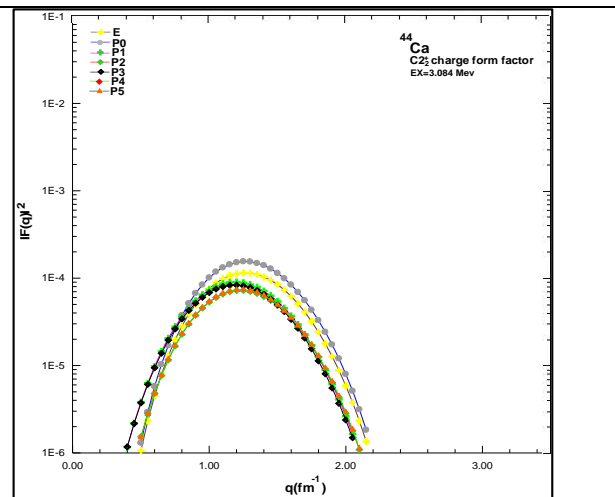


Fig.2. Charge form factor for the 2_2^+ state in ^{44}Ca using $E_x=8.918$ MeV.





Sadeq S. Mashaan and Firas Z. Majeed

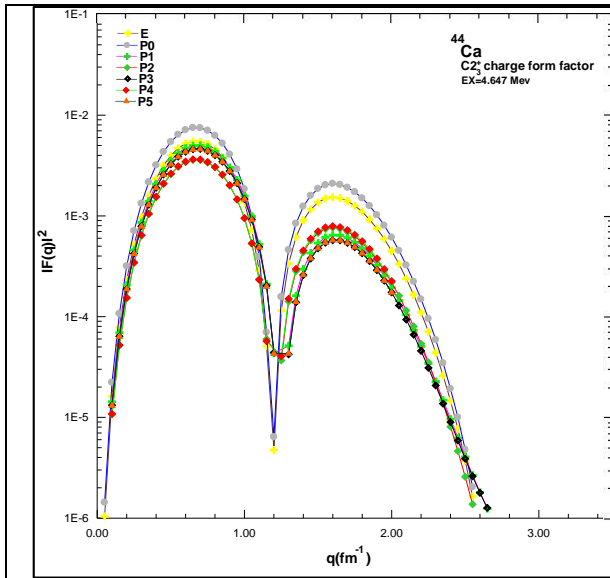


Fig.3. Charge form factor for the 2_3^+ state in ^{44}Ca using $Ex=9.121$ MeV.

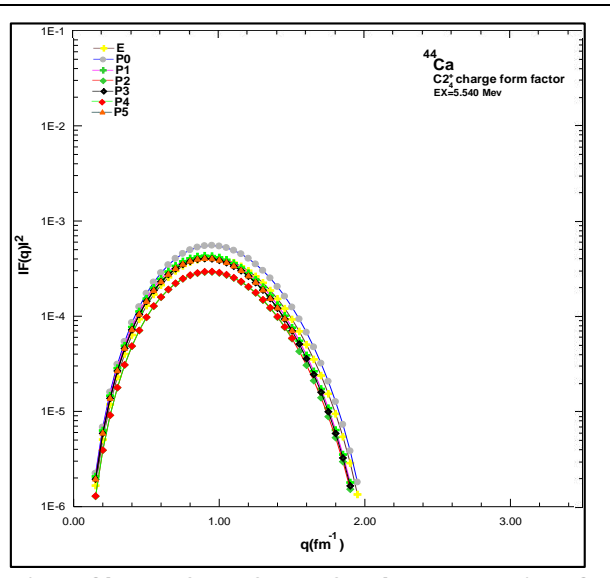


Fig.4. Charge form factor for the 2_4^+ state in ^{44}Ca using $Ex=9.469$ MeV.

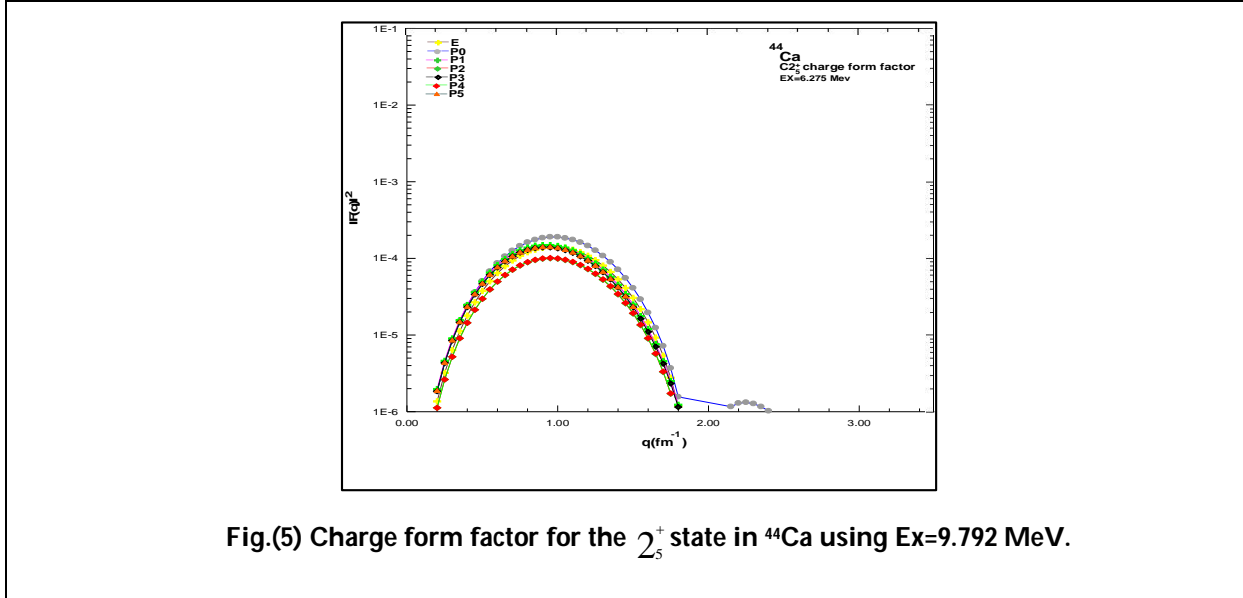


Fig.(5) Charge form factor for the 2_5^+ state in ^{44}Ca using $Ex=9.792$ MeV.





Effects of Gamma Rays Irradiation on the Optical Properties of Mn Doped NiO Thin Films, Obtained by Co-Precipitation Method

Ahmed Nsaif Jasim^{1*}, Asaad Ahmed Kamel¹, Zainab Saad Mahdi¹, Zaid Abdel Hadi Abd and Sorina Iftimie²

¹Physics Department, College of Science, University of Diyala, Iraq.

²Physics and Biophysics Department, Faculty of Physics-Electricity, Solid State, University of Bucharest, Iraq.

Received: 23 Oct 2018

Revised: 27 Nov 2018

Accepted: 29 Dec 2018

*Address for Correspondence

Ahmed Nsaif Jasim

Physics Department,

College of Science,

University of Diyala, Iraq.

Email: ahmedphy@sciences.uodiyala.edu.iq



This is an Open Access Journal / article distributed under the terms of the **Creative Commons Attribution License** (CC BY-NC-ND 3.0) which permits unrestricted use, distribution, and reproduction in any medium, provided the original work is properly cited. All rights reserved.

ABSTRACT

Manganese-doped nickel oxide thin films (2%, 4%, 6%, and 8%) were fabricated by co-precipitation route and were subjected to irradiation with gamma rays of energy of 0.662 MeV. The source of gamma rays radiation was Cs137. The optical properties of obtained Ni_(1-x)Mn_xO samples were analyzed before and after the irradiation process. All measurements were performed at room temperature, in ambient atmosphere, using a (750 Lambda Perkin Elmer spectrometer). Investigations of optical transmission, optical bandgap, extinction coefficient, and optical conductivity were carried out, and it was observed that by increasing the Mn doping ratio the replacement rate of Ni²⁺ ions with Mn²⁺ ones increased. Due to this behavior the optical transmission and bandgap values decreased for pristine samples, and the decrease is more noticeable after the irradiation process, e.g. a decrease of almost 10% was determined for the bandgap of irradiated Ni_(1-x)Mn_xO thin film. Moreover, the larger values of optical conductivity calculated after the irradiation process proved that the number of point-like defects increased, especially Ni²⁺ vacancies.

Keywords: Mn, NiO, precipitation method, bandgap, diluted magnetic semiconductors.

INTRODUCTION

Nowadays, the advances in spintronics, magneto-electronics and magneto-opto-electronics are great [1] due to the progress of diluted magnetic semiconductors (DMS). DMS are non-magnetic materials that after doping with





Ahmed Nsaif Jasim et al.

transition metal ions gain ferromagnetic features. Nickel oxide (NiO) has cubic structure, large Neel temperature ($T_N = 523 \text{ K}$), wide bandgap of 3.2 – 3.8 eV, at room temperature, and long-term chemical and physical stability [2-8]. Nevertheless, NiO can be easily doped to achieve p-type conductivity; either by introducing Ni²⁺ vacancies or by doping with cations [9] and this transforms it from a Mott-Hubbard insulator into a material that exhibits ferromagnetism at room temperature [10]. One of the metals used for doping of NiO is manganese (Mn), and was already proved that the magnetic properties of Ni_(1-x)Mn_xO ternary compound are completely different compared to NiO or Mn[11]. Also, was found that the coercivity values increase with Mn doping percentage [12-15]. Moreover, Mn-doped zinc oxide was proved to change the magnetic state of spin-glass to ferromagnetic one, by increasing the holes concentration [16]. Such changes are possible because Ni²⁺ or Zn²⁺ can easily replaced Mn²⁺ or Mn³⁺ ions [17,18].

This paper is focused on the investigation of optical properties of pristine and irradiated Ni_(1-x)Mn_xO thin films, obtained by the chemical co-precipitation method. While plenty of papers in literature are dedicated to induced changes of magnetic properties of NiO doped with different metals, simulating DMS materials, few have emphasis on the analysis of their optical properties and less on the effects induced by gamma rays irradiation. In this study, investigations of optical transmission, optical bandgap, extinction coefficient and optical conductivity were carried out and discussed before and after irradiation process.

EXPERIMENTAL PROCEDURES

Materials

Nickel acetate tetra hydrate, [Ni(CH₃COO)₂.4H₂O], 98% purity, and manganese (II) acetate, [Mn(CH₃COO)₂.4H₂O], 98% purity, were purchased from Merck company, and were used without further purification. Optical glass substrates were used for the deposition of tailored thin films and were subsequently cleaned with acetone and distilled water for 15 minutes.

Fabrication and characterization of Ni_(1-x)Mn_xO thin films

0.1 M Ni(CH₃COO)₂.4H₂O solution was prepared by dissolving 2.4887 g of solid nickel salt in 100 mL distilled water. 0.1 M Mn(CH₃COO)₂ solution was prepared by dissolving 1.7303 g of solid manganese salt in the same volume of distilled water. All the amounts of used materials were weighed using a balance with 10⁻⁴ g sensibility. After preparation, each solution was stirred for 60 min, at room temperature, using a magnetic stirrer. Different volumes of 2%, 4%, 6%, and 8% of Mn(CH₃COO)₂.4H₂O solution were blended with Ni(CH₃COO)₂.4H₂O solution. In order to obtain a good homogeneity, the latter mixture was stirred for 30 min, in the same conditions as the precursor solutions. The final blend solution was sprayed onto optical glass substrates and the obtained Ni_(1-x)Mn_xO thin films were subjected to irradiation with gamma rays. The source of gamma rays radiation was Cs137 and the energy was 0.662 MeV. Optical investigations were performed using a (750 Lambda Perkin Elmer) spectrometer and the values of transmittance, bandgap, extinction coefficient and optical conductivity of fabricated samples were determined and discussed before and after irradiation process. The thickness of Ni_(1-x)Mn_xO layers was determined to be 300 ± 5 nm.

2.3. *Reaction mechanisms* The main reactions involved in the preparation of Mn doped NiO thin films can be written as follows:



RESULTS AND DISCUSSIONS

The optical transmission spectra of grown Ni_(1-x)Mn_xO thin films, drawn before and after gamma rays irradiation, are presented in Figure 1. All measurements were performed in ambient atmosphere in the 300 – 900 nm range. One can





Ahmed Nsaif Jasim et al.

easily notice that for the non-irradiated samples, by increasing the percentage of manganese (Mn) doping, the optical transmittance decreases. We assume this behavior is associated with the replacement of Ni²⁺ ions with Mn²⁺ ones and the latter were incorporated into NiO lattice. A similar behavior was noticed by S. Iftimieet al. for ZnSe_{1-x}O_x thin films [19], grown by rf-magnetron sputtering. Moreover, after gamma rays irradiation process, the optical transmission strongly decreased, and same behavior was noticed for the absorption coefficient (data not shown here). It is known that in the case of Ni_(1-x)Mn_xO thin films the replacement of Ni²⁺ ions can be done either with Mn³⁺ or Mn²⁺ ions [20]. Also, the Coulombian attraction force between Ni vacancies and Mn³⁺ ions are stronger than for Mn²⁺ ions, conferring high chemical and physical stability of Ni_(1-x)Mn_xO samples. We assume that the strong decrease of the optical transmission after gamma rays irradiation process is due to an increase of the number of interactions between Ni vacancies and Mn³⁺ ions, so the crystalline arrangement was modified. All prepared samples are direct bandgap semiconductors and for them the dependence of absorption coefficient on incident photons energies near the fundamental absorption edge is described by the following equation [21,22]:

$$\alpha(\hbar\omega) = \frac{(\hbar\omega - E_g)^{1/2}}{\hbar\omega} \dots\dots\dots(1),$$

in which E_g is the optical bandgap corresponding to Γ point of the first Brillouin zone and $\hbar\omega$ is the incident energy. In Table 1 the determined values of the optical bandgap of fabricated Ni_(1-x)Mn_xO layers are summarized, before and after irradiation process. For the calculation of bandgap values equation (1) was applied. NiO has a direct bandgap of about 3.8 – 4.0eV, at room temperature. By increasing the Mn doping percentage, the bandgap values decrease due to the mixed transitions between 2p – 3d states of MnO and 3d – 3d states of NiO and MnO. This consideration was made also by D.K. Kanan and E.A. Carter [23] but for other oxide compounds. After gamma rays irradiation, the bandgap decreases but the pristine behavior is conserved indicating most likely that the electronic properties were not slightly altered. Nevertheless, because the optical transmission strongly decreased after the irradiation process, we assume this is correlated with the increase of the concentration of point-like defects. A similar observation was made by S. Antoheet al. for CdS/CdTe heterojunction when was irradiated with alpha particles [24]. The extinction coefficient, denoted here with k_0 , refers to the imaginary part of complex refractive index, and is a measure of attenuation when electromagnetic waves propagates through the material. The expression of k_0 [25] is:

$$k_0 = \frac{\alpha \lambda}{4\pi} \dots\dots\dots(2)$$

in which α is the absorption coefficient and λ is the wavelength of incident radiation. In Figure 2 the extinction coefficient dependences on the incident radiation energy, before and after irradiation with gamma rays, are presented. The values of the extinction coefficient strongly decreased after irradiation process, yet this is not something surprising because the absorption coefficient decreased after gamma rays irradiation. In order to prove that the assumptions we made were correct, the optical conductivity measurements were performed (see Figure 3). The increase of optical conductivity after gamma rays irradiation process confirms that the number of Coulombian interactions between Ni²⁺ vacancies and Mn²⁺ ions increased. This is due because the concentration of point-like defects was increased by the irradiation process. We assume the number of Ni²⁺ vacancies increased, acting as acceptor impurities and introducing a distinct energy level. However, the energy of acceptor impurities seems to be very close to that of the valence band, so the most electronic properties of pristine samples were conserved.

CONCLUSIONS

Thin films of doped Ni_(1-x)Mn_xO with different percentages of manganese (Mn – 2%, 4%, 6%, and 8%) were fabricated by co-precipitation method and were subjected to irradiation with gamma rays with energy of 0.662 MeV. The physical quantities describing the optical properties of obtained samples, such as optical transmission, bandgap,





Ahmed Nsaif Jasim et al.

extinction coefficient and optical conductivity, were analyzed and discussed one hand in terms of Mn doping ration and on the other hand in terms of induced changes by irradiation process. The optical transmission values decreased with both the increase of Mn doping ratio and after irradiation process, and for the latter one the decrease was more distinct. Same behavior was observed for the optical bandgap; the decrease after gamma rays irradiation was almost 10% for all fabricated Ni_(1-x)Mn_xO thin film. Significant larger values were determined for optical conductivity of irradiated samples proving that the number of point-like defects was increased. The obtained results indicate that despite the changes induced by irradiation process, the features of the optical behavior of non-irradiated samples were mostly preserved.

REFERENCES

1. G.A. Tiruye, D.M. Torrero, J. Palma, M. Anderson, R. Marcilla, *All-solid state supercapacitors operating at 3.5V by using ionic liquid based polymer electrolytes*, Journal of Power Sources **279** (2015) 472-480.
2. P. Mallick, C. Rath, A. Rath, A. Banerjee, N.C. Mishra, *Antiferro to superparamagnetic transition on Mn doping in NiO*, Solid State Communication **150** (2010) 1342-1345.
3. G. Wang, L. Zhang, J. Zhang, *A review of electrode materials for electrochemical supercapacitors*, Chemical Society Reviews **41** (2012) 797-828.
4. S. Sankar, S.K. Sharma, N. An, H. Lee, D.Y. Kim, Y.B. Im, Y.D. Cho, R. Sankar Ganesh, S. Ponnusamy, P. Raji, L.P. Purohit, *Photocatalytic properties of Mn-doped NiO spherical nanoparticles synthesized from sol-gel method*, Optik **127** (2016) 10727-10734.
5. R.J. Powell, W.E. Spicer, *Optical properties of NiO and CoO*, Physical Review B **2** (1970) 2182-2193.
6. G.A. Sawatzky, J.W. Allen, *Magnitude and origin of band gap in NiO*, Physical Review Letters **53** (1984) 2339-2342.
7. J. Wu, C.W. Nan, Y. Lin, Y. Deng, *Giant dielectric permittivity observed in Li and Ti doped NiO*, Physical Review Letters **89** (2002) 217601.
8. Y. Nakamura, H. Ogawa, T. Nakashima, A. Kishimoto, H. Yanagida, *Strain-dependent electrical conduction in the system NiO-CaO*, Journal of the American Ceramic Society **80** (1997) 1609-1611.
9. P. Kuiper, G. Kruizinga, J. Ghijsen, G.A. Sawatzky, H. Verweij, *Character of holes in Li_xNi_{1-x}O and their magnetic behavior*, Physical Review Letters **62** (1989) 221.
10. D. Hong, W. Yan, Q. Liu, T. Yao, Z. Sun, S. Wei, *Structures and magnetic properties of Mn-doped NiO thin films*, Journal of Physics D: Applied Physics **47** (2014) 295001.
11. W. Yan, Z. Sun, Z. Li, Q. Liu, T. Yao, Z. Pan, C. Wang, F. Hu, Y. Jiang, Z. Qi, F. Zeng, S. Wei, *Valence state-dependent ferromagnetism in Mn-doped NiO thin films*, Advanced Materials **24** (2012) 353-357.
12. L.S. Nair, D. Chandran, V.M. Anandakumar, K. RajendraBabu, *Structure and room-temperature ferromagnetism evolution of Sn and Mn-doped NiO synthesized by a sol-gel process*, Ceramics International **43** (2017) 11090-11096.
13. D. Guruvammal, S. Selvaraj, S.M. Sundar, *Effect of Ni doping on the structural, optical and magnetic properties of ZnO nanoparticles by solvothermal method*, Journal of Alloys and Compounds **682** (2016) 850-855.
14. V. Pazhanivelu, A. Paul Blessington Selvadurai, R. Kannan, R. Murugaraj, *Structural, optical and intrinsic defects induced magnetic properties of the ZnO:Fe nanoparticles*, Journal of Materials Science: Materials in Electronics **27** (2016) 5549-5556.
15. D. Sharma, R. Jha, *Transition metal (Co, Mn) co-doped ZnO nanoparticles: effect on structural and optical properties*, Journal of Alloys and Compounds **698** (2017) 532-538.
16. K. Vallalperuman, M. Parthibavarman, S. Sathishkumar, M. Durairaj, K. Thavamani, *Synthesis and characterization of Co and Mn doped NiO nanoparticles*, Korean Journal of Chemical Engineering **31** (2014) 639-643.
17. K.K. Lyu, T.L. Phan, S.C. Yu, S.K. Oh, N.H. Dan, *Influence of annealing temperature on spin dynamics of Mn in metal oxides: Electron Spin Resonance study*, IEEE Transactions on Magnetics **46** (2010) 2028-2031.
18. Z.V. Saponjic, N.M. Dimitrijevic, O.G. Poluektov, L.X. Chen, E. Wasinger, U. Welp, D.M. Tiede, X.B. Zuo, T. Rajh, *Charge separation and surface reconstruction: A Mn²⁺ doping study*, The Journal of Physical Chemistry B **110** (2006) 25441-25450.





Ahmed Nsaif Jasim et al.

19. S. Iftimie, F.F. Baiasu, A. Radu, V.A. Antohe, S. Antohe, L. Ion, *On the structural, optical and morphological properties of ZnSe_{1-x}O_x thin films grown by rf-magnetron sputtering*, Chalcogenide Letters **15**(2018) 389-394.
20. M. Kobayashi, J. Hwang, G. Song, Y. Ooki, M. Takizawa, A. Fujimori, Y. Takeda, S-I Fujimori, K. Terai, T. Okane, *Systematic changes of the electronic structure of the diluted ferromagnetic oxide Li-doped Ni_{1-x}Fe_xO with hole doping*, Physical Review B **78** (2008) 155322.
21. S. Iftimie, C. Tazlaoanu, A. Radu, R. Constantineanu, C. Vancea, N. Korganci, L. Ion, S. Antohe, *The spectral response of the photovoltaic cells based on CdS/CdTe heterojunction with different TCO's*, Digest Journal of Nanomaterials and Biostructures **9**(2014) 213-221.
22. R. Bazavan, L. Ion, G. Socol, I. Enculescu, D. Bazavan, C. Tazlaoanu, A. Lorinczi, I.N. Mihailescu, M. Popescu, S. Antohe, *Optical properties of pulsed-laser deposited ZnO thin films*, Journal of Optoelectronics and Advanced Materials **11** (2009) 425-428.
23. D.K. Kanan, E.A. Carter, *Band gap engineering of MnO via ZnO alloying: a potential new visible-light photocatalyst*, Journal of Physical Chemistry C **116**(2012) 9876-9887.
24. S. Antohe, V. Ghenescu, S. Iftimie, A. Radu, O. Toma, L. Ion, *Effects of alpha particles irradiation on the photo-electrical properties of CdS/CdTe heterojunctions*, Digest Journal of Nanomaterials and Biostructures **7**(2012) 941-946.
25. F. Stanculescu, M. Socol, E. Matei, A. Stanculescu, *Effect of heavy ions irradiation on the properties of benzil crystals*, Crystal Research and Technology **52**(2017) 1700047.

Table 1. The calculated values of optical bandgap of fabricated Ni_(1-x)Mn_xO thin films, before and after irradiation process with gamma rays.

Percent of manganese doping on nickel oxide films	Optical bandgap (E _g) (eV)	
	Before irradiation	After irradiation
2%	3.58	3.30
4%	3.57	3.25
6%	3.55	3.21
8%	3.53	3.20

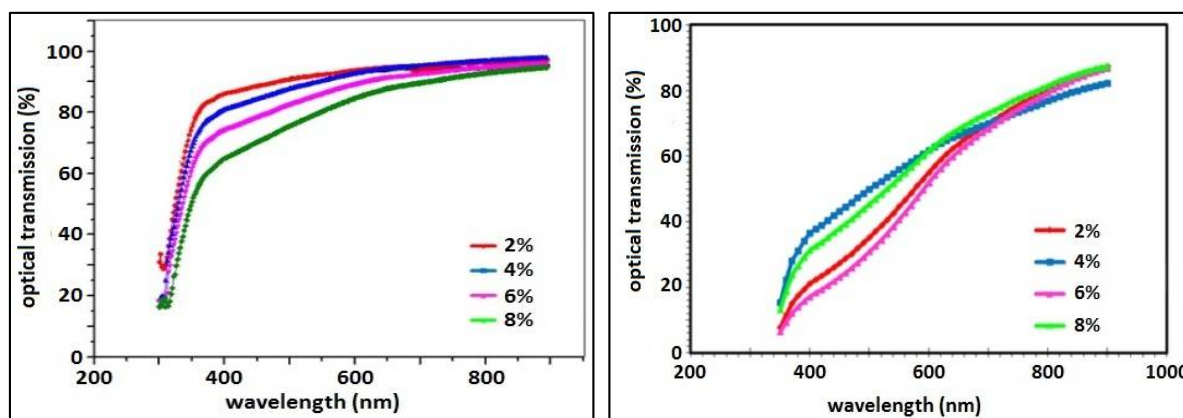


Fig.1. Optical transmission of fabricated Ni_(1-x)Mn_xO thin films, before (left side) and after (right side) irradiation with gamma rays. The gamma rays energy was 0.662 MeV.





Ahmed Nsaif Jasim et al.

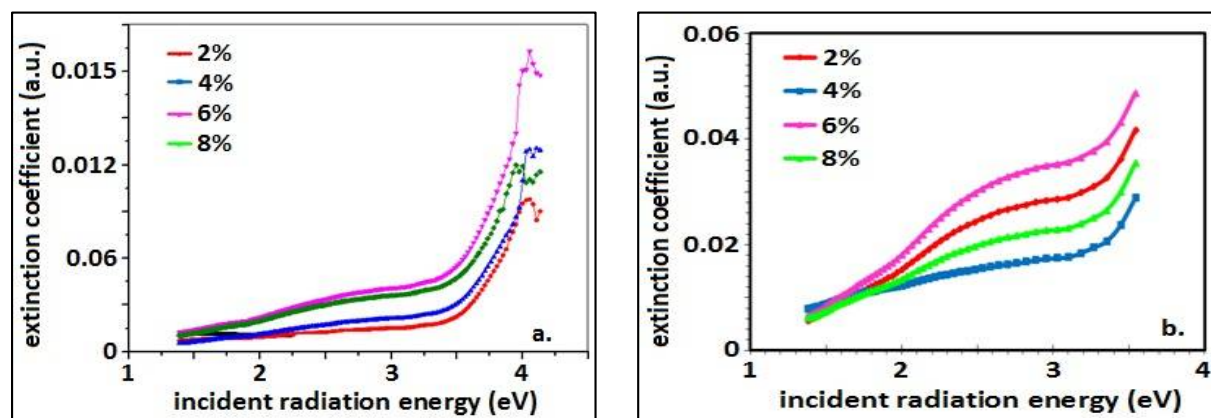


Fig.2. Extinction coefficient of fabricated of fabricated $Ni_{(1-x)}Mn_xO$ samples, before (a) and after (b) irradiation with gamma rays. The source of gamma rays was Cs137 and the energy was 0.662 MeV

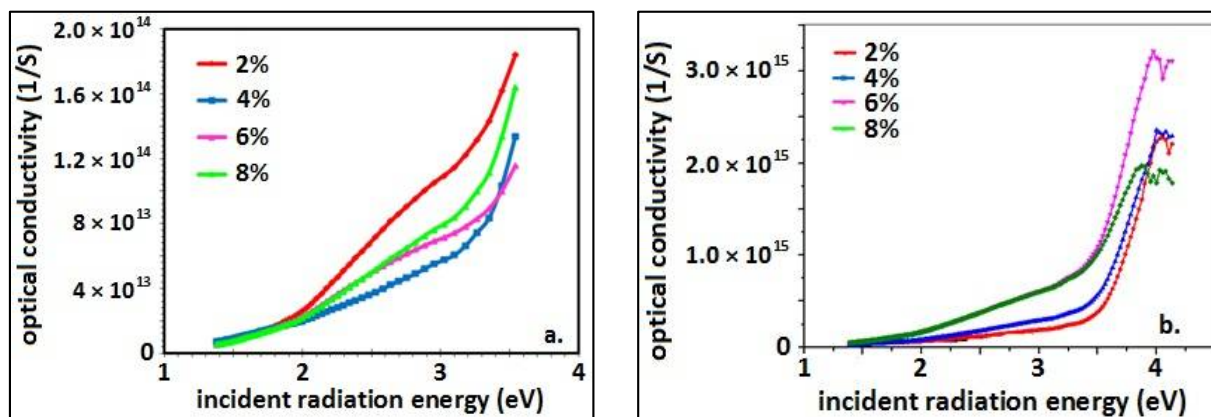


Fig .3. Optical conductivity dependence on the incident radiation energy for $Ni_{(1-x)}Mn_xO$ thin films, (a) before and (b) after irradiation with gamma rays. The energy of gamma rays was 0.662 MeV.





Effect of Heavy Metal Residues in Breast Milk: Intelligent Modeling

Tedjar L^{1*}, Bouharati S^{2,3}, Allag F³ and Bounechada M³.

¹Faculty of Medicine, Ferhat Abbas Setif1 University, Algeria

²Laboratory of Intelligent Systems, Ferhat Abbas Setif1 University, Algeria

³Faculty of Natural Science and Life, Ferhat Abbas Setif1 University, Algeria

Received: 21 Oct 2018

Revised: 25 Nov 2018

Accepted: 29 Dec 2018

*Address for Correspondence

Tedjar L

Faculty of Medicine,

Ferhat Abbas Setif1 University,Algeria.

Email: sbouharati@univ-setif.dz



This is an Open Access Journal / article distributed under the terms of the **Creative Commons Attribution License** (CC BY-NC-ND 3.0) which permits unrestricted use, distribution, and reproduction in any medium, provided the original work is properly cited. All rights reserved.

ABSTRACT

No one doubts the benefits of breast milk and the nutritional benefits it offers to both infants and mothers. Its composition offers bioactive elements, anti-infective, anti-inflammatory as well as growth factors. However, several chemicals can pass from breast milk to the child. Among these substances, heavy metals considered toxic are found in breast milk as residues accumulated by different processes. The analysis of the effect of these on infant growth is very complex. Several factors interfere. Given the complexity of the system, this study attempts to model the different factors and the effects they have on newborns. An intelligent system based on artificial neural networks is established. After learning the network, this will predict the impact of these residues and their consequences on the growth of the child.

Key words: Brest milk, Infant, Heavy metals, Artificial neural networks, Intelligent Systems.

INTRODUCTION

Breast milk and its use guarantee nutrition and optimizing the health of infants and their mothers (1). In addition, it contains several factors that ensure the growth of the infant by protecting it with bioactive elements, anti-infective and anti-inflammatory (2). This characteristic is not limited to humans; it concerns all mammals regardless of age, because its richness in protein and calcium gives it this specificity (3). Its composition provided from different food sources, maternal reserves or by synthesis of lactocytes (4). However, individual metabolisms regulating hormone levels are influenced by environmental and chemical factors to which they are exposed (5). This affects the production of breast milk itself and the physiology of lactation in general (6). With all these beneficial qualities, several chemicals can pass from breast milk to infants and can be a serious hazard (7). These chemical elements are mainly heavy metals. They are of domestic, industrial, medical or agricultural origin and spread in the environment affecting fauna and flora and are harmful to human health (8), (9). Since maternal nutrients are derived from agricultural soils which are rich in heavy metals from phosphate fertilizers and pesticides, in addition to heavy water



**Tedjar L et al.**

heavy-water irrigation (10), this has a direct impact on the health of the infant. These elements are stored in breast milk and even in the blood during pregnancy and breastfeeding (11). Knowing that several functional proteins contained in milk or blood interact with metal ions inducing malfunction of the metalloproteinase (12), (13). Given the importance and complexity related to the level of exposure of certain chemicals that affects the breastfeeding process (14), some analytical techniques are related to environmental exposure is interested in epidemiological investigations (15), (16). Some other methods explore absorption pathways, whereas recently other techniques use bio-markers (17). But virtually all of the studies on the subject, whether breast milk or infant foods, lack the quantification of heavy metals. This may be because of the difficulty in quantifying the amount of breast milk absorbed by the newborn during his or her breastfeeding phase (18). Since the system is very complex in its entirety, because the toxicity is a function of several factors that we evoke in what follows, this study proposes to analyze the effect of these factors on the infant's health by using an intelligent network analysis. As long as these networks have the capacity to support a large amount of data, their application in this case is adequate. The proposed network is two spaces (input-output) mapped in learning phase. When the transfer function between the two spaces is adjusted, it becomes possible to predict the effect of these elements on the health of the infant.

MATERIALS AND METHODS

The study highlights the drivers of heavy metal pollution that affect breast milk and its impact on breastfed newborns.

Factors

Despite several published studies on the concentration of heavy metals in breast milk and their variation during the lactation period, the results are inconclusive (19). The complexity comes from the fact that toxicity is a function of a multitude of imprecise and uncertain factors. The chemical elements concerned are mainly mentioned, their concentration and the duration of exposure. This has increased significantly with their use in industrial, agricultural, technological or agricultural applications (20). Also, what further complicates the process is that physical factors also have their effects. The temperature for example influences the adsorption and the retention of these elements (21). Other factors related to the mother whose liposolubility and protein-drug binding is a function of the number of pregnancy and age. This is related to maternal factors in terms of biochemical adaptation where the physiological aspect plays a vital role. (22). In general, we can classify factors that are related to the mother such as age, weight, number of pregnancies (primiparous or multiparous), level of education, occupation (woman who works or housewife, diet). The diet is directly related to heavy metals in breast milk (Pb, Cd, Al, As) depending on the mother's consumption of fish, preserved foods, or vegetables and alcohol consumption. Other factors related to the child such as (gestational age, baby's birth weight and height) .

Effect

Heavy metals in general have an effect on plants and animals, they are necessary for enzymatic activity and oxidation-reduction reactions (23). However, some heavy metals and at given concentrations have an adverse effect and affect cell organelles and even some enzymes involved in detoxification and repair (24). The metal ions of these even go as far as their interaction with DNA and can generate cell cycle modulations and thus carcinogenesis (25), (26), (27). Studies have reported that oxidative stress plays a role in the carcinogenicity of heavy metals such as arsenic, for example (28), (29), (30). Cardiovascular diseases, neurological disorders, diabetes, hearing loss, hematological, and immunological disorders can also result from environmental contamination by heavy metals. Their effects even affect the development of the child. Since young children are the most vulnerable to heavy metal intoxication by absorption and absorption of these elements via the gastrointestinal tract, the effect of arsenic, cadmium, lead and aluminum is more serious even at low doses (31), (32), (33), (34).





Tedjar L et al.

Artificial neural network proposed

Neural systems are imitations of the natural neural network. In this, it consists of two spaces (input-output). Instead of the signals received by the senses in the natural system, these are replaced by numerical values characterizing the input variables of the system. The reaction produced by the brain in the natural system is replaced by the output variable corresponding to the input values (35). The main step in the analysis by artificial neural networks is learning. This is the correspondence between the input variables and the output variable. A transfer function $f(x)$ is created. With each variation of one or more input variables in correspondence with the output variable, the function is adjusted. We notice that one of the advantages of these networks is that it is not necessary to change the function. It is sufficient to act on mathematical coefficients (weight) (36). The neural system possesses the dynamic analysis of the data of the real environment and the resolution of complex phenomena. These properties give it the opportunity to be applied in different fields, from medical to environmental field (37). In our case, the built system is three-layered: An input layer, an output layer, and a hidden layer (Figure 1).

Input Variables

Input variables are the factors that produce effects an effect on infants. (age of mother, weight of mother, number of pregnancies (primiparous or multiparous), level of education, occupation (woman who works or housewife), diet, gestational age, baby's birth weight and height of baby. Note that the mother's diet determines the nature of the heavy metal chemicals absorbed.

Output Variable

The output variable expresses the degree to which the infant is affected by the toxic effects associated with the presence of heavy metals in breast milk. This attack can be expressed by various diseases mentioned above. Each input or output variable is numerically encoded in levels (1,2,3) Table 1. For example, the age of the mother is coded in three levels (1: Young age, 2: Middle age, 3: Elderly), Pregnancies number (1: primiparous, 2: multiparous), the degree of toxicity of the baby is expressed by three levels as well (1: Low toxicity, 2: Medium toxicity, 3: Severe toxicity). In the same way, all the variables are expressed. It is then necessary to introduce all the possible combinations between the inputs coded levels and the output coded levels.

RESULTS AND DISCUSSION

The applied network system is three-layer (input, hidden and output) Figure 1. All possible combinations assigned to the input variables in correspondence with the output variable serve as an adjustment of the I / O transfer function. This is done during the learning phase. With the shape-preserving interpolant, the uses of the centred and scaled variable gives :

$$Z = (X - \mu) / \sigma$$

$$\mu = 28$$

$$\sigma = 16.598$$

The adjustment of the function is made by variations of the mathematical coefficients (weight). The function is optimized to the minimum error value. In our case, the optimum is reached after 58 adjustment cycles and represents $6.856 \cdot 10^{-8}$. Figure 2.



**Tedjar L et al.**

CONCLUSION

From the real cases of women, input variables are collected. Each variable combination is mapped to the corresponding output variable saved. The set of possible cases are coded on three levels (1, 2, 3) in the form of an Excel table. The proposed algorithm automatically reads the values from the table to establish the learning function. It should be noted that the higher the number of variables, the greater the accuracy. The function established with an optimal adjustment makes it possible to predict the he output variable that expresses the degree to which the infant is affected by the toxic effects associated with the presence of heavy metals in breast milk. This tool can be used to predict the effect of each factor at the input of the system. Just enter values at the input to read immediately the result that gives the output. The system only refers to the function already established. In this way, we can display any factor at the input of the system to take advantage of it

Conflict of interest

The author declares that there is no conflict of interests regarding the publication of this manuscript.

REFERENCES

1. Section on Breastfeeding (2012) Breastfeeding and the use of human milk. *Pediatrics* 129: e827-841.
2. Ballard O, Morrow AL (2013) Human milk composition: nutrients and bioactive factors. *Pediatr Clin North Am* 60: 49-74.
3. Zeluta A, Maurizi A, Frigola A, Esteve MJ, Coli R, Burini G. Antioxidant capacity of cow milk, whey and deproteinized milk. *J. Int. Dairy*. 2009;19:380-385.
4. Salama AK (2017) Lactational Exposure to Pesticides: A Review. *Toxicol Open Access* 3: 123.
5. Martin MB, Reiter R, Pham T, Avellanet YR, Camara J, Lahm M. Estrogen-like activity of metals in MCF-7 breast cancer cells. *Endocrinology*. 2006;144(6): 2425-36.
6. Sooyeon L and Shannon LK. Biological underpinnings of breastfeeding challenges: the role of genetics, diet, and environment on lactation physiology. *Am J Physiol Endocrinol Metab* 311: E405–E422, 2016. doi:10.1152/ajpendo.00495.2015
7. Wolf MS (1983) Occupationally derived chemicals in breast milk. *Am J Ind Med* 4: 259-281.
8. Paul BT, Clement GY, Anita KP, and Dwayne JS. (2012). Heavy Metals Toxicity and the Environment. *EXS*. 101: 133–164. doi:10.1007/978-3-7643-8340-4_6.
9. He ZL, Yang XE, Stoffella PJ. (2005). Trace elements in agroecosystems and impacts on the environment. *J Trace Elem Med Biol*. 19(2–3):125–140. [PubMed: 16325528]
10. Salem HM, Eweida AE, Farag A. Heavy metals in drinking water and their environmental impact on human health. *ICEHM2000*. 2000;542-556.
11. Örün E, Yalçın SS, Aykut O, Orhan G, Morgil GK, Yurdakök K, et al. (2011). Breast milk lead and cadmium levels from suburban areas of Ankara. *Sci Total Environ*. 409:2467–72.
12. Pozzi CMC, Braga CP, Vieira JCS, Cavecci B, Vitor de Queiroz J, de Souza Barbosa H, et al. (2017). Metal ions bound to the human milk immunoglobulin A: Metalloproteomic approach. *Food Chem*. 015;166:492–7.
13. Odintsova ES, Zaksas NP, Buneva VN, Nevinsky GA. (2011). Metal dependent hydrolysis of β -casein by slgA antibodies from human milk. *J Mol Recogit*. 24:45–59.
14. Jensen AA, Slorach SA (1991) Chemical Contaminants in Human Milk. CRC Press Inc., Boca Raton, FL.
15. Harper M, Weis C, Pleil JD, Blount BC, Miller A, et al. (2015). Commentary on the contributions and future role of occupational exposure science in a vision and strategy for the discipline of exposure science. *Journal of exposure science and environmental epidemiology* 25: 381-387.
16. Pleil JD, Blount BC, Waidyanatha S, Harper M (2012). Establishing exposure science as a distinct scientific discipline. *J Expo Sci Environ Epidemiol* 22: 317- 319



**Tedjar L et al.**

17. Bean HD, Pleil JD, Hill JE (2015). Editorial: new analytical and statistical approaches for interpreting the relationships among environmental stressors and biomarkers. *Biomarkers* 20: 1-4.
18. Moore SE, Prentice AM, Coward WA, Wright A, Frongillo EA, Fulford AJ, et al. (2007). Use of stable-isotope techniques to validate infant feeding practices reported by Bangladeshi women receiving breastfeeding counseling. *Am J Clin Nutr.* 85:1075–82.
19. H.-H. Chao et al. (2002). Arsenic, Cadmium, Lead, and Aluminium Concentrations in Human Milk at Early Stages of Lactation *Pediatrics and Neonatology* (2014) 55, 127e134. <http://dx.doi.org/10.1016/j.pedneo.2013.08.005>
20. Bradl, H., editor. *Heavy Metals in the Environment: Origin, Interaction and Remediation Volume 6*. London: Academic Press.
21. Hamelink, JL.; Landrum, PF.; Harold, BL.; William, BH., editors. (1994). *Bioavailability: Physical, Chemical, and Biological Interactions*. Boca Raton, FL: CRC Press Inc.
22. Verkleji, JAS. (1993). The effects of heavy metals stress on higher plants and their use as biomonitors In *Plant as Bioindicators: Indicators of Heavy Metals in the Terrestrial Environment*. Markert, B., editor. New York: VCH. p. 415-424.
23. WHO/FAO/IAEA. World Health Organization. Switzerland: Geneva; (1996). *Trace Elements in Human Nutrition and Health*.
24. Wang S, Shi X. (2001). Molecular mechanisms of metal toxicity and carcinogenesis. *Mol Cell Biochem.* 2001; 222:3–9. [PubMed: 11678608]
25. Wang S, Shi X. (2001). Molecular mechanisms of metal toxicity and carcinogenesis. *Mol Cell Biochem.* 222:3–9. [PubMed: 11678608]
26. Chang, LW.; Magos, L.; Suzuki, T., editors. (2008). *Toxicology of Metals*. Boca Raton, FL, USA: CRC Press; 1996.
27. Beyersmann D, Hartwig A. Carcinogenic metal compounds: recent insight into molecular and cellular mechanisms. *Arch Toxicol.* 82(8):493–512. [PubMed: 18496671]
28. Yedjou CG, Tchounwou PB. (2006). Oxidative stress in human leukemia cells (HL-60), human liver carcinoma cells (HepG2) and human Jerkat-T cells exposed to arsenic trioxide. *Metal Ions Biol Med.* 9:298–303.
29. Yedjou GC, Tchounwou PB. (2007). In vitro cytotoxic and genotoxic effects of arsenic trioxide on human leukemia cells using the MTT and alkaline single cell gel electrophoresis (comet) assays. *Mol Cell Biochem.* 2007; 301:123–130. [PubMed: 17216127]
30. Tchounwou PB, Centeno JA, Patlolla AK. (2004). Arsenic toxicity, mutagenesis and carcinogenesis – a health risk assessment and management approach. *Mol Cell Biochem.* 255:47–55. [PubMed: 14971645]
31. Jensen AA. Levels and trends of environmental chemicals in human milk. In: Jensen AA, Slorach SA, editors. (1991). *Chemical contaminants in human milk*. Boston: CRC Press Inc; 1991. p. 45e198.
32. Eklund G, Tallkvist J, Oskarsson A. (2004). A piglet model for studies of gastrointestinal uptake of cadmium in neonates. *Toxicol Lett* 2004;146:237e47.
33. Ziegler EE, Edwards BB, Jensen RL, Mahaffey KR, Fomon SJ. (1978). Absorption and retention of lead by infants. *Pediatric Res.* 12:29e34.
34. IPCS (International Programme on Chemical Safety). *Inorganic Lead. Environmental Health Criteria 165*. Geneva: World Health Organization; 1995.
35. Bouharati I., Babouche F., Bouharati K., Hamdi-Cherif M., and Bouharati S. (2018). An analysis of cranial radiography in post-mortem recognition. *Radiol Diagn Imaging, Volume 2(1): 1-3*. doi: 10.15761/RDI.1000124
36. Bouharati I., El-Hachmi S., Babouche F., Khenchouche A., Bouharati K., Bouharati S. *Radiology and management of recurrent varicose veins: Risk factors analysis using artificial neural networks. Journal of Medicine, Radiology, Pathology & Surgery* (2018), 5, 1–5
37. Khenchouche A, Bouharati K, Bouharati S, Mahnane A, Hamdi-Cherif M. (2017). Post mortem interval: Necrobiome analysis using artificial neural networks. *Comput Biol Bioinform.* 5:90-6.





Tedjar L et al.

Table 1. Coding input and output variables

Age mother	Weight mother	Pregnancies number	Education level	Occupation	Diet	Gestational age	Birth weight	Birth height	Degree of induced toxicity
1	1	1	1	1	1	1	1	1	1
2	2	2	2	2	2	2	2	2	2
3	3	3	3	3	3	3	3	3	3

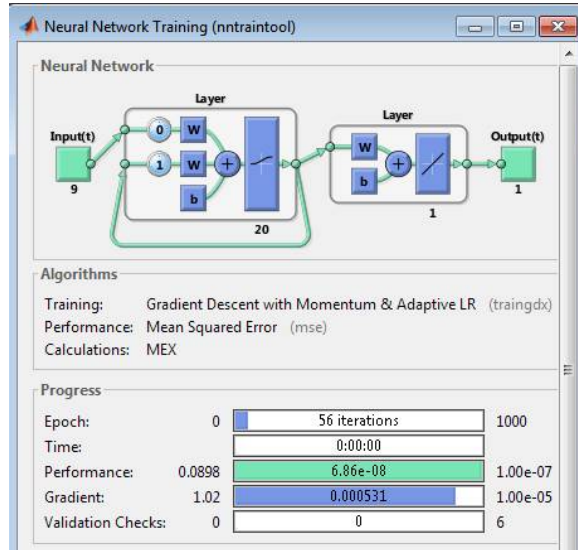


Figure 1. Block diagram of the system.

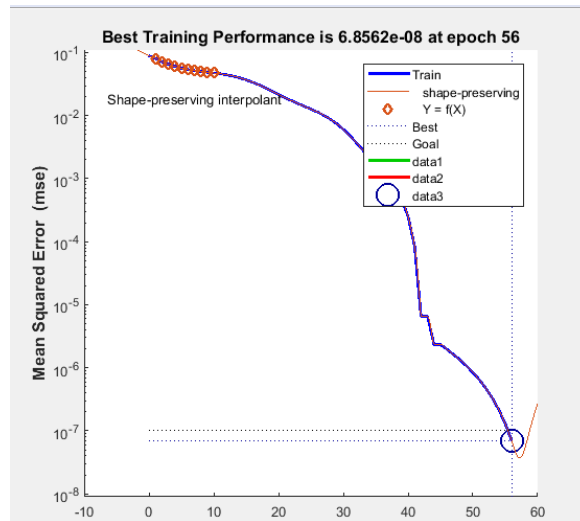


Figure 2. the adjusted transfer function





Toxic Pathological Changes on Albino Mice after Exposures to Cypermethrin

Salema Lafta Hassan*

Department of Pathology and Poultry Diseases, College of Veterinary Medicine, University of Baghdad, Iraq.

Received: 26 Oct 2018

Revised: 28 Nov 2018

Accepted: 31 Dec 2018

*Address for Correspondence

Salema Lafta Hassan

Department of Pathology and Poultry Diseases,
College of Veterinary Medicine,
University of Baghdad, Iraq



This is an Open Access Journal / article distributed under the terms of the **Creative Commons Attribution License** (CC BY-NC-ND 3.0) which permits unrestricted use, distribution, and reproduction in any medium, provided the original work is properly cited. All rights reserved.

ABSTRACT

The objective of the present study was to evaluate the toxic effect of cypermethrin on the histological state of internal organ of mice. Forty adult *Swiss Albino* mice at the age of two months were divided into four groups. The 1st group (G1) was administrated orally with with 1/10 LD50 (8.5 mg/kg bw) of cypermethrin daily for 8 weeks, 2nd group (G2) was administrated cypermethrin as G1 group and at the same time and at the same time vitamin C ((200 mg/kg bw)) with diet for 8 weeks. 3rd group (G3) was group was feeding with vitamin C (200 mg/kg bw) 4rd group (G4) was considered as control negative. At end of the experiments (8 weeks), all animals were sacrificed and Specimens were taken from liver and kidney. The tissues were kept in 10% formaldehyde solution, for fixation, and then processed routinely by using the histokinete. Tissue sections were embedded in paraffin blocks, and sectioned by microtome and stained with hematoxylin and eosin stain, then examined by using light microscope. Biochemical results showed that cypermethrin caused elevation in serum malondialdihyde (MDA), and peroxy nitrite concentration. The pathological lesions showed that the animals exposed to toxic dose of cypermethrin was characterized by inflammatory reaction, hemorrhage, congested blood vessels, necrosis, fibrosis and multiple granuloma lesions in liver and kidney while less lesions were recorded showed improvement against toxic effect cypermethrin in the groups treated with vitamin C.

Keywords: cypermethrin, vitamin C, Histopathological changes, internal organs, *Albino mice*.

INTRODUCTION

Cypermethrin is a synthetic pyrethroid insecticide used to kill insects on cotton and lettuce, also to kill cockroaches, fleas, and termites in houses and other buildings^[1]. Cypermethrin residues have been found in milk from cows wearing cypermethrin-impregnated ear tags (as a horn fly control measure)^[2]. cypermethrin has been found to accumulate in body fat, skin, liver, kidneys, adrenal glands, ovaries, and brain^[3]. The increased uses of pesticides in



**Salema Lafta Hassan**

agriculture have introduced serious hazards to the human beings and their livestock, prolonged exposure to some of these chemicals causes disturbance in the physiological activities beside other pathological features [4],[5] reported that cypermethrin induces systemic genotoxicity in mice as it causes DNA damage in vital organs like brain, liver, kidney, apart from that in the haematopoietic system. The present work studied the effect of cinnamon on kidney injury induced by cypermethrin in albino rats. Pesticide accumulation in tissue is associated with induction of oxidative stress and production of ROS. Increase in LPO was also associated with decrease in GSH and enzymatic antioxidants. It is postulated that accumulation of cypermethrin increased oxidative stress with increase in ROS. Increased ROS depleted the cellular level of GSH pool. The decrease in cellular level of GSH pool has further enhanced oxidative stress. The enhanced ROS damaged cell membrane structure leading to loss of function and reduced cell viability [6], the reduction in GSH level may be due to direct conjugation of GSH with electrophiles species produced by cypermethrin exposure or due to inhibition of GR and GPx. Reduction in SOD level may be due to excessive ROS. The excessive ROS may leading to cell damage [7].

MATERIALS AND METHODS

Animals and Experimental Design

Forty adult Swiss Albinomice age (2-3) months were allocated into four groups. The 1st group (G1) was administered orally with 1/10 LD50 (8.5 mg/kg bw) of cypermethrin daily for 8 weeks, 2nd group (G2) was administered cypermethrin as G1 group and at the same time and at the same time vitamin C (200 mg/kg bw) with diet for 8 weeks. 3rd group (G3) was feeding with vitamin C (200 mg/kg bw), 4th group (G4) was considered as control group. Pesticide: cypermethrin (95% purity) was obtained from Indian limited Chennai commercial cypermethrin-Cyano-(3-phenoxyphenyl)methyl(±)-cis/trans-3-(2,2 dichlorovinyl)2,2dimethyl-cyclopropanecarboxylate], was used at a dose level of 1/10 LD50 (8.5 mg/kg b.w.). Vitamin C (L-3-ketothreohexuronic acid lactone), was purchased from Pharmaceutical Industries, Egypt.

Biochemical assays

For biochemical study sera were obtained by centrifugation of the blood samples and stored at 20°C until assayed for the biochemical parameters (malondialdehyde) according to [8] and Peroxynitrite according to [9].

Histopathology

At the end of the experiments (8 weeks), all animals were authorized by open ether exposure (diethyl ether, (C₂H₅)₂O) and blood samples were taken for serum peroxynitrite and malondialdehyde concentration. Samples of liver and kidney were collected and fixed in 10% neutral buffer formalin for 72 hr for.

Statistical analysis

Statistical analysis was applied by two ways ANOVA and the mean difference was significant at the (P≤0.05) level by statistical package for social sciences [10].

RESULTS

Clinical signs were closely observed and continuously recorded along the period of experiment which is in 8 weeks, also any change in activity or behavior was noted.



**Salema Lafta Hassan****Biochemical analysis**

The effect of the cypermethrin plasma malondialdehyde and peroxy nitrite analytes in albino mice during chronic toxicity study is given in (Tab.1). There was a significant increase ($P \leq 0.05$) in the levels of the plasma malondialdehyde and peroxy nitrite after oral administration of cypermethrin as in G1 (3.95 ± 0.0058 , 3.86 ± 0.0041) and G2 (2.45 ± 0.059 , 2.50 ± 0.052) (8 weeks) in compared to G3 (0.30 ± 0.0050 , 38 ± 0.066) and G4 (0.18 ± 0.003 , 0.20 ± 0.021).

Histopathological Examinations**Histopathological changes of animals administrated orally with with 1/10 LD50 (8.5 mg/kg bw) of cypermethrin daily for 8 weeks****Liver**

The changes of liver showed severe areas of vacuolar degenerative changes of hepatocytes (fig. 1), congestion of blood vessels with infiltration of mononuclear inflammatory cells (fig.2). In addition for newly formed bile ductules, infiltration of mononuclear inflammatory cells as well as vacuolar degenerative changes of hepatocytes (Fig: 3), in other sections the changes showed a wide spread hemorrhage, cloudy swelling of hepatocyte with a severe thick fibrous connective tissue observed in the liver.

Kidney

The changes of kidney showed hemorrhage appeared in the intertubular spaces and severe areas of degenerative changes of renal tubules (fig. 4), also signs of per glomerular edema and necrosis of some renal tubules lining cells (fig. 5) in addition to congested blood vessels. The intertubular spaces were infiltrated by inflammatory cells. The walls of Bowman's capsule were eroded and the glomeruli were fragmented and atrophied.

Histopathological changes of animals administrated cypermethrin as G1 group and at the same time and at the same time vitamin C (200 mg/kg bw) with diet for 8 weeks**Liver**

The changes showed marked peri vascular mononuclear cells aggregation at the portal area and central vein with necrosis of hepatocytes (fig. 6), in addition to microabscess lesion in the parenchyma consisting from aggregation of activated macrophages, lymphocytes and hyper cellularity of kupffer cells.

Kidney

Histopathological section of the kidney explained congested blood vessels with neutrophils and mononuclear cells in their lumens. Histopathological changes of animals feeding with vitamin C.

Liver

The main lesions in the examined organs of this group characterized by marked mononuclear cells aggregation around blood vessels and central with hyper cellularity of kupffer cells in the liver (fig. 7).

Kidney

Mononuclear cells aggregation in the interstitial tissue and between renal tubules (Fig: 8).



**Salema Lafta Hassan****Control group**

There were no significant macroscopic findings.

DISCUSSION

The present study revealed high levels of serum of malondialdehyde and peroxynitrite radical in animals treated by cypermethrin, this result may indicate that cypermethrin act as oxidative agent that induced damage of the cell membrane via lipid peroxidation result in increasing levels of malondialdehyde and peroxynitrite radical which were the main lipid peroxidation products, this observation supports the idea that mentioned by^[11]who observed increase in malondialdehyde level and decrease in the activities of catalase, superoxide dismutase in liver of rat. Thus, the hepatotoxicity of cypermethrin observed in the current study may be due to oxidative stress induced by cypermethrin. In addition to these observations are in agreement with ^[12], reported that cypermethrin is induce free radicals in the liver of rabbits as well as lipid peroxidation in rat erythrocytes ^[13]thus induces oxidative stress. The results of histopathological examination of liver and kidney exhibited pathological changes in these organs and considered as toxic substance even in its low doses.

These observations are in agreement with ^[14]who reported that cypermethrin intoxication in rats resulted in necrosis of hepatic cells with pyknotic nuclei, disorganization of hepatic laminae and dilatation of sinusoids in hepatic structure. As well as Mamun^[12], who reported that liver and kidney of mice treated with cypermethrin showed vacuole formations in hepatocytes, dilation in the sinusoidal space, mononuclear cell infiltrations and congestion of blood vessels with hemorrhage. The present study revealed low levels of serum of malondialdehyde (MDA) and peroxynitrite radical in animals feeding vitamin C this result may indicate that the potential mechanism underlying the hepatoprotective effect of vitamin C that act as potent antioxidant and free radical scavenger, further helps reconstitution of the depleted GSH as it ameliorates the oxidative stress and enhance, as an important enzyme co-factor, the activities of GSH detoxification enzyme system ^[15]. This study indicated that vitamin C was often more efficient in its protective action against the cypermethrin. Vitamin C has a number of activities that could conceivably contribute to its immune-modulating effects.

It is a highly effective antioxidant, due to its ability to readily donate electrons, thus protecting important biomolecules (proteins, lipids, carbohydrates, and nucleic acids) from damage by oxidants generated during normal cell metabolism and through exposure to toxins and pollutants ^[16]. Vitamin C is also a cofactor for a family of biosynthetic and gene regulatory monooxygenase and dioxygenase enzymes ^[17]. Vitamin C has long been known as a cofactor for the lysyl and prolyl hydroxylases required for stabilization of the tertiary structure of collagen, and is a cofactor for the two hydroxylases involved in carnitine biosynthesis, a molecule required for transport of fatty acids into mitochondria for generation of metabolic energy. However, we demonstrated that mild pathological lesions in animal feed vitamins C these result due to effects of vitamin C which provide cellular defense against the uncontrolled generation of reactive oxygen species (ROS) from normal aerobic metabolism and by oxidative challenges such as pollution, infection, tissue damage and oxidative drug, which can damage biological membranes and DNA ^[18].

Furthermore, It has been confirmed that oxidation of leukocytes membrane lipids can change the synthesis of some complement proteins and consequently their functions ^[19]. Hence, alterations in leukocyte membrane due to different intakes of vitamin E and C, and also function of these vitamins through ROS pathway maybe modulate the complement activity and enhance immunity in fish. Vitamin C is a free-radical scavenger that can scavenge superoxide and peroxy radicals, hydrogen peroxide, hypochlorous acid, and oxidant air pollutants ^[20]. The antioxidant properties of vitamin C enable it to protect lung cells exposed to oxidants and oxidant-mediated damage caused by various pollutants, heavy metals, pesticides, and xenobiotics^[21]. Vitamins C and E are among the most





Salema Lafta Hassan

important nutrients influencing specific and non-specific immune responses of fishes [22] Vitamin C is an essential micronutrient and water-soluble antioxidant in biological fluids, which is associated to biochemical reactions in cells and tissues. Its deficiency can increase disease susceptibility in fishes affecting their immune system [23].

REFERENCES

1. Cox C. Cypermethrin. J. Pesticide Reform, 1996;16.2:15-20.
2. Braun H, Frank R, Miller I. Residues of cypermethrin in milk from cows wearing impregnated ear tags. Bull. Environ. Contam. Toxicol. 1985; 35: 61-64.
3. Hall BE, Vickers JA, Hopkins JA. A study to determine the bioaccumulation of 14C-cypermethrin radioactivity in the rat following repeated oral administration, Report No. 1980; 2487-72.
4. Kulkarni S, Hodgson M. Effect of pyrethroids on rat liver ATPase activities. J. Toxicol. Environ. Health, 1980; 14.203: 257- 266.
5. Patel S, Pandey A, Bajpayee M, Parmar D, Dhawan A. Cypermethrin- induced DNA damage in organs and tissues of the mouse: evidence from the comet assay. Mutat Res., 2006; 607:176-83.
6. Kale M, Rathore N, Jone S, Bhatnagar D. Lipid peroxidation damage on pyrethroid exposure and alterations in antioxidant status in rat erythrocytes. A possible involvement of reactive oxygen species. Toxicol. Lett., 1999;105:197-205.
7. Otitoju O, Onwurah IN, Grace TO, Ugwu CE. Oxidative stress and superoxide dismutase activity in brain of rats fed with diet containing permethrin. Biochem, 2008; 20:93-0.
8. Ohkawa H, Ohishi N, Yagi K. Assay for lipid peroxidase in animal tissue by thiobarbituric acid reaction. Anal Biochem. 1979; 95: 351-358.
9. van Uffelen BE, Van der Zee J, deKoster BM, Van Sterenink J, and Elferink JG. Intracellular but not extracellular conversion of nitroxyl anion into nitric oxide leads to stimulation of human neutrophil migration. Biochem. J. 1998; 330: 719-722.
10. SPSS. Statistical Package for Social Science, SPSS Users Guide. Statistics Version 16. N.C. USA. 2008.
11. Manna S, Bhattacharyya D, Mandal TK, Das S. Repeated Dose Toxicity of Alfa Cypermethrin in Rats. J. Vet. Sci. 2004; 5: 241-245
12. Mamamun MA, Illa IJ, Haque KMF, Ferdousi Z. Histological Study of the Effects of Cypermethrin on Liver and Kidney Tissues of Mice Model. Iosr Journal of Pharmacy and Biological Sciences, 2014; 9.5: 121-128.
13. Gabbianelli R, Falcioni G, Nasuti C, Cantalamessa F. Cypermethrin-Induced Plasma Membrane Perturbation on Erythrocytes from Rats: Reduction of Fluidity in the Hydrophobic Core and in Glutathione Peroxidase Activity. Toxicology, 2002; 175:91-101.
14. Gewal KK, Sandhu GS, Ranjithkaur RS, Sandhu HS. Toxic Impacts of Cypermethrin on Behavior and Histology of Certain Tissues of Albino Rats. Toxicol. Int., 2010; 17: 94-98.
15. Grajeda-Cota P, Ramirez-Mares MV, De Mejia EG. Vitamin C protects against *in vitro* cytotoxicity of cypermethrin in rat hepatocytes. Toxicol. *in Vitro*, 2004; 18: 13-19.
16. Carr A, Frei B. Does vitamin C act as a pro-oxidant under physiological conditions? FASEB J., 1999; 13:1007-1024.
17. Mandl J, Szarka A, Banhegyi G. Vitamin C: Update on physiology and pharmacology. Br. J. Pharmacol. 2009; 157:1097-1110.
18. Halliwell B, Gutteridge JM. The antioxidants of human extracellular fluids. Arch Biochem Biophys, 1990; 180: 1-8.
19. Obach A, Quentel C, Laurencin FB. Effects of alpha-tocopherol and dietary oxidized fish-oil on the immune-response of Sea Bass *Dicentrarchus labrax*. Dis Aquat. Org., 1993; 15: 175-185.
20. Pozzer A, Zimmermann P, Doering U, van Aardenne J, Tost H, Dentener F, Janssens-Maenhout G, Lelieveld J. Effects of business-as-usual anthropogenic emissions on air quality. Atmos. Chem. Phys., 2012; 12.69:15-69.
21. Haryanto B, Sukmasari T, Wintergerst E, Maggini, S. Multivitamin supplementation supports immune function and ameliorates conditions triggered by reduced air quality. Vitam. Miner., 2015; 4:1-15.





Salema Lafta Hassan

22. Puangkaew J, Kiron V, Somamoto T, Okamoto N, Satoh S..Nonspecific immune response of rainbow trout (*Oncorhynchus mykiss* Walbaum) in relation to different status of vitamin E and highly unsaturated fatty acids. Fish Shellfish Immunol., 2004; 16: 25-39.
23. Li Y, Lovell RT. Elevated levels of dietary ascorbic acid increase immune responses in channel catfish. J Nutr, 1985; 115: 123-131.

Table1: The effect of Cypermethrin on serum malondialdehyde and peroxynitrite concentration (mM/dl) administration of Cypermethrin to mice

Groups	Malondialdihyde	Peroxynitrite
G1	3.95 ± 0.0058 A	3.86± 0.0041 A
G2	2.45 ± 0.059 B	2.50 ± 0.052 B
G3	0.30 ± 0.005 C	0.38 ± 0.066 C
G4	0.18 ± 0.003 D	0.20 ± 0.021 D

Means with different capital letters means significant ($P \leq 0.05$) different among groups. G1: was administrated orally with Cypermethrin. G2: was administrated cypermethrin as G1 group and at the same time vitamin C. G3 was group was feeding with vitamin C. G4 was considered as control negative

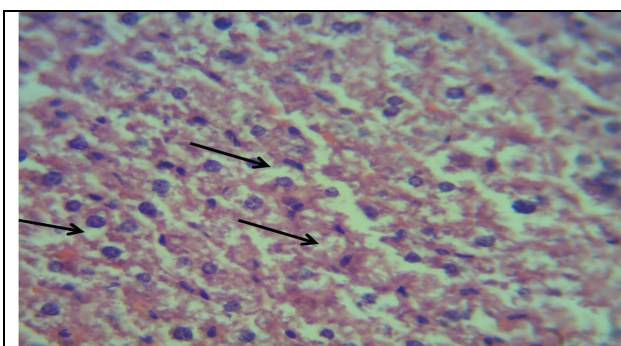


Figure 1: Histopathological section of liver at 8 weeks post treatment with cypermethrin shows:sever areas of vacuolar degenerative changes of hepatocytes black arrow(H and E stain 40X)

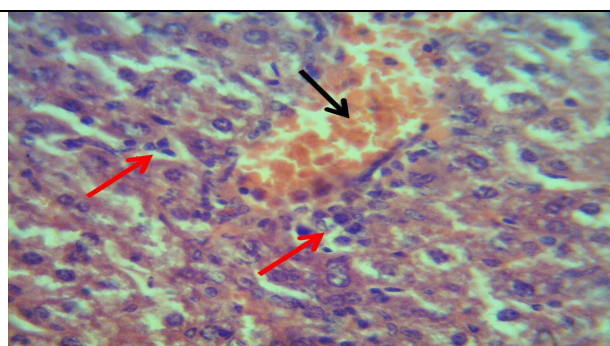


Figure 2: Histopathological section of liver at 8 weeks post treatment with cypermethrin shows:congestion of blood vessels black arrow with infiltration of mononuclear inflammatory cells red arrow(H and E stain 40X)

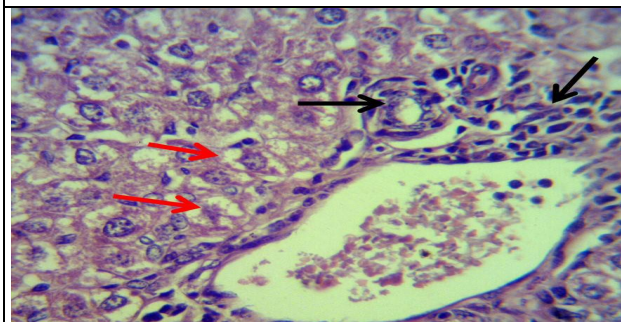


Figure 3: Histopathological section of liver at 8 weeks post treatment with cypermethrin shows: newly formed bile ductules, infiltration of mononuclear inflammatory cell black arrow sever areas of vacuolar degenerative changes of hepatocytes red arrow (H and E stain 40X)

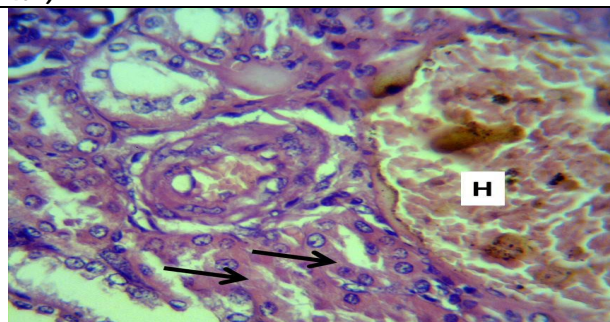


Figure 4: Histopathological section of kidney at 8weeks post treatment with cypermethrin shows: hemorrhages (H)and sever areas of degenerative changes of renal tubules (Black arrow) (H and E stain 40X)





Salema Lafta Hassan

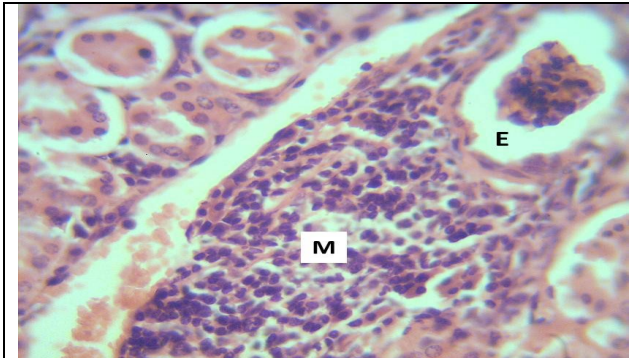


Figure 5: Histopathological section in kidney at 8 weeks post treatment with cypermethrin shows: peri glomerular edema (E) and mononuclear aggregation cell (M)(H and E stain 40X).

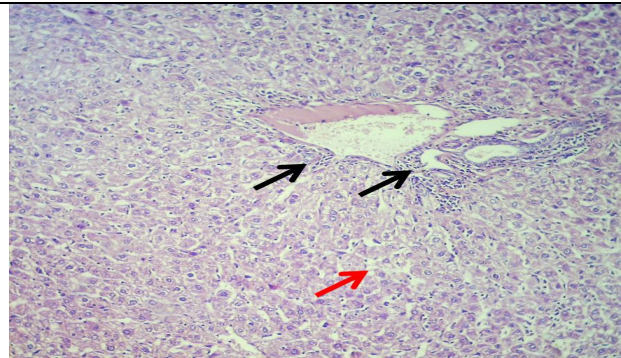


Figure 6: Histopathological section in liver at 8 weeks post treatment with cypermethrin and vitamin C shows: marked mononuclear cells aggregation in portal area around blood vessels and central vein (black arrows)& necrosis of hepatocyte (red arrow)(H and E stain10X).

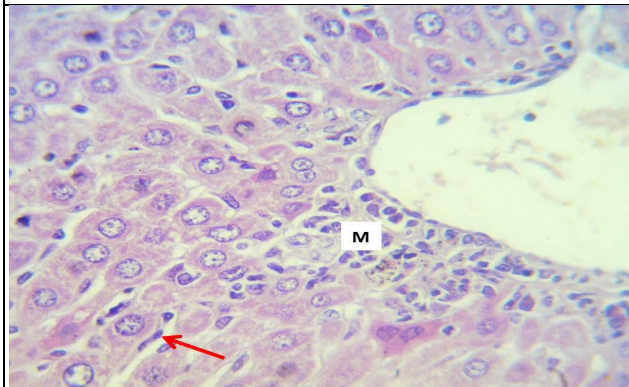


Figure 7: Histopathological section in liver at 8 weeks post treatment with vitamin C shows: marked mononuclear cells aggregation around central vein (M) with proliferation of kupffer cells (red arrow) (H and E stain40X)

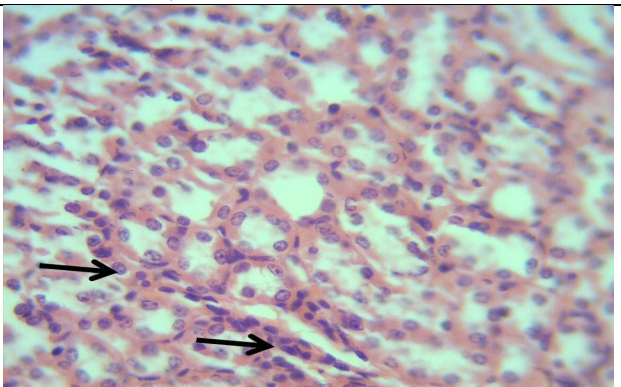


Figure 8: Histopathological section in kidney at 8 weeks post treatment with vitamin C shows marked mononuclear cells infiltration between renal tubules (Black arrow) (H and E stain 40X)





Petrography Study of the Euphrates Formation (Early Miocene) in Muthanna Area, Southern Desert, Iraq

Saleh A. Lazam*

Department of Physics, College of Science, Al Muthanna University, Iraq.

Received: 31 Oct 2018

Revised: 01 Dec 2018

Accepted: 02 Jan 2019

*Address for Correspondence

Saleh A. Lazam

Department of Physics,

College of Science,

Al Muthanna University, Iraq.

Email: sala@mu.edu.iq



This is an Open Access Journal / article distributed under the terms of the **Creative Commons Attribution License** (CC BY-NC-ND 3.0) which permits unrestricted use, distribution, and reproduction in any medium, provided the original work is properly cited. All rights reserved.

ABSTRACT

The petrographic study is based on 36 samples obtained from 12 surface sections. The aim of this study is to shed more light on the facies, and the environment deposition for Euphrates formation, which is results depositional environments are interpreted as categorized by Flugel 2013. The Euphrates Formation took place in different environments. These are shallow evaporatic environment, shallow restricted environment, shallow open marine environment and margin sand shoals environments.

Keywords: south Iraq, Early Miocene, Petrography, Depositional Environment, Microfacies.

INTRODUCTION

The area is located within the Southern Desert which is a part of the Stable Shelf of the Arabian Platform (Ibrahim, M.W., 1983). Many authors divided the Arabian Platform within the Iraqi territory into two main structural domains: the Stable Shelf to the west and the Unstable Shelf to the east (Ibrahim, M. W., 1981). Subdivided the Stable Shelf into two main zones (Buday, T., 1980) and (Buday, T., & Jassim, S. Z. 1987): the western Rutba-Jazira zone and the eastern Salman zone. The project area is located within the Salman zone (Fig 1). The exposed sedimentary sequence in the project area ranges from Late Eocene to Pliocene – Pleistocene in age with regional unconformities. Generally, the area lacks expressive Alpine related compressional structures [1]. The exposed Cenozoic rock units have monocline dipping towards northeast regional dip that does not exceed 2° [5,6,7]. Euphrates Formation beds exposed in the north of the study area (Fig 2). It covers a big part where the lower contact with Dammam Formation appears in Wadi Abu-Mris specified on the presence of conglomerates bed of Euphrates Formation, and the upper contact with Nfayil Formation occurs in the same area near Wadi Abu-Mris. The upper contact with Nfayil Formation is conformable based on the first appearance of Marl bed of Nfayil Formation about (2.0 m) in thickness. The whole sequence of Euphrates Formation consists of the following beds: At the base, a bed of conglomerate cemented by highly fossiliferous limestone with small Oyster shells, white to yellowish white with grey weathered surface, cross bedded, massive, slope forming, with (4-6) m thickness.



**Saleh A. Lazam**

Overlain by fossiliferous limestone grey to pinkish grey to pink, medium tough, about (2.0 m) in thickness capped by (1-1.5 m) of coquina limestone grey to reddish grey, medium tough with sharp contact. The total thickness of Euphrates Formation in project area is ranging from (8-10 m). The petrographic study includes the description of the mineralogical and textural constituents of each formation in order to interpretive of their depositional environment. The exposed formations in the project area from the oldest to youngest are Dammam, Euphrates, Nfayil and Zahra Formations of Tertiary age.

SAMPLING & METHODOLOGY

The petrographic study is based on 36 samples obtained from 12 surface sections. The aim of this study is to shed more light on the facies, diagenetic changes and the environment deposition for each formation. Petrographic study includes the microscopic examination of thin section of all collected samples under polarizing microscope to give us a clear idea about the main components and the texture of the rocks. All thin sections made in this work have been stained with Alizarine Red S according to the staining procedures of Friedman's [8] in order to differentiate between calcite and dolomite and for estimating their percentages in thin sections. The carbonate rocks of the formations are classified after Dunham's [9] with modification of Embry & Klovan [10] depending on the depositional texture of the rocks. Grain types as bioclasts, peloids, ooids and intraclasts can qualify this classification [11]. The identified microfacies of Euphrates Formation are compared with Standard Microfacies Types (SMF) and Facies Zones (FZ) of Wilson [12]. And their depositional environments are interpreted as categorized by Flugel [13]. Identified residual insoluble is dissolved using dilute hydrochloric acid by the way Carver [14]. (Table 1).

Microfacies and Lithofacies of the Euphrates Formation

The recognized microfacies and lithofacies are:

Mudstone

This microfacies is divided into the following submicrofacies:

Dolomudstone

Petrographically, this submicrofacies consists of micritic groundmass that replaced by very fine dolomite. It is unlaminate and unfossiliferous. It contains gypsum (8%) present as fibrous aggregates filling the pore space between dolomite crystals, (Plate 1.1). In addition, it contains dolomite pseudomorphs after gypsum while the lozenge shape of the original gypsum is still preserved. The main diagenetic processes affect this rock are dolomitization, dissolution, cementation and selective replacement of gypsum by dolomite. This microfacies is common in high intertidal to supratidal environment.

Bioclastic dolomudstone and calcareous bioclastic dolomudstone

It consists of bioclasts < 10% (miliolids, gastropods, pelecypods, ostracods, echinoderm plates and algae) embedded in a micritic groundmass that replaced completely by very fine to fine rhombic dolomite. Other component present is calcite as cement between dolomite crystals, filling vugs and poikiliotopically enclosing finer crystals of rhombic dolomite. Many diagenetic processes such as dolomitization and cementation influence this submicrofacies. It occurs in shallow marine restricted environment.



**Saleh A. Lazam****Bioclastic mudstone**

It consists of bioclasts <10% embedded in a micritic groundmass that partially recrystallized to microsparite and selectively dolomitized. The recorded fossils include miliolids, rotallid, neomorphosedostracods, shell fragments of pelecypods, bryozoa, brachiopods and algae. This submicrofacies contain quartz grains (about 3%) of very fine, medium and coarse (0.08- 0.4 & 0.64) mm, subrounded and anhedral to subhedral in shape. Recrystallization, dissolution and cementation are the main diagenetic changes affect this submicrofacies. Such submicrofacies occurs in restricted shallow marine environment.

Wackestone

This microfacies is classified into the following submicrofacies.

Intraclastic bioclastic dolo wackestone

The rocks of this submicrofacies are beige and gray color, medium tough to tough and very tough and enclosing abundant biomolds and intraclasts. Petrographically, it consists of bioclasts and intraclasts embedded in a micritic groundmass that completely replaced by very fine to fine dolomite. The bioclasts are intensively affected by many diagenetic changes so remains as ghosts and biomolds such as abundant shell fragments of pelecypods, ostracods and gastropods, miliolids and algae (Plate 1.2). Intraclasts (10-35%) are dolomitic in composition, consisting of aphanocrystalline and biogenic aphanocrystalline dolomite. Their size ranges from coarse to very coarse (0.9-1.2) mm. Intensive diagenetic processes affect this submicrofacies such as dolomitization, recrystallization of fossils, dissolution and cementation. This submicrofacies relates to SMF 9 and FZ7 of Flugel[13]. which formed in shallow open shelf lagoon.

Shelly bioclastic wackestone

The rocks contain bioclasts embedded in a micritic and microsparitic groundmass. The bioclasts include abundant shell fragments of pelecypods and gastropods, echinoderm plates and spines, *Miogypsina sp. Fig (1.10)*, miliolids, rotallids, brachiopods, recrystallized ostracods and algae, (Plate1.3). This submicrofacies contain quartz (0.5-3%) of fine to medium size (0.2- 0.42) mm. Some of them are coated by microcrystalline calcite. Iron oxide also present as patches, coating skeletal grains, between calcite crystals and filling veinlets. The bioclasts of this submicrofacies are affected by intensive diagenetic processes such as recrystallization, dissolution and cementation of most of the interior of the molds of dissolved shells by isopachous rim microcrystalline calcite. Al Hashimi[15] found that the presence of such submicrofacies indicated restricted circulation on marine platform. The exclusive shell debris suggests shallow water and bank interior facies.

Dolomitic fenestral algal wackestone

Only one sample is present within submicrofacies. Beige color and tough characterize this submicrofacies. Microscopically, it consists of fenestral fabric within micritic matrix that partially replaces by aphanocrystalline dolomite. Algae and few ostracods mainly represent bioclasts of this submicrofacies (Plate 1.4). It contains quartz (3%) of very fine to medium (0.08-0.48) mm, rounded and anhedral to subhedral. Some of the quartz grains are coated with microcrystalline calcite. The rock is affected by partial dolomitization, partial recrystallization of fossils and cementation of fenestral porosity by granular blocky and drusy calcite. It corresponds to SMF 21 and FZ8 of Flugel [13]. The presence of such submicrofacies indicates deposition in platform interior, common in intertidal and very shallow subtidal environments.





Saleh A. Lazam

Packstone

The following submicrofacies are recognized

Dolomitic bioclastic foraminiferal packstone

It contains bioclasts (abundant *peneroplis* sp. and miliolids) with few peloids embedded in a microsparitic groundmass that partially replaced by very fine dolomite. It contains quartz 1% of very fine to medium (0.1-0.28) mm, anhedral to subhedral and mostly coating with microcrystalline calcite. The main diagenetic processes affect this submicrofacies are recrystallization, partial dolomitization dissolution and cementation. Al-Hashimi [15] stated that the presence of abundant *peneroplis* sp. and miliolids indicate deposition in restricted circulation on marine platform (very shallow, hypersaline lagoon). Flugel [13] relates also this submicrofacies to SMF18 and restricted platform lagoon (FZ8).

Dolomitic fenestral algal Packstone

Petrographically, this submicrofacies is distinguished by variously sized irregularly fenestral coarse cavity within micritic matrix that partially replaced by aphanocrystalline dolomite. The fenestrae are filled with drusy and equigranular sparry calcite. This submicrofacies is considered as a characteristic intertidal facies and may be induced by algal mats. Partial dolomitization and cementation are the main diagenetic processes affect this submicrofacies. It corresponds to SMF 21 and typically developed in FZ 8 and FZ 9A (tidal zones of restricted lagoons and supratidal arid coasts).

Sandy bioclastic peloidal packstone and bioclastic peloidal packstone

The rocks of this submicrofacies are gray to yellowish and brownish gray, tough to very tough and some of them enclosing shell fragments of pelecypods. It contains abundant peloids and bioclasts embedded in a microsparitic groundmass and cement of sparry calcite. The peloids are mostly micritic although some of them recrystallized to microsparite and sparry calcite, spherical and elliptical in shape, commonly rounded and fine (0.2mm). Some of them dissolved leaving pelmolds. The bioclasts are mainly represented by miliolids, *peneroplis* sp., shell fragments of pelecypods, rotallid, echinoid spine, echinoderm plates and ostracods. Some of the fossils are subjected to recrystallization, others to leaching leaving biomolds, which latterly reduced by isopachous rim cement and blocky cement. It contains a variable amount of silt to very fine, fine, medium and slightly coarse (0.12-0.22 & 0.34-0.6) mm quartz grains. The main diagenetic processes affect this submicrofacies are recrystallization, dissolution and cementation. This submicrofacies corresponds to SMF 16 and FZ8 of Flugel [13]. It is common in protected shallow-marine platform interior environment with moderate water circulation.

Grainstone

The following submicrofacies are recognized:

Algal bioclastic grainstone

The rock is beige color, medium tough and enclosing large numbers of biomolds. It contains bioclasts (abundant algae, pelecypods, rotallids, *Elphidium* sp., *Peneroplis* sp. Fig (1.11) and recrystallized fossils) in sparry calcite cement. Quartz grains (1.5%) are present within this submicrofacies as anhedral, subrounded and ranging in size from silt to medium (0.04-0.5) mm. Dissolution and cementation of some biomolds by drusy calcite, equigranular sparry calcite and by isopachous rim cement growing within the molds and intraparticle porosity of dissolved shells. This





Saleh A. Lazam

submicrofacies relates to SMF 18 of Flugel[13] and developed in shallow lagoons (restricted platform, FZ 8) and in shelf lagoons with open circulation (FZ7).

Ooidal bioclastic grainstone

Microscopically, it consists of a bioclasts, ooids and composite ooids with sparry calcite cement. Fossils are abundant, diverse and well preserved including abundant *Peneroplis* sp., miliolids, *Miogyopsina* sp., *Dendritina* sp., *Elphidium* sp., rotallid, shell fragments of gastropods and pelecypods, brachiopods and ostracods. Ooids are very common and found in variable amounts, ranging in diameter from medium to coarse (0.32-0.82) mm, generally well sorted, spherical and ellipsoidal in shape, with a nucleus covered by one or more precipitated concentric layers. Their nuclei often consist of quartz, skeletal grains. Some of the nuclei are affected by dissolution leaving intraparticle porosity that reduced with calcite cement. Others have suffered recrystallization to sparry calcite. Composite ooids constitute about 3% are coarse and composed of several ooids enveloped by concentric lamellae. This submicrofacies contain quartz in trace amount. Many diagenetic processes such as recrystallization of some fossils, dissolution and cementation affect this submicrofacies. This submicrofacies corresponds to SMF 15 and shoal near an outer platform margin (FZ 6, winnowed edges sands).

Peloidal bioclastic grainstone

Microscopically, it contains bioclasts (*Peneroplis* sp., *Elphidium* sp., miliolids, algae, shell fragments of pelecypods, gastropods, ostracods and recrystallized fossils), peloids and few ooids embedded in a sparry calcite cement (Plate 1.5). This submicrofacies contain quartz grains (3%) as very fine to fine, subrounded and anhedral to subhedral in shape. Recrystallization of most shell fragments, dissolution and cementation of dissolved shell fragments by isopachous rim cement are the main diagenetic processes affect this submicrofacies. This submicrofacies is similar to SMF 18 and restricted platform (FZ8) of Flugel[13].

Ooidal bioclastic peloidal grainstone

Microscopically, it consists of abundant peloids, bioclasts and ooids with sparitic cement. In some places, the grains are in contact with each other. Peloids are micritic in composition although recrystallized to microsparite and sparry calcite, spherical in shape and fine to medium in diameter (0.16-0.4) mm. The bioclasts (10%) are represented by *Peneroplis* sp., miliolids, rotallids and shell fragments of pelecypods and ostracods. Ooids (3%-8%) are micritic in composition and mostly recrystallized to microsparite and sparry calcite, (Plate1.6). Recrystallization of allochemical components, dissolution and cementation of most of the shell fragments by blocky calcite and with isopachous rim cement around the grains and inside of the molds are the predominant diagenetic processes in this submicrofacies. This submicrofacies relate to SMF 16 and protected shallow- marine environments with moderate water circulation (FZ8) of Flugel[13].

Sandy dolomitic bioclastic Intraclastic floatstone

It is distinguished by beige color and yellowish at parts and enclosing large numbers of intraclasts (0.3-2.0) cm. It consists of intraclasts, bioclasts and quartz grains embedded in a micritic groundmass that partially replaced by dolomite. Intraclasts are composed of microsparite and with size exceeds 2mm. The bioclasts are represented by *peneroplissp.*, *Elphidiumsp.*, miliolids and ostracods. Quartz grains (10%) are very fine to medium and coarse, rounded to subrounded and anhedral to subhedral, (Plate1.7). Partial dolomitization, dissolution and cementation are the main diagenetic changes affect this microfacies. This microfacies is similar to SMF 24 and platform interior (FZ 8, tidal flats).



**Saleh A. Lazam****Crystalline limestone lithofacies**

Petrographically, calcite forms the main constituents, which present in the form of anhedral interlocking fine to medium crystals forming a sort of mosaic texture (Plate 1.8). The limestone of this lithofacies has most probably resulted from recrystallization of originally micritic matrix. This is supported by the occurrences of fossils as ghosts such as shell fragments of gastropods, ostracods, few miliolids and *peneroplissp*. This stage represents the highly stage of recrystallization.

Crystalline dedolomite lithofacies

Calcite forms the main constituents occurring as fine calcite interlocking rhombohedra and as poikiliotopic coarse crystals enclosing finer of rhombic calcite and dolomite. It contains iron oxides as patches and as filling pores. The main diagenetic affects this lithofacies are dedolomitization and dissolution. The association of dedolomite calcite and iron oxides reflect development during late subaerial exposure by the combined weathering and oxidation effects (epigenetic changes)

Crystalline dolostone lithofacies

Dolomite forms the main components of this lithofacies. It occurs as fine (0.06 mm), anhedral to rhombohedral and few of them have zoning. No fossils recorded in this lithofacies. Dolomitization and dissolution are the main diagenetic affect this lithofacies (Plate 1.9).

Diagenetic processes

The diagenetic processes and products have been distinguished by petrographic observations and staining of thin sections. The diagenetic processes encountered in the study rocks include dolomitization, dedolomitization, , micritization, dissolution and porosity development, cementation and replacement of sulphates. The description of each process is given below:

Dolomitization**Early diagenetic dolomitization**

The majority of dolomite rocks in the study area are of early origin. This process is confirmed by the presence of aphanocrystalline and very finely crystalline dolomite that completely or partially replaced micritic matrix in mudstone, wackestone, packstone and floatstone and relatively rare in grainstonesubmicrofacies. It has affected the Euphrates rocks is limited (Plate2.1). Many factors are responsible for the replacement of sediment by dolomite. These factors are (1) predolomitization mineralogy, (2) particle size, (3) permeability variations and (4) organic matter [16].

Late diagenetic dolomitization

The effect of this process on the rocks of the study area is very limited. in Euphrates Formations is noticed only in crystalline dolostone. This process is indicated by the presence of fine to medium euhedral to rhombohedral interlocking crystals of dolomite. Most of them have zoning. This process is formed under hypersaline environment (Plate 2.2).



**Saleh A. Lazam****Dedolomitization**

It is a diagenetic replacement of dolomite by calcite. This process is very limited. In Euphrates Formation, the dolomite crystals are completely replaced by fine and rhombic interlocking crystals of calcite in one sample and in other sample are indicated by the presence of poikiliotopic coarse calcite enclosing finer crystals of dolomite. It is associated with iron oxides reflecting deposition during late subaerial exposure (epigenetic changes).

Recrystallization

This process is indicated by the presence of microsparite (4-10) μ and sparry calcite >10 μ . (Plate 2.3), the recrystallization either is partially or completely affects the rocks of few facies as noticed in ooidal bioclastic peloidal grainstone and crystalline limestone lithofacies. The complete recrystallization is accompanied by partial or complete destruction of pre-existing rock texture.

Micritization

This process is very common in Euphrates Formations. It is the first diagenetic alteration produces a micritic envelope around skeletal grains that originally composed of aragonite and / or high mg calcite, (Plate 2.4). The existence of micrite envelope is important for the preservation of grain shapes. Molluscan, miliolids and *Peneroplis sp.*, are the most noticed fossils affected by this process. This process is produced by the combination of boring algae penetrates inward from the exterior of the skeletal particles and precipitation where the waters are supersaturated by calcium carbonate [17],[18]. Such a process was found to be most common in intertidal and supratidal environments (e.g. [17,19]).

Dissolution and porosity development

This process is gained through solution and dolomitization and reduced through cementation [20]. It is the most diagenetic extensive and dominant in the study area and divided into two main groups according to [20]. These are:

Fabric-selective pores

Both primary and secondary fabrics control fabric selective pores. These pores are of several different types.

Intraparticle porosity

This porosity is developed within individual particles or grains, particularly within the chambers of skeletal fragments (e.g. intragranular pores in foraminifera) and dissolution of the nuclei of some ooids and composite ooids. In the study area, most of the recognized submicrofacies are affected to various extents by this process. This type of solution is formed under the influence of meteoric phreatic and meteoric vadose environment.

Interparticle porosity

This porosity is primary and occurred between individual particles (skeletal and non-skeletal grains). Most of These pores are reduced by sparry calcite and silica cement.



**Saleh A. Lazam****Fenestral porosity**

It is open space irregularly distributed in micrite or microsparite that mostly replaced by dolomite. It is very common in most rocks of the study area, mostly filled either partially or completely by sparry calcite cement (granular, drusy and isopachous cement) and mostly associated with supratidal and intertidal, algal-related and mud-dominated sediments (Plate2.5).

Intercrystalline porosity

These pores are developed between dolomite crystals in crystalline dolostone. The intercrystalline porosity has more likely resulted from dolomitization, which caused an increase of pore space when limestone changed to dolomite. These pores are mostly reduced by calcite cement.

Non-fabric selective pores

This occurs where the pores are developed independent of original textures. These are:

Vuggy porosity

These pores are extremely irregular with no definite shape and mostly reduced by sparry calcite cement .

Veins

They are very limited in the study area, and mostly reduced by calcite cement.

Cementation

Cementation comprises processes leading to the precipitation of minerals in primary or secondary pores and requires the supersaturation of pore fluids with respect to the mineral. In the study area, the rocks are cemented by three types of minerals; carbonate (calcite and dolomite), gypsum and silica. The following types of cement are recognized: The common carbonate cements are:

Isopachous rim cement

This cement is very common in most of rocks of the study area and considered of early type. This type of cement is characterized by calcite and/or dolomite rim cement growing with equal thickness around grains and as lining the intragranular pores of many skeletal grains ,non skeletal grains (oids), within the molds of dissolved shells (aragonite shells), underside the fenestral porosity and around quartz grains consisting microcrystalline calcite and/or dolomite.

This type of cement is formed under the influence marine phreatic environments in Euphrates Formations Fig (2.7).

Granular sparry calcite cement

It is present as equant crystals occupied either partially or completely biomolds, intraparticle, fenestral porosity, veinlets, interparticle and intercrystalline pores. It is generally present in the grainstonefacies. It has taken place in several diagenetic environments and over a lengthy period of time, usually in meteoric vadose and meteoric phreatic. Fig (2.8).





Saleh A. Lazam

Drusy calcite cement

This type occurs in an intraskeletal pores, molds and fenestral porosity as fine lining the interior of the walls and then increased in size towards the center of the pores (Plate2.6). The increase in size of calcite crystals was interpreted as arising from competitive growth [18]. In Euphrates Formations, it is formed in the carbonate sediments that were deposited in the intertidal or supratidal or that they were brought into the subaerial environment shortly after deposition.

Blocky calcite cement

This type of cement is very common in the rocks of the Euphrates Formation. It consists of medium to coarse-grained crystals without a preferred orientation. It occurs inside molds, intraskeletal grains, interparticulate pores and within fenestral porosity. This process represents meteoric phreatic environment.

Replacement of sulphates

This process is very limited in the study area and only observed in Euphrates Formation in dolomudstone submicrofacies. The sulphate mineral is selectively replaced by dolomite pseudomorphs while the lozenge shape of the original gypsum is still present.

CONCLUSION

The Euphrates Formation is composed of fossiliferous limestone, dolomitic, sandy, marly oolitic and pelletal dolomite and coquina. The suggested environment of Euphrates formation is semi – restricted marine platform facies of warm sea, normal salinity, an intensive action resulted in well sorted and rounded Ooid and pellets, and given of early Miocene age. Miliolids, rotalids, shell fragments, gastropods, pelecypods, echinoids, ostracods, algae (stromatolites), bryozoa and corals. The assemblage fauna recognized in this study can be correlated with the fossils assemblages of the formation in different areas such as: Samawa area by [21], West Najaf-Nukhaib by [22], and West Samawa area by [23]. The age of Euphrates Formation is assigned to Early Miocene due to the presences of *Miogypsina* sp., *Peneroplis farsensis* HENSON, *Ammonia beccarii* LINNE ([24, 22, 23, 25, 26, 27] and [28]). Depositional environments of Euphrates Formation is dominated by *Elphidium*, *Ammonia beccarii*, *Miogypsina*, *Peneroplis*, *Rotalia*, miliolids species. Miliolids are characterized mostly as bay and inner shelf environments [29]. *Rotalia* and *Elphidium* occurred frequently in the shallowest zone [30]. Therefore Euphrates Formation is believed to be lagoon backreef shoal (Fig 3) (shallow marine environments) [31, 32, 33, 34, 35, 26, 27, 36].

REFERENCES

1. Ibrahim, M. W. (1983). Petroleum geology of southern Iraq. AAPG Bulletin, 67(1), 97-130.
2. Ibrahim, M. W. "Lithostratigraphy and subsurface geology of the Albian rocks of South Iraq." Journal of Petroleum Geology 4.2 (1981): 147-162.
3. Buday, T., 1980. The Regional Geology of Iraq. ; Stratigraphy and Paleogeography, Iraq, 445p.
4. Buday, T., & Jassim, S. Z. (1987). The Regional geology of Iraq, vol. 2: Tectonism, Magmatism and Metamorphism. Publication of GEOSURV, Baghdad, 352.
5. Fouad, S. (2015). Tectonic map of Iraq, scale 1: 1000 000, 2012. Iraqi Bull Geol Min, 11(1), 1-7.
6. Sissakian, V. K., & Ibrahim, F. A. (2005). Geological Hazards Map of Iraq, scale 1: 1000 000. GEOSURV, Baghdad, Iraq.
7. Hassan, K. M., Yacoub, S. Y., & Amir, E. A. (1995). The Geology of Al-Salman Quadrangle. sheet NH-38-6, scale 1: 250 000. GEOSURV, Baghdad, Iraq.





Saleh A. Lazam

8. Friedman, G. M. (1959). Identification of carbonate minerals by staining methods. *Journal of Sedimentary Research*, 29(1).
9. Dunham, R.J., 1962. Classification of carbonate rocks according to depositional texture. In: *Classification of carbonate Rocks* (ED. by W.E. Ham). pp. 108-121. Mem. Am. Ass. Petrol.
10. Embry III, A. F., & Klovan, J. E. (1971). A late Devonian reef tract on northeastern Banks Island, NWT. *Bulletin of Canadian Petroleum Geology*, 19(4), 730-781.
11. El-Anwar, E. A., Mekky, H. S., Darweesh, H. H., & Aita, S. K. (2018). Utilization of some Miocene limestones as building materials from Egyptian North Western Coastal area (Abu Sir Ridge). *Carbonates and Evaporites*, 33(1), 79-86.
12. Scheibner, C., & Speijer, R. P. (2008). Late Paleocene–early Eocene Tethyan carbonate platform evolution—A response to long- and short-term paleoclimatic change. *Earth-Science Reviews*, 90(3-4), 71-102.
13. Flügel, E. (2013). *Microfacies of carbonate rocks: analysis, interpretation and application*. Springer Science & Business Media.
14. Carver, R. E. (1971). *Procedures in sedimentary petrology*. John Wiley & Sons Incorporated.
15. Al-Hashimi, H. A., & Amer, R. M. (1985). Tertiary microfacies of Iraq. Directorate General for Geological Survey and Mineral Investigation.
16. Boukhary, M., Abdelghany, O., Bahr, S., & Hussein-Kamel, Y. (2005). Upper Eocene larger foraminifera from the Dammam Formation in the border region of United Arab Emirates and Oman. *Micropaleontology*, 51(6), 487-504.
17. Bathurst, R. G. (1972). *Carbonate sediments and their diagenesis* (Vol. 12). Elsevier.
18. Swei, G. H., & Tucker, M. E. (2012). Impact of diagenesis on reservoir quality in ramp carbonates: Gialo Formation (Middle Eocene), Sirt Basin, Libya. *Journal of Petroleum Geology*, 35(1), 25-47.
19. Neumeier, U. (1999). Experimental modelling of beachrock cementation under microbial influence. *Sedimentary geology*, 126(1-4), 35-46.
20. Choquette, P. W., & Pray, L. C. (1970). Geologic nomenclature and classification of porosity in sedimentary carbonates. *AAPG bulletin*, 54(2), 207-250.
21. Al-Hashimi, H. A. J., & Amer, B. M. (1977). Stratigraphy and paleontology of the subsurface rocks of Samawa area. *J Geol Soc Iraq* (Special issue), 7-39.
22. Amer, R. M. (1980). Biostratigraphic and Micropaleontologic Study of West Najaf–Nukhaib Area, West Desert Iraq. *GEOSURV, int. rep.*, (1097).
23. Abdul Munium, A. (1983). Biostratigraphy of Lower Eocene–Upper Miocene of west Samawa area, Iraq. *GEOSURV, int. rep.*, (1326).
24. Daneshian, J., & Dana, L. R. (2007). Early Miocene benthic foraminifera and biostratigraphy of the Qom Formation, Deh Namak, central Iran. *Journal of Asian Earth Sciences*, 29(5-6), 844-858.
25. Kender, S., Kaminski, M. A., & Jones, R. W. (2008). Early to middle Miocene foraminifera from the deep-sea Congo Fan, offshore Angola. *Micropaleontology*, 477-568.
26. Heidari, A., Mahboubi, A., Moussavi-Harami, R., Gonzalez, L., & Moalemi, S. A. (2014). Biostratigraphy, sequence stratigraphy, and paleoecology of the Lower–Middle Miocene of Northern Bandar Abbas, Southeast Zagros basin in south of Iran. *Arabian Journal of Geosciences*, 7(5), 1829-1855.
27. Zabihi, F., Vahidinia, M., Mahboubi, A., & Bakhtiar, H. A. (2013). Facies analysis and sequence stratigraphy of the Asmari Formation in the northern area of Dezful Embayment, south-west Iran. *Studia Universitatis Babeş-Bolyai Geologia*, 58.
28. Al-Ghreri, M. F., Al-jibouri, A. S., & Al-Ahmed, A. A. (2014). Facies architecture and sequence development of the Euphrates formation in western Iraq. *Arabian Journal of Geosciences*, 7(7), 2679-2687.
29. Achalhi, M., Münch, P., Cornée, J. J., Azdimousa, A., Melinte-Dobrinescu, M., Quillévéré, F., ... & Moussa, A. B. (2016). The late Miocene Mediterranean-Atlantic connections through the North Rifian Corridor: New insights from the Boudinar and Arbaa Taourirt basins (northeastern Rif, Morocco). *Palaeogeography, Palaeoclimatology, Palaeoecology*, 459, 131-152.
30. Culver, S. J. (1988). New foraminiferal depth zonation of the northwestern Gulf of Mexico. *Palaios*, 69-85.
31. Tucker, M. E., & Wright, V. P. (2009). *Carbonate sedimentology*. John Wiley & Sons.





Saleh A. Lazam

32. Pomar, L. (2001). Ecological control of sedimentary accommodation: evolution from a carbonate ramp to rimmed shelf, Upper Miocene, Balearic Islands. *Palaeogeography, Palaeoclimatology, Palaeoecology*, 175(1-4), 249-272.
33. Sattler, U., Immenhauser, A., Schlager, W., & Zampetti, V. (2009). Drowning history of a Miocene carbonate platform (Zhujiang Formation, South China Sea). *Sedimentary Geology*, 219(1-4), 318-331.
34. Beavington-Penney, S. J., & Racey, A. (2004). Ecology of extant nummulitids and other larger benthic foraminifera: applications in palaeoenvironmental analysis. *Earth-Science Reviews*, 67(3-4), 219-265.
35. Lazam, S. A. (2017). Mineralogical & Petrographic Microfacies Study of the Zahraa formation (Pliocene–Pleistocene) in Sawa Lake Surrounding area-IRAQ. *Almuthanna Journal of Pure Science (MJPS)* 4(1).

Table 1. proportion of Insoluble residual (Ireland, 1971) and Ratio Calcite- dolomites

Age	Th.(m)	lithology	Description	INSOLUBLE RESIDUE I.R%	CALCITE %	DOLOMITE %
Early Miocene	1.5		Highly Fossiliferous (Coquina) ,pale grey with rusty and red materials.	2	91.07	3.2
				1.9	94.50	1.8
	2		Fossiliferous Limestone ,pale gray ,cough, with rusty and materials.	0.9	96	2.02
				0.77	95.8	1.89
	6		Conglomerate; composed of silicate pebbles range in size (0.5-5 cm) cemented by pale green highly fossiliferous limestone ,slope forming & massive	2.3	84.06	3.7
				1.9	89.1	1.5
				15	88	1.4

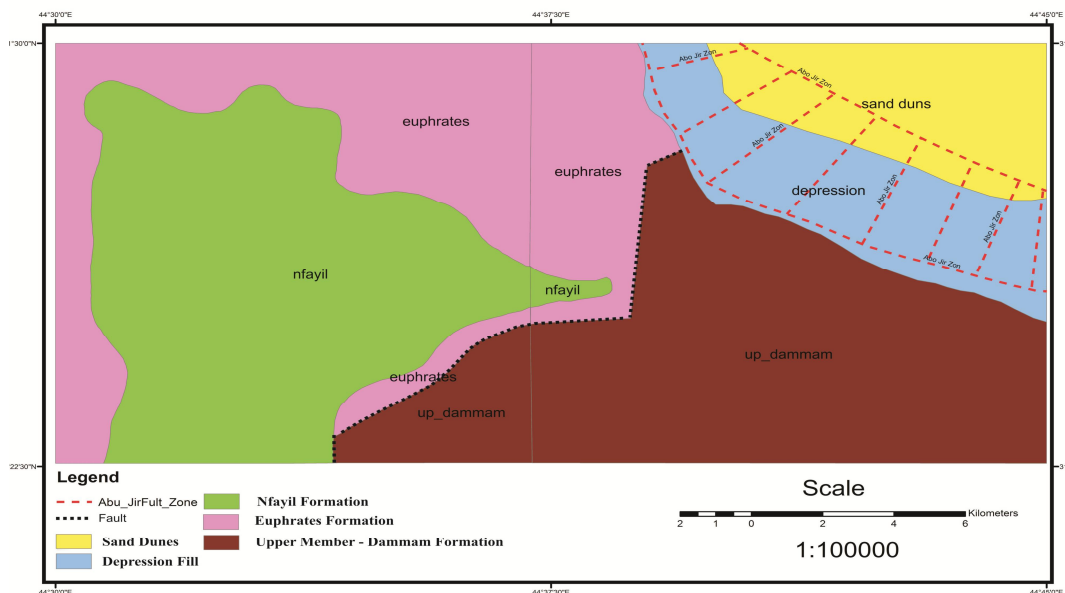


Fig.1. Structural features of the study area.[5]



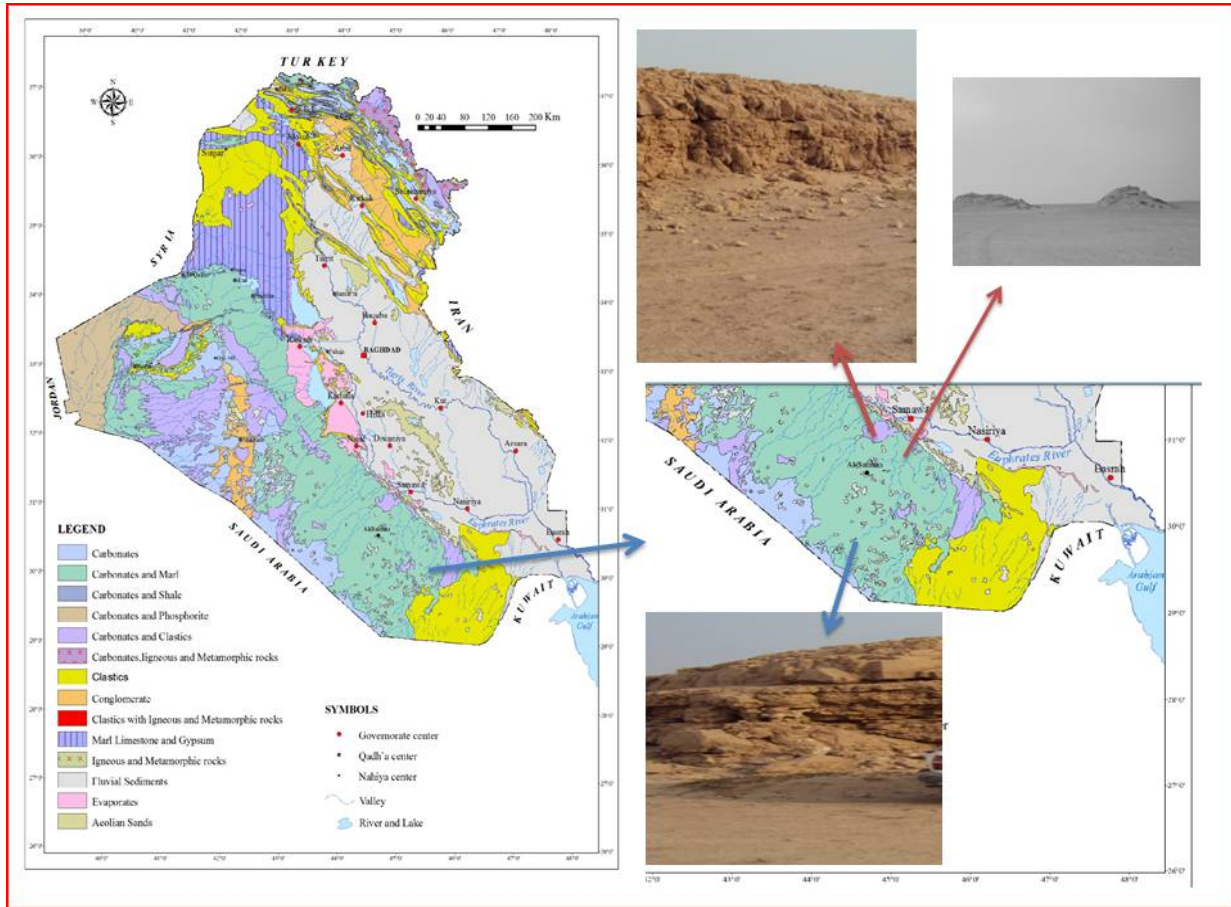


Fig. 2. Geological map of Iraq which showing the the studied area. [6]

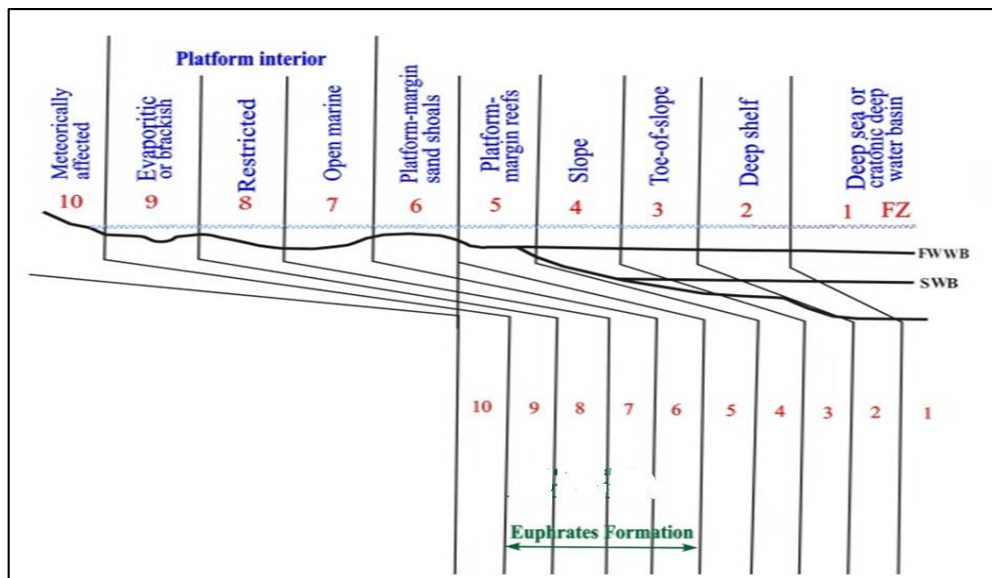


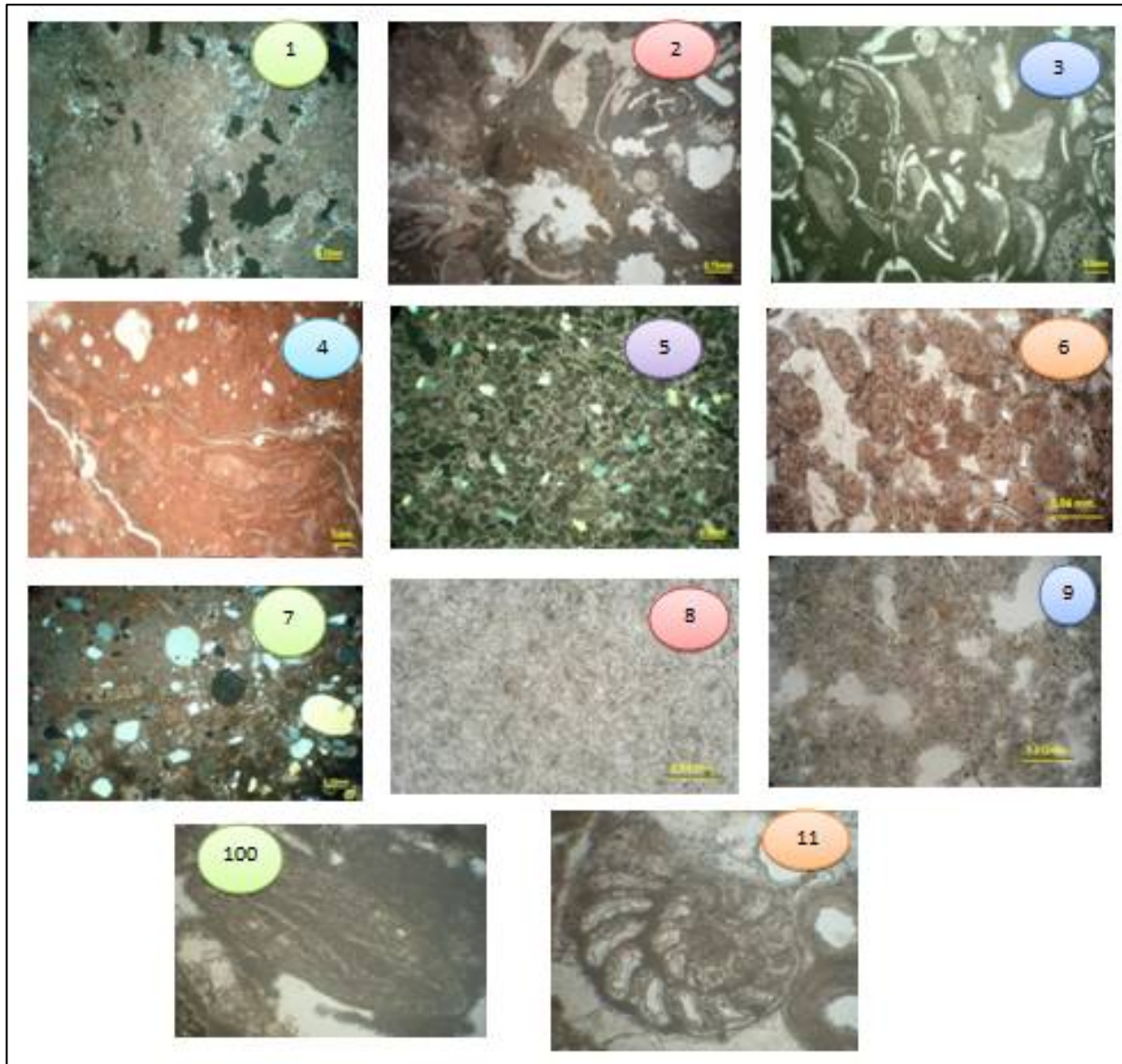
Fig. 3. Depositional environments of Euphrates Formation according to Flugel (2013).





Saleh A. Lazam

Plate 1



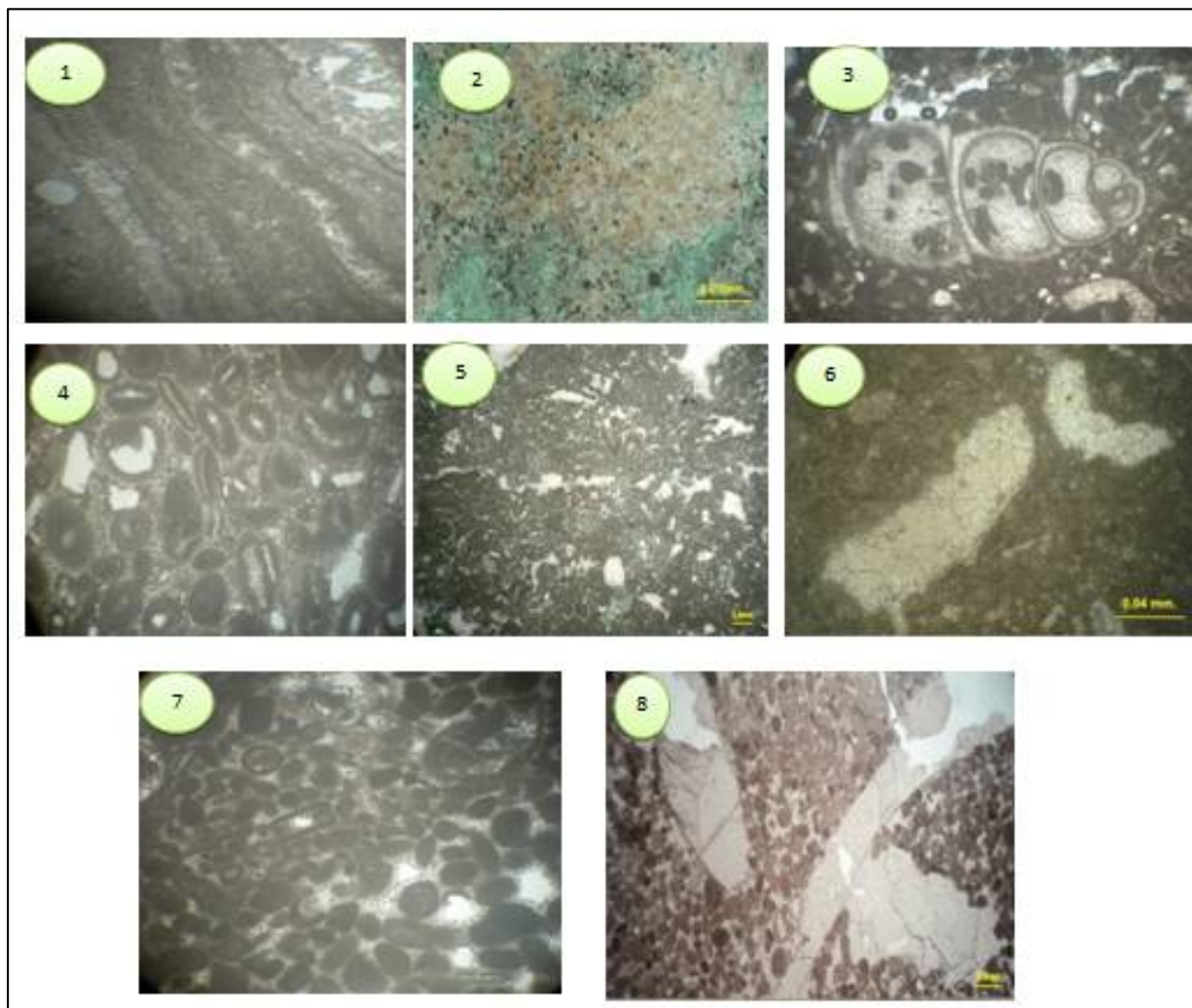
1 . Dolomudstone	2. Intraclastic Bioclastic Dolo Wackestone
3. Shelly bioclastic wackestone with <i>Miogypsina</i> sp	4. Dolomitic fenestral algal wackestone.
5. Peloidal bioclastic grainstone.	6. Ooidal Bioclastic Peloidal Grainstone
7. Sandy dolomitic bioclastic Intraclastic floatstone	8. Crystalline limestone
9. Crystalline dolostone.	10. <i>Miogypsinoglobulina</i> MICHELOTTI, X2.5
11. <i>Peneroplis farsensis</i> HENSON, X6.3	





Saleh A. Lazam

Plate 2



1. Algae (Stromalites), X10. Early diagenetic dolomitization affects groundmass and algae	2. Late diagenetic dolomitization
3. Recrystallization Gastropods, X10.	4. Micritization Oolitic limestone facies, X6.3
5. sparry calcite cement	6. Blocky calcite cement
7. Isopachous rim cement ,Pelletic limestone facies, X6.3	8. Granular sparry calcite cement





Observation of Interaction of the ICME with Earth Bow Shock and Related Effects on Earth

Rabab Mazhir Jassim* and Amjad Al-Sawad

Department of Astronomy and Space, College of Science, University of Baghdad, Baghdad, Iraq.

Received: 28 Oct 2018

Revised: 30 Nov 2018

Accepted: 02 Jan 2019

*Address for Correspondence

Rabab Mazhir Jassim

Department of Astronomy and Space,
College of Science,
University of Baghdad,
Baghdad, Iraq.
Email: sala@mu.edu.iq



This is an Open Access Journal / article distributed under the terms of the **Creative Commons Attribution License** (CC BY-NC-ND 3.0) which permits unrestricted use, distribution, and reproduction in any medium, provided the original work is properly cited. All rights reserved.

ABSTRACT

We observed 2515 CME during the period 12th of July 1996 till 25th of May 2016, with over 500 km/s and more than 60° of angular width, seen by LASCO/SOHO. Some shock waves driven by CMEs have been registered by CELEAS/SOHO and there were information about their CMEs at Sun. We use those events as a tool to calibrate a method of calculation for the travel time of the CME since many of the events observed by CELEAS have no information about their source at Sun. A MATLAB fitting method was used for the linear fit according to calculate the travel time of the ICME from the liftoff time of the associated CME until the time passage of the shock wave by CELEAS. The speed record for the height and location of the CME by LASCO was taking to achieve this fitting. On the other hand, the events without origin source registered by CELEAS were compared to possible associated CME and solar flare registered by LASCO and GOES respectively. In those events, the travel time was calculated between the liftoff time of the CME (mean value for linear and quadratic fit) and the arrival time registered by CELEAS. A comparing was taken for those results with our MATLAB fitting. About 42% of the events from the first method were online with our calculation but only 25% of the events were on line with our calculation in the second method. We compare both results to the magnetic storm registration and then isolate the events from western hemisphere and compare them to the magnetic storm which cause aurora phenomenon registered by SWPC NOAA. We found 71% of those events were well connected. This study has been done for the first time in Iraq for shock wave from Sun hitting our planet.

Keywords:CME, ICME, SEPS, Shock Wave.





INTRODUCTION

The ignition of the CME mechanism is still unsolved due to the complex developing of the magnetic field inside the sun, which emerges on the solar disc through the active regions. Usually it started with bright filament seen in H-alpha lines and in most large CMEs it will be associated with solar flare, which works as a trigger for the launch of the CME. In the corona the magnetic field develop to close loop filled with hot plasma. This can be seen as many different emissions in electromagnetic radiation such as hard and soft X-rays, gamma ray and radio emissions in different ranges of bursts. Studies since last century came to conclusion that CMEs with speed acceding 500 km/s and with angular width larger than 60° can accelerate different species of particles to relative speeds and high energies up to GeV. The hole phenomena called Solar Energetic Particle (SEP) event. Acceleration of SEPs has been under debate since it has been observed at first time. It was thought to be due to solar flare and the acceleration take place in the lower corona within 5 solar radii. During the flare, annihilation of magnetic field will transfer the energy to kinetic energy of energetic particles, and this indicates the importance of the flare as a source of SEPs.

Later on, the favorability turned to the CME and bulk of acceleration thought to be in the interplanetary medium. In both cases the main accelerator was the shock wave accompany with the eruption. Generally, both, coronal shock, at flare sight and interplanetary shock, in the interplanetary medium, are considered the main source for SEPs, but which one more important is still in debate. Thus, shock waves can play an important role in the solar corona and interplanetary space, since they are able to accelerate particles (electrons, protons and heavy ions) up to high energies. In the solar corona, shock waves can be generated by two different mechanisms, usually called the piston mechanism and the blast wave mechanism. CMEs can act as a piston, driving bow-shock waves in the corona and into the interplanetary (IP) medium. The blast waves can be produced in the impulsive flare phase due to sudden heating and the pressure pulse [1]. It should be emphasized that a shock is a discontinuity well-defined in magnetohydrodynamics (MHD) and, consequently, independent of the exciting agent. It represents a discontinuity with a transmitted mass flow, which is decelerated from a super-Alfvénic to a sub-Alfvénic speed. Thus, the shock is a dissipative structure, in which kinetic energy of a directed plasma flow is partly transferred to heating of the plasma. Since the necessary dissipation doesn't take place by means of particle collisions, these shocks are usually called collisionless shocks [2].

The different between coronal shock and interplanetary shock acceleration is also changing the aspect and name of the associated phenomena. The same eruptions called CME and ICME respectively. The main differences between CMEs and ICMEs are the regions in space in which they are observed and the methods by which they are detected. CMEs are detected directly mostly through white light observations, (although closer to the sun they can also be observed in other ways, e.g. radio, UV), but are often related to solar surface eruptions in the lower solar atmosphere. These eruptions, while not directly related to the eruption of the CME, are probably a consequence of the same eruptive mechanism, and so can provide information on CME location and structure. They cannot, unfortunately, provide us with information on CME composition or energy. ICMEs, on the other hand, are observed in white light, radio scintillation and directly, but not until they are some considerable distance from the sun or in a particular region where the STEREO instruments can observe them. We can track their appearance across larger distances and directly measure their magnetic properties and composition when a spacecraft gets hit by one. While we can accumulate detailed information on the ICME, we cannot obtain a great amount of accurate information about its origins [3].

Because we do not have sufficient information on the transition from CME to ICME, we can only make general associations between them. For example, an ICME observed near the Earth with an insitu spacecraft can be matched with an Earth-directed CME from a reasonable extrapolation based on the speeds of each, and ICME images can be matched for location and timing with their CME counterparts [4&5]. In this study, we observe the ICME hit the earth and the associated effect of it taking Aurora phenomena as an indicator for the interaction between ICME and Earth.



**Rabab Mazhir Jassim and Amjad Al-Sawad**

On the other hand, we found the source of the ICME at Sun and calculate the traveling time using the observation in white light for the speed development of the original CME seen by LASCO/SOHO. The important of this study is shown in finding connection between effective CMEs as an accelerator of SEPs and as an effective solar event on Earth.

Method of Measurements

The method used in this study depend on empirical approach in order to determine the source of the shock wave that hit the earth, the later effect and the connection between these two factors, thus:

First

From the LASCO data catalogue, the CME will be chosen according to the criteria that identify the CME to be effective, accordingly it should has a speed ≥ 500 km/s and angular width $\geq 60^\circ$.

Second

Because the event chosen should be frequent and powerful enough to insure an effect on Earth, the period was chosen between 1996-2016, to cover the 23 and 24 solar cycles.

Third

LASCO will give the extrapolation of the fitting for the CME after taking many shots by the camera on it and use two kinds of fitting, linear and quadratic. The mean value for them will be to obtain the calculate liftoff time for the CME and will be considered as a starting time for the travel of the shock until the shock passage on Earth.

Fourth

When CELEAS record a shock passage within 1-3 days after the liftoff, the time will be registered as a time arrival to Earth since we can neglect the 1.5 million km for the location of SOHO from Earth toward Sun, comparing with about 150 million km, the total travel distance between Earth and Sun.

Fifth

There are two cases concerning the CELEAS calculation for the travel time of the shock and thus the determination of the source of it at Sun. In some cases CELEAS will give the travel time and determine the source accordingly and in this case their results will be considered and compared to the source we found on LASCO. In another cases, no registration for the travel time neither the source and in those cases MATLA will be used to obtain the calculation for the travel time and source.

Sixth

The observation of the Aurora events at Earth will be taken and then will find the association of the shock wave passage registered by both ways mentioned above.

Finally

Calibration for the results calculated by our fitting and buy CELEAS through comparative statistics in order to determine the certainty of the associated Aurora and the eruption at Sun.





Rabab Mazhir Jassim and Amjad Al-Sawad

RESULTS

Result and Data Analysis for selective events

Part 1: The events, which have origin at Sun registered by CELEAS but not identical with our calculation and have effects on the earth.

Event 1

SOHO/LASCO observation

On October 19th 2001 a halo was observed with FC2AT at 01:27 UT heliocentric height of 2.86 R_⊙, erupted from the western hemisphere with a linear speed of 558 km/s and an acceleration of -25.6 m/s². The lift off time was at 00:44±00 UT. As shown as in Fig. (3.1).

Goes Detection

A X1.6 long duration solar flare was detected by SXT at 16:13 UT and end 16:43 UT in the H α location N15W29 with a NOAA active region 9661, EIT detector showed that the CME was associated with this flare.

SOHO/CELIAS/MTOF

A shock wave arrival was observed on October 21st 2001 at 16:05 UT and caused by the above-mentioned CME with a 63 hours traveling time. And calculated us 73.74 hours, error limit is 0.5529. this event interval time doesn't recorded with interval time calculated but effect on the earth explain in aurora.

Aurora phenomena

The first of two coronal mass ejections en route to Earth swept past our planet on Oct 21st at 16:45 UT. The interplanetary magnetic field turned sharply south when the disturbance arrived, setting the stage for a possible display of Northern Lights [6].

Part 2

Events with origin at Sun registered by CELEAS and were identical with our calculation and have aurora.

Event 1

SOHO/LASCO observation

On April 21st 2002 angular width 69 with FC2AT at 01:27 UT heliocentric height of 4.93 R_⊙, erupted from the western hemisphere. with a linear speed of 749 km/s and an acceleration of 0.7m/s². The lift off time was at 00:28±0 UT. As shown as in Fig. (3.2).



**Rabab Mazhir Jassim and Amjad Al-Sawad****Goes Detection**

A X1.5 long duration solar flare was detected by SXT at 00:43 UT and end 02:38 UT in the H α location S14W84 with a NOAA active region 9906, EIT detector showed that the CME was associated with this flare.

SOHO/CELIAS/MTOF

A shock wave arrival was observed on April 23th 2002 at 04:08UT and caused by the above-mentioned CME with a 50.5 hours traveling time. And calculated us 56.22 hours , error limit is 0.3806 this event interval time doesn't recorded with interval time calculated but effect on the earth explain in aurora.

Aurora phenomena

The coronal mass ejection (CME) that reached Earth at 04:50 UT on April 23rd left the Sun on April 21st -- hurled into space by a powerful X1-class explosion near sunspot 9906 triggered a 3-to-5 hour long G2-class geomagnetic storm.

Part 3

Events without origin source at Sun registered by CELEAS but interval time calculated with ELOT were identical, and effects on Earth.

Event 1**SOHO/LASCO observation**

On Oct. 22th 2011 a halo was observed with FC2AT at 10:24 UT heliocentric height of 2.65 R \odot , erupted from the North-west hemisphere with a linear speed of 1005 km/s and an acceleration of 17.7 m/s² . The lift off time was at 10:13 \pm 5 UT. As shown as in Fig. (3.3).

Goes Detection

A M1.3 long duration solar flare was detected by SXT, EIT detector showed that the CME was associated with this flare.

SOHO/CELIAS/MTOF

A shock wave arrival was observed on Oct. 24th 2011 at 17:50 UT and caused by the above-mentioned CME with a 51 hours traveling time. It is identical with ELOT 38:38 hours, error limit is 0.6354. Our calculation for the shock travel time is identical with the observed result. The effect on the earth is in association with aurora.

Aurora phenomena

A coronal mass ejection (CME) hit Earth on Oct. 24th at approximately 18:00 UT. The impact strongly compressed Earth's magnetic field, directly exposing geosynchronous satellites to solar wind plasma, and sparked an intense geomagnetic storm. As night fell over North America, appear auroras.





Rabab Mazhir Jassim and Amjad Al-Sawad

DISCUSSION AND CONCLUSIONS

The tracking of the CME propagation in the IP medium and its driven shock wave is still unaccomplished task. This fact is due to the lack of the tracking space instruments along this propagating path which is about 1AU. The satellites orbiting the heliosphere and the geosphere are not covering all of these distances. Between 70 solar radii from Sun until near the borders of the magnetosphere in about 1.5 million km tracking, especially in white light is not possible yet. Thus, some studies took advantage of radio emission tracking and compare it to some models of electron density for Sun such as [7]. The tracking depends on the estimation of the changing in velocity and there for acceleration. Still comparison needed for plane sky survey with such studies in order to estimate the different in the acceleration (decelerated or accelerated).[8]. Applied Reiner method to two CMEs by using a model for magnetic field structure with imaginary 1 AU spacecraft in the magnetic tube and prove that the first CME was decelerating and thus the its IP shock wave became deficient to accelerate SEP.,[9]. Compare four CMEs accelerations calculated by two ways, one way by LASCO and another by [7] and found differences in the results between the two ways.

The determination of the travel time depends on the clear association between a CME erupted at Sun and the time of the shock passage at Earth. During the solar maximum, CMEs erupt frequently, so one might find many CMEs eruptions simultaneously. On the other hand, no certainty can be achieved for association of IP shock to coronal shock with multi solar eruptions unless very intensive analysis takes place with multi observation points. Moreover, sometimes in one AR can occur two eruptions in association, such solar flare followed by a CME. In this case it is very difficult task to know to which one eruption the shock wave belong. If two AR at Sun in same half of solar disc then it is also the same as previous case. These difficulties and many more can only be determined with low error limit, if we find better way for fitting for the propagation proses for the CME from corona to IP and then Earth. This study was done for the first time in Iraq, even though it calculates the propagation with most simple mathematical tools.

We observe 2515 CMEs during the solar cycle 23 and 24 within the period 12th Of July 1996 till 25th of May 2016, at Sun and follow their associated IP shock wave until it passage the SOHO spacecraft assuming that this point is the nearest possible one to Earth. Data registration has been done with multi observation from three instruments LASCO, EIT and CELEAS on board SOHO and one instrument SXT on board GOES. We divided the observed CMEs primarily into two groups from shock passage point of view: shock waves with their origin CMEs and shock wave with unknown origin CMEs and calibrate our calculation that we use MATLAB in it accordingly and we found the following:

1. About 42% of our calculated travel time was consistence with CELEAS travel time for shock waves with registered origin CMEs.
2. Only 25% of our calculated result was consistence with the ELOT method for the travel time of shock waves that have no registered origin CMEs on CELEAS.
3. About 59% of the two groups' events were Westside events and only 29% of them were consistence with our results.
4. About 71% of the events from the first group were Westside events and 46% of them were consistence with our results.
5. All the western side events were associated with solar flare from different classes.
6. From the first group 79% found to be associated with Aurora at Earth and the rest were associated with the second group and only 40% were consistence with our results.

REFERENCES

1. Klassen A., Bothmer V., Mann G., Reiner M. J., Krucker S., Vourlidis A., and Kunow H., "Solar energetic electron events and coronal shocks", A&A, DOI: 10.1051/0004-6361:20020205, vol.385, pp. 1078-1088, 2002 .
2. Forbes T. G., Linker J. A. , Chen J., Cid C., Ko` Ta J., Lee M. A., Mann G., Miki`C Z., Potgieter M. S., Schmidt J. M., Siscoe G. L., Vainio R., Antiochos S. K. and Riley P., "CME theory and models", Space Science Reviews , DOI: 10.1007/s11214-006-9019-8, vol. 123, pp.251–302, 2006 .





Rabab Mazhir Jassim and Amjad Al-Sawad

3. Howard, T., "Coronal Mass Ejections", published by Spring by-Verlag New York, 376, 1st edition, 2011.
4. Cane, H.V., & Richardson, I.G., "Space Physics", Journal of Geophysical Research, 108, PP 1156, 2003.
5. Howard, T. A.; Tappin, S. J., " Interplanetary shocks unconnected with earthbound coronal mass ejections", Geophysical Research Letters, 32, Issue 14, PP:14106, 2005.
6. <http://spaceweather.com/archive.php?view=1&day=18&month=03&year=2015>.
7. M. J. Reiner, M. L. Kaiser, J.-L. Bougeret, "CORONAL AND INTERPLANETARY PROPAGATION OF CME/SOCKS FROM RADIO, IN SITU AND WHITE-LIGHT OBSERVATIONS", The Astrophysical Journal, 663:1369 – 1385, July 10, 2007.
8. Kocharov T. Laitinen, A. Al-Sawad, O. Saloniemi, E. Valtonen, M. J. Reiner., "Gradual Solar Energetic Particle Event Associated with a Decelerating Shock Wave", The Astrophysical Journal, 700:L51–L55, July 20, 2009.
9. Al-Sawad, A.; Saloniemi, O.; Laitinen, T. L.; Kocharov, L. G.; Valtonen, E. "Probing successive coronal mass ejections using high-energy protons", 31st International Cosmic Ray Conference - Łódź July 7-15, 2009.

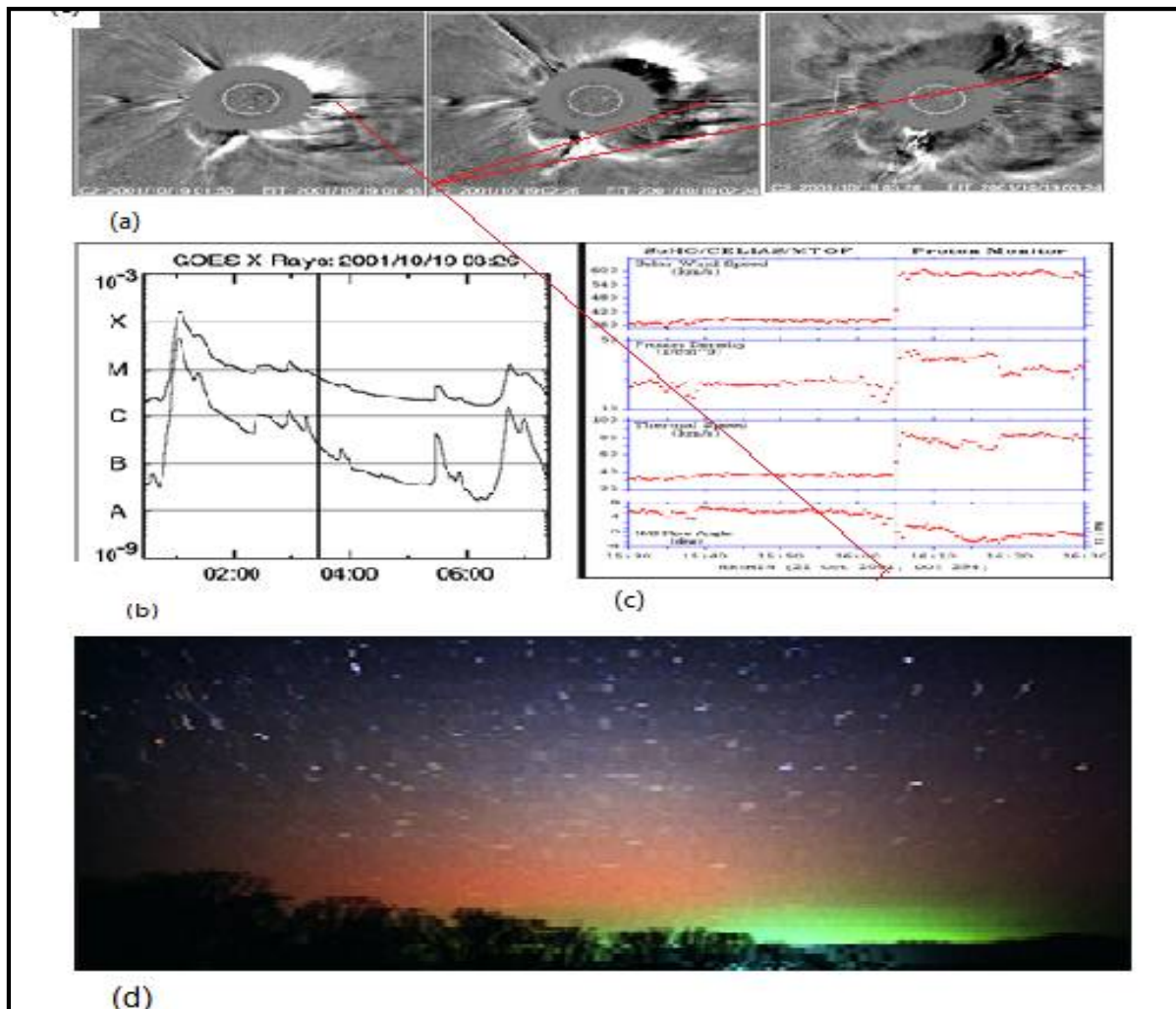


Fig.1. The analysis of the 21th-19th of Oct. 2001 event : (a) indicates the FC2AT of the CME detected by SOHO/LASCO. (b) The soft X-ray detected by GOES satellite for the associated flare. (c) CELIAS/MTOF registered shockwave arrival time and the end of injection. (d) aurora phenomena from space weather





Rabab Mazhir Jassim and Amjad Al-Sawad

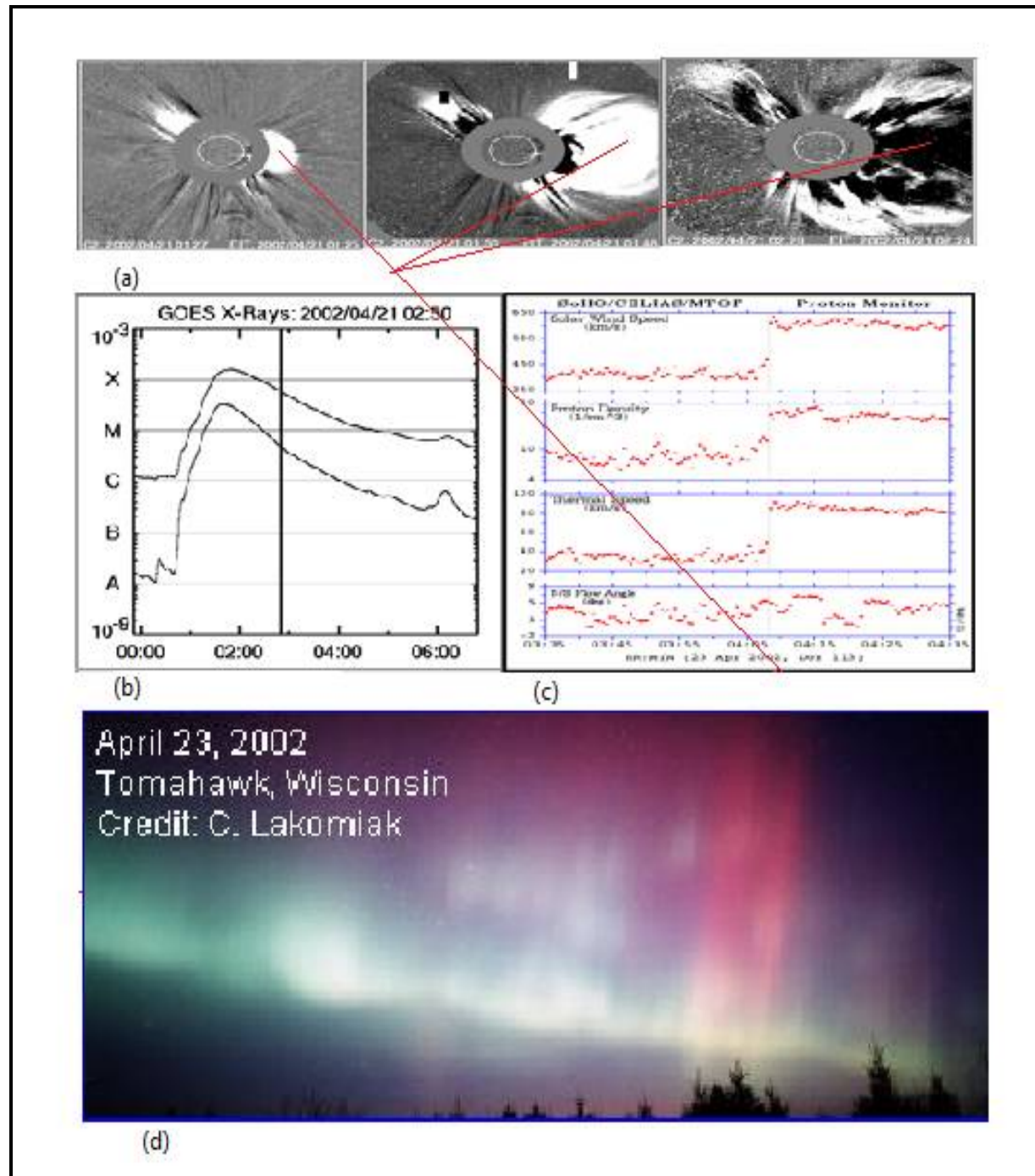


Fig.2.The analysis of *the 23rd - 21st* of April 2002 event : (a) indicates the FC2AT of the CME detected by SOHO/LASCO. (b) The soft X-ray detected by GOES satellite for the associated flare.(c) CELIAS/MTOF registered shockwave arrival time and the end of injection.(d) aurora phenomena from space weather.



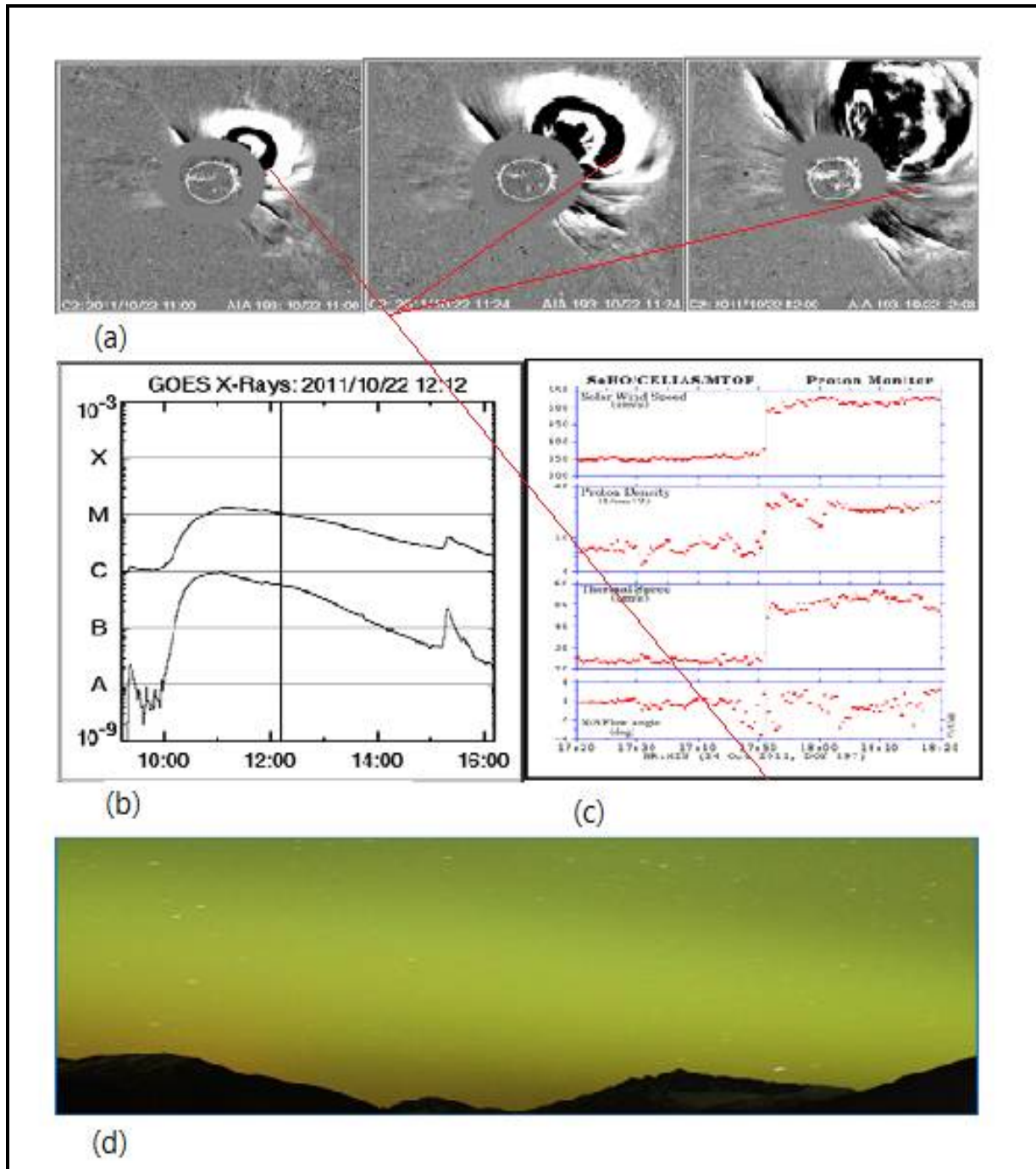


Fig. 3. The analysis of the 24th-22nd of Oct. 2011 event :(a) indicates the FC2AT of the CME detected by SOHO/LASCO. (b) The soft X-ray detected by GOES satellite for the associated flare.(c) CELIAS/MTOP registered shockwave arrival time and the end of injection.(d) aurora phenomena from space weather





Study (I-V) Characteristics and Panchen Curve of the Plasma Glow Discharge with Different Inter Electrodes Spacing

Mohammed.K. Khalaf^{1*}, Muhammed.Sh.Muhammed², Sabri. J. Mohammed³ and Thair.Kh.Salih⁴

¹Chief Scientific Researchers, Ministry of Sciences and Technology, Baghdad, Republic of Iraq.

²Education Mission, Education Department, Salah al-Din, Iraq

³ Physics Department, University of Tikrit, Republic of Iraq.

⁴Education Mission, Education Department, Salah al-Din, Iraq.

Received: 27 Oct 2018

Revised: 29 Nov 2018

Accepted: 03 Jan 2019

*Address for Correspondence

Mohammed.K. Khalaf

Chief Scientific Researchers,

Ministry of Sciences and Technology,

Baghdad, Republic of Iraq.



This is an Open Access Journal / article distributed under the terms of the **Creative Commons Attribution License** (CC BY-NC-ND 3.0) which permits unrestricted use, distribution, and reproduction in any medium, provided the original work is properly cited. All rights reserved.

ABSTRACT

In this paper includes results plasma spectra measurements of argon gas, the different distance between cathode and anode, Also, plasma parameters are obtained by optical emission spectroscopy Moreover includes electrical characteristics and analysis for the experimental measurements of reactive glow discharge system. Electrical properties like the Panchen curve, current-voltage, and current-pressure relations were studies. Also, plasma parameters measured by spectrometer were examined. In this present work, we investigate the properties of reactive magnetron sputtering plasma using Vanadium target with applied (660-820) V, and working pressure (0.6 to 0.35) mbar

Keywords: Magnetron sputtering, Panchen curve, Vanadium.

INTRODUCTION

This chapter includes results and analysis for the experimental measurements of reactive glow discharge system. Electrical properties like Panchen curve, current-voltage, and current-pressure relations were studies. The distance between cathode and anode, Optical Emission Spectroscopy is the most popular technique to investigate glow discharges since it is simple and that it produces no perturbation in the plasma. All plasmas emit radiation depending on their gas composition and plasma parameters. The purpose of the optical diffusion spectroscopy (OES) is to measure and analyze this radiation for understanding the plasma [1]. The remarkable advantage of OES is its aggressive measurement process. By just measuring the radiation from the plasma there is no need to bring a probe system in contact with the plasma (like Langmuir-Probe or Multiple Resonance Probe) which might influence the plasma itself. Furthermore, OES enables one to investigate very small plasmas; often smaller as probes

16378





Mohammed.K. Khalaf et al.

themselves. One of the most commonly used remote diagnostic methods is optical spectroscopy (OES), which is the illuminated section of general radio therapy. In OES, visible light is usually collected by a lens and focused on a spectrometer gap [2] [3]. From the information which take from optical emission spectroscopy we can measure electron temperature and electron density. Electron temperature and electron density obtained by the following equation respectively:

$$\frac{I_1}{I_2} = \left(\frac{\lambda_{n,m,z}}{\lambda_{k,i,z}} \right) \left(\frac{A_{k,i,z}}{A_{n,m,z}} \right) \left(\frac{g_{k,z}}{g_{n,z}} \right) e^{\left(\frac{-E_{k,z} - E_{n,z}}{KT_e} \right)} \dots\dots\dots (1)$$

$$n_e = \left(\frac{2\pi m_e K}{h^3} \right)^{3/2} \times \left(\frac{2A_{k,i,z} g_{k,i,z} \lambda_{N,M,Z} I_2}{A_{n,m,z} g_{n,m,z} \lambda_{k,i,z} I_1} \right) e^{\left(\frac{-E_{k,i} - E_{n,m}}{KT_{ex}} \right)} \times T_e^{3/2} \dots\dots\dots (2)$$

Reported by [4] the electron density increasing and electron temperature decrease with increasing gas pressure, while electron temperature increase with increasing the power. Although numerous studies have shown that due to the electrical properties of the plasma, little attention is given to the properties of the plasma spectrum[5].

EXPERIMENTAL SETUP

represent a DC plasma glow discharge characteristics for argon and oxygen gases. The variation of discharge current with the discharge voltage for inter-electrode spacing (d) from 3cm to 8 cm step 1cm with working pressure 0.8 mbar was examined. An electric field accelerates the ions and electrons which then collide with atoms of working gas giving rise to discharge current and gas temperature. The discharge in our device is operated in the abnormal regime. In this mode all cathode surface is fully covered by the discharge and an increase of the current leads to an increase of the current density on the cathode surface therefore, to an increase in the voltage. The plasma behaves electrically rather similar to a resistor. The results show that the relation between current and voltage (V) of a glow discharge is highly non-linear, (i.e.: abnormal glow); and in this region the Figs (3) show the current-voltage characteristics of the dc glow discharge at fixed argon gas pressure (6.7x10⁻² mbar) with different inter-electrodes spacing (d) for argon gas presented for vanadium. From this figure, it can be seen that at (5 cm) inter electrode spacing the discharge current become higher compared to other distances for all used targets Changes the plasma characteristic can be worthy of attentions when a tiny amount of oxygen was added, So get appropriate information about the properties of oxygen plasma enables us to know the optimal operating conditions with certain plasma characteristics The I-V characteristic, at different O₂ percentage in (Ar/O₂) gas mixture shown in figure (4), where gas pressure is kept at fixed value at 0.08 mbar. From this figure depict [6] that the discharge current increase with increasing applied voltage, that means the electrical discharge are operation in the abnormal glow discharge region. It is clearly seen that, at the same applied voltage and gas pressure, the discharge current decreases by increasing the O₂ percentage in (Ar/O₂) gas mixture. The decrease in the discharge current with increased O₂ percentage, this may be attributed to follows: the ionization cross –section of O₂ is smaller than that of Ar[7]. In addition, since the electron affinity of oxygen, discharges in oxygen contain negative ions, which result in the increase of plasma resistance due to reduction of electron density and thus the discharge current decreases [8].

Panchen’s Law Results

The electrical characteristics of discharge plasma, such as Panchen’s curve as well as dependencies of discharge current on the applied voltage and gas pressure inside the vacuum chamber, are of importance to introduce the homogeneity of the generated plasma. In the following Panchen curves for plan parallel electrodes with working gas is high purity noble gases (argon) were obtained by measuring the breakdown voltage as a function of *pd* parameter with two planar stainless steel electrodes. The results within the range of DC voltage lower than 700 V and pressure *P* = 9.2 x1⁻² to 6.5x10⁻¹mbar for different electrodes separation. In fig.(5) Five different curves can be observed





Mohammed.K. Khalaf et al.

for the five different electrodes gaps (4,5,6,8) cm, the curves behaved nearly in the same way and obey general behavior of the standard Panchen's curve. On the left-hand side of the minimum for each curve lies in the same region (between 0.6 and 1 mbar cm). Each curve has a singularity [8]. V_B has behavior on pd product; the curve V_B decreases speedily when increasing Pd and then rises with a minimum value; on the right-hand of the minimum value is very steep is relatively smooth. Two opposite process work: while the pd value increases. For one thing, the colliding numbers of electrons and atoms rise due to the increasing intensity pressure, and it is agreeable for discharge. On the other hand, dropping in average free path and the energy that the electrons obtain from the electric field also minimize in each free path, and it is unfavorable for discharge. The ignition voltage relies on the various of these two process[9].

Table (1) shows the minimum breakdown voltage (V_B)_{min} and (pd)_{min} at different distance electrodes. It can be show that increasing d near and to the right of the minimum and leads to the rise of (V_B). The change of the breakdown curves to above (V_B) and pd values with the increase of the inter electrode distance is due to the emergence of the charged particles diffusion to chamber wells. The optimize minimum breakdown voltage (V_B)_{min} and (pd)_{min} at different distance electrodes equals to 5 cm have been established with the scheme shown in figure (5)[10]

CONCLUSION

The I-V characteristics of a gas discharge were deduced as a plasma system operated in an abnormal glow discharge region, which is a very important parameter in the sputtering deposition. Also, the high discharge current occurs at Panchen minimum, and when argon flow (Ar).

REFERENCES

1. A.K.Shrestha, R. Shrestha, H. B. Baniya, R. B. Tyata, D. P. Subedi, and C. S. Wong, "Influence of Discharge Voltage and Pressure on the Plasma Parameters in a Low Pressure DC Glow Discharge," *Int. J. Recent Res. Rev.*, vol. VII, no. 2, 2014.
2. C. Aragón and J. A. Aguilera, "Characterization of laser induced plasmas by optical emission spectroscopy: A review of experiments and methods," *Spectrochim. Acta Part B At. Spectrosc.*, vol. 63, no. 9, pp. 893–916, Sep. 2008.
3. *and M. Meyyappan†† A. A. Bol'shakov,* B. A. Cruden,† R. Mogul,‡ M. V. V. S. Rao,§ S. P. Sharma,¶ B. N. Khare, "Radio-Frequency Oxygen Plasma as a Sterilization Source," *AIAA*, vol. 42, pp. 823–832, 2004.
4. J. K. Rhee, D. B. Kim, S. Y. Moon, and W. Choe, "Change of the argon-based atmospheric pressure large area plasma characteristics by the helium and oxygen gas mixing," *Thin Solid Films*, vol. 515, no. 12, pp. 4909–4912, Apr. 2007.
5. F.J.Gordillo-Vázquez, M. Camero, and C. Gómez-Aleixandre, "Spectroscopic measurements of the electron temperature in low pressure radiofrequency Ar/H₂/C₂H₂ and Ar/H₂/CH₄ plasmas used for the synthesis of nanocarbon structures," *Plasma Sources Sci. Technol.*, vol. 15, no. 1, pp. 42–51, Feb. 2006.
6. W.A Gambling, H. Br. Edels, "Breakdown Potentials of Gases", *J. Appl. Phys*, Vol.5, (1965)p. 36 .
7. L.K.Athab, "Synthesis and Electrical Discharge Characterization of Silver nanoparticle in TiO₂ Thin Film by Plasma Sputtering Technique," p. 164, 2017.
8. A. Garamoon1, A Samir, F. Elakshar1 and E. Kotp, |*Plasma Sources Sci. Technol.* Vol.12 (2003), P. 417–420
9. Mohammed K. Khalaf, " Low-pressure plasma Reactor for Materials Surfaces Processing", Ph.D. Thesis, Dep. Phys., University of Baghdad, Iraq, (2010).
10. I.B.Chapman, "Glow Discharge Processes: Sputtering and Plasma Etching". John Wiley & Sons. INC, New York, (1980).





Mohammed.K. Khalaf et al.

Table .1. Minimum breakdown voltage and pd minimum for Ar gas at different distance

d (cm)	4 cm	5 cm	6 cm	8 cm
Breakdown voltage(V_B)min	320	316	326	330
P.dmin(mbar.cm)	0.68	0.69	0.8	0.95

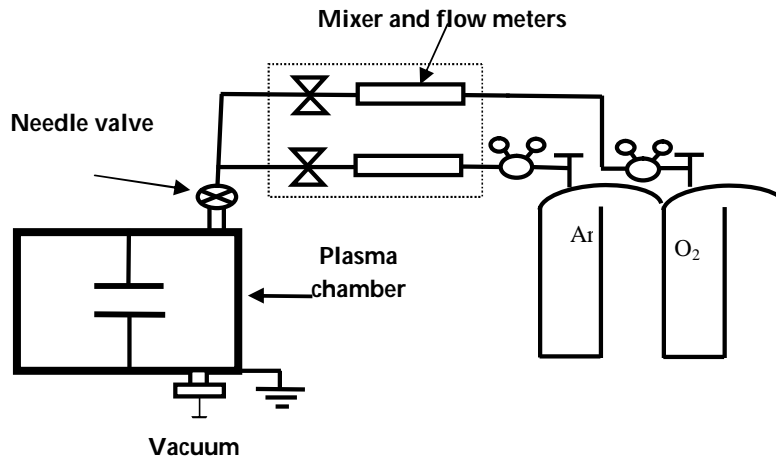


Figure 1. The main experimental set-up used in this work

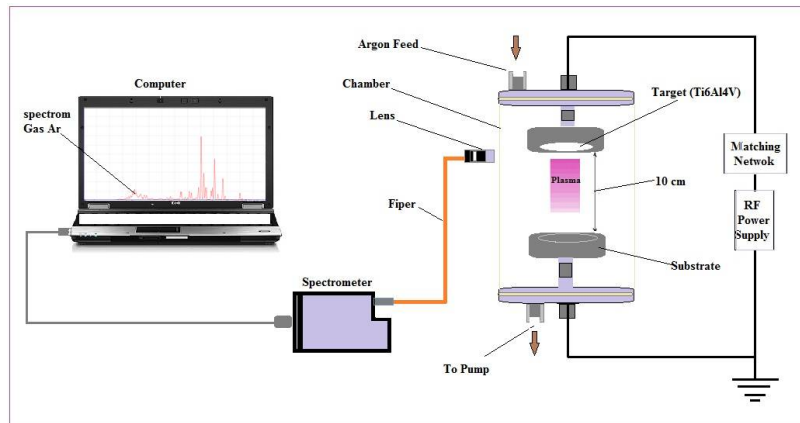


Figure 2. Optical emission spectroscopy experimental setup.





Mohammed.K. Khalaf et al.

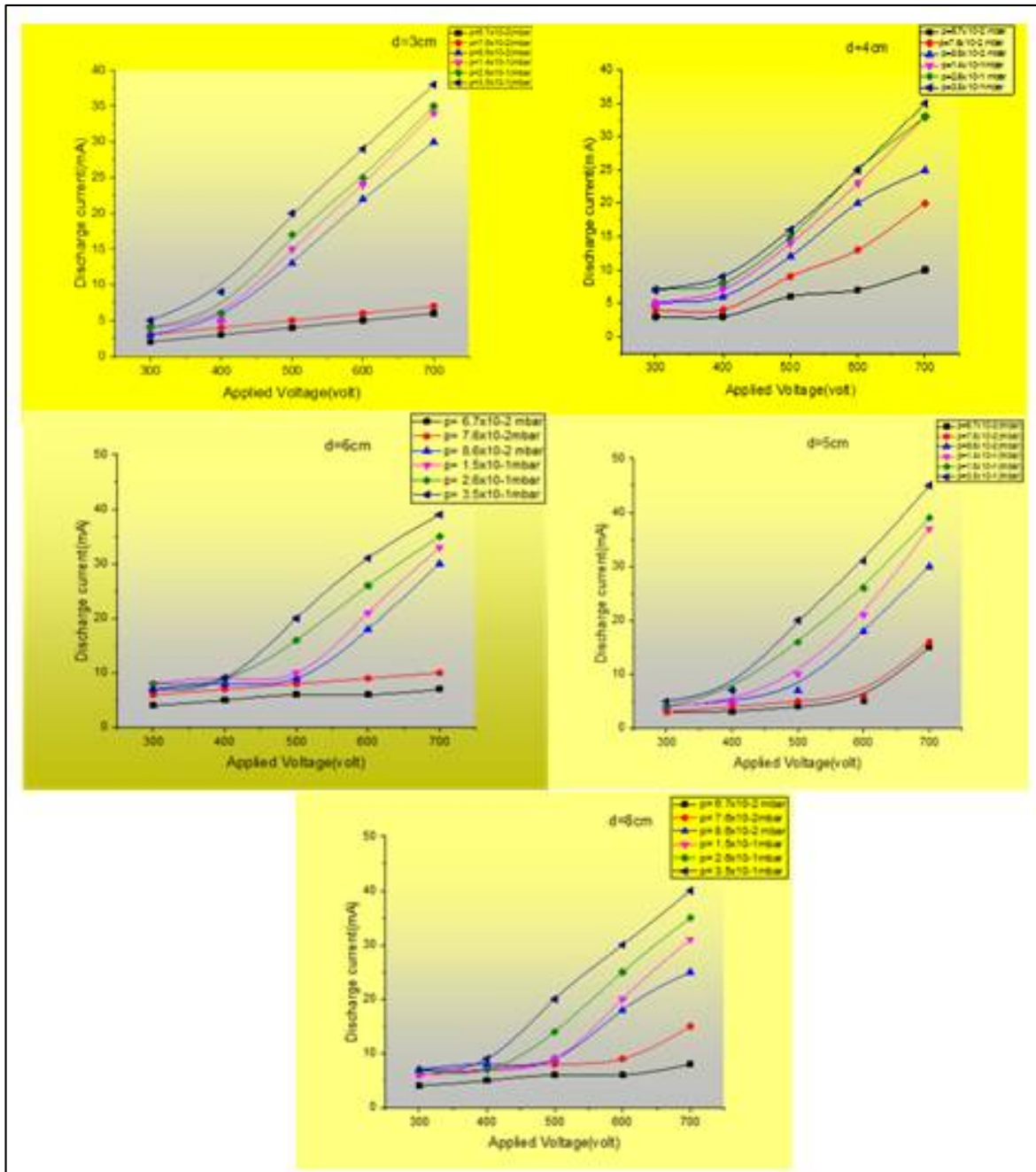


Fig.3.The variation of discharge current with applied voltage at Different working pressures of Ar gas for different inter electrodes Spacing





Mohammed.K. Khalaf et al.

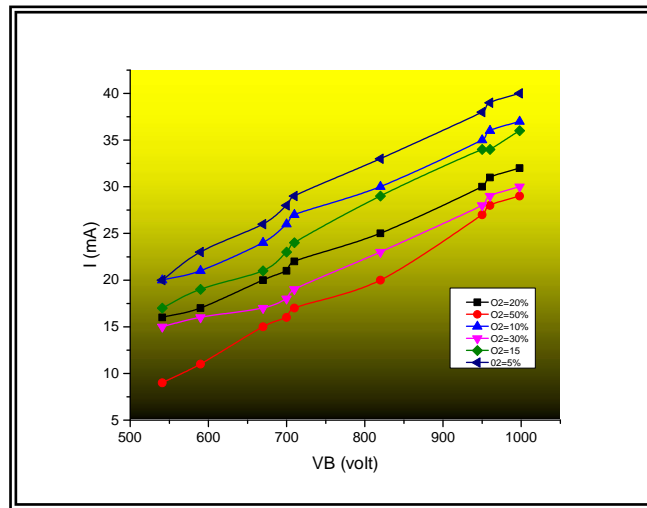


Fig.4. The discharge current –volt characteristic curve at different O₂percentage at working pressure of (0.08mbar) at the distance between the electrodes (5 cm)

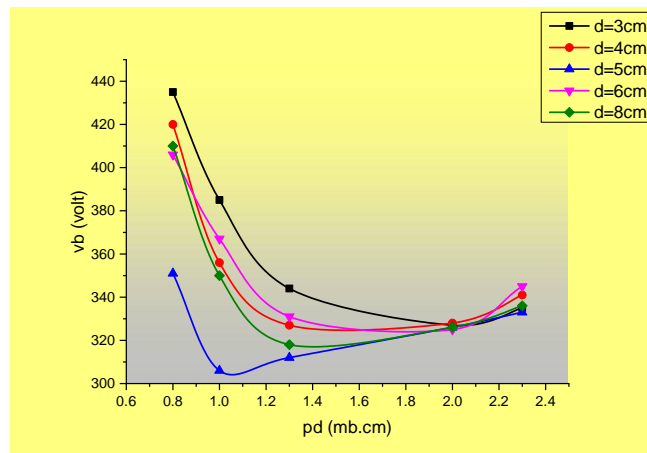


Fig.5. Panchen's curves of the Ar gas discharge plasma at different electrodes separation





Design and Test of Electrochemistry of Electrodes Catalysis for an Alkaline Fuel Cell

Haleemah J. Mohammed* and Nathera .A. Ali

Department of Physics, College of Science, University of Baghdad, Iraq.

Received: 26 Oct 2018

Revised: 28 Nov 2018

Accepted: 03 Jan 2019

*Address for Correspondence

Haleemah J. Mohammed

Department of Physics,

College of Science,

University of Baghdad, Iraq.

Email: alhamdaniya2003@yahoo.com



This is an Open Access Journal / article distributed under the terms of the **Creative Commons Attribution License** (CC BY-NC-ND 3.0) which permits unrestricted use, distribution, and reproduction in any medium, provided the original work is properly cited. All rights reserved.

ABSTRACT

This paper was aimed to design an alkaline fuel cell from anode and cathode mesh electrodes. The electrodes were coated with nickel oxide nanocatalysts. The outer wall of the cell consists of organic glass sheets. Also, which carries electrically charged molecules from one electrode to another and stimulates, accelerating interactions in the electrodes. Hydrogen is the primary fuel, produces from an electrolyser, Nickel oxide nanocatalysts was prepared by Chemical deposition, The Structural characteristics was studied through of X-ray diffraction (XRD) of the prepare for determining the yielding phase, Also the sample will test using an atomic force microscope to find the roughness of the prepared surface, Voltages were also obtained at 1.74 volts and current at 3.01 A of an alkaline fuel cell. In addition, study the characterization of the electrochemical parameters.

Key words: an alkaline fuel cell, nickel oxide nanocatalysts, Chemical deposition, electrolyser.

INTRODUCTION

Fuel cells are electrochemical devices that convert chemical energy to interact directly into electrical energy. Depending on the type of fuel cells used in electricity was classified into different groups. Each fuel cell has two electric electrodes, named, respectively the negative electrode and the positive electrode. An electrolyte membrane also, which carries the charge of molecules electrically from one electrode to the other and a catalyst [1]. The oldest fuel cells that were carefully developed and made possible electricity generation of hydrogen using KOH complex liquid electrolytes were alkaline fuel cells (AFCs) [2], Nano particles attracted wide interests because of their good properties namely optical, electronic, magnetic, thermal, mechanical properties, battery use for electrodes, gas sensors, electrochemical films, photoelectric devices[3]. The introduction of nanotechnology, which contributes significantly to sustainable economic growth. Nanotechnology is a generic term used to describe materials and



**Haleemah J. Mohammed and Nathera .A. Ali**

phenomena on a nanometer. Specifically, it means not only minimizing but also the subtle changes in atoms and molecules to design and control the properties of nonmaterial. With an emphasis on the energy field, nanotechnology has the potential to significantly reduce Of the impact of energy production, Storage and use An already sustainable energy system, the scientific community is considering further development of nanotechnology for energy [4], The researcher Yasuhiro Mizukoshi and Katsumi Yamada evaluated the electrochemical properties of NiO/Au. High-velocity electrochemical changes was obtained within one second by improvements in penis length and film thickness for the NiO film[5], The researcher Tomokazu Sakamoto and his group NIO/Nb2O5/C, NIO/C, and Ni/C catalysts was manufactured for electro-hydrazine electrooxidation by evaporation drying method followed by thermodynamic nano materials have been extensively tested in recent decades because of their high surface area, which severely affects their physical properties. And on reported nanostructure shapes [6], The researcher Eileen Hao Yu, and his group studied new catalysts. And anion exchange membranes. In addition, alkaline fuel cell systems and new configurations were studied[7], The researcher István Bakos and his group used a layer of nano particles to partially cover Ni thin-film to provide the most effective use of the HOR catalyst. The Pd / Ni electrodes were prepared by spontaneous and electrolytic deposition of Pd on nickel-pure polycrystalline surfaces [8].

MATERIALS AND METHODS**Preparation of NiO nanoparticles**

1 g of NiCl₂ (6H₂O) powder and add 10 mL ammonia gradually (Approx. 15 min) to under the strong stirring to produce Ni + 2 solutions. Due to the NiCl₂ exothermic reaction with ammonia, ammonia slowly added to the precursors. The temperature of the solution was 75 ° C, and the pH was in a range to nine. Then add the deionized water as a precipitating agent while continuing under the strong stirring solution until the green sediment was formed. The resulting precipitates were filtered and washed twice with deionized water and ethanol. For the production of black NiO nanoparticles. And dry at 105 ° C for 90 minutes in the oven. As shown in 'Figure 1a'

Synthesis of catalysts

For the purpose of electrical insulation and control of the movement of ions electrons between the electrodes of the alkaline cell, the catalyst was prepared, and the electrodes are prepared for this purpose by placing, The desired electrode after attaching it to the negative electrode, the other carbon connected to the positive electrode of the power supply (5.6V and 0.90A) (1 L). The distance between the electrodes is 3 mm, the coating solution was added by taking 0.5 g of Nickel chloride salt (NiCl₂•6H₂O) and dissolved in 1 liter of deionized water, Where it is a clear solution green color in mixing a process to immerse the electrodes almost, and for three hours, until you a gray coating layer of NIO catalyst atoms was produced. After the coating was completed, it was cleaned with deionized water and dried. As shown in 'Figure 1 b,c'. The electrolysis cell consists of stainless steel plates of type 314 No. 2 isolated from each other, for the purpose of isolating each gas separately (hydrogen and oxygen), including a plate of organic glass. These electrodes are immersed in an electrolyte solution, prepared from distilled water and added to 28% of potassium hydroxide. The outer wall consists of organic glass to prevent leakage of gases (14.5 x 12) cm² from the 0,1 cm thick of and these electrodes were connected to a solar cell operating at 10 volts and a current of up to 3 shown in 'Figure 2'. A fuel cell alkaline consists of nano nickel oxide catalyst a porous anode and nano nickel oxide catalyst a porous cathode, with these two electrodes separated by is (KOH). An oxidant is fed to the cathode to supply hydrogen while is fed in the anode to supply hydrogen. The electrolyte supports the transfer of ions between an anode and cathode to support the reverse electrolysis reaction. The outer wall of the cell consists of organic glass sheets.





Haleemah J. Mohammed and Nathera .A. Ali

RESULTS AND DISCUSSION

The surface morphology of the nano NiO catalyst has been verified using AFM studies that are fully focused on the nano scale characterization. AFM images show nickel oxide prepared at a substrate temperature of 350 ° C with a uniform granular surface morphology, We have studied the surface morphology of the catalytic layers: a sponge-like structure is produced when the current density increases, where nano crystalline can be seen and distributed throughout the entire surface. As well as Analysis of the morphology of the catalyst Porous under varying current density conditions. In the low current density, the network was obtained very highly spaced, randomly oriented and highly correlated of pores. However, the increase in the current density of small pores showing forms, leading to a catalyst It was found that the particle size was 65 nm as shown in 'Figure 3 a, size, distribution, and morphology are closely related to the preparation techniques [3,9]. The XRD patterns indicate that the nano composite is well 'Figure 4 the obtained patterns are presented in Fig. 4, XRD analysis showed a series of diffraction peaks at 2θ of 27.21°, 42.08°, 61.82°, and 75.94° ° can be assigned to (111), (200), (220), (219) and (2 11) planes, The diffraction peaks show good crystalline nanoparticles and match very well with ideal lattice constants , n this paper , The XRD pattern shows that the samples are single phase and distinct diffraction peak except the characteristic peaks of FCC phase NiO was detected. This result shows that the physical phases of the NiO nanoparticles have higher purity prepared[10].

Organic glass plates were used in the outer surface of this cell, and electrodes were attached to the Stainless Steel Restaurant with Nickel oxide Plated Mesh (2) applied by electroplating process. Hydrogen gas was released from the dissolution of water molecules in electrolysis to analyze water to the cell through anode electrode Touch a layer of the nano-nickel oxide catalyst, which in turn separates the hydrogen molecules into atoms, and then the protons and electrons pass through an external load cycle accompanied by the movement of hydrogen ions (OH⁻¹) from the negative electrode through the electrolyte solution of the anode electrode, Oxygen molecules At the cathode, the electrode merges with the electrons that travel through the outer load circuit to form the water molecule again at the anode pole, accompanied by an increase in the valiant cell temperature to more than 70 ° C, to obtain a power of 1.74 volts and a current of 3.01 A. As shows 'Figure 5 , ' The amount of energy produced by the alkaline cell depends on the thickness and quantity of the plates. The atoms are the nickel oxide that stimulates the hydrogen molecules and converts them into electrons in the form of energy, As well as the purity and amount of hydrogen provided to the alkaline cell. The higher the purity, the higher the energy and the oxygen from the other electrode (cathode) This increases the energy and efficiency of the cell. In this paper, cell operation using oxygen from the electrolysis system was tested [11] [12]. Table 1 , The dimensions of mesh electrodes. And Table 2 shows increased electrical conductivity with an increase in the flow rate of hydrogen due to the amount of hydrogen gas.

Note:
$$\sigma = \frac{I \cdot L}{V \cdot W \cdot T} \quad (1)$$

σ electrical conductivity I: current (A), L: sample length (cm) W: sample width (cm), T: sample and thickness (cm)

As shown in 'Figure 6' the voltage of fuel cell decreased with the current same flow rate. at 0.5 L/min flow rate of H₂ gas ,It was drown using the Origin Lab program. As shown in 'Figure 7' electrical conductivity increases with in the current.Same in rate of hydrogen and oxygen gases, hydrogen has the highest energy density per unit weight than any other chemical fuel for many applications. It can be converted directly into electricity by cell in an electrochemical process. As shown in 'Figure8 the variation of cell voltage decreases with i increases current density (current/area) for the cell operating his voltage drop is the straightforward resistance to the flow of electrons through the material of the electrodes and the various interconnections, There are four major factors which contribute to the decrease in cell performance. The primary four sources of losses are fuel cross-over, ohmic polarisation and concentration hydrogen[14].





Haleemah J. Mohammed and Nathera .A. Ali

CONCLUSION

We have presented a simple chemical method for producing nano nickel oxide. In this research, Nano nickel oxide catalysts were synthesized successfully for Membrane for fuel cell application. Through this study found that the voltage of fuel cell decreased with the current same flow rate. While electrical conductivity increases with increasing in the current. As well as decreased with the voltage same flow rate. With increases current density. The alkaline fuel cell has been selected for its advantages. Operating temperature is a wide range, The composition of these cells is simple, Quick start, The cost is low because of the simplicity of the material.

REFERENCES

1. Khemraj Barhate , Madhuri Sharon , L.N. Singh and Maheshwar Sharon, 2011, "Development of Hydrogen Electrode for Alkaline Fuel Cell", Department of Physics, Babasaheb Ambedkar Technical University, Lonere, Maharashtra, The Open Fuel Cells Journal, 4. 30-33.
2. G. E. Evans and K. V. Kordesch, 1967 , "Hydrazine Air Fuel Cells," vol. 158, pp. 1148-1152.
3. K. Anandan and V. Rajendran, 2012, " Structural, optical and magnetic properties of well dispersed NiO nanoparticles synthesized by CTAB assisted solvothermal process" Nanoscience and Nanotechnology: An International Journal Universal Research Publications. All rights reserve ISSN: 2278 -1374. <http://www.urpjournals.com>.
4. Elena Serrano a, Guillermo Rus b, Javier García-Martínez b, 2009, "Nanotechnology for sustainable energy University of Alicante, Carretera Alicante-San Vicente s/n, E-03690 Alicante, Spain b Dpt. Structural Mechanics, University of Granada, Politécnico de Fuentenueva, 18071 Granada, Spain Renewable and Sustainable Energy . Reviews 13 2373–2384.
5. Yasuhiro Mizukoshi and Katsumi Yamada ,2014, " Electrochromic Characteristics of NiO/Au Composite Nanorod Array Membrane" Bull. Soc. Photogr. Imag. Japan. Vol. 24 No. 1: 12–17.
6. Tomokazu Sakamoto, Teruyuki Masuda, Koji Yoshimoto, Hirofumi Kishi, Susumu Yamaguchi, Daiju Matsumura, Kazuhisa Tamura, Akihiro Hori, Yousuke Horiuchi, Alexey Serov, Kateryna Artyushkova, Plamen Atanassov, and Hirohisa Tanaka ,2017, " NiO/Nb₂O₅/C Hydrazine Electrooxidation Catalysts for Anion Exchange Membrane Fuel Cells' Journal of The Electrochemical Society, 164(4) F229-F234 .
7. Eileen Hao Yu, Xu Wang, Ulrike Krewer, Lei Lid and Keith Scotta ,2012, " Direct oxidation alkaline fuel cells: from materials to systems" Energy Environmental Science Cite this: Energy Environ. Sci., 5, 5668 , www.rsc.org/ees.
8. István Bakos, András Paszternák, David Zitoun, 2015, " Pd/Ni Synergistic Activity for Hydrogen Oxidation Reaction in Alkaline Conditions" Electrochimica acta 176: 1074-1082 .
9. K.C. Liu, M.A. Anderson, 1996, " Porous nickel oxide/nickel films for electrochemical capacitors", J. Electrochem. Soc. 143 124–130.
10. D. Syamala Bai, R. Padma Suvarn, C. Bala Murali Krishna ,2016, "Characterization and DC Conductivity Studies of NiO Nano Particle" Indian Journal of Advances in Chemical Science 4(1) 98-101.
11. A. Moroza, I. Stamatina, L. Stamatina, A. Dumitru, and K. Scott, 2007, " Carbon electrodes for microbial fuel cells". Nano-*SAE* Research Centre, University of Bucharest, MG-38, 077125, Bucharest-Magurele, Romania School of Chemical Engineering and Advanced Materials, University of Newcastle upon Tyne, NE1 7RU, England, Journal of Optoelectronics and Advanced Materials Vol. 9, No. 1, p. 221 – 224, January .
12. Yongjun Leng, Lizhu Wang, Michael A. Hickner, and Chao-Yang Wang, 2015, "Alkaline membrane fuel cells with in-situ cross-linked ionomers", Electrochimica Acta 152 93–100.
13. Pakkanen, A., 2007, "Hydrogen fuel cell vehicle and a standalone renewable energy based re- fuelling station", masters degree of programmers in renewable energy, University of Jyväskylä.
14. ung-Chou Lin, H. Russell Kunz, James M. Fenton, Suzanne S. Fenton, 2003, " The Fuel Cell – An Ideal Chemical Engineering Undergraduate Experiment " Revised as of July 14.





Haleemah J. Mohammed and Nathera .A. Ali

Table 1. The dimensions of mesh electrodes

Samples	Width, W(cm)	Length, L (cm)	Thickness (cm)
Mesh electrode	3	3.5	0.1

Table 2. Show the relationship between the Electrical conductivity with current and voltage

Electrical conductivity σ (S/cm)	Current (A)	Voltage (V)	Current density (A/cm ²)
14.83	3.01	1.74	0.29
16.77	3.15	1.61	0.3
18.36	3.32	1.55	0.32
23.81	3.75	1.35	0.36
31.38	4.54	1.24	0.43
37.30	5.31	1.22	0.51
41.06	5.75	1.2	0.55

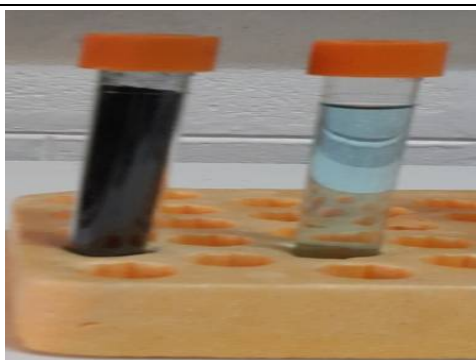


Figure 1a. Preparation of nano NiO



Figure 1b. Electroplating process



Figure 1c. the membrane



Figure 2. The electrolysis cell





Haleemah J. Mohammed and Nathera .A. Ali

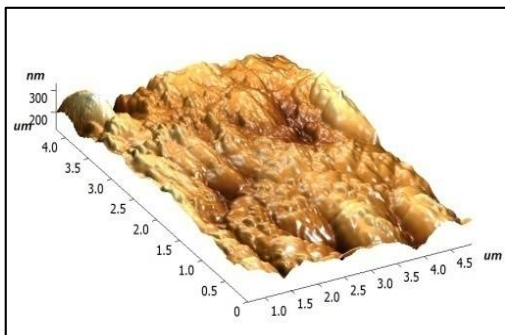


Figure 3a. Atomic force microscope of nano NiO catalyst

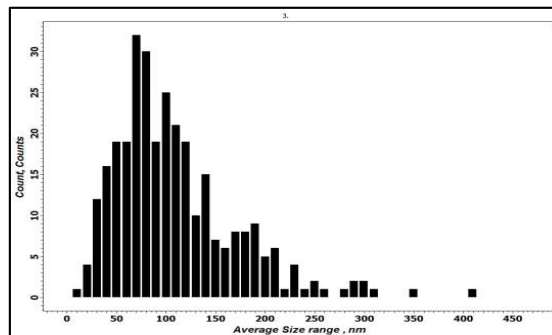


Figure 3b. Histogram of their size distribution of nano NiO catalyst

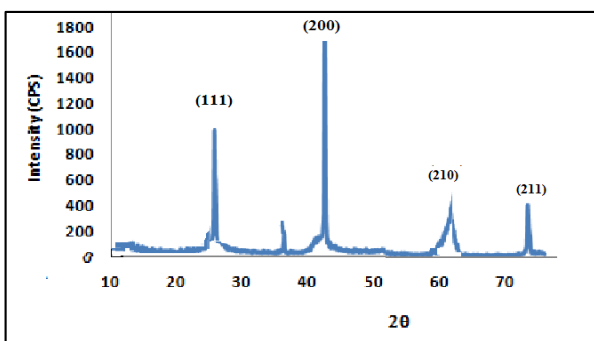


Figure 4. X-ray diffraction analysis of NiO nanoparticles



Figure 5. The fuel cell

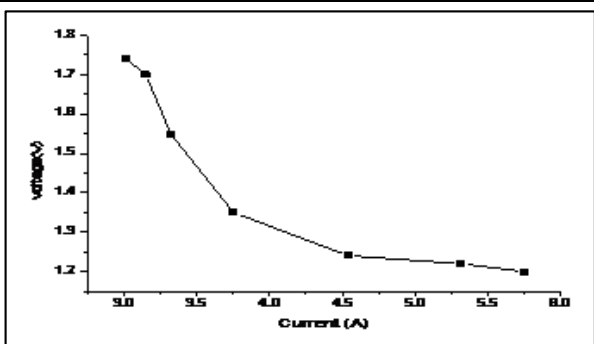


Figure 6. current-voltage at 0.5 L/min flow rate of H2 gas

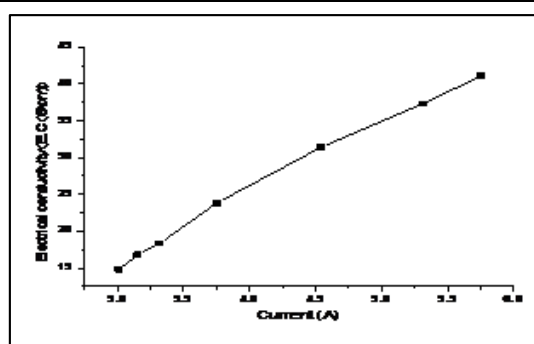


Figure 7. Electrical conductivity with current at 0.5 L \ min flow rate of H2 gas





Haleemah J. Mohammed and Nathera .A. Ali

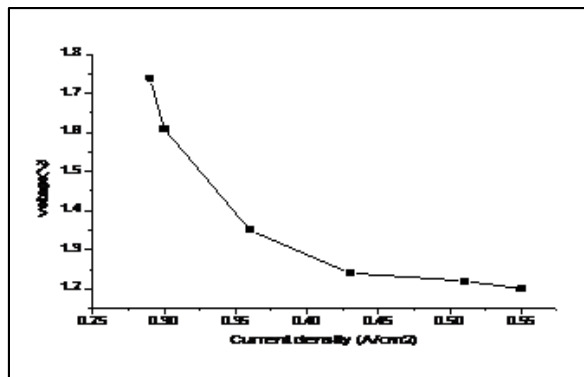


Figure 8.current density- Voltage at 0.5 L/min flow rate of H2 gas





The Optical Spectroscopy uses for Different Elements

T.A Ali Al-dulaimi*, Areeg Al-hamadani, Mohammed Al-Gherairy , Rafid Al-Zuhairi, Amar Al- timimi and Waleed Alewee

Collage of Science, University of Diyala, Diyala, Baquba, Iraq.

Received: 27 Oct 2018

Revised: 30 Nov 2018

Accepted: 03 Jan 2019

*Address for Correspondence

T.A Ali Al-dulaimi

Collage of Science,
University of Diyala,
Diyala, Baquba, Iraq.



This is an Open Access Journal / article distributed under the terms of the **Creative Commons Attribution License** (CC BY-NC-ND 3.0) which permits unrestricted use, distribution, and reproduction in any medium, provided the original work is properly cited. All rights reserved.

ABSTRACT

In this research we found the calibration constant for the monochromator by using Neon emission lamp and Mercury emission lamp. Then we measured the visible spectrum for Hydrogen and Helium to find the Rydberg constant and the allowed energy transitions for the Helium. Finally we calculated the dissociation energy for the Iodine by measuring the Iodine-vapor absorption spectrum.

Keywords: calibration, Mercury, lamp, spectrum, Helium, Hydrogen, energy

INTRODUCTION

The optical spectroscopy is technique to study the properties of physical objects based on measuring how an object emits and interacts with light and to measure energy transitions as we did in this research. When the electrons inside the atom are excited by an external energy, which is a voltage in our research, they will excite to the upper level and then come back by emitting an photon with an energy (wavelength) equal to the difference between these two levels. From this wavelength we can find the emission spectra and from these spectra we can find several physical quantities such as the allowed transition energy, the calibration constant. Also we can find the absorption spectrum, which is the absorption of electron to an photon with energy equal to the energy that is the difference between two levels, to find dissociation energy as will see later on. The transition energy level can be radiative or non-radiative involving both the absorption and emission. When the photon with certain energy (wavelength) hit the molecule, the molecule will excite to higher state by absorb the photon and then decay to lower state by emitting a photon and this photon will not be necessary to have the same energy with the incident one. Therefore, there might be a difference between the absorbed and emitted photon energies as shown in the figure (1), so if the energies of the absorbed and emitted photon are equal it called Rayleigh, if not it called anti-Stokes when the electron decay to the level lower energy than the one it originated from, or it called Stoke if the electron decay to level higher energy than the one it originated from[1].





T.A Ali Al-dulaimi et al.

The Emission and Absorption Spectra

Emission and absorption spectra are techniques that are used physics. Emission is the ability of a substance to emit light, when it interacts with radiation. Absorption is the opposite of emission, where energy, light or radiation, is absorbed by the electrons of a particular matter. In other words, absorption is the ability of the electrons to absorb light which makes them excited to a higher energy levels. Absorption is used to determine the absorption level for an object by using the absorption spectra as shown in figure (2) for the Hydrogen.

The Hydrogen Balmer Series and Rydberg Constant

The Hydrogen atoms lamp emit series of lines in the visible part of the spectrum and this series are known as Balmer series, which is the transition from $n > 3$ to $n = 2$, where n is the principle quantum number, according to Johann Balmer, who was able to describe the wavelength of these lines by using equation(1). The individual lines in the Balmer series are given the names Alpha, Beta, Gamma and Delta, and each of them corresponds to a n_f value of 3, 4, 5, and 6 respectively, and the Balmer lines are in the visible part of the spectrum[3] as shown in figure(2) above

$$\lambda = B \left\{ \frac{n^2}{(n^2 - 4)} \right\} \dots\dots(1)$$

where B is the Balmer constant which is equal to 364.50682 nm, n is an integer (principle quantum number $n > 2$) and λ is the wavelength.

Then Rydberg generalized the Balmer formula as shown in the equation(2)

$$\frac{1}{\lambda} = \frac{4}{B} \left\{ \frac{1}{2^2} - \frac{1}{n_f^2} \right\} = R \left\{ \frac{1}{2^2} - \frac{1}{n_f^2} \right\} \dots\dots(2)$$

where λ is wavelength R is Rydberg Constant

$$R = \frac{4}{B} = 1.0973 \text{ cm}^{-1}$$

Boher Model

According to Boher model the electron can orbit about the nucleus of an atom by stable orbit as shown in equation(3) without loss or gain an energy unless the electron jamb from one allowed orbit to another [4]

$$l = m_e v_n r_n = n \frac{h}{2\pi} \dots\dots(3)$$

Where m_e is the electron mass v_n is the speed of the electron and r_n is its radius as it orbits with an integral number n of the quantity $h/2\pi$, and n is principal quantum number. Since the electron move around the nucleus "proton" with stable orbit, there should be electric force F_E to hold the electron in its orbit and this force is known as Coulomb's Law equation(4), also the electric force should equal to the centripetal force F_C equation(5).

$$F_E = \frac{1}{4\pi\epsilon_0} \frac{e^2}{r_n^2} \dots\dots(4)$$





T.A Ali Al-dulaimi et al.

Where e is the magnitude of charges of the electron and proton, ϵ_0 is the permittivity of free space, r_n is the radius of the orbit.

$$F_C = \frac{v_n^2 m_e}{r_n} \dots\dots (5)$$

Where m_e is the mass of the electron and v_n is the speed of the electron as moves in the circular orbit of radius r_n . Since F_E and F_C we can write equations 4 and 5 as shown in equation(6)

$$\frac{1}{4\pi\epsilon_0} \frac{e^2}{r_n^2} = \frac{v_n^2 m_e}{r_n} \dots\dots (6)$$

Hence from equations 3 and 6 we can find

$$r_n = \epsilon_0 \frac{n^2 h^2}{\pi m_e e^2} \dots\dots (7)$$

And

$$v_n = \frac{1}{\epsilon_0} \frac{e^2}{2nh} \dots\dots (8)$$

According to Boher model the Boher radius is when $n=1$ so equation(7) will be as shown in equation(9) and in Boher model the total energy E_n equation(10) for the electron is the sum of the potential energy equation(11) and kinetic energy equation(12)

$$v_1 = \frac{1}{\epsilon_0} \frac{e^2}{2h} \dots\dots (9)$$

$$E_n = KE_n + PE_n \dots\dots (10)$$

$$PE_n = \frac{1}{4\pi\epsilon_0} \frac{e^2}{r_n} \dots\dots (11) \quad KE_n = \frac{m_e v_n^2}{2} \dots\dots (12)$$

Now we can substitute equations (7) and (8) into equations (11) and (12) and then into equation (10). we find the total electron energy as in equation (13)

$$E_n = \frac{-1}{\epsilon_0^2} \frac{m_e e^4}{8n^2 h^2} \dots\dots (13)$$

Finally we can find ΔE the transition from initial value to the final value as in equation(14)

$$\Delta E_n = \frac{m_e e^4}{8\epsilon_0^2 h^2} \left[\frac{1}{n_i^2} - \frac{1}{n_f^2} \right] \dots\dots (14)$$





T.A Ali Al-dulaimi et al.

And since $\Delta E=hc/\lambda$ we can rewrite equation(14) as in the equation (15)

$$\frac{1}{\lambda} = \frac{m_e e^4}{8\epsilon_0^2 h^3 c} \left[\frac{1}{2^2} - \frac{1}{n_f^2} \right] \dots\dots (15)$$

So we can see from equation (15) the factor in front of the bracket is exactly same as Rydberg Constant so

$$R = \frac{4}{B} = \frac{m_e e^4}{8\epsilon_0^2 h^3 c} = 1.0973 \text{ cm}^{-1}$$

Or in the form of the Rydberg unit of energy[5]

$$1R = 13.605 \text{ eV}$$

Birge–Sponer method

It is method to find the dissociation energy, which is the standard enthalpy change when a bond is cleaved by homolysis[6], by observing transitions between vibration energy levels where the vibration energy levels approximation to the first order as it given in equation(16).

$$E_v = \left(v + \frac{1}{2}\right)\omega_e - \left(v + \frac{1}{2}\right)^2 \omega_e x_e \dots\dots (16)$$

Where the v is vibration quantum number such that $v=0,1,2,3,\dots$, ω_e vibration wavenumber and x_e is the anharmonicity constant. To find the Spectroscopic dissociation energy we have to set $\left(\frac{dE_v}{dv} = 0\right)$ to determine the maximum value of the vibration quantum number. So the Spectroscopic dissociation energy as shown in equation(17). Also we can find the thermodynamic dissociation energy, which is related to the Spectroscopic dissociation energy by equation (18).

$$D_e = E_{v_{max}} = \frac{\omega_e^2}{4x_e \omega_e} \dots\dots (17)$$

$$D_0 = D_e - E_0 = \frac{(\omega_e - \omega_e x_e)^2}{4x_e \omega_e} \dots\dots (18)$$

So the $-\omega_e x_e$ is the slop that can find by using the Birge–Sponer plot as shown in the figure(3) after plotting between $\Delta\omega_e$ on y-axis and v on the x-axis.

Researchal Set-Up

Monochromator

Monochromator is a device, as shown in the figure (4),that can produce monochromatic light. It can use for the optical dissociation with a prism or for the diffraction by using diffraction grating. We used in this research the





T.A Ali Al-dulaimi et al.

monochromator with diffraction grating technique. There are two types of diffraction grating the plane gratings and concave grating but we used the concave grating, which is an optical device that its surface is covered by a reflective coating[2], or in her words it is a device that separating the incident light into colors as shown in the figure (5). The concave grating is located inside the monochromator and the monochromator has two slits one for the input light and the other for output light and all the input, output slits and the concave grating are located in such a way called Rowland circle.

Photomultiplier

The PMT is a vacuum tube that has an input window photocathode, focusing electron, an electron multiplier and an anode as shown in the figure (6). When the photon incidents to the PMT will absorb and electron will emit from the photocathode and this electron will focusing to the dynode, and this electron will amplify several times in the dynode until the electrons reach the anode[7]

High Voltage Power Supply

It device that supply a voltage to the PMT because usually the PMT needs high voltage and we supply the PMT by 950 volts in this research by using the high voltage power supply with a negative polarity.

Light Sources

We used in this research the cold cathode light, which is cathode that is not electrically heated by a filament and used in gas-discharge lamps, and the light sources that we used are Hydrogen, Helium, Neon, Mercury. In addition to cold cathode types we used the Tungsten-Halogen.

Software

We used the Analog-to-digital converter that converts the output of the PMT signals from analog to digital so that the computer can read and plot the signal. Also we used the Lab view program to scan the spectrum and Igor program to plot the data.

Procedure

The Calibration Constant

We found the calibration constant by scanning the Mercury source lamp, from 5000Å^0 to 7500Å^0 and Neon sources lamp, 2600Å^0 to 6000Å^0 and we set the velocity of the monochromator to $100 \frac{\text{Å}^2}{\text{minute}}$, and their spectra are as shown in the figures (7) and (8), respectively. Then we identified the peaks for each of them after that we compared the measured values for each peak with the actual value that is given in the lab manual. Then we plotted the actual on the y-axis and the measured values on the x-axis as shown in the figure (9).

Rydberg Constant

We used seven different Hydrogen lamps to find the Rydberg constant. As we know that there are sex different series that describe the spectrum line emissions of the Hydrogen atom. However, we chose the Balmer series, which is the transition from $n \geq 3$ to $n = 2$ where n is principle quantum number, because the Balmer series are located in the visible part of the spectrum. Therefore we scanned the Hydrogen in the visible part of the spectrum, which is





T.A Ali Al-dulaimi et al.

from 3500 \AA^0 to 6500 \AA^0 , and the spectrum for the seven Hydrogen lamps as shown in the figure (10). Then we identified the peaks from all seven sources and calibrated them by multiplying them by the calibration constant that we found in part (1). After that we used equation(2) to plot between $(1/\lambda)$ after converted the (λ) to cm^{-1} unit, which is the unit of the energy, on the y-axis and (n) principle quantum number on the x-axis as shown in the figure(11) and the slope is Rydberg constant, which is $1.0859 \times 10^7 \pm 527 \text{ cm}^{-1}$. Finally we can see from figure(10) there are four different peaks and we were able to know the transition for each wavelength such that the first wavelength(4868 A) is corresponding the transition from $n=4$ to $n=2$, the second one (4355 A) is corresponding to the transition from $n=5$ to $n=2$, the third one (4117 A) is corresponding to the transition from $n=6$ to $n=2$, and the fourth one (3991 A) is corresponding to the transition from $n=7$ to $n=2$.

Helium Spectra and Its Transition

The Helium atom has two electrons and according to Pauli Exclusion Principle the two electrons cannot occupy the same quantum state simultaneously. Therefore, the states with an antisymmetric spin function are known as *parahelium*, and states with a symmetric spin function are known as *orthohelium*. Since the ground state always has a symmetric spatial function, it is always parahelium, but the excited states all come in both forms as shown in the figure (12). And we scanned the Helium in the visible range of the spectrum as shown in figure (13). Finally we identified the peaks then find the correspond transition for each wavelength as indicated in the table(1) below.

Iodine-vapor Absorption and Dissociation Energy

In this part of the research we used the Tungsten-Halogen as a light source and we focused the light such that it can pass through the non-aluminized areas of the bulb, which contains the Iodine-vapor, to the monochromator. Then we recorded the absorption spectrum in the visible part of the spectra as shown in the figure (14). We can see from figure (14) the spectrum is continuous the reason for that is the incident light has many different wavelengths and the spectrum represents the part of the incident light that has not been absorbed. Also we can see from the Iodine-vapor that the spectrum has a convergence limit point at wavelength equal to 5200A and at this point the spacing between the peaks decreasing to zero and beyond this point the spectrum is continuous because the excited state of the Iodine-vapor molecule is not bound. Therefore we identified the absorption spectrum of from 5200 A to 6000 A. And we identified the wavelengths and compared them with the actual values that are given in the laboratory manual in order to know the upper state quantum number and then find $\Delta\omega$, which is the difference in energy between two levels for example $\Delta\omega_{16} = \omega_{16} - \omega_{15}$ as shown in the figure(between as shown in the table (2)).

Then we plotted "Birge-Sponer plot " between $\Delta\omega$ on the y-axis and ν' on the x-axis as shown in the figure (16). The slope, which represents the $2x_g\omega_g$ value, was 1.9901 ± 0.318 and the vertical intercept, which represents the $(\omega_g - \omega_g x_g)$ value, was 132.16 ± 9 . Finally we were able to calculate the following quantities:

- 1- The harmonic frequency from

$$\omega_g - \frac{\text{slope}^2}{2} = \text{vertical intercept} = 132.16 \text{ so } \omega_g = 133.155 \text{ cm}^{-1}.$$

- 2- The anharmonicity constant value from $-2x_g\omega_g = \text{slope} = -1.9901$ so $x_g = 0.00747$.

- 3- The spectroscopic dissociation energy

$$D_g = E_{Vmax} = \frac{\omega_g^2}{4x_g\omega_g} = 4388.2 \text{ cm}^{-1}.$$

- 4- The thermodynamic dissociation energy $D_0 = \frac{(\omega_g - \omega_g x_g)^2}{4x_g\omega_g} = 4388.2 \text{ cm}^{-1}$

- 5- The Summary





T.A Ali Al-dulaimi et al.

In this research we measured both emission spectrum for Mercury , Neon, Helium and Hydrogen, and the absorption spectrum for the Iodine-vapor. And we found the calibration constant, which was 1.001, by using the Mercury and Neon spectrum after compared the measured values with the actual values. Then we found the Rydberg Constant by using the Hydrogen spectrum in visible part of the spectrum , which is Balmer Series, and it was $1.0859 \times 10^5 \pm 527 \text{ cm}^{-1}$. Also we identified the correspond transition for Helium after identify all the peaks from its spectrum plot and calibrated them and all these transitions are shown in table (1).

Finally we found the spectroscopic dissociation energy for the Iodine-vapor, which was $D_e = 4388.2 \text{ cm}^{-1}$, by using its absorption spectrum and the thermodynamic dissociation energy ,which was $D_0 = 4388.2 \text{ cm}^{-1}$, by using its absorption spectrum too, also we found the harmonic frequency ,and the anharmonicity constant value .

REFERENCES

- [1]http://www.tau.ac.il/~phchlab/researchs_new/LIF/theory.html
- [2]http://ssioptics.com/cart/index.php?dispatch=pages.view&page_id=31#concave
- [3]http://en.wikipedia.org/wiki/Balmer_series
- [4]http://en.wikipedia.org/wiki/Bohr_model
- [5]http://en.wikipedia.org/wiki/Rydberg_constant
- [6]http://en.wikipedia.org/wiki/Bond-dissociation_energy
- [7]Photomultiplier Tubes Basics and Applications , third edition.
- [8]<http://hyperphysics.phy-astr.gsu.edu/hbase/quantum/helium.html>
- [9]http://en.wikipedia.org/wiki/Rydberg_constant#cite_ref-codata_2-0
- [10]<http://home.sou.edu/~chapman/ch445/Iodine.htm>

Table.1. Helium Transition

Measured $\lambda(\text{Å})$	Calibrated $\lambda(\text{Å})$	Actual $\lambda(\text{Å})$	Transitions
3982.01	3985.99	3972	2s \rightarrow 4d
4043.55	4047.6	4026.2	2p \rightarrow 5d
4137.07	4137.07	4143.8	6d \rightarrow 2p
4485.51	4489.99	4471.68	4d \rightarrow 2p
4724.72	4729.44	4713.37	4s \rightarrow 2p
4930.07	4935	4921.9	4d \rightarrow 2p
5022.42	5027.44	5015.7	3p \rightarrow 2s
5863.36	5869.22	5875.6	3d \rightarrow 2p
6654.35	6661	6678.2	3d \rightarrow 2p





T.A Ali Al-dulaimi et al.

Table.2. $\Delta\omega$ values

upper state quantum number n_f	Wavelength λA^0	$\frac{1}{\lambda} cm^{-1}$	$\Delta\omega cm^{-1}$
15	5761.5	17356	----
16	5731.4	17447	91
17	5691.6	17569	122
18	5664.3	17654	84
9	5641.3	17726	71
20	5610.2	17824	98
21	5570	17953	128
22	5545	18034	80
23	5520	18115	81
24	5493	18204	89
25	5470	18281	76
26	5445.6	18363	81
27	5423.5	18438	74
28	5402.2	18510	72
29	5380.7	18584	73
30	5361.1	18652	67
31	5344.6	18710	57
32	5323.4	18784	74
33	5305.3	18849	64
34	5288.3	18909	60
35	5268.2	18981	72
36	5255.3	19028	46
37	5240.3	19082	54
38	5224.2	19141	59





T.A Ali Al-dulaimi et al.

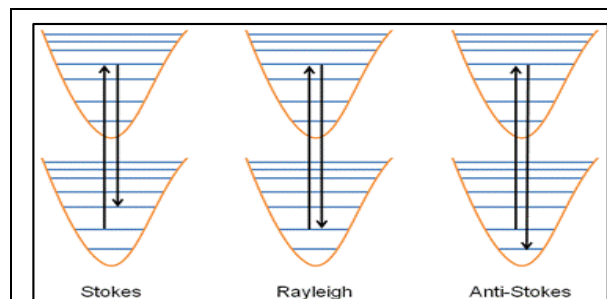


Fig.1. Stokes ,Rayleigh, and Anti-Stokes transitions

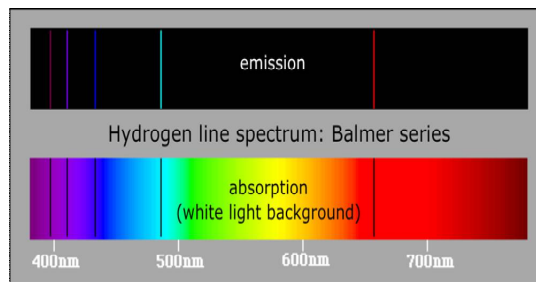


Fig .2.Hydrogen Spectra

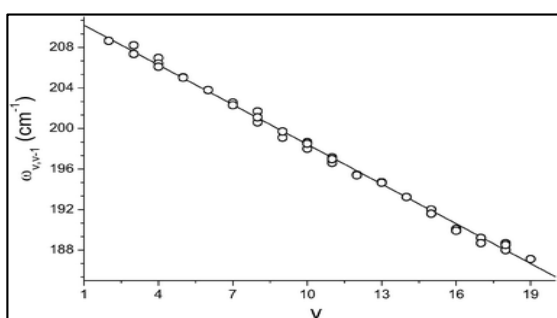


Fig.3. Birge-Sponer plot



Fig .4. The Monochromator

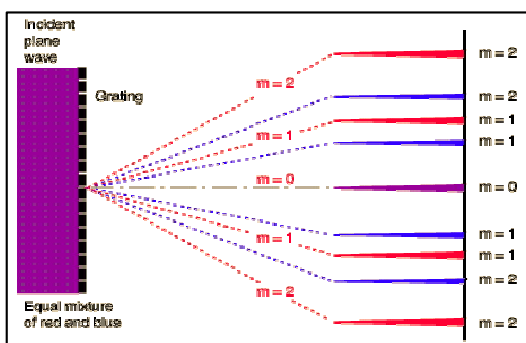


Fig .5. Diffraction Grating

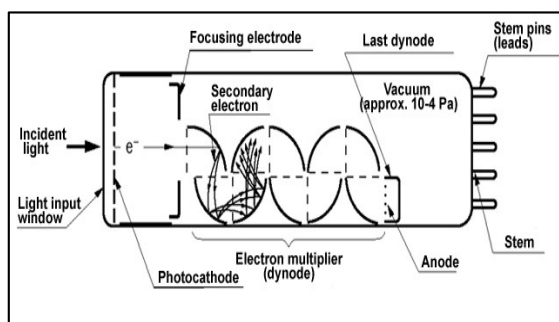


Fig .6. PMT

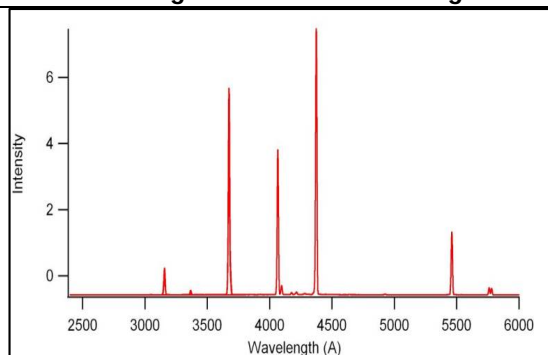


Fig.7. Hg Spectrum

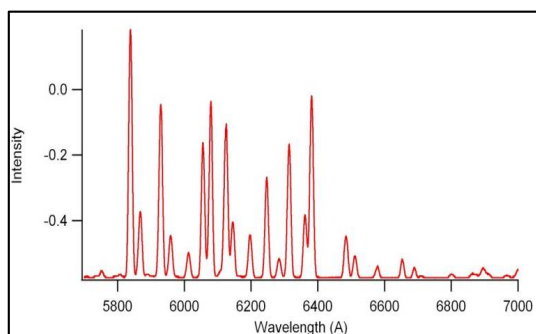


Fig.8. Ne Spectrum





T.A Ali Al-dulaimi et al.

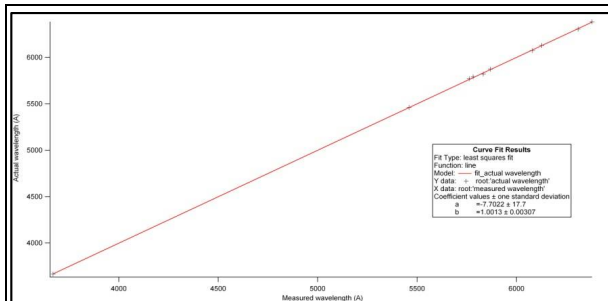


Fig.9. Calibration constant

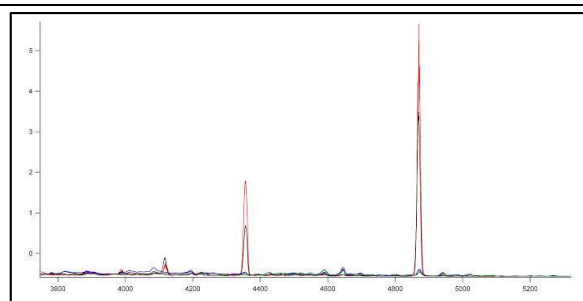


Fig.10. The Spectra for seven Hydrogen lamps

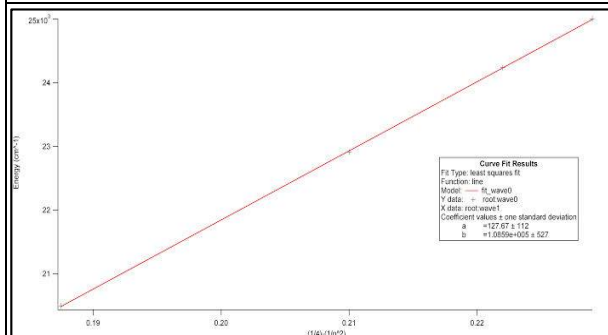


Fig.11. Rydberg Constant Plot

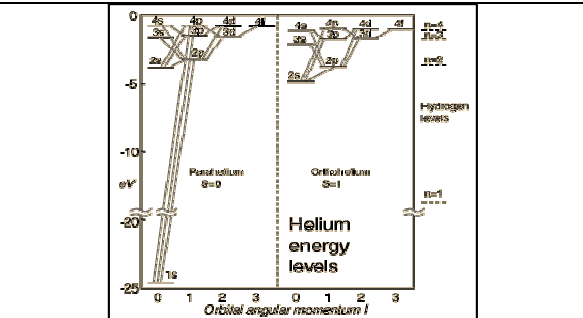


Fig.12. Transitions in the Helium atom[8]

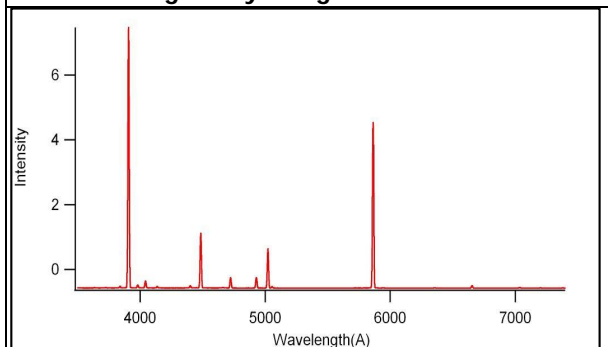


Fig.13. Helium Spectrum

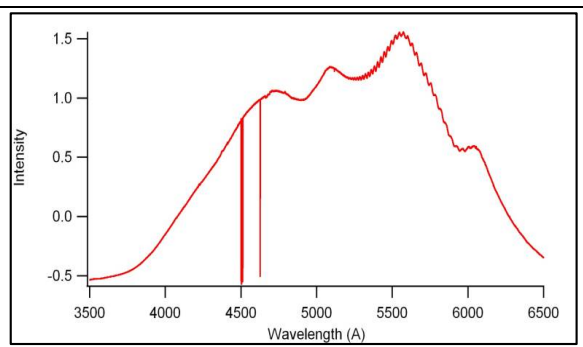


Fig.14. Iodine-vapor Spectrum

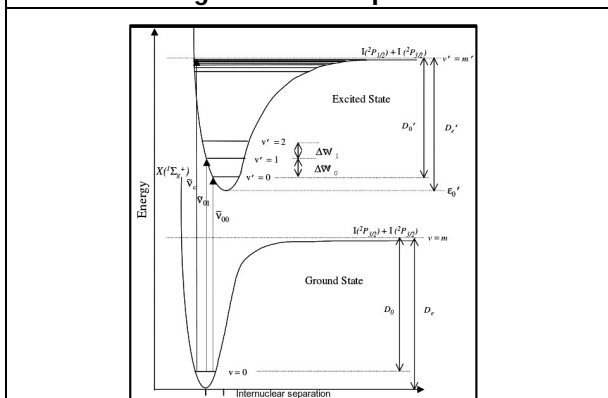


Fig.15. Electronic states of the iodine molecule

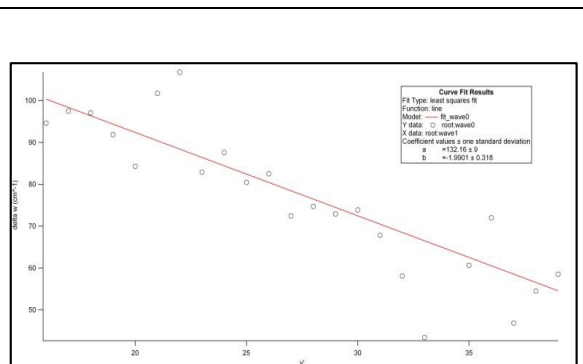


Fig.16. Birge-Sponer plot

